Departament de Teoria
del Senyal i Comunicacions
UNIVERSITAT POLITÈCNICA DE CATALUNYA

Ph.D. Dissertation

POLARIMETRIC DIFFERENTIAL SAR INTERFEROMETRY WITH GROUND-BASED SENSORS

Luca Pipia

Xavier Fàbregas Cànovas, Thesis Advisor

Barcelona, July 2009

A Tore[†] *e Maria, Francesco e Fabrizio*

...per essermi stati sempre accanto
in questo lungo, lungo viaggio…

Akwnoledgments

The author would like to thank the following institutions which have contributed, in one way or another, to this work:

- The European Commission for providing the pre-doctoral fellowship during the first two years of this thesis in the framework of the *Applied Multiparameter Environmental Remote Sensing – AMPER* (contract number HPRN-CT-2002-00205) of the *Research Training Network* (*RTN*) Programme.

- The *Universitat Politècnica de Catalunya* (*UPC*) for providing a two-year pre-doctoral grant in the framework of the the *UPC RECERCA* Programme.

- CICYT (Comisión Interministerial de Ciencia y Tecnología) for providing financial support for the last part of the research undertaken in this tesis, under the projects TEC 2005-06836-C0201 and TEC2008-06764-C02-01.

- The Institut Geològic de Catalunya (IGC) and the Institut Cartogràfic de Catalunya (ICC) for funding the experimental campaign in Sallent and for their support in providing ground-truth measurements.

Contents

Chapter 1

Introduction

Remote Sensing may be defined as the science of obtaining information about phenomena without being in physical contact with them. More concrete definitions refer to remote sensing as the science of acquiring, processing and interpreting data describing the interaction between the electromagnetic energy and the matter. There exist several remote sensing technologies. They may be classified either according to the electromagnetic energy source or the frequency the specific sensor works at. In the first case, it is distinguished between *active* remote sensing, when the illumination source is provided by the measuring sensor itself, and *passive* remote sensing, when the sensor measures the spontaneous radiation of the observed objects. Contrarily, the second classification essentially distinguishes between *microwave* and *optical* systems. Among the different remote sensing systems, Synthetic Aperture Radars (SAR) probably represents the most successful example of active microwave sensor.

Synthetic Aperture Radar (SAR) is a coherent active microwave technique able to provide bi-dimensional reflectivity images of areas of interest with high spatial resolution, independently of he day-night cycle and weather conditions. Although the potentials of SAR technology had been grasped since the first experiments in the 1970s, it was with the operative introduction of interferometry [Zebker,86] and polarimetry [Zebker,87] in the 1980s that the field of SAR remote sensing changed dramatically, opening the door to a wide spectrum of operational and research applications.

First polarimetric studies with SAR sensors dealt with the characterization of the scattering mechanisms from different types of natural surfaces through the analysis of their multi-frequency/multi-polarization response [Ulaby,82] [Zyl,87] [Zyl,89]. With the successive

development of polarimetric airborne systems, such as the TOPSAR [TOPSAR], C/X-SAR [CXSAR], EMI-SAR, E-SAR [ESAR], RAMSES [Debois,02], and the availability of multi-frequency polarimetric SAR data, several refined EM models were developed for the description of the scatterers' properties [Ulaby,90]. Besides, following the idea of decomposing the scattering complexity into elementary processes, different coherent [Cameron,90] [Krogager,90] and incoherent [Cloude,97] [Huynen,70] [Holms,88] [Holms,98] decomposition methods were also proposed during last two decades. Their employment encompasses a wide spectrum of applications, such as agriculture, forestry, hydrology, sea-ice monitoring and classification, and oceanography, and turns polarimetry into an operative technology for the retrieval of geo- and bio-physical parameters.

SAR interferometry deals with the estimation of terrain topography by combining two complex SAR images acquired from slightly different look angles. Despite the possibility to relate the phase difference between a pair of SAR images to the terrain relief dates back to 1974 [Graham,74], first results using airborne and satellite-borne SAR sensors were obtained about one decade later [Zebker,86] [Gabriel,88]. The technique remained in an early development stage until the launch of the European Space Agency (ESA) ERS-1 radar satellite, in 1991, made high quality interferometric data widely available. From that moment on, a great deal of remote sensing investigation started being focused on the development of interferometric processing techniques as well as on the definition of future implementations' requirements.

The most notable application of SAR interferometry is the so-called differential interferometry. Through the combination of ERS-1 images separated in time with a Digital Elevation Model (DEM), SAR interferometry was demonstrated to represent a powerful tool to monitor Earth's geodynamic phenomena [Massonet,93]. After removing the interferometric phase contribution of topography using an external DEM, the remaining phase, called differential phase, directly describes the total amount of radial deformation occurred during the acquisitions time span with an accuracy in the order of wavelength fractions. This approach is usually defined as classical differential SAR interferometry (DInSAR). When multi-temporal SAR acquisitions are available, it also possible to estimate the temporal evolution of the deformation process in terms of linear and non-linear components through the combination of time-independent samples. The algorithms carrying out this type of analysis are usually referred to as advanced DInSAR technques. Alternative coherence-based and amplitude-based approaches for the estimation of pixels'

trustfulness and the retrieval of the corresponding differential information can be found in [Ferretti,00] [Ferretti,01] and [Mora,03] [Lanari,04] [Fornaro,09], respectively.

In the last years, the introduction of polarimetric techniques in interferometric applications has yielded the development of a new research field defined as polarimetric SAR interferometry or PolInSAR. By joining the capability of polarimetry to separate independent scattering mechanisms and the sensitivity of interferometry to phase centers' elevation, PolInSAR techniques aims at volumetrically characterizing the distribution of the scatterers within the observed scenario. Estimation of forested areas' [Cloude,98] [Papathanassiou,01] and buildings' [Guillaso,05] elevation, forest biomass [Mette,03] [Lavalle,08] and glaciers monitoring [Landes,07] are just examples of very promising applications based on PolInSAR observations. All these techniques have been mainly assessed with SAR acquisitions from air-borne systems such as TOP-SAR (NASA/JPL, USA)[TOPSAR], C/X-SAR (CCRS, Canada)[CXSAR], EMI-SAR (Danish Center for Remote Sensing), E-SAR (DLR, Germany) [ESAR], RAMSES (ONERA, France) [Debois,02]. With the recent launch of polarimetric satellite-borne SAR systems, namely the *L*-band ALOS PalSAR in February 2006, the *X*-band TerraSAR-X in July 2007, the *C*-band RadarSAT2 in December 2007), a great deal of interest is now focused on their extension to satellite observations, which will provide the further advantages of platform higher stability and synoptic views of the Earth surface.

If the use of satellite-borne systems is extremely successful for the study of the evolution of slow-time processes over wide areas, it reveals being often unsuitable when high flexibility in terms of revisiting time is needed, as to foresee possible hazard conditions. For this reason, during the last years the research activity of several remote sensing groups has been devoted to the development of terrestrial SAR systems. Easy to deploy, extremely cheaper if compared to space-borne solutions, ground-based SAR (gbSAR) sensors represent a cost-effective solution for the continuous monitoring of small scale phenomena. These systems basically consist of a continuous-wave (CW) radar [Skolnik, 90] [Soumek, 99] mounted on a sliding support and synthesizing in time an aperture longer than the physical dimension of their real antennas. They aim at merging the SAR capability to obtain 2D reflectivity images and the advantages offered by a terrestrial platform, namely the high stability, the perfect knowledge of sensor's track and the absence of any revisiting time constrain. First experiments reaches back to 90s of last century, when in-door experiments were carried out to better understand the microwave backscattering characteristic of

vegetations and soils [Morrison,96]. Afterwards, several outdoor systems were designed to be easily deployable at a wide set of environments for differential applications. The solution mostly adopted [Bennet,96] [Pieraccini,00] [Luzi,04] [Zhou,04] [Nico,05] [Noferini,05] is the use of a Vector Network Analyzer (VNA) for the transmission of stepped-frequency *bandpass* signal at each position of the rail. The employment of VNAs constitutes an advantage as well a drawback for a gbSAR implementation. On the one hand, VNAs provide a high versatility to generate tones from low up to high frequencies and the opportunity to simplify the hardware complexity. On the other hand, the time required for the sweeping process may come to be comparable to the decorrelation of troposphere medium [Pipia,08] or of the scenario itself. In fact, acquisition time turns out to be linearly proportional to parameters as signal bandwidth or cross-range minimum sampling, as well as the number of polarization channels to be gathered. Accordingly, only single-pol gbSAR systems have been herein employed for long-time monitoring activities, with time performance going from 12 up to 20 minutes for about two meter long synthetic apertures. Few examples of out-door VNA-based polarimetric gbSARs can be also found in [Zhou,04] [Morrison,08]. Despite the very interesting results these systems provided in near-range measurements campaigns, they never came to an operative configuration for the long-time observation of wider scenarios. It can be concluded that VNA-based architecture does not constitute a feasible solution for multi-polarization gbSAR continuous observations.

A breakthrough in the gbSAR research field is represented by the polarimetric interferometric sensor developed by the Remote Sensing Laboratory (RSLab) at the Universitat Politècnica de Catalunya (UPC) [Aguasca,04]. A specific hardware based on a Direct Digital Subscriber (DDS) chipset was devised for time-optimizing the process of microwave signal generation and trasmission. The design of the instrument is flexible and adaptable to different frequency bands (L, C, X, and Ku-band), ensuring a wide range of applications with commercial off-the-shelf components. As a result, the time required for the scanning process reduces significantly with respect to any VNA-based system. Indeed, the UPC sensor constitutes a reliable prototype of a new generation of fast gbSAR systems that make it possible to acquire high-quality zero-baseline PolSAR data without any revisit time constraint. The importance of this fact is twofold. On the one hand, fast gbSARs provide a new dimension of analysis of the scatterers' dispersion properties yet unexplored, i.e. the time. On the other hand, they open a still unexplored research line where two up-to-now independent topics, the differential SAR interferometry and the SAR polarimetry, may

converge. Since the two main factors limiting any advanced DInSAR technique are the number of trustful points within the observed area and the quality of corresponding phase information, the scope of this thesis is essentially to answer to the following two questions:

"Can a polarimetric formulation of the DInSAR analysis improve the quality of the deformation process estimation with respect to single-polarization approach?" And *"How to proceed in order to effectively extract useful differential information from long-time polarimetric SAR observations?*"

In order to cope with these two issues, long-time polarimetric data sets acquired using the UPC ground-based SAR system are employed. Accordingly, the work presented in this PhD dissertation is mainly divided into two main parts.

The first one deals with the description of the techniques that had to be developed to make the UPC system operative and its acquisitions easy to use, including the mathematical formulation of its working principles, the specific processing chain that its raw data requires, the geocoding procedure necessary for the correct interpretation of the retrieved information, and the algorithms compensating for the atmospheric artefacts that usually affect gbSAR differential acquisitions.

The second part deals with the study of the benefits that polarimetric SAR measurements may provide with respect to single-polarization data for differential applications. For this purpose, a one-year collection of gbSAR polarimetric measurements acquired by RSLab in an area subject to subsidence phenomena will be employed.

The organization of the thesis is consequently as follows:

In **Chapter 2**, the main concepts of radar polarimetry will be briefly recalled. The polarization properties of the electromagnetic waves will be introduced as a powerful tool to better understand the behavior of scatterers within an observed scenario. In particular, attention will be given to the relation between propagating-wave polarization features and transmitting/receiving antennas polarizations. Then, the main descriptor of the scattering problem, i.e. the scattering matrix [*S*], will be brought in to outline the basic properties of deterministic and non-deterministic targets. The Chapter ends up with an overview of the different coherent and incoherent polarimetric decomposition theorems available in the literature.

In **Chapter 3**, a mathematical formulation of the acquisition process performed by UPC gbSAR system and a theoretical description of its range and cross-range imaging properties will be carried out. Concerning the range domain, specific hardware solutions make the system unique in the

scientific community. Accordingly, the description of the range processing chain will be focused on the particular case of the UPC sensor. Contrarily, the main properties of thie cross-range domain are shown to be related to the short dimension of the aperture that a terrestrial platform is able to synthesize. Then, the analysis of the slow-time domain will be representative of any gbSAR sensor.

Chapter 4 will provide a comprehensive analysis of the processing chain developed for the UPC sensor's raw data. First, a brief comparison between the architecture of VNA-based and DDS-based gbSAR systems will be carried out. Then, the whole processing chain leading to calibrated PolSAR data sets will be discussed in detail, paying special attention to the parameters affecting the quality of amplitude and phase information. The problem of polarimetric measurements meaningfulness and of the limitations arising from the use of wide beamwidth antennas will be also addressed. In the end, the test-sites chosen for the two main experimental campaigns held during this PhD research will be briefly introduced.

In **Chapter 5**, the basic formulations of InSAR and Differential InSAR (DInSAR) techniques will be adapted to the gbSAR case. The geometrical relation between the interferometric phase and the height/radial displacement of a scatterer will be carried out for the specific case of Short Synthetic Aperture (SSA). Then, the concept of coherence, as a useful quality-descriptor of the estimated interferometric phase will be introduced. Special care will be taken in the simplification of many decorrelation factors affecting the air- and space-borne SAR acquisitions but negligible in gbSAR data sets. In the last part, the problem of DEM retrieval from gbSAR interferometric data and images geocoding will be addressed. The classical approach proposed in literature, which deals with the two issues separately, will be briefly recalled. Afterwards, an alternative iterative method worked out in the framework of this thesis and solving the two problems at once will be put forward and assessed using real gbSAR data.

Chapter 6 will describe the way changes in the troposphere directly affect gbSAR zero-baseline (*0B*) differential coherence and phase. First, the simplest condition of propagation through a homogeneous medium will be studied. A linear propagation model will be introduced to work out a set of coherence-based techniques compensating for phase artefacts due to refractive index changes. Then, the problem of the inhomogeneity characterizing the troposphere medium under turbulent atmospheric conditions is addressed. Changes of the medium during the aperture synthesis will be shown to generate unpredictable atmospheric artefacts in zero-baseline gbSAR

acquisitions. The need to reduce as much as possible the gbSAR acquisition time in order to fulfil the troposphere homogeneity hypothesis during the whole aperture synthesis, and, hence, guarantee the reliability of the retrieved scattering information, will be finally emphasized.

In **Chapter 7**, the problem of the temporal stability of polarimetric response from an urban environment at short time-scale, i.e., one-day, and long time-scale, i.e., months, is introduced. The measurements campaign the Remote Sensing Lab (RSLab) carried out in the village of Sallent, northeastern Spain, will be presented in detail. The field experiment was funded by the Institut Geològic de Catalunya (IGC) and aimed at studying the subsidence phenomenon induced by the salt mining activity of the past decades using the UPC sensor. One-day collections of PolSAR data were monthly acquired at X-band from June 2006 to July 2007 with exactly the same observation geometry. The high sampling step used for the daily acquisitions will give the opportunity to observe the non-stationary polarimetric answer pixels within the urban scene often present. This unexpected behavior will be analyzed using both coherent and incoherent descriptors. Afterwards, a filtering procedure aiming at reducing the randomness of the backscattering from the deterministic environment will be proposed. The improvements provided by the filtering procedure will be finally assessed in terms of polarimetric time-entropy decrease over the urban area.

In **Chapter 8**, the problem of retrieving deformation information from zero-baseline polarimetric gbSAR acquisitions will be tackled. First, a pre-processing chain compensating for the atmospheric phase artefacts arising in long-time span gbSAR differential interferograms will be put forward. Then, an advanced DInSAR technique, the Coherent Pixel Technique (CPT) [Mora,03], will be employed to look into the benefits provided by fully polarimetric data. After applying the classical technique to each polarization channel separately, a new polarimetric criterion will be proposed. For the first time, the polarimetric information contained in the different polarimetric channels will be combined to enhance the performance of the selection technique in terms of number of reliable pixels and differential coherence quality. The results in terms of deformation-rate map retrieval achieved with the two approaches will be compared and the advantages offered by SAR polarimetry for differential applications pointed out. Afterwards, the possibility to extend polarimetric coherence-optimization techniques [Colin,06] [Sagues,00] [Cloude,98] to the *0B* case will be briefly investigated. Special emphasis will be given to the statistical hypothesis each optimization method relies on and to the main scattering properties

characterizing the urban scenario of Sallent. In the end, preliminary results will be shown to stress the advantage and drawbacks of the different optimization approaches and the need to better understand their effect in terms of phase-centers movement when polarimetric time-stationarity and spatial-homogeneity hypotheses are not fulfilled.

Finally, **Chapter 9** will summarize the obtained results and draw the main conclusions coming out from this PhD research study.

Chapter 2

Radar Polarimetry

The polarization properties of the electromagnetic waves constitute the fundamentals of radar measurements. They describe the vector nature of their electric and magnetic fields during propagation and must be taken into account in order to better understand the scattering behavior of an illuminated scenario. In this Chapter, the main concepts of radar polarimetry are reminded. Particular attention is given to the relation between traveling-wave polarization features and transmitting/receiving antennas polarizations. Then, the main descriptors of the scattering problem will be brought in to highlight the basic properties of deterministic and non-deterministic (or distributed) scatterers. The Chapter ends up with a brief overview of the different coherent and incoherent scattering decomposition theorems available in the literature.

2.1 Electromagnetic waves polarization

The concept of electromagnetic wave polarization directly derives from a particular solution of Maxwell's electromagnetic equations. Since detailed descriptions are available in [Conciauro,03],[Balanis,89], we report here just the main results of the whole mathematical formulation that are required to easily follow the study presented in this PhD dissertation. The Maxwell's equations for a linear homogeneous isotropic medium in the space-time harmonic domains are

$$\begin{aligned}
\nabla \times \vec{E}\left(\vec{r},t\right) &= -j\omega\mu_0\mu_r \vec{H}\left(\vec{r},t\right) \\
\nabla \times \vec{H}\left(\vec{r},t\right) &= j\omega\varepsilon_0\varepsilon_r \vec{E}\left(\vec{r},t\right) + \vec{J}\left(\vec{r},t\right) \\
\nabla \cdot \vec{E}\left(\vec{r},t\right) &= \frac{1}{\varepsilon_0\varepsilon_r}\rho\left(\vec{r},t\right) \\
\nabla \cdot \vec{H}\left(\vec{r},t\right) &= 0
\end{aligned} \tag{2.1}$$

where ($\vec{E}$, $\vec{H}$, $\vec{J}$) are the electric field, magnetic field and electric current density vectors, respectively, ω is the so-called *angular* frequency, ε_0 and μ_0 the electric permittivity and magnetic permeability in free space, ε_r and μ_r keep into account the specific properties of the medium, and ρ stands for the charge density. In the case of *free-source* and lossless medium, ε_r and μ_r are real and the linear equations system in Eq. 2.1 can be reduced to an uncoupled problem leading to the wave equation

$$\nabla^2 \vec{E}\left(\vec{r},t\right) + k^2 \vec{E}\left(\vec{r},t\right) = 0 \tag{2.2}$$

where the term ∇^2 is the linear vector Laplace operator [Conciauro,03] and *k* is the wavenumber parameter defined as

$$k = \omega\sqrt{\varepsilon_0 \varepsilon_r \mu_0 \mu_r} = \frac{\omega}{c}\sqrt{\varepsilon_r \mu_r}\,, \tag{2.3}$$

being *c* the speedlight in the vacuum. The time-space distribution of the electric field is obtained by solving the wave equation in Eq. 2.2 and it is equal to

$$\vec{E}\left(\vec{r},t\right) = \mathrm{Re}\left\{\vec{E}_0 e^{j\omega t} e^{-j\vec{k}\cdot\vec{r}}\right\} \tag{2.4}$$

where $\mathrm{Re}\{\cdot\}$ is the real operator of complex numbers and $\vec{k}$ is a generic vector whose module fulfills Eq. 2.3. Equal phase-fronts of $\vec{E}\left(\vec{r},t\right)$ are determined by setting $\omega t - \vec{k}\cdot\vec{r}$ to a constant value. It easy to note that at a fixed time instant, they correspond to planes of equal electric field amplitude orthogonal to $\vec{k}$ and propagating in the direction of $\vec{k}$. Such waves are known as plane electromagnetic (*EM*) monochromatic waves [IEEE,79]. Owing to the constraint on the module of $\vec{k}$, also the case of planar wave propagating into the opposite direction, i.e. $-\vec{k}$, is a solution of Eq. 2.2. Although plane waves are the simplest solution of the wave equation, it is worth stressing their usefulness for many real problems, as in the description of waves at large distances from their sources. The transverse vectorial nature of waves pointed out by Eq. 2.4 leads to the concept of the so-called wave polarization. If a right-handed orthogonal coordinate system $\left(\hat{h},\hat{v},\vec{k}\right)$ is adopted, the electric field $\vec{E}\left(\vec{r},t\right)$ (hereafter denoted just with $\vec{E}$) at each time can be decomposed as

$$\vec{E} = \left(\vec{h}\cdot\vec{E}\right)\hat{h} + \left(\vec{v}\cdot\vec{E}\right)\hat{v} = E_h\hat{h} + E_v\hat{v} \tag{2.5}$$

where the two components E_h and E_v are given by the projections of $\vec{E}$ onto the reference unit vectors and are equal to

$$\begin{aligned} E_h &= \mathrm{Re}\left\{\left(\vec{E}_0\cdot\vec{h}\right)e^{-j\vec{k}\cdot\vec{r}}e^{j\omega t}\right\} = \mathrm{Re}\left\{E_{h0}e^{j\delta_h}e^{j\omega t - j\vec{k}\cdot\vec{r}}\right\} = E_{h0}\cos\left(\omega t - \vec{k}\cdot\vec{r} + \delta_h\right) \\ E_v &= \mathrm{Re}\left\{\left(\vec{E}_0\cdot\vec{v}\right)e^{-j\vec{k}\cdot\vec{r}}e^{j\omega t}\right\} = \mathrm{Re}\left\{E_{v0}e^{j\delta v}e^{j\omega t - j\vec{k}\cdot\vec{r}}\right\} = E_{v0}\cos\left(\omega t - \vec{k}\cdot\vec{r} + \delta_v\right) \end{aligned}. \tag{2.6}$$

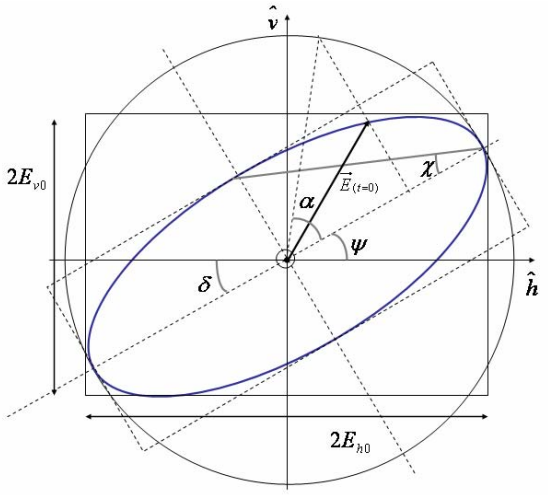

Fig. 2.1: Polarization Ellipse in the $\left(\hat{h},\hat{v},\vec{k}\right)$ Cartesian Reference.

Putting in evidence the quantity $\cos\left(\omega t-\vec{k}\cdot\vec{r}+\delta_h\right)$ and after some mathematics, Eq. 2.6 can be replaced by

$$\left(\frac{E_h}{E_{h0}}\right)^2+\left(\frac{E_v}{E_{v0}}\right)^2-2\frac{E_hE_v}{E_{h0}E_{v0}}\cos\delta=\sin\delta \tag{2.7}$$

where δ is the phase difference $\delta_v-\delta_h$. The last expression corresponds to the equation of a conic curve in Cartesian coordinates. Since the associated determinant is non-negative, Eq. 2.7 always describes an ellipse usually referred to as *polarization ellipse*. This is the curve that the tip of the electric field traces out on the plane orthogonal to $\vec{k}$ during wave propagation.

2.1.1 Waves polarization descriptors

The three quantities E_{h0}, E_{v0} and δ, define completely the polarization ellipse, as it is shown in Fig. 2.1. The first two terms correspond to the projections of the conic semi-axes onto the $\left\{\hat{h},\hat{v}\right\}$ reference system; contrarily, δ has no graphical interpretation. For this reason, more suitable parameters, denoted as the *orientation* ψ, the *ellipticity* χ and total intensity A_0, are commonly employed for the same purpose. The first two are based on the description of the geometrical properties of the polarization ellipse and defined as

$$\tan 2\psi=2\frac{E_{h0}E_{v0}}{E_{h0}^2-E_{v0}^2}\cos\delta \tag{2.8}$$

$$\sin 2\chi=2\frac{E_{h0}E_{v0}}{E_{h0}^2+E_{v0}^2}\sin\delta \tag{2.9}$$

where χ varies in the [-π/4, π/4] interval and ψ in the [-π/2, π/2] interval. As χ tends to zero, the ellipse degenerates to a straight line with tilt-angle equal to ψ and the polarization state is denoted

with the term *linear*. At the extremes of χ domain, the ellipse becomes a circle and polarization state is consequently defined *circular*. In the latter case, the value of ψ becomes irrelevant. The sign of χ determines the handedness of the electric field polarization. According to IEEE definition [IEEE,79], when a wave propagates in the $+\vec{k}$ direction, positive and negative values χ respectively define left-handed (anti-clockwise rotation) and right handed (clockwise rotation) states, while for $-\vec{k}$ propagations the situation inverts. Finally, the total intensity of the wave is given by

$$A_0 = E_{h0}^2 + E_{v0}^2 \tag{2.10}$$

that, together with ψ and χ, uniquely characterized a plane wave. The same information can be also expressed by the complex polarization ratio ρ, which relates the two orthogonal components of $\vec{E}(\vec{r})$ [Boerner, 98] as follows:

$$\rho = \frac{E_v}{E_h} e^{j(\delta_v - \delta_h)} = \frac{\cos(2\chi)\sin(2\psi) + j\sin(2\chi)}{1 - \cos(2\chi)\cos(2\psi)} = \tan\alpha e^{j\delta}. \tag{2.11}$$

The second equality in Eq. 2.11 points out the mathematical relation between the complex ρ and the couple of real parameters (χ,ψ); the two terms α and δ are usually referred to as Deschamps angles [Deschamps,51]. If the first descriptors are suitable for a graphical interpretation of the wave polarization concept, ρ makes it possible to mathematically introduce the concept of polarization orthogonality. For a given polarization state ρ, it is possible to define an orthogonal polarization state $\rho_\perp$ by the condition [Lüneburg,95]

$$\rho\rho_\perp^* = -1 \tag{2.12}$$

where the symbol * denotes the complex conjugate operation. Expressing the complex polarization ratio as a function of the orientation and ellipticity angles, the orthogonal polarization state can be obtained as

$$\rho(\psi,\chi) \Rightarrow \rho_\perp(\psi,\chi) = \rho\left(\psi + \frac{\pi}{2}, -\chi\right). \tag{2.13}$$

It is worth noting that the two unitary vectors $\hat{h}$ and $\hat{v}$ used to introduce the *polarization state* of a plane wave fulfill the condition described by Eq. 2.12. It follows that the electric field $\vec{E}$ in Eq. 2.5 is expressed as a linear combination of two orthonormal polarization states and that the polarization properties of the wave are completely defined by these two components. Then, it is possible to represent this information in a more practice way using a 2D complex vector defined as

$$\vec{E}_{hv} = \begin{bmatrix} E_h \\ E_v \end{bmatrix} = \begin{bmatrix} E_{h0} e^{j\delta_h} \\ E_{v0} e^{j\delta_v} \end{bmatrix}. \tag{2.14}$$

Eq. 2.14 is usually referred to as Jones vector [Born, 59] [Lüneburg,95] [Boerner, 98] and it is related to the parameters ψ, χ and ρ by the following expressions

$$\vec{E}_{hv}(\psi,\chi,\alpha) = E_0 e^{j\alpha}\begin{bmatrix}\cos\psi & -\sin\psi\\ \sin\psi & \cos\psi\end{bmatrix}\begin{bmatrix}\cos\chi & j\sin\chi\\ j\sin\chi & \cos\chi\end{bmatrix}\hat{h} \tag{2.15}$$

$$\vec{E}_{hv}(\rho,\alpha) = E_0 e^{j\alpha}\frac{1}{\sqrt{1+\rho\rho^*}}\begin{bmatrix}1 & -\rho^*\\ \rho & 1\end{bmatrix}\hat{h} \tag{2.16}$$

where α is the absolute phase at time $t=0$. It must be pointed out that once a reference system is fixed, the same Jones vector represents different polarization states if the wave propagates along $+\vec{k}$ of $-\vec{k}$, causing an ambiguity. In order to compensate this lack of consistency, the subscripts "+" and "-" are usually employed, distinguishing between $+\vec{k}$ and $-\vec{k}$ cases as follows

$$\vec{E}(\vec{r},t) = \mathrm{Re}\left\{\vec{E}_{hv+}e^{j\omega t - j\vec{k}\cdot\vec{r}}\right\} \tag{2.17}$$

$$\vec{E}(\vec{r},t) = \mathrm{Re}\left\{\vec{E}_{hv-}e^{j\omega t + j\vec{k}\cdot\vec{r}}\right\} \tag{2.18}$$

where E_{hv-} and E_{hv+} are related by a conjugate operation and denoted as the *directional* Jones vectors [Graves,56] [Lüneburg,02]. It is worth recalling that the employment of $\{\hat{h},\hat{v}\}$ basis for the description of plane waves' polarization properties is arbitrarily. Any other orthonormal basis $\{\hat{n},\hat{n}_\perp\}$ may be employed for the same purpose. Let ρ_n, χ_n and ψ_n be the complex polarization ratio, orientation and ellipticity associated to the polarization state $\hat{n}$ in the $\{\hat{h},\hat{v}\}$ reference, respectively. The Jones vector describing the same plane wave in the new polarization basis $\{\hat{n},\hat{n}_\perp\}$ is given by

$$\vec{E}_{n,n_\perp} = [U_2]_{\hat{n},\hat{n}_\perp}\,\vec{E}_{hv} \Rightarrow \begin{bmatrix}E_n\\ E_{n_\perp}\end{bmatrix} = \frac{1}{\sqrt{1+\rho_n\rho_n^*}}\begin{bmatrix}1 & \rho_n^*\\ -\rho_n & 1\end{bmatrix}\begin{bmatrix}e^{j\delta_n} & 0\\ 0 & e^{j\delta_n}\end{bmatrix}\begin{bmatrix}E_h\\ E_v\end{bmatrix} \tag{2.19}$$

where the phase term δ_n is obtained as

$$\delta_n = \arctan(\tan\chi_n \tan\psi_n)\,. \tag{2.20}$$

The matrix $[U_2]_{\hat{n},\hat{n}_\perp}$ is a 2×2 complex unitary matrix belonging to the SU(2) group [Cloude,86], whose columns are the vectors of the new basis $\{\hat{n},\hat{n}_\perp\}$ expressed in the original basis $\{\hat{h},\hat{v}\}$. Accordingly, given two arbitrarily othonormal polarization basis $\{\hat{n},\hat{n}_\perp\}$ and $\{\hat{m},\hat{m}_\perp\}$, the electric field $\vec{E}$ can be expressed as

$$\vec{E} = E_n\hat{n} + E_{n\perp}\hat{n}_\perp = E_m\hat{m} + E_{m\perp}\hat{m}_\perp \tag{2.21}$$

and the two Jones vectors are related by the transformation

$$\vec{E}_{m,m_\perp} = [U_2]_{(\hat{n},\hat{n}_\perp \to \hat{m},\hat{m}_\perp)} = [U_2]^{-1}_{\hat{m},\hat{m}_\perp} [U_2]_{\hat{n},\hat{n}_\perp} \vec{E}_{n,n_\perp} . \tag{2.22}$$

The last representation of the polarization state of a plane wave to be mentioned is the Stokes vector [Born,59] hereinafter denoted with $\vec{g}$. In the case of monochromatic waves propagating in the $+\vec{k}$ direction, the corresponding Stokes vector in the linear polarization basis $\{\hat{h},\hat{v}\}$ is defined as

$$\vec{g} = \begin{bmatrix} g_0 \\ g_1 \\ g_2 \\ g_3 \end{bmatrix} = \begin{bmatrix} |E_h|^2 + |E_v|^2 \\ |E_h|^2 - |E_v|^2 \\ 2\,\mathrm{Re}\{E_h^* E_v\} \\ 2\,\mathrm{Im}\{E_h^* E_v\} \end{bmatrix} . \tag{2.23}$$

The first component g_0 is the wave intensity while g_1 describes the power unbalance between the horizontal and vertical component of wave polarization. Concerning g_2 and g_3, they can be respectively interpreted as the amount of linear $\mp\pi/4$ and right/left circular polarizations characterizing the traveling plane wave [Born,59] [Schmeider,69]. A direct mathematical relation can be found between the four Stokes quantities and the previous sets of polarization descriptors, as follows

$$\begin{bmatrix} g_0 \\ g_1 \\ g_2 \\ g_3 \end{bmatrix} = \begin{bmatrix} E_{h0}^2 + E_{v0}^2 \\ E_{h0}^2 - E_{v0}^2 \\ 2E_{h0}E_{v0}\cos\delta \\ -2E_{h0}E_{v0}\sin\delta \end{bmatrix} = \begin{bmatrix} A_0 \\ A_0 \cos 2\psi \cos 2\chi \\ A_0 \sin 2\psi \cos 2\chi \\ -A_0 \sin 2\chi \end{bmatrix} . \tag{2.24}$$

Although $\vec{g}$ is a four-dimensional vector, from Eq. 2.24 it follows that

$$g_0^2 = g_1^2 + g_2^2 + g_3^2 . \tag{2.25}$$

A plane wave fulfilling the condition in Eq. 2.25 is called completely polarized wave because it behaves in a perfect deterministic manner. In this case, the terms g_1, g_2 and g_3 of the Stokes vector can be interpreted in terms of Cartesian components in a 3D real space and the polarization state *P* of a monochromatic plane wave can be mapped as a point on a sphere with radius g_0 called *Poincaré* sphere. As it is shown in Fig. 2.2, the latitude and longitude of *P* are given by the doubled ellipticity 2χ and orientation 2ψ, respectively. According to the interpretation given to these two parameters, it follows that, for a $+\vec{k}$ propagation, the left-handed polarization states are mapped in the north hemisphere whereas the right-handed ones in the south hemisphere. All the linear polarization states are instead represented by equatorial points, while the north and south poles correspond to the left-handed and right-handed circularly polarized waves, respectively.

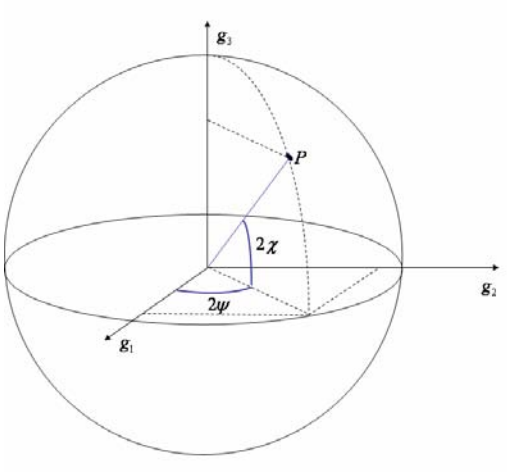

Fig. 2.2: Representation of fully-polarized plane wave on the Poincaré Sphere

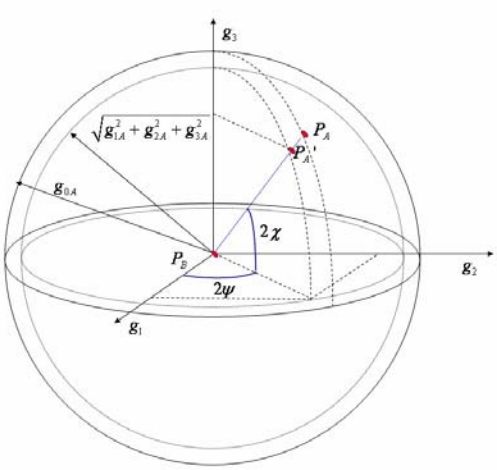

Fig. 2.3: Representation of partially-polarized (P_A-P_A') and fully-depolarized (P_B) plane waves on the Poincaré Sphere

The orthogonality condition stated in Eq. 2.12 translates into diametrically opposite points on the Poincaré sphere. As pointed out for the Jones vector formalism, also the coordinates of the Stokes vector are related to the specific polarization basis used for the description of the electric field. If the reference system changes, so do the quantities (g_1, g_2, g_3) in order to conserve the physical properties of the described wave. Without entering into details, we just point out that the Stokes vector describing the same plane wave but in a new polarization basis $\{\hat{n}, \hat{n}_\perp\}$ is obtained through a homomorphism transformation given by a real 4×4 matrix $[O]_{4\times4}$ [Cloude,96] that can be directly calculated from $[U_2]_{\hat{n},\hat{n}_\perp}$. Details about the mathematical formulation can be found in [Cloude,86].

2.1.2 Partially-polarized waves

There are two main advantages offered by Stokes representation. The first one is that physical dimension of $\vec{g}$ components is intensity, which makes it possible to determine the polarimetric properties of the wave via power measurements. This is crucial for example in optical polarimetry. The second reason is its ability to deals with partial polarized or quasi-monochromatic (QM) waves [Born,59]. These correspond to propagating plane waves for which the energy is concentrated in a narrow-band around a mean frequency. In contrast to monochromatic waves, the electric field of QM waves does not trace a clear time-invariant ellipse during the propagation. As a consequence, they cannot be represented using the Jones vector or any other equivalent description but must be analyzed as a random process. For this purpose, a generalized formulation of the Stokes vector may be employed. Denoting with <.> the statistical average over time or ensemble averages, $\vec{g}$ may be redefined as

$$\vec{g} = \begin{bmatrix} g_0 \\ g_1 \\ g_2 \\ g_3 \end{bmatrix} = \begin{bmatrix} \left\langle |E_h| \right\rangle^2 + \left\langle |E_v| \right\rangle^2 \\ \left\langle |E_h| \right\rangle^2 - \left\langle |E_v| \right\rangle^2 \\ \left\langle 2\,\mathrm{Re}\{E_h^* E_v\} \right\rangle \\ -\left\langle 2\,\mathrm{Im}\{E_h^* E_v\} \right\rangle \end{bmatrix} \tag{2.26}$$

and the equality stated in Eq. 2.25 turns into the inequality

$$g_0^2 \geq g_1^2 + g_2^2 + g_3^2 . \tag{2.27}$$

The polarized component of a quasi-monochromatic wave is given by the degree of polarization D_p defined as

$$D_p = \frac{\sqrt{\sum_{i=1}^{3} g_i^2}}{g_0} . \tag{2.28}$$

This descriptor ranges from 0 to 1, corresponding to the extreme cases of a fully depolarized and fully polarized wave. A geometrical interpretation of the Stokes vector's component is still possible, as shown in Fig. 2.3.

2.2 The scattering problem

When the electromagnetic plane waves generated by the transmitting antenna of a radar system illuminates a surface, part of the incident energy is absorbed and the rest is scattered away according to its geometrical and physical properties. A fraction of this scattered power propagates back towards the receiving antenna. The objective of the scattering analysis is essentially to retrieve information about the illuminated target by studying the properties of the received scattered signal. Before introducing the basic tools employed for the scatterers description, it is important to define the observation geometry under which targets are generally observed.

Let $(\hat{x}, \hat{y}, \hat{z})$ define a global Cartesian reference system centered at the target's position P within the scenario, as it is depicted in Fig. 2.4. The points P_{Tx} and P_{Rx} indicate the positions of the transmitting and receiving antennas. The propagation direction of the wave illuminating the target and of the wave scattered towards the receiving antenna are defined by the unitary vectors $\hat{k}_i$ and $\hat{k}_s$. These two vectors may be expressed in the $(\hat{x}, \hat{y}, \hat{z})$ reference system as

$$\begin{aligned} \hat{k}_i &= -\cos\phi_i \sin\vartheta_i \hat{x} - \sin\phi_i \sin\vartheta_i \hat{y} - \cos\vartheta_i \hat{z} \\ \hat{k}_s &= \cos\phi_s \sin\vartheta_s \hat{x} + \sin\phi_s \sin\vartheta_s \hat{y} + \cos\vartheta_s \hat{z} \end{aligned} . \tag{2.29}$$

Under far-field hypothesis [Balanis,89], the incident and scattered waves can be assumed plane and the corresponding electric fields can be completely described by orthonormal polarization

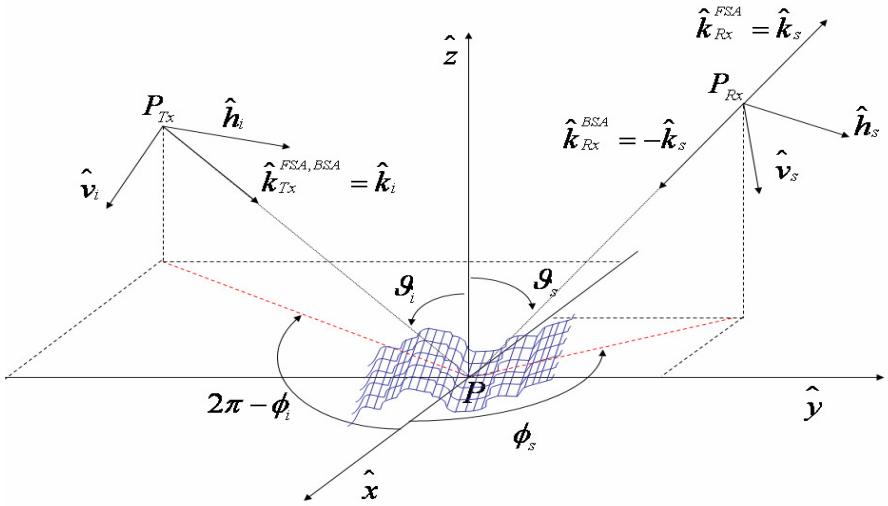

Fig. 2.4: Scattering Geometry and coordinates system in the FSA and BSA conventions.

bases. If a linear polarization basis $\{\vec{h},\vec{v}\}$ is employed, the transverse components of the illuminating and scattered fields can be hence referred to the local reference systems $\{\hat{h}_i,\hat{v}_i,\hat{k}_{Tx}\}$ centered at P_{Tx} and $\{\hat{h}_s,\hat{v}_s,\hat{k}_{Rx}\}$ centered at P_{Rx}, respectively. At this point, it is worth noting that there exist two different conventions for the definition of $\hat{k}_{Tx}$ and $\hat{k}_{Rx}$. The first one, called *Forward Scattering Alignment* or *FSA*, is consistent with the direction in which waves propagate [Ulaby,90]. The second one is the *Backward Scattering Alignment* or *BSA* and defines the polarization of a plane wave with respect to a propagation direction that always points away from the antenna, even when the antenna is used as receiver [Ulaby,90]. For the reference centered at P_{Tx} and describing the transmitted wave, the two conventions coincide:

$$\begin{aligned} \hat{k}_{Tx}^{FSA,BSA} &= \hat{k}_i \\ \hat{h}_i^{FSA,BSA} &= \hat{z}\times\hat{k}_i = \hat{h}_i \\ \hat{v}_i^{FSA,BSA} &= \hat{h}_i\times\hat{k}_i = \hat{v}_i \end{aligned} \quad . \tag{2.30}$$

On the contrary, for the receiving antenna centered at P_{Rx}, it results

$$\begin{aligned} \hat{k}_{Rx}^{FSA} &= \hat{k}_s = -\hat{k}_{Rx}^{BSA} \\ \hat{h}_s^{FSA} &= \hat{z}\times\hat{k}_s = \hat{h}_s = -\hat{h}_s^{BSA} \\ \hat{v}_s^{FSA} &= \hat{k}_s\times\left(\hat{z}\times\hat{k}_s\right) = \hat{v}_s = \hat{v}_s^{BSA} \end{aligned} \quad . \tag{2.31}$$

In the bistatic configuration of Fig. 2.4, where transmitter and receiver are located at different positions, there are not relevant reasons to prefer one convention to the other. Contrarily, in the monostatic situation, i.e. when the location of the transmitting and receiving antennas coincides, the use of *BSA* makes it possible to employ the same reference system for the two antennas, with a

significant simplification of the scattering formalism. Since SAR data are mostly acquired in this second mode, the *BSA* convention is generally preferred.

2.2.1 Scattering matrix [*S*] and polarimetric signature

When a scatterer is illuminated by an electromagnetic plane wave transmitted by a far-off antenna, the incident electric field may be described by the Jones vector formalism in the $\{\vec{h},\vec{v}\}$ polarization basis as follows

$$\vec{E}^{i}_{h_i v_i} = \begin{bmatrix} E^{i}_{h} \\ E^{i}_{v} \end{bmatrix}. \tag{2.32}$$

If the receiving antenna is located in the scatterer far-field or Fraunhofer zone [Balanis,89] also the measured scattered wave can be assumed to be locally plane and the transverse scattered electric field can be hence expressed as

$$\vec{E}^{s}_{h_s v_s} = \begin{bmatrix} E^{s}_{h} \\ E^{s}_{v} \end{bmatrix}. \tag{2.33}$$

At this point, the whole scattering problem can be interpreted as a mapping of an incident two-dimensional complex vector onto a new scattered one. Under far-field assumptions, this transformation process is linear [Kennaugh,54] and the relation between $\vec{E}^{i}_{h_i v_i}$ and $\vec{E}^{s}_{h_s v_s}$ is then given by

$$\vec{E}^{s}_{h_s v_s} = K e^{-j2\vec{k}\cdot\vec{r}} \begin{bmatrix} S_{hh} & S_{hv} \\ S_{vh} & S_{vv} \end{bmatrix} \vec{E}^{i}_{h_i v_i} = K[S]\vec{E}^{i}_{h_i v_i}. \tag{2.34}$$

where K takes into account the attenuation due to the antenna-to-scatterer distance r while [*S*] is the 2×2 complex *Scattering* matrix containing the information about the scatterer. The diagonal terms of [*S*] are called *co-polar* channels, the off-diagonal terms *cross-polar* channels. Slightly different formulations available in the literature for the scattering matrix can be found in [Guissard,94].

Once an orthonormal polarization basis is defined for the transmitting and receiving antennas, the elements of [*S*] essentially correspond to the complex weight of each component of the incident wave in the *i* reference when it is projected onto the *s* reference basis. Another interpretation of [*S*] is reading by rows: each row contains the complex coefficients defining the polarization state of the scattered wave in the *s* reference when the Jones vector of incident wave in the *i* reference has just one no-null component. This second description turns out to be useful for [*S*] real measurements. For instance, the term S_{hv} can be measured when the transmitter is vertically

polarized, the receiver horizontally polarized, and both antennas point towards the target, as shown in Fig. 2.4. In Chapter 4, it will be shown that this alignment hypothesis is not always fulfilled in gbSAR observations due to the high aspect angles under which targets may be observed [Soumek,99]. As a consequence, the meaningfulness of polarization orthogonal measurements in gbSAR acquisition geometry might be compromised.

In the most general case, the degree of freedom (*DF*) of the scattering matrix [*S*] is 8, corresponding to 4 amplitude and 4 phase terms. Yet, polarimetric applications are often concerned with the analysis of the reciprocal phase relations among the channels and not with absolute value. It follows that a common phase term is generally put in evidence, reducing *DF* to 7. The scattering matrix [*S*] may be hence rewritten as

$$[S] = e^{j\phi_{hh}} \begin{bmatrix} |S_{hh}| & |S_{hv}| e^{j(\phi_{hv}-\phi_{hh})} \\ |S_{vh}| e^{j(\phi_{vh}-\phi_{hh})} & |S_{vv}| e^{-j(\phi_{vv}-\phi_{hh})} \end{bmatrix} \tag{2.35}$$

where the *hh* channel has been chosen as phase reference. The *DF* further decreases for reciprocal scatterers in *monostatic* observation geometry. In this case, the reciprocity theorem [Ulaby, 90] demonstrates that the scattering matrix in the *BSA* convention is symmetric ($S_{hv} = S_{vh}$) and that *DF* reduces hence to 5 (3 amplitude and 2 relative phase quantities). The horizontal and vertical linear polarizations have been used for the introduction of the scattering matrix because of the possibility to easily visualize the orientation of the electric field components they provide. Nonetheless, any orthonormal polarization reference can be employed for the description of scatterer's properties.

In order to express [*S*] with respect to an arbitrary orthonormal elliptical polarization basis $\{\hat{n}, \hat{n}_\perp\}$ from a measuring basis $\{\hat{m}, \hat{m}_\perp\}$, it can be applied the following Consimilarity transformation [Lüneburg,02]

$$[S]_{\hat{m},\hat{m}_\perp} = [U_2]^T_{(\hat{n},\hat{n}_\perp \to \hat{m},\hat{m}_\perp)} [S]_{\hat{n},\hat{n}_\perp} [U_2]_{(\hat{n},\hat{n}_\perp \to \hat{m},\hat{m}_\perp)} \tag{2.36}$$

where $[U]^T_{(\hat{n},\hat{n}_\perp \to \hat{m},\hat{m}_\perp)}$ has been defined in Eq. 2.22 and *T* denotes the matrix transpose operator. From the properties of SU(2) group, it follows that there are three properties of [*S*] that keep *invariant* whatever polarization basis is employed, namely

a) the determinant of [S]
b) the span of the matrix, which is defined as the quadratic sum of its elements and corresponds to the total power $span = |S_{nn}|^2 + 2|S_{nn_\perp}|^2 + |S_{n_\perp n_\perp}|^2$
c) the equality $S_{hv} = S_{vh}$, as long as the BSA convention is used.

Therefore, given a [*S*] matrix for a combination of transmit and received polarizations, it is possible to generate [*S*] for any other arbitrary combination and to emphasize different scattering properties of a target by playing with the polarization basis used as reference. This leads to the concept of *polarimetric signature* or *power density plots* (PDP) of a target in the monostatic case, which consists in analyzing the power response of a target in any possible polarization state [Ulaby,82]. For a generic polarization state ρ, the corresponding co-polarized and a cross-polarized PDPs are given by

$$\begin{aligned} P_c(\rho) &= \left|\vec{E}(\rho)^T [S]_{mn} \vec{E}(\rho)\right|^2 \\ P_x(\rho) &= \left|\vec{E}(\rho_\perp)^T [S]_{mn} \vec{E}(\rho)\right|^2 \end{aligned} \tag{2.37}$$

where $\vec{E}(\rho)$ is the Jones vector described in Eq. 2.16 and *T* denotes the vectorial transposition operation. The scattering matrix of power-normalized canonical targets and their corresponding polarimetric signatures are shown as example in Table 2.1. It can be observed as the trihedral, and consequently the trihedral-like scatterers, are characterized by an odd number of reflections and present a rotation symmetry in the Line-of-Sight (LOS). The dihedrals-like scattering corresponds to an even numbers of reflections and it is sensitive to the target's orientation angle. Similar sensitivity is shown by dipole-like scattering, which is generally associated to wire-shaped targets. Finally, helices convert incident linear polarizations into circular polarizations. This type of scattering can be modeled as a double reflection mechanism of two dihedrals in a specific geometrical configuration [Krogager,93].

In the past decades, a great deal of interest was centered on the optimization of the co-polar and cross-polar backscattered power through the PDPs analysis. The main objective was the characterization of the observed target through the calculation of the optimum polarization states maximizing $P_c(\rho)$ (pseudo eigen-polarizations or cross-polar nulls of [*S*]) and $P_{c\perp}(\rho)$ (co-polar nulls of [S]) [Graves,56] [Kennaugh,51]. A classification method based on the study of targets polarimetric phenomenology was first proposed in [Huynen,70] and dealt with the geometrical interpretation of 5 parameters (the DF of [S] in the backscattering case) provided by the optimization process. A graphical representation of these optimum states and of the classification parameters was also given using the Poincaré sphere and is usually referred to as Huynen standardized polarization fork [Boerner,98]. After being put aside during some years for alternative decomposition techniques, this approach has been recently taken up again as basis for new decomposition [Touzi,07] and classification [Sidjadi,06] strategies.

Trihedral $[S]_T = \begin{bmatrix} -1 & 0 \\ 0 & -1 \end{bmatrix}$	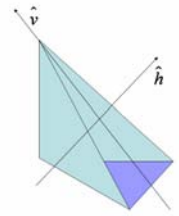	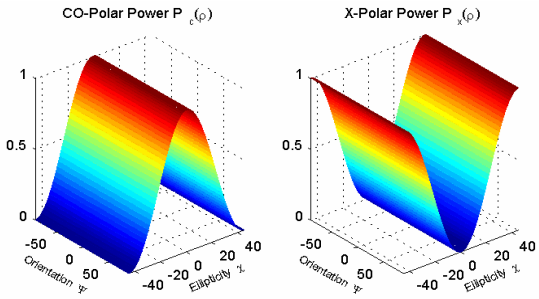	
ϕ -Tilted Dihedral $[S]_{Dh_\phi} = \begin{bmatrix} \cos 2\phi & \sin 2\phi \\ \sin 2\phi & -\cos 2\phi \end{bmatrix}$	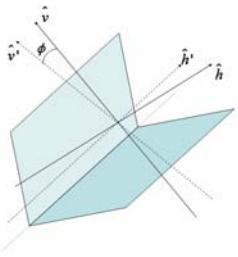	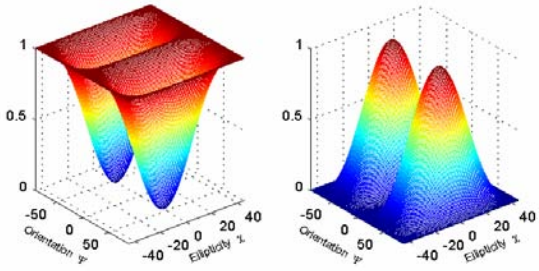	
Vertical Dipole $[S]_d = \begin{bmatrix} 0 & 0 \\ 0 & 1 \end{bmatrix}$	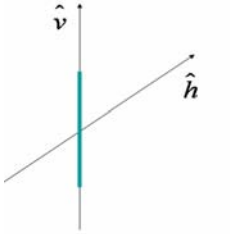	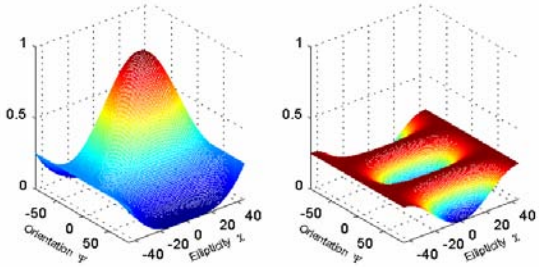	
ϕ -Tilted Dipole $[S]_{d\phi} = \begin{bmatrix} \cos^2\phi & 0.5\sin 2\phi \\ 0.5\sin 2\phi & \sin^2\phi \end{bmatrix}$	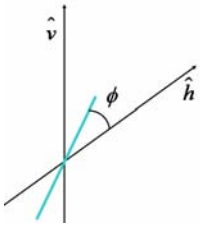	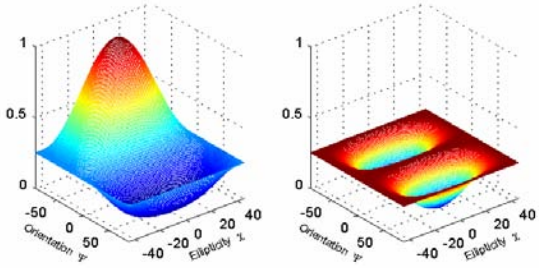	
Left-Handed Helix $[S]_{LH} = \frac{1}{2}\begin{bmatrix} 1 & j \\ j & 1 \end{bmatrix}$	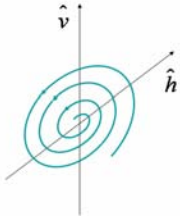	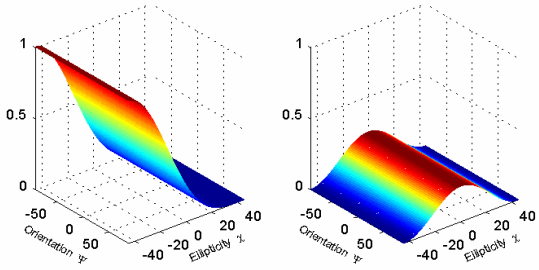	
Right-Handed Helix $[S]_{RH} = \frac{1}{2}\begin{bmatrix} 1 & -j \\ -j & 1 \end{bmatrix}$	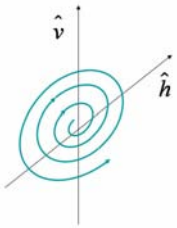	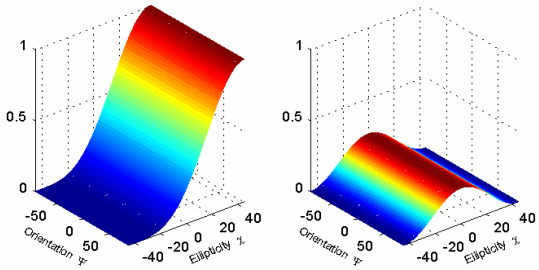	

Table 2.1 : Polarimetric backscattering signatures of power-normalized canonical targets in $\{\vec{h}, \vec{v}\}$ polarization basis .

2.2.2 Coherent Target Decompositions (CTD)

Instead of looking for an absolute characterization of the target scattering behavior, coherent target decompositions analyze the measured scattering matrix [*S*] in terms of linear superposition of elementary matrices associated to canonical scattering mechanisms. Among the several backscattering techniques available in the literature, the most renowned ones are the Pauli's [Coude,96], the Krogager's [Krogager,90] and the Cameron's [Cameron,90] decompositions. For this reason, they are briefly described in the following.

The Pauli's factorization splits up [*S*] in the $\{\vec{h},\vec{v}\}$ polarization basis into a trihedral-like, a dihedral like and a 45ºtilted dihedral-like or volumetric components as follows

$$[S] = a[S]_T + b[S]_{Dh_0} + c[S]_{Dh_{\pi/4}} \tag{2.38}$$

where a, b and c are complex coefficients whose amplitude is related to the way the total power (*span*) is distributed among the three orthonormal elementary mechanisms. It worth noting that only the first component is roll invariant, whereas the last two ones entail a specific orientation of the two dihedrals with respect to the LOS.

The rationale of Krogager's decomposition [Krogager, 90] [Krogager, 93] is to extend the property of roll invariance to all the components by releasing the orthogonality condition. In this case, the last two terms are substituted with a dihedral-like target with a generic orientation β varying in the $(-\pi,\pi]$ range and a left or right handed helix. In order to guarantee the *uniqueness* of the decomposition, the scattering matrix must be rotated along the LOS of a specific angle ϕ_H provided by the cross-polar null condition [Fabregas,95][1]. Therefore, the Krogager's decomposition factorizes the ϕ_H -rotated [*S*] as follows

$$[S]_{\phi_H} = a[S]_T + e^{j[\arg(a)-\arg(b)]}\left(d[S]_{D_\beta} + f[S]_H\right). \tag{2.39}$$

where *a* and *b* are the same of Eq. 2.38 while *d* and *f* accounts for the two new contributions. Although it is mathematically predicted, it must be pointed out that the helix-like behavior is quite rare to be detected in real cases.

The approach of Cameron decomposition is again different. It relies on two properties that the passive targets are supposed to fulfill: the reciprocity and the symmetry. The first condition imposes the cross-polar term of the measured scattering matrix to be equal. The second condition deals with the extraction of the symmetric component from [*S*]. This is performed out by finding

[1] The subscript *H* for the rotation angle ϕ_H is due to the fact that it corresponds to the target's orientation angle provided by the Huynen Decomposition [Huynen,70]

the rotation about the LOS canceling the third component of the Pauli's Decomposition. Resuming, [*S*] is rewritten by Cameron as

$$[S] = A\left[\cos\tau S_{SYM}^{\max} + \sin\tau S_{SYM}^{\min}\right] \tag{2.40}$$

where A is the *span* square root (see Section 2.3), τ is the *degree of symmetry* of the target, $S_{SYM}^{\max}$ and $S_{SYM}^{\min}$ are respectively the maximum and minimum symmetric components of [*S*]. Details about the way to estimate these two parameters and the scattering mechanism classification based on $S_{SYM}^{\max}$ analysis are given in [Cameron, 96] [Touzi,07].

2.3 Non-deterministic scatterers

The matrix [*S*] constitutes a powerful tool able to describe the scattering properties of scatterers converting a fully-polarized incident plane wave into a scattered wave whose degree of polarization D_p is still unitary. These scatterers, which are referred to as *deterministic* or *point* targets, are characterized by a stable behavior in space and time. Typical examples are man-made structures.

Contrarily, when a natural scenario is observed, the degree of polarization of the scattered wave generally reduces whatever the polarization of the incident wave, giving origin to the so-called speckle phenomena. In this case, scatterers are defined as *distributed* or *non-deterministic*. A detailed description of speckle and of its statistical properties can be found in [Lopez,03]. For the purpose of this PhD dissertation, just a brief description of speckle physical existence is given in the following.

2.3.1 Speckle phenomenon

The speckle phenomenon is due to the high ratio between the resolution of the measuring system and the wavelength of the transmitted signal. Under the Born hypothesis of no mutual interactions among scatterers [Born,59], the single reflections of an incident wave illuminating a high number of scatterers coherently sum to provide a unique [*S*] matrix for each resolution cell of the image. It follows that speckle is not related to a specific imaging technique but, in general, to the features of the measurement methodology. As a matter of fact, its effects were first observed in optical imaging [Goodman,76] and only after detected in microwave acquisitions from Synthetic Radar Aperture (SAR) sensors [Lee,80] [Lee,81]. Remanding to next Chapters for the description of SAR imaging principles, the main concern is here to point out just the statistical properties of speckle. Although speckle is generated by deterministic reflection mechanisms, the high number

of interactions makes the scattering from homogeneous areas a noise-like random process [Lopez,03]. If the number of scatterers inside the resolution cell is large enough to fulfill the Central Limit Theorem, both real and imaginary parts of the backscattered signal are zero-mean Gaussian distributed [Goodman,76]. This case is usually referred to as *fully*-developed speckle [Lopez,03]. When only few scatterers are present within the resolution cell, the gaussian model stops being valid and a more complex statistical distributions is required [Daba,94]. In this case, speckle is said to be *partially* developed. In the extreme case of an isolated target inside the resolution cell, the scattering process becomes completely deterministic and no speckle is present.
In order to cope with speckle and retrieve reliable information about the macroscopic features of the illuminated area, filtering techniques are necessary [Oliver,98]. Owing to the statistical properties of the elements of [*S*] in case of fully-developed speckle, no filtering operation can be successfully applied to this first order descriptor. Accordingly, higher order descriptors must be estimated to extract useful information.

2.3.2 Distributed-target Descriptors

Let $[\Psi]$ indicate a set 2x2 complex matrices which are constructed as an orthonormal basis under a hermitian inner product. A vectorial formulation of the scattering matrix [*S*] may be obtained as

$$\vec{k}_\Psi = \frac{1}{2} V([S][\Psi]) \tag{2.41}$$

where *V* is the matrix *trace* operator [Mirsky,90] equal to the sum of the diagonal elements of a matrix. The second order descriptor $[M_\Psi]$ associated to $[\Psi]$ is given by

$$[M_\Psi] = E\left\{\vec{k}_\Psi \cdot \vec{k}_\Psi^{\dagger}\right\} \tag{2.42}$$

where $E\{\cdot\}$ denotes the ensemble average operation and † is the transpose-conjugate operator. Generally, *ergodicity* and *spatial homogeneity* hypotheses [Papoulis,84] are invoked to replace $E\{\cdot\}$ in Eq. 2.42 with a spatial averaging operation $\langle\cdot\rangle$. In the bistatic case, the dimension of $\vec{k}_\Psi$ is 4 and $[M_\Psi]$ is a 4×4 hermitian matrix. In the monostatic case the symmetry of [*S*] reduces the dimension of $\vec{k}_\Psi$ to 3 and consequently $[M_\Psi]$ becomes a 3×3 hermitian matrix. The elements of $\vec{k}_\Psi$ and $[M_\Psi]$ strictly depend on the basis $[\Psi]$ chosen for vectorizing [*S*]. Among all the possible $[\Psi]$, the so-called lexicographic basis $[\Psi_L]$ and the Pauli basis $[\Psi_P]$ are mainly employed[1]. They are respectively defined as

[1] Another second order descriptor, which is not described in the frame of this work, is the Müller/Kennaugh matrix [*M*]/[*K*], which is derived from the Stokes vector formalism in the bistatic/monostatic case. In [Cloude,86], the matrix [*M*]/[*K*] is directly obtained from [*T*], confirming that the amount of information concerning the scatterer is exactly the same. Yet, a complete description of [*M*]/[*K*] formulation can be found in [Kennaugh, 51] [Kennaugh, 54] [Huynen,70].

$$\begin{aligned}[\Psi_L] &= \left\{ \begin{bmatrix} 1 & 0 \\ 0 & 0 \end{bmatrix}, \frac{1}{\sqrt{2}} \begin{bmatrix} 0 & 1 \\ 1 & 0 \end{bmatrix}, \begin{bmatrix} 0 & 0 \\ 0 & 1 \end{bmatrix} \right\} \\ [\Psi_P] &= \left\{ \frac{1}{\sqrt{2}} \begin{bmatrix} 1 & 0 \\ 0 & 1 \end{bmatrix}, \frac{1}{\sqrt{2}} \begin{bmatrix} 1 & 0 \\ 0 & -1 \end{bmatrix}, \sqrt{2} \begin{bmatrix} 0 & 1 \\ 1 & 0 \end{bmatrix} \right\} \end{aligned} . \tag{2.43}$$

where the terms $\sqrt{2}$ are necessary to keep $V\left([\Psi][\Psi]^{\dagger}\right)$ invariant, namely the total power backscattered by the target. If now [*S*] is expressed in the linear polarization basis $\{\vec{h},\vec{v}\}$, the corresponding scattering vectors $\vec{k}_L$ and $\vec{k}_P$ are given by

$$\begin{aligned} \vec{k}_L &= \left[S_{hh}, \sqrt{2} S_{hv}, S_{vv} \right] \\ \vec{k}_P &= \left[S_{hh} + S_{vv}, S_{hh} - S_{vv}, \sqrt{2} S_{hv} \right] \end{aligned} . \tag{2.44}$$

Note that the lexicographic scattering vector turns out to be directly related to the system measurable quantities. On the contrary, the Pauli scattering vector is closer to the physical and geometrical properties of the scattering process (see Section 2.4). The *Covariance* matrix [*C*] and the *Coherency* matrix [*T*] are obtained from Eq. 2.42 as follows

$$\begin{aligned} [C] &= \left\langle \vec{k}_L \cdot \vec{k}_L^{\dagger} \right\rangle \\ [D] &= \left\langle \vec{k}_P \cdot \vec{k}_P^{\dagger} \right\rangle \end{aligned} . \tag{2.45}$$

The two second order descriptors are not independent: they are related by the unitary transformation

$$[T] = [D][C][D]^{T} \tag{2.46}$$

where

$$[D] = \frac{1}{\sqrt{2}} \begin{bmatrix} 1 & 0 & 1 \\ 1 & 0 & -1 \\ 0 & \sqrt{2} & 0 \end{bmatrix} \tag{2.47}$$

is a SU(3) matrix preserving the norm of the scattering vector [Cloude,95]. This guarantees that the two matrices have the same *eigenvalues* but not the same *eigenvectors*. In the case of deterministic targets, the rank of the [*T*] or [*C*] keeps equal to 1. This means that [*S*], or any scattering vector $\vec{k}_{\Psi}$, is sufficient to describe their scattering properties while the averaging operation has no significant effect. On the contrary, the rank increases when non-deterministic target are analyzed. Its final value depends on the randomness of the reflection mechanism within the averaged area, being equal to 3 for completely random, or volumetric, scattering processes. A full-rank [*T*] (or [*C*]) is characterized by 9 degrees of freedom, 4 more than the mathematical dimension of [*S*]. These added dimensions arise from the average operation and point out as the first order scattering descriptor ([*S*] or $\vec{k}_{\Psi}$) is unfit to completely describe non-deterministic

scatterers. In other words, [*T*] or [*C*] must constitute the starting point for any attempt to characterize distributed targets' scattering process.

2.3.3 Incoherent Target Decompositions (ICTD)

In order to describe the scattering properties of non-deterministic targets, three different strategies have been followed during last years: model-based decompositions, phenomenological studies, and eigen-decomposition methods. The rationale of model-based decompositions is the factorization of [*T*] or [*C*] as the combination of simpler or canonical second order descriptors

$$[T]=\sum_{i=1}^{k}[T]_i \qquad [C]=\sum_{i=1}^{k}[C]_i \,. \tag{2.48}$$

The most representative example is the Freeman decomposition [Freeman,98], which basically models the Covariance matrix as the sum of three contributions: single-bounce/*surface*, double-bounce/*dihedral-like* and *volume-scattering*. The first two terms are deterministic and then described by rank-1 Covariance matrices; the last term is modeled as the scattering from a set of randomly oriented dipoles (see Table 2.1) and described by a fully-ranked Covariance matrix.

The phenomenological approach was first proposed by Huynen and deals with the idea that it is always possible to decompose the measured [*T*] into a deterministic rank-1 Coherency matrix $[T]_O$ plus a roll-invariant noise matrix $[T]_N$. In its original formulation [Huynen,70], the symmetry of the deterministic target is assumed to provide a unique solution. This hypothesis is instead relaxed in [Holms,88], which accounts for possible helical-type scattering mechanisms within the averaged area.

The eigen-decomposition methods rely on the properties of any eigenvalue-based analysis to automatically provide basis invariant and mathematically orthogonal solutions. As $[M_\Psi]$ in Eq. 2.42 is hermitian by construction (see Eq. 2.45), it is always possible to find a unitary matrix $[U_3]$ belonging to SU(3) group diagonalizing $[M_\Psi]$ as follows

$$[M_\Psi]_D=[U_3]^{-1}[M_\Psi][U_3]=\begin{bmatrix}\lambda_1 & 0 & 0\\ 0 & \lambda_2 & 0\\ 0 & 0 & \lambda_3\end{bmatrix}_{\lambda_1\geq\lambda_2\geq\lambda_3} . \tag{2.49}$$

where the terms λ are the real eigenvalues and the columns of $[U_3]$, hereon denoted with the set of vectors $(\vec{u}_1,\vec{u}_2,\vec{u}_3)$, are the eigenvectors of $[M_\Psi]$. It is worth pointing out that whereas the formers do not depend on the set of orthogonal 2x2 matrices chosen for the vectorization of [*S*], the latters are strictly related to the expansion basis $[\Psi]$. Owing to the direct physical

interpretation of $\vec{k}_P$ components, the Pauli basis $[\Psi_P]$ is usually employed for the diagonalization process. Hence, $[M_\Psi]$ turns into the Coherency matrix [*T*] and can be factorized as

$$[T] = \sum_{i=1}^{3} \lambda_i \vec{u}_i \vec{u}_i^{\dagger} = \sum_{i=1}^{3} \vec{k}_i \vec{k}_i^{\dagger} = \sum_{i=1}^{3} [T_i] . \tag{2.50}$$

It is important to note that each matrix $[T_i]$ is a rank 1 and defines a pure (or deterministic) scattering mechanism completely described by the *i-th* scattering vector

$$\vec{k}_i = \sqrt{\lambda}_i \vec{u}_i . \tag{2.51}$$

Information about the *type* of scattering is given by the unitary eigenvectors $\vec{u}_i$ while the weight it has on the total power of [*T*] is defined by the eigenvalue λ_i. According to the *Scattering Vector Reduction Theorem* [Cloude,97], it is also possible to factorize each scattering eigenvector as follows

$$\vec{u}_i = \begin{bmatrix} \cos\alpha_i \\ \sin\alpha_i \cos\beta_i e^{j\delta_i} \\ \sin\alpha_i \sin\beta_i e^{j\gamma_i} \end{bmatrix} \tag{2.52}$$

where the terms (δ_i, γ_i) are general scattering phase angles, while α_i and β_i describe the type of scattering and the orientation of the scatterer along the LOS, respectively. The two angles α_i and β_i, as well as any other eigenvector parameters, depend on the basis $[\Psi]$ used to define the scattering vector $\vec{k}_\Psi$. This means that this interpretation is correct as long as $[\Psi_P]$ is adopted for the scattering vector definition. Table 2.2 shows the values of the parameters in Eq. 2.52 for the canonical scattering mechanisms described in Table 2.1. The power interpretation given to the eigenvalue corresponding to each eigenvector permits to associate an appearance probability P_i to each scattering mechanism contribution [Cloude,95]:

$$P_i = \frac{\lambda_i}{\sum_{i=1}^{3} \lambda_i} . \tag{2.53}$$

At this point, let *x* be a generic parameter extracted the eigenvector factorization in 2.52 and (x_1,x_2,x_3) be the set of value of *x* provided by the three scattering mechanisms $\vec{u}_i$. Taking into consideration Eq. 2.53, it is possible to associate the parameter *x* with a random sequence of the values x_i whose appearance frequency is described by P_i. Therefore, the best estimation $\underline{x}$ of *x* in the maximum likelihood sense [Cloude,97] is obtained as

$$\underline{x} = P_1 x_1 + P_2 x_2 + P_3 x_3 . \tag{2.54}$$

Canonical Scatterer	α	β	γ	δ
Sphere	0º	∞	∞	∞
Dihedral at θ	90º	2θ	δ	γ
Dipole at θ	±45º	2θ	ϕ_c	ϕ_c
Helix	0º	±45º	δ +90º	γ -90º

Table 2.2: Parameters defined by the Scattering Vector Reduction theorem for the canonical scatterers in Table 2.1. The symbol ∞ stands for no fixed value while ϕ_c is the phase of the complex constant term multiplying each canonical scattering matrix.

Following the previous reasoning, it is possible to estimate the main scattering vector $\vec{\underline{k}}_0$ characterizing the area used for the estimation of [T] as

$$\vec{\underline{k}}_0 = \sqrt{\underline{\lambda}} \begin{bmatrix} \cos\underline{\alpha} \\ \sin\underline{\alpha}\cos\underline{\beta}e^{j\underline{\delta}} \\ \sin\underline{\alpha}\sin\underline{\beta}e^{j\underline{\gamma}} \end{bmatrix}. \tag{2.55}$$

where

$$\underline{\alpha} = \sum_{i=1}^{3} P_i\alpha_i \quad \underline{\beta} = \sum_{i=1}^{3} P_i\beta_i \quad \underline{\gamma} = \sum_{i=1}^{3} P_i\gamma_i \quad \underline{\delta} = \sum_{i=1}^{3} P_i\delta_i \ . \tag{2.56}$$

Since the physical properties of distributed targets are independent of the way the measurements have been carried out, specific roll-invariance descriptors are generally employed for their description. Two complementary polarimetric descriptors are obtained from the eigenvalues of [T], which fulfill this condition by construction. They are known as polarimetric entropy H and anisotropy A and defined as

$$H = -\sum_{i=1}^{3} P_i \log P_i \tag{2.57}$$

$$A = \frac{\lambda_2 - \lambda_3}{\lambda_2 + \lambda_3}. \tag{2.58}$$

Although both descriptors varies in the [0,1] range, their physical meaning is different. The entropy H describes the randomness of the scattering process within the averaged samples, i.e., it provides a description of the depolarized component of the plane wave scattered back to the sensor. The limit values respectively describe the cases of complete polarized (H=0) and complete unpolarized (H=1) scattered wave. An equivalent interpretation can be given in terms of multiple scattering mechanisms coexisting in the area employed for [T] estimation. Low values of H means $\lambda_1 > 0,$ and $\lambda_2 = \lambda_3 \simeq 0$, i.e., only one dominant scattering mechanism is present within the averaged area. In this case, the rank of [T] is close to 1 and the target can be assumed

deterministic. On the contrary, a high value of H means secondary scattering mechanisms are present; nonetheless, the entropy is not sufficient to state if one or two secondary mechanisms are contributing to the total backscattered power. This answer is given by the anisotropy A, which considers only the other two eigenvalues λ_2 and λ_3 and becomes meaningful just for medium-high values of H. Values of A close to 1 indicate that just one strong secondary mechanism is present ([T] is rank 2) whereas low values of A stand for two secondary mechanisms with approximately the same power.

Concerning the eigenvectors, it can be easily shown that only the terms α_i are roll-invariant. The SU(2) unitary matrix defining a θ rotation along the LOS is defined in [Cloude,97] as

$$\left[U_R(\theta)\right] = \begin{bmatrix} 1 & 0 & 0 \\ 0 & \cos 2\theta & \sin 2\theta \\ 0 & -\cos 2\theta & \cos 2\theta \end{bmatrix}. \tag{2.59}$$

Denoting with $[\Sigma]$ the diagonal matrix containing the eigenvalues of $[T]$, the rotated Coherency matrix $\left[T(\vartheta)\right]$ may be obtained as

$$\left[T(\vartheta)\right] = \left[U_R(\theta)\right][T]\left[U_R(\theta)\right]^{-1} = \left[U_R(\theta)\right][U_3][\Sigma]\left([U_3]\left[U_R(\theta)\right]\right)^{-1} = [U'][\Sigma][U']^{-1}. \tag{2.60}$$

Owing to the particular structure of $\left[U_R(\theta)\right]$, the first row of $[U_3]$ and $[U']$ is not modified by the rotation transformation, demonstrating that the terms α_i are constant. This result is consistent with the physical interpretation given to these angles, which define the *type* of the scattering mechanisms but not their orientation along the LOS. For the same reason, the averaged term $\underline{\alpha}$, which describes the dominant scattering *type* within the area employed to estimate [T] estimation, turns to be roll-invariant as well. Finally, it is worth pointing out that unlike H and A, the term $\underline{\alpha}$ is strictly related to the basis $[\Psi]$. It follows that the physical interpretation given in Table 2.2 is meaningful as long as the Pauli Basis $[\Psi_P]$ is employed for the expansion of the scattering matrix [S].

Chapter 3

Ground-based Synthetic Aperture Radar

Synthetic Aperture Radar (SAR) is a coherent active microwave remote sensing technique able to provide bi-dimensional reflectivity images with high spatial resolution. Satellite and airborne missions carried out by international space agencies ([NASA], [ESA], [JAXA], [CSA], and [DLR]) have demonstrated the feasibility of using microwave sensors to carry out regular, repetitive and synoptic views of Earth's features over extense areas. The continuous improvement of the spatial resolution and the implementation of multi-frequency and multi-polarization capabilities have constituted the main guidelines of SAR sensor devise. But if the use of air- [Prats,08] [Perna,08] and space-borne [Ferretti,01] [Mora,03] [Lanari,04] systems has turned out to be extremely successful for the observation of slow-time processes over wide areas, it has revealed being unsuitable when the emphasis focused on the details of smaller scale phenomena and a high flexibility in terms of revisiting time is needed. In order to fulfill these requirements, during the last years the research activity of several groups of the remote sensing community [Pieraccini,00] [Zhou,04] [Nico,04] [Aguasca,04] [Noferini,05] [Bernardini,07] [Lee,08] has dealt with the development of terrestrial SAR systems. Easy to deploy, extremely cheaper with respect to airborne or satellite solutions, ground-based SAR sensors represent an optimum solution for several applications. Despite many analogies may be found between terrestrial and flying platforms, an accurate study is mandatory in order to extend classical SAR formulation to ground-based SAR (gbSAR) systems. In this Chapter, a detailed description of the gbSAR sensor projected and developed at the Universitat Politècnica de Catalunya (UPC) [Aguasca,04] is

presented. The range domain is first analyzed. As specific hardware solutions make the UPC system unique in the scientific community, the mathematical formulation here presented is tailored to the imaging propertied of this sensor. Afterwards, the cross-range imaging process is considered. Contrarily to the range domain, the features of cross-range domain are just related to the short dimension of the aperture synthesized by the terrestrial platform. It follows that the study carried out in this second part is general and may be applied to any gbSAR system.

3.1. Ground-Based Synthetic Aperture Radar

Ground-based SAR systems (gbSAR) aim at merging the capability to obtain 2D reflectivity images by synthesizing a short apertures in time with the advantages offered by a terrestrial platform such as high stability, perfect knowledge of sensor's track and absence of any revisiting time constraint. The main drawback is instead related to their deployment on the earth surface, which limits the extension of the illuminated scene and its maximum range distance.

It is common knowledge that frequency-modulated continuous wave (FM-CW) radars constitute the optimum solution when a short-range system has to been projected [Skolnik,90]. They share several properties with the pulsed systems that are normally boarded on airborne and satellite platforms, such the range-resolution principles. In addition, they offer advantages such as the simpler hardware design, the potential minimal spread in the transmitted pulse and the fact that peak power is usually little greater than average power. This is the reason for which all the gbSARs in the literature basically consist in a continuous-wave (CW) radar front-end moving along a linear unit. Echoes received from the different positions are collected and coherently processed to retrieve reflectivity information of the scenario. Despite the common idea, important differences characterize the sensors proposed by the different research groups. Postponing an analysis of the particular technological choices adopted for the UPC sensor to Chapter 4, we provide here a theoretical description of the whole system, from the transmitted signal generation to the final focused complex image.

3.2. Range domain description

When an electromagnetic plane wave illuminates a target, part of the incident energy is absorbed and the rest is scattered away according to the geometrical and physical properties of the observed scene. A Radar, acronym for "radio detection and ranking", is an active system that operates by radiating electromagnetic energy and detecting the echoes returned from reflecting objects. The

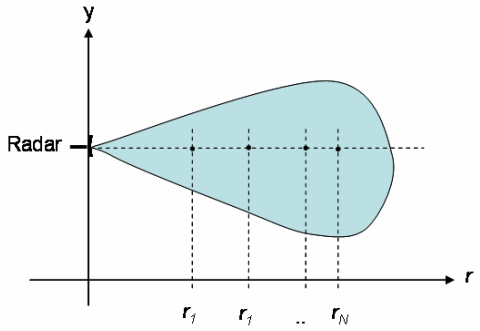

Fig. 3.1: *N* point targets aligned along the *boreside* direction of the radar.

transmitted signals are often modulated in order to enhance the spatial resolution of the system. In SAR, the so-called *chirp*-modulation is mostly used. This modulation employs sinusoidal waveforms whose instantaneous angular frequency increases or decreases linearly over time. The resulting radar signal may be defined as

$$p(t) = \prod\left(\frac{t - T_p/2}{T_p}\right) e^{j\beta t + j\alpha t^2} \tag{3.1}$$

where T_p is the chirp duration, α is the rate at which angular frequency changes (*chirp-rate*) whereas the term β is the angular frequency carrier. The main advantage that this modulation offers is its time-length and bandwidth are not directly related as for simple rectangular pulses. This means that high range resolution can be obtained without managing short-time high power peaks, with relevant simplification of hardware devices [Skolnik,90]. If B is the pulse bandwidth in Hz, the range resolution is given by

$$\Delta r = \frac{c}{2B} = \frac{\pi c}{2\alpha T_p} \tag{3.2}$$

where c is the speed of light. Let's consider the two-dimensional scenario depicted in Fig. 3.1, where a group of N point targets is aligned along the *boreside* direction. The generic point target n at a radial distance r_n from the radar is characterized by a radar cross section σ_n (RCS) and a phase ϕ_n [Ishimaru,78]. The complex reflectivity function Γ describing the scenario is

$$\Gamma(t) = \sum_{n=1}^{N} \sqrt{\sigma_n} e^{j\phi_n} \delta\left(t - \frac{2r_n}{c}\right) = \sum_{n=1}^{N} \sqrt{\sigma_n} e^{j\phi_n} \delta(t - t_n) \tag{3.3}$$

where the term t_n is called round-trip delay. The signal scattered back from the illuminated scene can be expressed as the convolution between Eq. 3.1 and Eq. 3.3 as follows

$$s(t) = \Gamma(t) * p(t) = \sum_{n=!}^{N} \sqrt{\sigma_n} e^{j\phi_n} p(t - t_n) = \sum_{n=1}^{N} \sqrt{\sigma_n} e^{j\phi_n} \prod\left(\frac{t - (T_p/2 + t_n)}{T_p}\right) e^{j\beta(t-t_n) + j\alpha(t-t_n)^2}. \tag{3.4}$$

$s(t)$ is the signal at the receiving antenna of the radar and is referred to as radar *raw data*. For the sake of simplicity, the attenuation of the signal due to propagation has been omitted in Eq. 3.4.

3.2.1. Matched-filter vs deramping focusing

Among the several techniques have been proposed in the literature for range-domain focusing purposes, the matched filter is probably the widest used one. It is the optimal solution for maximizing the signal-to-noise ratio (SNR) in presence of additive stochastic noise [Curlander,91]. Basically, it detects the common elements of the known transmitted signal in the backscattered one by convolving the latter with a conjugated time-reversed version of the first:

$$s_M(t) = s(t) * p^*(-t) = \sum_{n=1}^{N} \sqrt{\sigma_n} e^{j\phi_n} h(t - t_n) \tag{3.5}$$

where $h(t)$, called *point spread function* (*psf*), describes the response of the range imaging system and it is defined as

$$h(t) = F^{-1}\left[\left| P(\omega) \right|^2 \right] \tag{3.6}$$

where $P(\omega)$ is the transmitted signal Fourier transform and F^{-1} denotes the inverse Fourier transformation. The function $h(t)$ is mainly related to the bandwidth of the transmitted signal and it defines the ability to resolve targets in the range dimension. The matched filter is adopted for the range-processing of the raw data acquired by the most of pulsed SAR sensors.

An alternative approach, which turns out to be particularly suitable for the UPC system, is the deramping technique [Soumek,99]. From a mathematical point of view, it consists in multiplying the conjugated received signal by the phase term of the chirp in Eq. 3.1, yielding

$$s_c(t) = s^*(t) e^{j\beta t + j\alpha t^2} = \sum_n \sqrt{\sigma_n} e^{j\phi_n} \prod \left(\frac{t - \left(T_p / 2 + t_n \right)}{T_p} \right) e^{j\left(\beta t_n - \alpha t_n^2 \right)} e^{j 2\alpha t_n t} . \tag{3.7}$$

The terms related to the round-trip delay and weighted by the carrier β and by the chirp-rate α introduce an absolute phase offset, while the information concerning the target's position is carried by the sinusoid $e^{j 2\alpha t_n t}$. Denoting with F the Fourier transform, the range-compressed response from the illuminated scene may be obtained by transforming the Eq. 3.7 as follows

$$S_c(\omega) = F\left[s_c(t) \right] = \sum_{n=1}^{N} \sqrt{\sigma_n} e^{j\phi_n} e^{j\left(\beta t n + \alpha t_n^2 - \omega t_n \right)} H\left(\omega - \frac{4\alpha r_n}{c} \right) = \sum_{n=1}^{N} S_{cn}(\omega) \tag{3.8}$$

where $H(\omega)$ is the deramped *psf* equal to

$$H(\omega) = F\left[\prod\left(\frac{t - T_P/2}{T_P}\right)\right] = T_p \mathrm{sinc}(\omega T_P). \tag{3.9}$$

A capital letter has been used since the function describing the useful information is obtained in the *spectral* domain. Although deramping and matched-filter focusing procedures are completely different, their ability to resolve targets in the range domain is approximately the same. This can be seen by imposing the condition $|P(\omega)| = 1$, and noting that shape of the two *psf*s is almost identical. Nonetheless, despite the amplitude term given by the two techniques is almost equivalent, it is worth pointing out that the absolute phase significantly changes. From Eq. 3.5 and Eq. 3.8, it can be observed that the one-dimensional range profile describing the targets' location is essentially obtained as the superimposition of *psf* replicas centered at the corresponding t_n (matched filter) or at angular frequencies proportional to t_n (deramping). But while in the first case $h(t)$ is modulated just by $\sqrt{\sigma_n}e^{j\phi_n}$, the deramping process introduces additional phase terms proportional to the targets' range location. Since the absolute phase plays a key role in SAR imaging process, all these terms will be examinated carefully in Section 3.5.

3.2.2. Deramping of pulsed and CW radar signals

Heretofore, the mathematical formulation provided for the two range-compression techniques does not entail specific hypothesis about the way the radar works, i.e., pulsed signals or continuous signals. Yet, it is easy to understand that the features of $s(t)$ differ significantly in the two cases. In order to better describe this issue, the case of two targets T_1 and T_2 at 250 and 470 time units (*tu*) from the sensor has been considered. Fig. 3.2a and Fig. 3.2b show the real part of the transmitted signal and the echo from the two targets for the two different radar systems. Fig. 3.3a and Fig. 3.3b show the result obtained in the two cases after the deramping-based range compression. It is worth pointing out that, for the sake of clearness, just one pulse and one FM modulation have been considered in the plots. Besides, different values of T_p and α have been employed to keep the *chirp* bandwidth constant. A brief analysis makes it possible to stress a basic difference between the two radar systems. In the pulsed case, the transmitted and the reflected signal do not overlap in time. Accordingly, the same antenna is generally used for the two operations. In the continuous case, two different antennas are required and the echoes are meaningful only for round-time delays shorter than the time duration of the chirp. Besides, the higher the target-to-sensor distance, the higher the angular frequency of the deramped signal associated to its position. In the case of air- and space-borne sensors, the direct use of Eq. 3.7 would lead to very high frequency

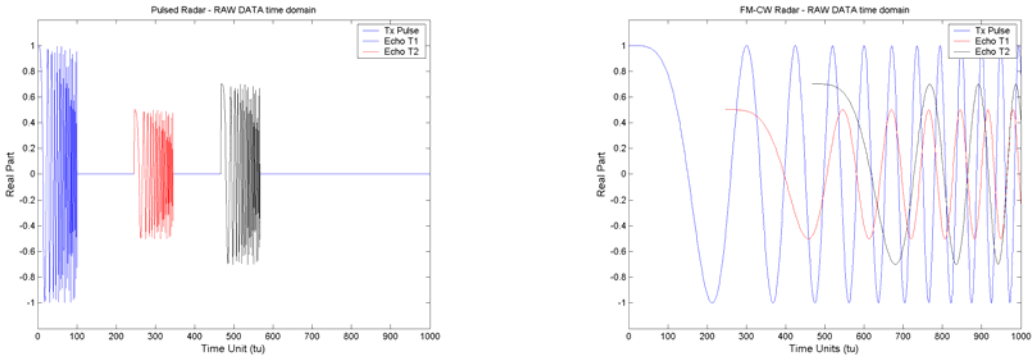

(a) (b)

Fig. 3.2: Range raw data in case of pulsed (a) and FM-CW (b) radar. The blue plot represents the transmitted chirp-modulated signal, the red and black plots are the echoes from two targets T1 and T2, respectively. The same chirp bandwidth has been used by imposing $\alpha_{PULSED} T_{p\,PULSED} = \alpha_{FM-CW} T_{p\,FM-CW}$.

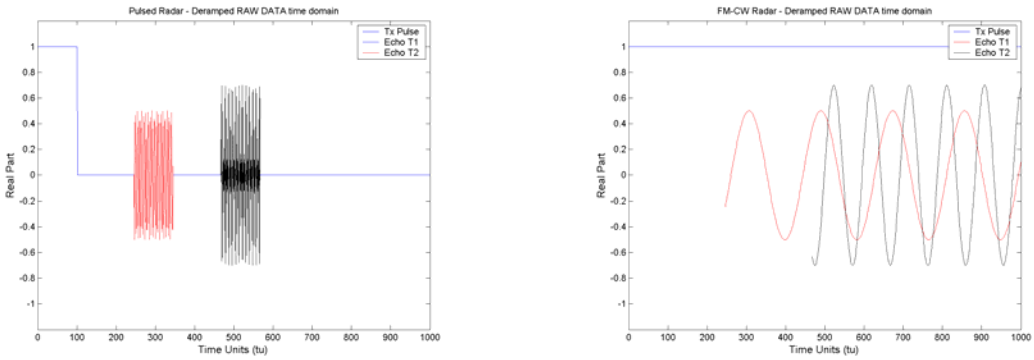

(a) (b)

Fig. 3.3: Deramped range raw data in case of pulsed (a) and FM-CW (b) radar. The blue plot represents the transmitted chirp-modulated signal, the red and black plots are the echoes from the targets T1 and T2 in Fig. 3.2, respectively. The same chirp bandwidth has been used by imposing $\alpha_{PULSED} T_{p\,PULSED} = \alpha_{FM-CW} T_{p\,FM-CW}$.

components that could not be practically sampled. In order to easily fulfill the Nyquist sampling criterion [Proakis,98], a modified version may be used. Denoting with ΔR the swath of the radar in range and with R_c its central position, the region of interest may be expressed as

$$r \in \left[R_c - \frac{\Delta R}{2}, R_c + \frac{\Delta R}{2} \right] \tag{3.10}$$

and the spectral support band Δω of the corresponding time-signal $s_c(t)$ is

$$\Delta\omega = \left[\frac{4\alpha}{c}\left(R_c - \frac{\Delta R}{2} \right), \frac{4\alpha}{c}\left(R_c + \frac{\Delta R}{2} \right) \right]. \tag{3.11}$$

A baseband conversion of $s_c(t)$ may be performed by reformulating Eq. 3.7 as

$$s_{cb}(t) = s_c(t) e^{-j\frac{4\alpha}{c} R_c t} = s_c(t) e^{-j\omega_c t} = s(t) e^{j\beta t + j\alpha t^2 - j\omega_c t} \tag{3.12}$$

Anyway, the wide swath these platforms provide usually causes $\Delta\omega$ to be wider than the chirp's bandwidth. In this case, the deramping sampling condition turns out to be more constraining than

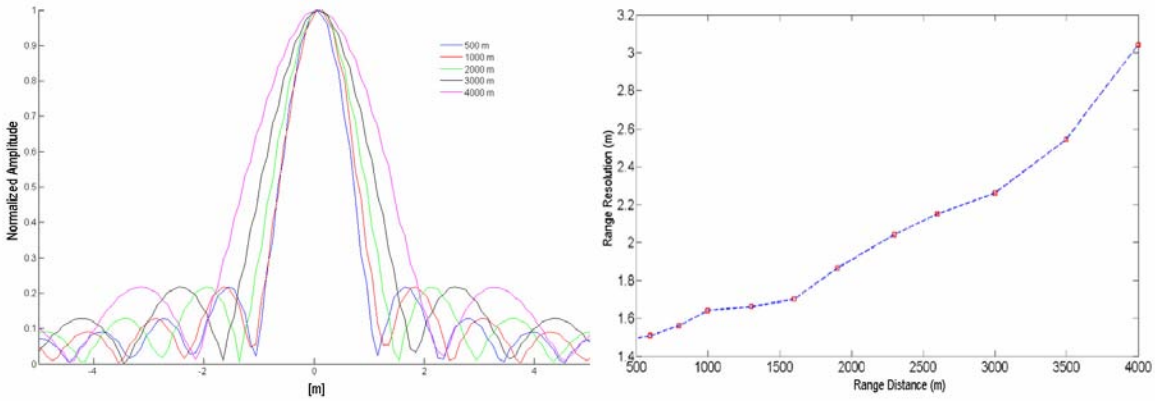

(a) (b)

Fig. 3.4: Simulated range profiles (a) and retrieved -3dB resolution (b) of a collection of point targets aligned along the antenna's *boreside* direction. The modulation effect due to the different observation window [$t_{OBS} = T_p - t_n$] turns into a decrease of the range resolution. The value of T_p used for the simulation is 50μs, which correspond to the duration usually employed for UPC gbSAR measurements. Changes are significant for range distance higher than 2 km.

the matched filter requirement. For this reason, this second approach is normally chosen for range-compression of air-borne and satellite SAR acquisitions, while the deramping technique turns out to be more convenient in the case a few kilometers swath has to be monitored at short range distance. Another difference between pulsed and FM-CW radars is related to the intrinsic measurement methodology they are based on. For the first group, the time duration of the backscattered chirp signal is fixed independently of the range distance of the observed scene. For the second one, this quantity becomes a function of target range location. As it is shown in Fig. 3.3b, being T_p the time duration of the chirp and t_n the round-trip delay from the n-*th* scatterer, the time during which the reflected chirp is observed is $\left(T_p - t_n\right)$ seconds. It follows that Eq. 3.8 is valid when $t_n << T_p$. When this condition is not fulfilled, Eq. 3.8 should be replaced by a more general expression equal to

$$\begin{aligned} S_c(\omega) &= \sum_{n=1}^{N} \sqrt{\sigma_n} e^{j\phi_n} e^{j\left(\beta tn + \alpha t_n^2\right)} F\left[\prod\left(\frac{t-\left(T_p/2+t_n\right)}{T_p - t_n}\right) e^{j2\alpha t_n t}\right] = \\ &= \sum_{n=1}^{N} \sqrt{\sigma_n} e^{j\phi_n} e^{j\left(\beta tn + \alpha t_n^2 - \omega t_n\right)} H_{t_n}\left(\omega - 2\alpha t_n\right) \end{aligned} \tag{3.13}$$

where

$$H_{t_n}(\omega) = F_{(t)}\left[rect\left(\frac{t - T_p/2}{T_p - t_n}\right) e^{j2\alpha t_n t}\right]. \tag{3.14}$$

It can be noticed that the observation window modulates the range resolution through the Fourier transformation compression but the corresponding resolution variation is very slow. This is shown in Fig. 3.4a and Fig. 3.4b, where the normalized range *psf* and the corresponding -3dB resolution

are displayed for different range distances along the *boreside* direction. The curves describing point scatterers located in the first two kilometers overlap almost perfectly whereas the response starts widening significantly after 3 km. Since the maximum area usually monitored by a ground-based SAR sensor is about 3 square kilometers, the approximation of Eq. 3.13 to Eq. 3.8 is generally correct. When wider scenarios are to be studied, the mathematical formulation in Eq. 3.13 provides a more precise description of the radar system range performance.

3.2.3.Saw-tooth cosine chirp in CW radar

The ground-based SAR sensor developed by the Remote Sensing Lab at UPC consists of a moving FM-CW radar: the system generates a cosine-chirp signal and carries out the deramping process at hardware level by beating the received signal with a copy of the transmitted one. According to this radar technology [Skolnik,90], a high S/N ratio is obtained by repeating the signal modulation as many times as desired and by successively time-averaging the collected echoes. In order to achieve a more realistic description of the UPC system, the mathematical formulation of the previous section must be modified. For the sake of simplicity, the effects of a repeated chirp modulation and cosine-chirp and not exponential chirp transmission description will be analyzed separately and the combined effects will be finally deduced.

3.2.3.1. Exponential chirp in CW radar

In order to simplify the mathematical expressions, the following substitution will be applied

$$a(t) = \prod\left(\frac{t - T_p/2}{T_p}\right). \tag{3.15}$$

The exponential-chirp signal generated by the UPC FM-CW radar may be expressed as the convolution between a chirp signal and a pulse train, as follows

$$p(t) = \left[a(t)e^{j\beta t + j\alpha t^2}\right] * \sum_{k'=0}^{N_{AVG}-1}\delta\left(t - k'T_p\right) = \sum_{k'=0}^{N_{AVG}-1} a\left(t - k'T_p\right)e^{j\beta\left(t-k'T_p\right)}e^{j\alpha\left(t-k'T_p\right)^2} \tag{3.16}$$

where N_{AVG} is the number of times the FM modulation is repeated at each position of the synthetic aperture. Let's consider now a generic target *n* at the distance r_n from the sensor. The backscattered signal at the receiving antenna is

$$\begin{aligned} s(t) &= \sum_{k=0}^{N_{AVG}-1}\sqrt{\sigma_n}e^{j\phi_n}a\left(t - kT_p - t_n\right)e^{j\beta\left(t-kT_p-t_n\right)}e^{j\alpha\left(t-kT_p-t_n\right)^2} = \\ &= \sqrt{\sigma_n}e^{j\phi_n}e^{-j\beta t_n}e^{j\alpha t_n^2}\sum_{k=0}^{N_{AVG}-1} a\left(t - kT_p - t_n\right)e^{j\beta\left(t-kT_p\right)}e^{j\alpha t^2 - j2\alpha k T_p t + j\alpha k^2 T_p^2}e^{-j2\alpha t_n t}e^{j2\alpha t_n k T_p} \end{aligned}. \tag{3.17}$$

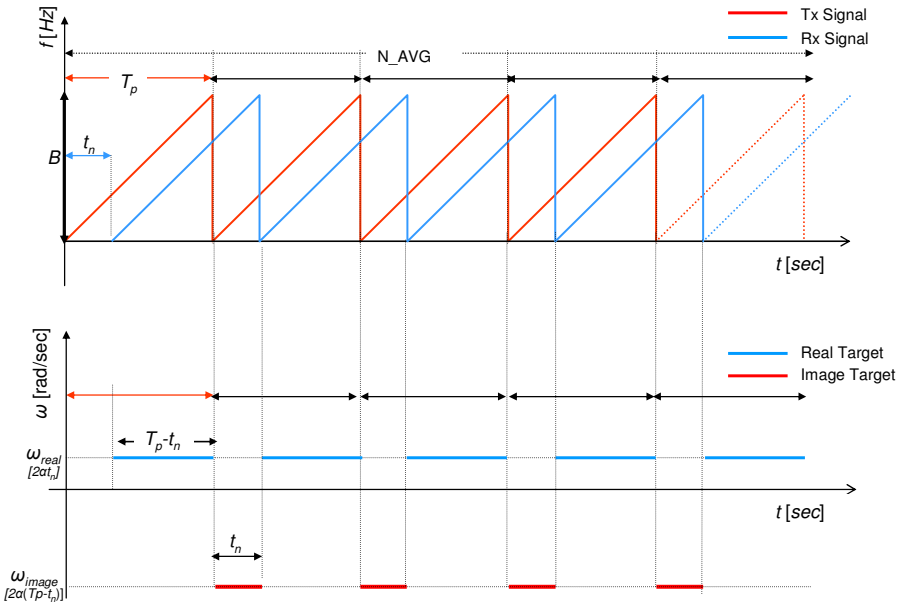

Fig. 3.5: Sketches of the deramping process performed at HW level by the UPC gbSAR system using a copy of the transmitted signal and of the spectral components of the deramped output.

The deramping process is then performed by multiplying the conjugate received signal $s(t)$ by a copy of the transmitted signal $p(t)$. Accordingly, the deramped signal $s_c(t)$ is given by

$$\begin{aligned} & s_c(t) = s^*(t)\, p(t) = \\ & = \sqrt{\sigma_n}\, e^{j\phi_n} e^{j\beta t_n - j\alpha t_n^2} \sum_{k=0}^{N_{AVG}-1} \sum_{k'=0}^{N_{AVG}-1} a^*\left(t - kT_p - t_n\right) a\left(t - k'T_p\right) e^{j\beta T_p (k-k')} e^{j2\alpha T_p (k-k')t} e^{j\alpha T_p^2 \left(k'^2 - k^2\right)} e^{-j2\alpha t_n T_p k} e^{j2\alpha t_n t} \end{aligned} \tag{3.18}$$

where the index k is associated to $s(t)$ and k' to $p(t)$. A graphical description of Eq. 3.18 is given in Fig. 3.5. Let's analyze all the possible contributions to $s_c(t)$. When $k' = k$, it results

$$a^*\left(t - kT_p - t_n\right) a\left(t - k'T_p\right) = a'\left(t - kT_p - t_n\right) \tag{3.19}$$

where $a'(t) = 1$ for $\left[kT_p + t_n\right] \le t \le \left[(k+1)T_p\right]$. In this case, Eq. 3.18 simplifies to

$$s_c^1(t) = \sqrt{\sigma_n}\, e^{j\phi_n} e^{j\beta t_n - j\alpha t_n^2} \sum_{k=0}^{N_{AVG}-1} a'\left(t - kT_p - t_n\right) e^{-j2\alpha t_n T_p k} e^{j2\alpha t_n t} \,. \tag{3.20}$$

When $k' = k+1$, it results

$$a^*\left(t - kT_p - t_n\right) a\left(t - (k+1)T_p\right) = a''\left(t - (k+1)T_p\right) \tag{3.21}$$

where $a''(t) = 1$ for $(k+1)T_p \le t \le (k+1)T_p + t_n$. In this case, Eq. 3.18 reduces to

$$s_c^2(t) = \sqrt{\sigma_n}\, e^{j\phi_n} e^{j\beta t_n - j\alpha t_n^2} \sum_{k=0}^{N_{AVG}-1} a''\left(t - (k+1)T_p\right) e^{-j\beta T_p} e^{j\alpha T_p^2 (2k+1)} e^{-j2\alpha t_n T_p k} e^{j2\alpha\left(t_n - T_p\right)t} \,. \tag{3.22}$$

When $k' \neq \{k, k+1\}$, the overlapping area between the two rectangular pulses is zero and the contribution to the double sum is null, that is

$$a^*\left(t - kT_p - t_n\right) a\left(t - k'T_p\right) = 0 \qquad \forall t \in (0, +\infty) \,. \tag{3.23}$$

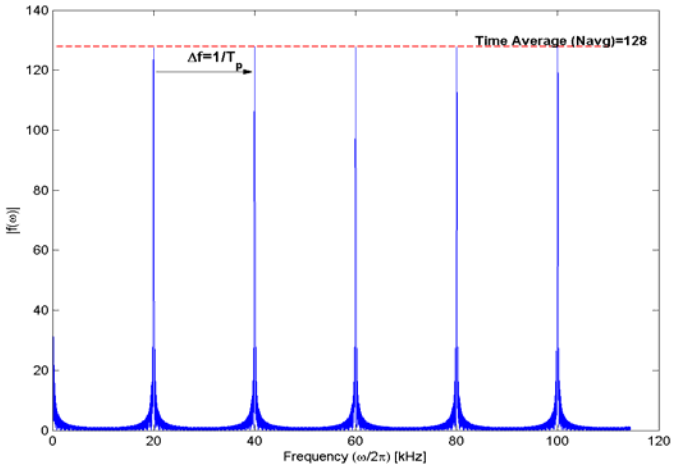

Fig. 3.6: Weighting function introduced by the time-averaging operation applied to the deramped signal in FM-CW radar architecture. The periodicity is related to time duration of the chirp T_p. The value of the maximum is the time-average factor and corresponds to the weight of each time sample of the deramped averaged output.

Summarizing, it is possible to rewrite Eq. 3.18 as follows

$$s_c(t) = s_c^1(t) + s_c^2(t). \tag{3.24}$$

The final step of range-compression process deals with the estimation of $s_c(t)$ spectrum. Invoking the linearity of Fourier transform, it can be written

$$S_c(\omega) = F\left[s_c(t)\right] = S_c^1(\omega) + S_c^2(\omega). \tag{3.25}$$

The term $S_c^1(\omega)$ in Eq. 3.25 is given by

$$S_c^1(\omega) = \sqrt{\sigma_n}\, e^{j\phi_n} e^{j\beta t_n - j\alpha t_n^2} \sum_{k=0}^{N_{AVG}-1} e^{-j2\alpha t_n T_p k} \int_{-\infty}^{+\infty} a'\left(t - kT_p - t_n\right) e^{j2\alpha t_n t} e^{-j\omega t}\, dt. \tag{3.26}$$

By temporary substituting $t' = t - t_n - kT_p$ and $\omega' = \omega - 2\alpha t_n$, Eq. 3.26 may be mathematically simplified as follows

$$\begin{aligned} S_c^1(\omega) &= \sqrt{\sigma_n}\, e^{j\phi_n} e^{j\beta t_n - j\alpha t_n^2} \sum_{k=0}^{N_{AVG}-1} e^{-j2\alpha t_n T_p k} \int_{-\infty}^{+\infty} a'(t') e^{-j\omega'\left(t' + \left(t_n + kT_p\right)\right)} dt' = \\ &= \sqrt{\sigma_n}\, e^{j\phi_n} e^{j\beta t_n - j\alpha t_n^2} \sum_{k=0}^{N_{AVG}-1} e^{-j2\alpha t_n T_p k} e^{-j\omega'\left(t_n + kT_p\right)} \int_{-\infty}^{+\infty} a'(t') e^{-j\omega'(t')} dt' \\ &= \sqrt{\sigma_n}\, e^{j\phi_n} e^{j\beta t_n - j\alpha t_n^2} \sum_{k=0}^{N_{AVG}-1} e^{-j2\alpha t_n T_p k} e^{-j\omega'\left(t_n + kT_p\right)} A'(\omega') \\ &= \sqrt{\sigma_n}\, e^{j\phi_n} e^{j\beta t_n + j\alpha t_n^2} e^{-j\omega t_n} A'(\omega - 2\alpha t_n) \sum_{k=0}^{N_{AVG}-1} e^{-j\omega k T_p} \end{aligned}. \tag{3.27}$$

The last term of Eq. 3.27 is a geometrical series admitting analytical solution [Proakis,98] given by

$$\begin{aligned} S_c^1(\omega) &= \sqrt{\sigma_n}\, e^{j\phi_n} e^{j\beta t_n + j\alpha t_n^2} e^{-j\omega t_n} A'(\omega - 2\alpha t_n) \left[\frac{\sin\left(\frac{\omega N_{AVG}}{2}\right)}{\sin\left(\frac{\omega}{2}\right)} e^{-j\frac{\omega}{2}(N_{AVG}-1)} \right] = \\ &= \sqrt{\sigma_n}\, e^{j\phi_n} e^{j\beta t_n + j\alpha t_n^2} e^{-j\omega t_n} A'(\omega - 2\alpha t_n) f(\omega) = S_{c0}(\omega) f(\omega) \end{aligned}. \tag{3.28}$$

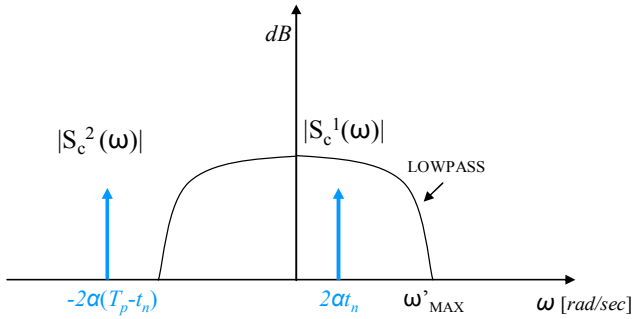

Fig. 3.7: Graphical representation of the spectrum of the beating-based deramped signal described by Eq. 3.25. The two narrow-band signals define the location of the real target $S_c^1(\omega)$ and of an image-target $S_c^2(\omega)$, respectively.

The term $S_{c0}(\omega)$, which represents the spectrum obtained in Eq.3.8 when the deramping of a single chirp-modulation is considered, is now weighted by the term $f(\omega)$. The periodicity of this function is defined by the term T_p, as it is shown in Fig. 3.6. At the same time, T_p defines also the frequency step of the sampled deramped signal, which is given by

$$\Delta f = \frac{1}{T_p}. \tag{3.29}$$

This means that, as a discrete version of the signal in Eq.3.28 is considered, each sample is multiplied by a constant weight factor given by the maximum of the periodic function displayed in Fig. 3.6 and numerically equal to the number of modulation replicas. As far as the properties of *chirp* modulation do not change, $f(\omega)$ is constant. It follows that Eq. 3.28 may be rewritten in a discrete form as

$$\omega \to n\Delta\omega \Rightarrow S_c^1(\omega) = \sqrt{\sigma_n} e^{j\phi_n} e^{j\beta t_n + j\alpha t_n^2} e^{-jn\Delta\omega t_n} A'(n\Delta\omega - 2\alpha t_n) N_{AVG} = S_{c0}(n\Delta\omega) N_{AVG}. \tag{3.30}$$

The second spectral component in Eq. 3.25 may be expressed as

$$S_c^2(\omega) = \sqrt{\sigma_n} e^{j\phi_n} e^{j\beta t_n - j\alpha t_n^2} \sum_{k=0}^{N_{AVG}-1} e^{-j\beta T_p + j\alpha T_p^2(2k+1) - j2\alpha t_n T_p k} \int_{-\infty}^{+\infty} a''(t-(k+1)T_p) e^{j2\alpha(t_n - T_p)t} e^{-j\omega t} dt. \tag{3.31}$$

Using the same strategy of Eq. 3.26, Eq. 3.31 can be simplified by temporary imposing $t' = t-(k+1)T_p$ and $\omega' = \omega - 2\alpha(t_n - T_p)$, yielding

$$\begin{aligned} S_c^2(\omega) &= \sqrt{\sigma_n} e^{j\phi_n} e^{j\beta t_n - j\alpha t_n^2} \sum_{k=0}^{N_{AVG}-1} e^{-j\beta T_p + j\alpha T_p^2(2k+1) - j2\alpha t_n T_p k} \int_{-\infty}^{+\infty} a''(t-(k+1)T_p) e^{j2\alpha(t_n - T_p)t} e^{-j\omega t} dt \\ &= \sqrt{\sigma_n} e^{j\phi_n} e^{j\beta(t_n - T_p) - j\alpha t_n^2 - j\alpha T_p^2 - j\omega T_p + j2\alpha t_n T_p} A''(\omega - 2\alpha(t_n - Tp)) \sum_{k=0}^{N_{AVG}-1} \left(e^{-jTp(\alpha T_p - j\alpha t_n + \omega)}\right)^{2k}. \end{aligned} \tag{3.32}$$

Despite the presence of new phase terms with respect to Eq. 3.27, it can be observed that the spectral components of the signal $S_c^2(\omega)$ are again modulated by a geometrical series. Yet, instead of attaining to solve it, it is sufficient to notice that whereas $S_c^1(\omega)$ locates the target correctly in range, $S_c^2(\omega)$ generates an image replica at an incorrect frequency position:

$$\begin{aligned}&\omega_{real}=2\alpha t_n \Rightarrow r_n=\frac{c}{4\alpha}\omega_{real}\\&\omega_{image}=2\alpha\left(t_n-T_p\right)\Big|_{t_n\le T_p}=-2\alpha\left|t_n-T_p\right|\Rightarrow r_{nimage}=-\frac{c}{4\alpha}\omega_{image}\end{aligned}. \tag{3.33}$$

The *psf*s characterizing real and image targets are different, since they are related to the Fourier transform of $a'(t)$ and $a''(t)$, respectively. Accordingly, the resolution of *image* target is poorer than the real one's. A schematic diagram resuming the spectral contributions generated by the beating-based deramping process is shown in given in Fig. 3.7. It is worth pointing out that no useful information in carried by the *image* target. From a mathematical point of view, the *image* target is always centered at negative frequency and can be easily distinguished. From the practical point of view, it is located at an absolute angular frequency much higher than the *real* one's and it can be easily erased by lowpass filtering the deramped signal $s_c(t)$ before carrying out its A/D conversion.

3.2.3.2. Cosine chirp in CW radar

The signal generated by UPC gbSAR system is not a pure exponential-chirp but a cosine-chirp [Barber,85]. Remanding to Chapter 4 for the hardware description of the generation process, this section analyzes the spectral features of the deramped signal when a real and not complex chirp is implemented. For the sake of simplicity, just one modulation is considered.

Using the same formulation of Section 3.2, a cosine-chirp signal may be expressed as

$$p(t)=\mathrm{Re}\left\{a(t)e^{j\beta t+j\alpha t^2}\right\}=a(t)\cos\left(\beta t+\alpha t^2\right). \tag{3.34}$$

The signal backscattered by the *n*th target may be then reformulated as follows

$$s(t)=\left[\sqrt{\sigma_n}e^{j\phi_n}a(t-t_n)\cos\left(\beta(t-t_n)+\alpha(t-t_n)^2\right)\right]. \tag{3.35}$$

The deramping process implemented at HW level by UPC sensor consists in multiplying directly the received signal in Eq. 3.34 by a copy of the transmitted signal in Eq. 3.35. By invoking the Euler's formula [Pagani,90], the deramped signal in the time domain is decomposed into four contributions as follows

$$\begin{aligned}s_c(t)=p(t)s(t)&=1/4\sqrt{\sigma_n}e^{j\phi_n}a(t-t_n)\left[\left(x_{1n}^*+x_{1n}\right)\left(x_{2n}+x_{2n}^*\right)\right]\\&=1/4\sqrt{\sigma_n}e^{j\phi_n}a(t-t_n)\left[x_{1n}^*x_{2n}+x_{1n}^*x_{2n}^*+x_{1n}x_{2n}^*+x_{1n}x_{2n}\right]\\&=\left[s_c^I(t)+s_c^{II}(t)+\left(s_c^I(t)\right)^*+\left(s_c^{II}(t)\right)^*\right]\\&=\left[s_c^I(t)+s_c^{II}(t)+s_c^{III}(t)+s_c^{IV}(t)\right]\end{aligned} \tag{3.36}$$

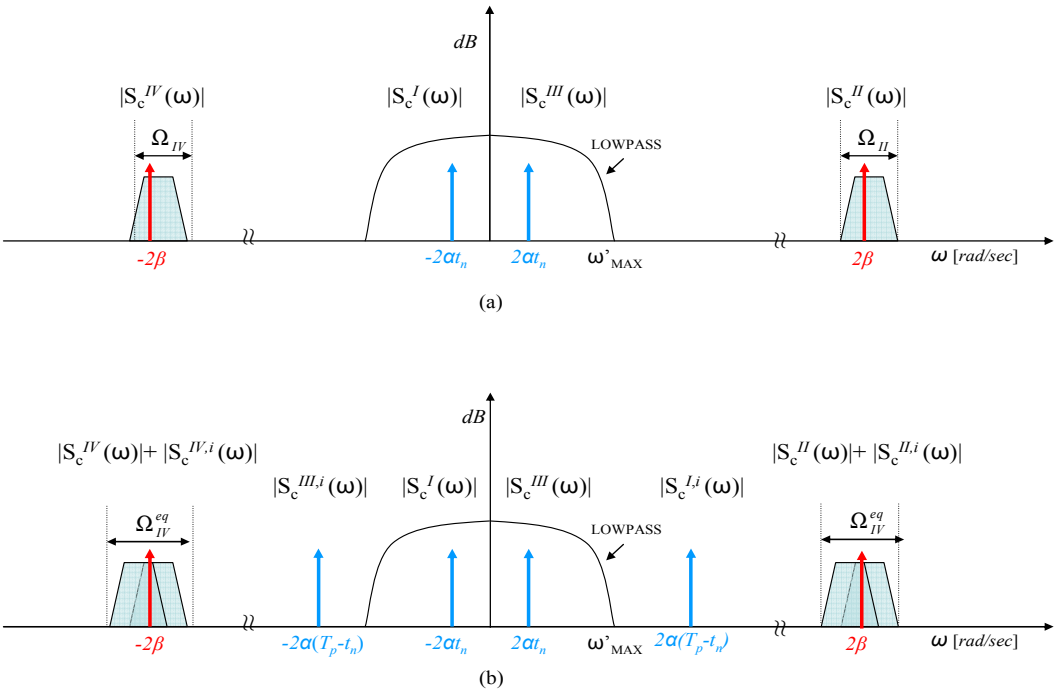

Fig. 3.8: Spectral components of deramped cosine-chirp signal in the cases of a single FM modulation (a) and sawtooth FM modulation (b). The presence of symmetric image targets centered at $\pm 2\alpha(T_p - t_n)$ in the second case reduces the range ambiguity of the radar system. The subscript *i* denotes the contributions of image targets.

where $x_{1n} = e^{j\beta(t-t_n)+j\alpha(t-t_n)^2}$ and $x_{2n} = e^{j\beta t + j\alpha t^2}$. According to the properties of the Fourier transform, the spectrum of $s_c(t)$ is made up of the following four terms

$$S_c(\omega) = S_c^I(\omega) + S_c^{II}(\omega) + S_c^{III}(\omega) + S_c^{IV}(\omega) \tag{3.37}$$

where $S_c^I(\omega) = \left[S_c^{III}(-\omega)\right]^*$ and $S_c^{II}(\omega) = \left[S_c^{IV}(-\omega)\right]^*$. Owing to the symmetry among the four components, it is reasonable to limit the analysis just to the first two terms in Eq. 3.37:

$$S_c^I(\omega) = F\left[\frac{\sqrt{\sigma_n}}{4} e^{j\phi_n} a(t-t_n) e^{j\left(\beta t_n - \alpha t_n^2\right)} e^{j2\alpha t_n t}\right] \tag{3.38}$$

$$S_c^{II}(\omega) = F\left[\frac{\sqrt{\sigma_n}}{4} e^{j\phi_n} a(t-t_n) e^{j\left(\beta t_n - \alpha t_n^2\right)} e^{j(-2\beta - 2\alpha t + 2\alpha t_n)t}\right]. \tag{3.39}$$

The terms $S_c^I(\omega)$ and $S_c^{III}(\omega)$ are two replicas of the range *psf* described in Eq. 3.9 respectively centered at $\omega_I = -2\alpha t_n$ and $\omega_{III} = 2\alpha t_n$. The other two terms, i.e., $S_c^{II}(\omega)$ and $S_c^{IV}(\omega)$, represent two bandpass signals centered at $\omega_{II} = -2\beta$ and $\omega_{IV} = 2\beta$ with spectral maximum support in the case of *upchirp* ($\alpha > 0$) equal to

$$\Omega_{II} \in \left[-2\alpha(2T_p - t_n), 2\alpha t_n\right] \tag{3.40}$$

$$\Omega_{IV} \in \left[-2\alpha t_n, 2\alpha(2Tp - t_n)\right]. \tag{3.41}$$

In the case of *downchirp* modulation ($\alpha < 0$) the extremes in Eq. 3.40 and Eq. 3.41 flip. In order to estimate the two spectral contribution $S_c^{II}(\omega)$ and $S_c^{IV}(\omega)$, the Stationary Phase Method [Raney,92] may be employed. Details concerning the analytical solution of the problem are postponed to *Appendix A,* while a graphical description of the results is shown in Fig. 3.8a. It is important to note that the useful part of the spectrum, that is the components of $S_c(\omega)$ containing information about target's real position, is represented by $S_c^{I}(\omega)$ and $S_c^{III}(\omega)$. On the contrary, the other two contributions centered around $\pm 2\beta$, i.e., $S_c^{II}(\omega)$ and $S_c^{IV}(\omega)$, are useless. Accordingly, they can be easily erased by lowpass filtering the deramped signal $s_c(t)$.

3.2.3.3. Saw-tooth cosine chirp in CW radar

The spectral analysis of Section 3.2.3.1 has dealt with modeling the transmitted signal $p(t)$ with a single exponential-chirp. Nevertheless, the linearity of the problem makes it possible to extend its results to the cosine-chirp case. The main drawback of working with a saw-tooth chirp modulation is the generation of an *image* target at a specific frequency relating its real position r_n and the chirp duration T_p. Accordingly, *image* replica of the different spectral components in Eq. 3.37 are obtained in the case of saw-tooth cosine-chirp.

Concerning $S_c^{II}(\omega)$ and $S_c^{IV}(\omega)$, their *image* replicas $S_c^{II,i}(\omega)$ and $S_c^{IV,i}(\omega)$ are located at very high frequency. Owing to the symmetry of the problem, they correspond to bandpass signals centered at the same carrier frequency but with spectral support, for $\alpha > 0$, equal to

$$\Omega_{II}^{i} = \left[-2\alpha t_n, 2\alpha\left(2T_p - t_n\right)\right] \tag{3.42}$$

$$\Omega_{IV}^{i} = \left[-2\alpha\left(2T_p - t_n\right), 2\alpha t_n\right]. \tag{3.43}$$

It can be noticed that the spectral bands defined by Eq. 3.40 and 3.42 partially overlap, as well as the ones in Eq. 3.41 and 3.43. Being always $0 < T_p - t_n \le T_p$, the total band supports can be approximated as

$$\Omega_{II}^{eq} = \left[-4\alpha T_p, 4\alpha T_p\right] \tag{3.44}$$

$$\Omega_{IV}^{eq} = \left[-4\alpha T_p, 4\alpha T_p\right]. \tag{3.45}$$

Regarding the other two contributions in Eq. 3.37, i.e., $S_c^{I}(\omega)$ and $S_c^{III}(\omega)$, they generate two *image psf*s denoted with $S_c^{I,i}(\omega)$ and $S_c^{III,i}(\omega)$ and respectively centered at $-2\alpha\left(T_p - t_n\right)$ and $2\alpha\left(T_p - t_n\right)$. The complete spectrum of the deramped signal obtained with the UPC gbSAR is shown in Fig. 3.8b. In terms of range resolution, it is possible to state that working with a cosine-

chirp instead of an exponential-chirp is absolutely equivalent. In fact, the spurious components arising from this HW simplification do not interfere with the useful information. They can be nicely eliminated by low-pass filtering the deramped signal before the A/D conversion (see Chapter 4). Just a decrease in the S/N ratio due to the fact that the power associated to a target distributes over several terms must be reported (factor ¼ in Eq. 3.36). The main drawback of *cosine*-chirp modulation is the reduction of the system maximum range.

In the case of exponential-chirp, real and *image* targets can be easily discriminated by the sign of the associated frequency carrier. Theoretically, the no-ambiguous range distance is reduced of a factor 2 as follows

$$r_{\max} = \frac{cT_p}{2} \tag{3.46}$$

Yet, a band-guard is generally suggested for the reduction of range ambiguity from high-reflectivity targets.

In the case of *cosine*-chirp, Eq. 3.46 is not correct. Owing to the symmetry of spectral component, targets characterized by a round-trip delay higher than $T_p/4$ generate an image target at a lower frequency that might be wrongly interpreted. Accordingly, the low-pass filter must be tuned to guarantee the power of *image* targets entering the useful frequency band B_G is a certain threshold below the power of the farthest target to be detected. Once the maximum range distance r_{MAX} is fixed, B_G can be calculated from the radar equation [Skolnik,90] as

$$B_G = \frac{2\alpha}{c\pi}\left[r_{MAX} \frac{1-10^{-TH_{dB}/40}}{1+10^{-TH_{dB}/40}} \right] \tag{3.47}$$

where α is the chirp-rate and TH_{dB} is the chosen threshold expressed in dB. Then, the cut-off frequency of the low-pass filter is given by the expression

$$f_{CUT-OFF} = \frac{2\alpha}{c\pi}\left[r_{MAX}\left(1-\frac{1-10^{-TH_{dB}/40}}{1+10^{-TH_{dB}/40}} \right) \right]. \tag{3.48}$$

An *upchirp* modulation ($\alpha>0$) has been considered in this description. In case a *downchirp* is transmitted, the positive and negative spectrum inverts, as well as the phase term related to the the chirp-rate α. Contrarily, the propagation terms related to the carrier β do not vary. This must be taken into account when dealing with interferometric applications (see Chapter 5) in order to correctly describe propagation phase differences. Finally, it is worth stressing that the information contained in the positive and negative parts of the spectrum is identical. This means that, after the low-pass filtering $s_c(t)$ and estimating the corresponding $S_c(\omega)$, either the positive or negative

frequency components can be used for focusing purpose. Since in this PhD dissertation the IEEE propagation convention [IEEE,79] is adopted, the analysis will be focused on the positive spectrum of the range-compressed signal.

3.2.4. Residual video phase (RVP) error estimation

As it has been pointed out in Section 3.3, the use of the deramping process generates several phase terms that uniquely depend the targets' range distance. From Eq. 3.8, the phase contribution of the range-compressed signal $S_c(\omega)$ from the nth target results

$$\angle S_{cn}(\omega) = \phi_n + \beta t_n + \alpha t_n^2 - \omega t_n + \angle H(\omega - 2\alpha t_n). \tag{3.49}$$

The first term is related to the target's backscattering properties. Contrary, the last one is determined by the system's features. Many SAR applications are based on the assumption that the absolute phase linearly depends on the targets' range position. Hence, the quantity αt_n^2, usually denoted as *Residual Video Phase* (*RVP*) error, represents an undesired term. *RVP* impacts SAR imagery because it varies over a coherent processing interval as the round-trip time delay changes [Carrara,95] and must be removed. For focusing purposes, careful attention must be paid also to the term ωt_n, which arises from the Fourier transform of Eq. 3.7. The general relation between the angular frequency ω and range r is given by

$$\omega = 2\alpha t = \frac{4\alpha r}{c}. \tag{3.50}$$

If a continuous sampling of $s_c(t)$ was carried out, it would be possible to estimate the frequency ω_n corresponding to target's exact position r_n and fulfilling the condition

$$\omega_n t_n = 2\alpha t_n^2. \tag{3.51}$$

The absolute phase of *psf* maximum describing the location of the target would simplifies to

$$\angle S_{cn}(\omega)\big|_{\omega=2\alpha t_n} = \phi_n + \beta t_n - \alpha t_n^2 \tag{3.52}$$

and the compensation of the term $-\alpha t_n^2$ would be trivial. Being a sampled version of $s_c(t)$ really available, the absolute phase description must be reformulated for a discrete domain and Eq. 3.52 becomes

$$\angle S_{cn}[k_{MAX}\Delta\omega] = \phi_n + \beta t_n + \alpha t_n^2 - k_{MAX}\Delta\omega t_n + \angle H[k_{MAX}\Delta\omega - 2\alpha t_n] \tag{3.53}$$

where $\Delta\omega$ defined the angular frequency increment and k_{MAX} represents the index of the sample closest to the real position of the target in the range-compressed profile. At this point, it is worth noting that the last term in Eq. 3.53 can be neglected as $\angle H(\omega - 2\alpha t_n)$ is very smooth around *psf*

maximum and equal to zero. Then, the expression simplifies to

$$\angle S_{cn}\left[k_{MAX}\Delta\omega\right] = \phi_n + \beta t_n - \alpha t_n^2 + \Delta Q \tag{3.54}$$

where ΔQ is the quantization error given by

$$\Delta Q = 2\alpha t_n^2 - k_{MAX}\Delta\omega t_n \,. \tag{3.55}$$

In order to analyze the effects of the time-sampling step on the *RVP* error compensation, it is convinient to express ΔQ as a function of the system parameters. To this end, some comments about the time-sampling of $s_c(t)$ are in order. Being the range position of a target associated to an angular frequency component (Eq. 3.50), the radar maximum range is limited by the maximum *alias-free* sampled frequency $\omega_{r\max}$. Let N be the number of time-samples that the gbSAR system acquires during chirp time-length T_p. The time sampling step Δt results

$$\Delta t = \frac{T_p}{N-1} \simeq \frac{T_p}{N} \text{ for } N \gg 1 \,. \tag{3.56}$$

The corresponding sampling angular frequency ω_s and the maximum $\omega_{r\max}$ are

$$\omega_S = \frac{2\pi}{\Delta t} \simeq \frac{2\pi T_p}{N} \tag{3.57}$$

$$\omega_{r\max} = \frac{\omega_S}{2} = \frac{\pi T_p}{N-1} \simeq \frac{\pi T_p}{N} \Rightarrow r_{\max} = \frac{c\omega_{r\max}}{4\alpha} \simeq \frac{c\pi T_p}{4\alpha N} \,. \tag{3.58}$$

The frequency-separation $\Delta\omega$ between successive elements of $S_c[\omega]$ is related to observation period of the signal T_p in the time domain and results

$$\Delta\omega = \frac{\omega_{r\max}}{N/2} = \frac{\omega_S/2}{N/2} \simeq \frac{2\pi}{T_p} \,. \tag{3.59}$$

The range resolution is then given by

$$\Delta r = \frac{\Delta\omega c}{4\alpha} = \frac{\pi c}{2\alpha T_p} \,, \tag{3.60}$$

which corresponds to the general expression given in Eq. 3.1. Defining the mth non-null samples of $s_{cn}[t]$ as

$$s_{cn}\left[m\right] = \sqrt{\sigma_n}\, e^{j\phi_n} e^{j\beta t_n - \alpha t_n^2 + j2\alpha t_n m\Delta t} \qquad m = 1,2,..N \,, \tag{3.61}$$

the kth element of $S_c[\omega]$ is given by the *Fast Fourier Transform* (FFT) [Proakis,98] of Eq. 3.61 and is equal to

$$S_{cn}\left[k\right] = \sum_{m=0}^{N-1} s_{cn}[m] e^{-j\frac{2\pi}{N}km} = \sqrt{\sigma_n}\, e^{j\phi_n} e^{j\beta t_n - j\alpha t_n^2} \sum_{m=0}^{N-1} e^{j\frac{2m}{N}\left(\alpha t_n T_p - \pi k\right)} \,. \tag{3.62}$$

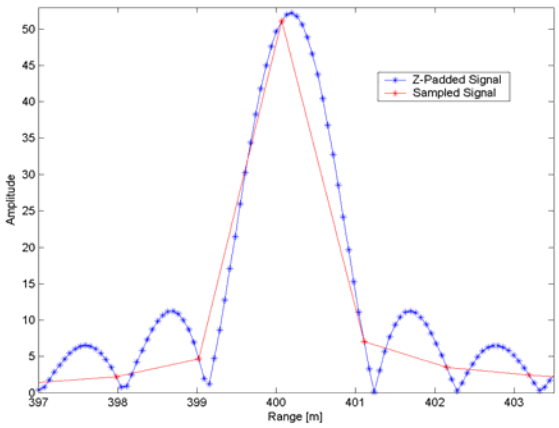

Fig. 3.9: Range-compressed (red) and zero-padded range-compressed (blue) backscattered signals from a target at (400,0,0), respectively. The parameters of the simulated *chirp* are T_p=50μS, N=4096, B=144 MHz.

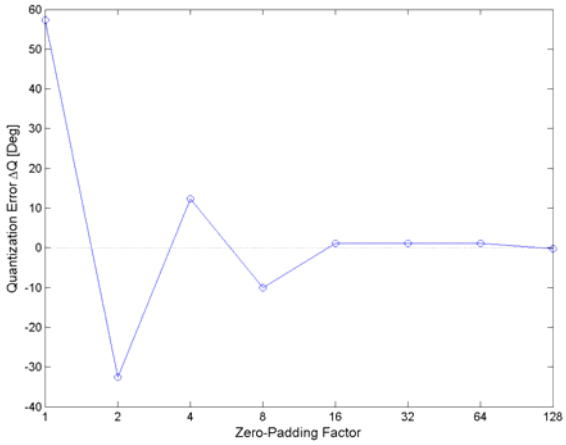

Fig. 3.10: Reduction of the quantization error ΔQ in Eq. 3.64 as a function of zero-padding factor. From a factor 16 the phase difference can be considered negligible.

The index k_{MAX} identifying the position of the nth target corresponds to the value of k maximizing the sum in Eq. 3.62, i.e., minimizing the quantity ($\alpha t_n T_p$-πk). It follows that the quantization error ΔQ introduced by the *RVP* is related to this difference and becomes null only in the case the frequency $2\alpha t_n$ is sampled exactly. Since target's position is unknown, this condition cannot be guaranteed for any index k. An example is shown in Fig. 3.9, where it is possible to observe that the maximum of amplitude might not correspond to the real position of the target. Yet, the smaller the term $\Delta\omega$, the smaller the quantization error. In theory, this can be achieved via hardware by extending the chirp time duration. Yet, an easier solution is to interpolate the compressed signal before the compensation of the *RVP* error. The blue plot in Fig. 3.9 represents the improvement obtained with zero-padding technique in the reconstruction of amplitude of the range-compressed signal. In this case, a more accurate estimate of target's position is obtained.

In order to quantify the improvement in the reconstruction of the absolute phase, a term describing the interpolation step must be introduced in the formulation. Denoting with f_z the zero-padding factor, Eq. 3.62 may be modified as follows

$$S_{cn}[k] = \sqrt{\sigma_n}\, e^{j\phi_n} e^{j\beta t_n - \alpha t_n^2} \sum_{m=0}^{N-1} e^{j\frac{2m}{f_z N}\left(\alpha t_n f_z T_p - \pi k\right)} . \tag{3.63}$$

The analytical solution of Eq. 3.63 [Proakis,98] leads to rewrite Eq. 3.54 as

$$\angle S_c[k] = \phi_n + \beta t_n - \alpha t_n^2 + \Delta Q = \phi_n + \beta t_n - \alpha t_n^2 + \frac{N-1}{f_z N}\left(\alpha t_n T_p f_z - \pi k\right) \text{ for } k = 1,2..,Nf_z \tag{3.64}$$

and the index identifying the range position of the target is then given by

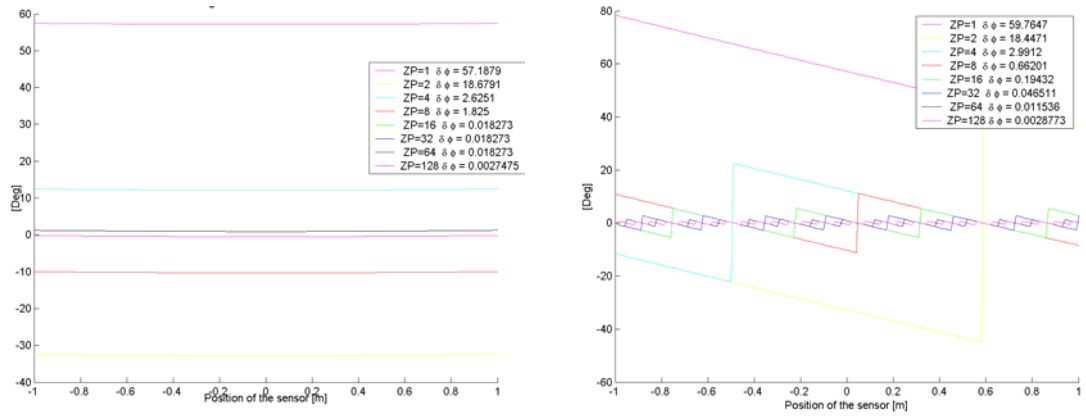

(a) (b)

Figs. 3.11: Error ΔQ affecting the absolute phase of the signal backscattered by a boreside-aligned (a) and a 20º squinted (b) targets along an aperture of 2 meters with a cross-range sampling step of 1 cm. ΔQ has been calculated for $k = k_{MAX}$ at each position of the sensor for the two targets as a function of the interpolation factor f_z. In the legends, it is reported the Mean Square Error $\delta\phi$ given by Eq. 3.66 for the different f_z .

$$k_{MAX} = round\left(\frac{\alpha t_n T_p f_z}{\pi}\right). \tag{3.65}$$

Theoretically, the higher the interpolation factor, the lower the value of ΔQ, as it is shown by the blue plot in Fig. 3.10. Practically, negligible improvements have been observed for f_z higher than 16. Targets at the same radial distance from the antenna are characterized by the same error. It is interesting to study how this error changes when the transmitting and the receiving antennas move. For the sake of simplicity, the radar is assumed to cover a distance L along a linear trajectory orthogonal to the *boreside* direction and the scenario is reduced to two point scatterers at the same radial distance from the position $L/2$ but at different angular position. The quantization error ΔQ in the maximum defining the position of the two targets at each position of the radar is displayed in Fig. 3.11a and Fig.3.11b, respectively. As expected, in both cases ΔQ converges to zero as the interpolation factor f_z increases. But whereas for the boreside target ΔQ is an offset which reduces as f_z increases, for the squinted target a higher sensitivity to antenna position can be observed. The reason is due to effects of the Range Cell Migration (RCM) [Curlander,91] in short synthetic aperture, as it will be exhaustively explained in next section. The global effect on the absolute phase may be estimated in terms of mean-square error with respect to the theoretical value as

$$\delta\phi = \frac{1}{N_u - 1}\sum_{i=1}^{N_u} \angle S_{cn}\left[k_{MAX\,i}\right] - \left(\beta t_{ni} - \alpha t_{ni}^2\right) \tag{3.66}$$

where N_u is the number of cross-range samples and $S_{ni}[k_{MAXi}]$ is the maximum of the range-compressed profile when the sensor is located at the position i of the aperture. In the legend of Fig.

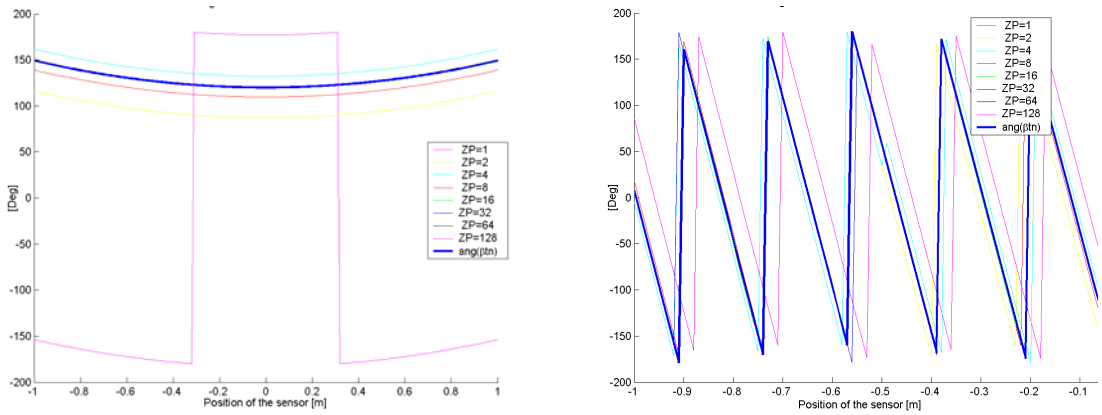

(a) (b)

Figs. 3.12: Absolute phase after the RVP error compensation concerning the boreside-aligned (a) and the 20º squinted (b) targets described in Fig. 3.11 for different interpolation factors f_z. The blue thick line is the linear phase term βt_n the compensation is expected to retrieve.

3.11a and Fig. 3.11b, it can be observed that for $f_z \geq 16$ the term $\delta\phi$ is perfectly negligible. In other terms, for interpolation factor higher that 16, it is possible to assume that the frequency defining target's position is correctly sampled. Accordingly, it is meaningful to define a correction function $F[k]$ equal to

$$F[k] = e^{j\alpha\left(\frac{\Delta\omega k}{2\alpha}\right)^2} \quad \text{for} \quad k = 1, 2.., Nf_z \tag{3.67}$$

and the interpolated compressed signal compensated for the *RVP* error $S_c^{RVP}[k]$ is finally obtained as

$$S_c^{RVP}[k] = S_c[k]F[k]. \tag{3.68}$$

Since RVP error is related just to the deramping process, the same $F[k]$ is used for whole synthetic aperture. The plots in Fig. 3.12a and Fig. 3.12b describe the quality of the RVP error compensation as a function of f_z concerning the two targets described before. The thick blue line represents the theoretical linear component of the absolute phase the compensated profiles converges to. Again, the results show as negligible improvements are obtained for $f_z > 16$. Since the *operative* interpolation factor must be chosen as a trade-off between quantization error reduction and time-consuming performance, an interpolation factor equal to 16 has been employed for UPC gbSAR real data processing. The term $S_c^{RVP}[k]$ in Eq. 3.68 is now characterized by a linear dependence with the range distance r_n and can be fruitfully employed for cross-range imaging.

3.3. Cross-range domain description

In SAR raw data, the *range* dimension is related to the time-delay of the echoed signals

propagating at the lightspeed and is usually referred to as *fast-time* domain. On the contrary, the azimuth or cross-range dimension is related to the speed of the platform on which the radar system is boarded. By comparison, it is usually defined as *slow-time* domain. The term synthetic aperture derives from the acquisition procedure, which is essentially based on the movement along a linear trajectory of the radar system synthesizing in time an imaginary aperture much longer than the physical dimensions of the transmitting and receiving antennas. It is the collection of echoes acquired in the *slow-time* domain that provides the information necessary to retrieve bidimensional complex images of the illuminated scene. Despite all SAR sensors share this basic idea, the features of targets focused in the slow-time dimension depend on the platform used for the measurements. If satellite and airborne acquisition geometries are quite similar and exploit all the potentials of synthetic aperture technique, the use of a terrestrial platform introduces significant limitations. For this reason, a brief description of SAR classical formulation is first given. Then, the main properties of the ground-based aperture synthesis are derived as a special case.

3.3.1. Cross Range Domain: classical formulation

Let's consider the swath that a radar system mounted on a moving platform delineates on the Earth's surface, as it is sketched in Fig. 3.13. For the sake of simplicity, the stripmap acquisition mode and a perfect flat Earth are considered. A comprehensive description of other modes, such as scan-SAR or spotlight, can be found in [Soumeck,99] [Carrara,95].

Let a Cartesian reference system $(\hat{x},\hat{y},\hat{z})$ be centered at P_0 and oriented such that y axis is parallel to the flight direction and z axis to the normal to the flat surface. Being $P_T\left(x_T, y_T, z_T\right)$ the position of a generic target T within the swath and $P_S\left(0,u(t),0\right)$ the position of the moving platform at time t, the time-functions describing the target's distance to the sensor and its corresponding *aspect* angle are given by

$$r_T(t)=\sqrt{x_T{}^2+\left(y_T-u(t)\right)^2+z_T{}^2} \tag{3.69}$$

$$\theta_T(t)=\arctan\left(\frac{y_T-u(t)}{r_{T0}}\right). \tag{3.70}$$

The antennas footprint at -3dB defines the two positions of the trajectory where T starts being visible and finally disappears, or, in other terms, the length L_{saT} of the synthetic aperture in Fig. 3.13. The time interval Δt_{Lsa} during which T is observed by the sensor can be hence expressed as

$$\Delta t_{Lsa}=\frac{L_{sa}}{v}=\frac{\Delta\Omega r_{T0}}{v}=\frac{\lambda}{vd_a}r_{T0} \tag{3.71}$$

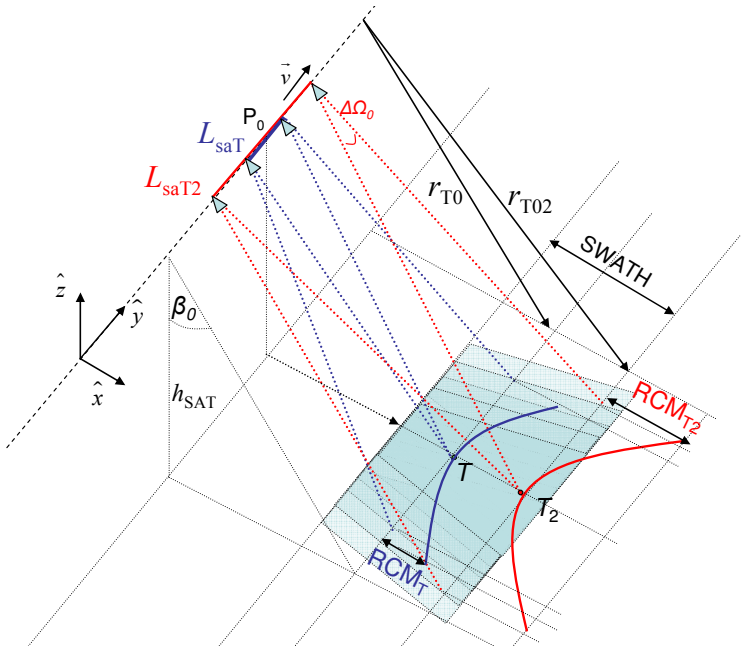

Fig. 3.13: Stripmap acquisition mode of a SAR sensor mounted on air- and space-borne platforms. The targets T and T_2 at different zero-doppler positions are used to stress the proportionality of the RCM effects (RCM_T and RCM_{T2}) and of the synthetic aperture length (L_{saT} and L_{saT2}) to the range distance.

where $\Delta\Omega_0$ defines the azimuth beamwidth of the antennas, d_a its corresponding physical size in the y dimension, and v the platform constant speed. The closest approach of the sensor to the target is usually referred to as zero-Doppler distance [Curlander,91] and is given by the condition

$$r_{T0} = \sqrt{x_T^{\,2} + z_T^{\,2}} \; . \tag{3.72}$$

In the case of narrow-beam Tx/Rx antennas, the hyperbolic function in Eq. 3.69 can be approximated to a parabolic curve using the Taylor expansion around r_{T0}, yielding

$$r(t) \approx r_{T0} + \frac{y^2}{2r_{T0}} = r_{T0} + \frac{(vt)^2}{2r_{T0}} \, . \tag{3.73}$$

The quadratic term in Eq. 3.73 introduces the so-called *range cell migration* (RCM) effect and describes the geometric locus of points that the signal energy from a punctual scatterer follows in the two-dimensional SAR data. This effect is related to the changing range delay to the target as it passes through the antenna beam and may introduce shifts of several range bins. In the classical SAR formulation, the RCM is the same for targets characterized by the same zero-Doppler, and increases with r_{T0}, as stressed by the target T_2 in Fig. 3.13. The phase variation of the backscattering signal due to Eq. 3.73 is given by

$$\varphi(t) = -\frac{4\pi}{\lambda}\left[r_{T0} + \frac{v^2 t^2}{2r_{T0}} \right] \tag{3.74}$$

whereas its instant frequency can be calculated as

$$f(t) = \frac{1}{2\pi}\frac{d\varphi(t)}{dt} = -\frac{2v}{\lambda r_{T0}}t \,. \tag{3.75}$$

The total frequency variation during the time required for the aperture synthesis is referred to as azimuth or Doppler bandwidth B_a and is equal to

$$B_a = -\frac{2v^2}{\lambda r_{T0}}\Delta t_{Lsa} = \frac{2v}{d_a} \,. \tag{3.76}$$

The basic hypothesis is that the movement of the platform during the transmitted signal's round-trip delay is perfectly negligible. This assumption is usually meaningful, being always $c \gg v$, and it is usually referred to as *stop&go* approximation [Soumek,99]. It can be noticed that B_a does not depend on target's zero-Doppler position r_{T0} but only on two physical parameters of the system: the platform's speed v and the physical dimension of the antenna d_a. It follows that the resolution of the synthetic aperture technique in the cross-range dimension can be directly obtained from the azimuth bandwidth as

$$\delta a = \frac{v}{B_a} = \frac{d_a}{2} \,. \tag{3.77}$$

The expression in Eq. 3.77 represents the most important achievement of radar imaging provided by the synthetic aperture technique. As the spectral properties of targets are constant over the whole image, δ_a is independent of the sensor-to-target distance. This property is generally exploited by the main cross-range SAR focusing algorithms, which are briefly described in the following: the range-Doppler, the wavenumber or ω-k and the Chirp–scaling algorithms.

The range-Doppler algorithm is commonly used for processing continuously collected SAR data into 2D images. It is computationally efficient and, for typical space-borne imaging geometries, it constitutes an accurate approximation to the exact SAR transfer function [Curlander,91]. The wavenumber or *ω-k* algorithm is based on the hypothesis that the reflected field is originated from each scatterer of the scene at the same instant (*radiation reflecting model*) [Stolt,78]. The rationale of this approach is to pass from an unevenly- to an evenly-sampled spectrum using the *Stolt* operator [Cafforio,91]. The chirp-scaling technique [Raney,94] [Moreira,96] is based on the scaling properties of chirp signal for the correction of RCM before cross-range processing.

At this point, few comments concerning the three algorithms are in order. Some approximations are introduced in the range-Doppler and chirp-scaling algorithms. They mainly deal with the

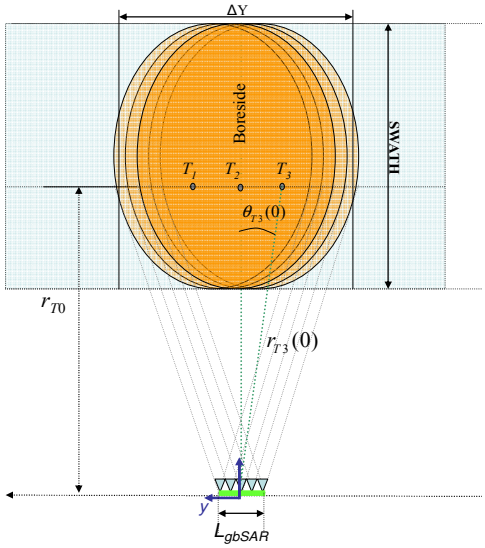

Fig. 3.14: Observation geometry characterizing ground-Based SAR acquisitions (L_{gbSAR} <<ΔY). The target T_1, T_2 and T_3 have the same zero-Doppler position r_{T0}.

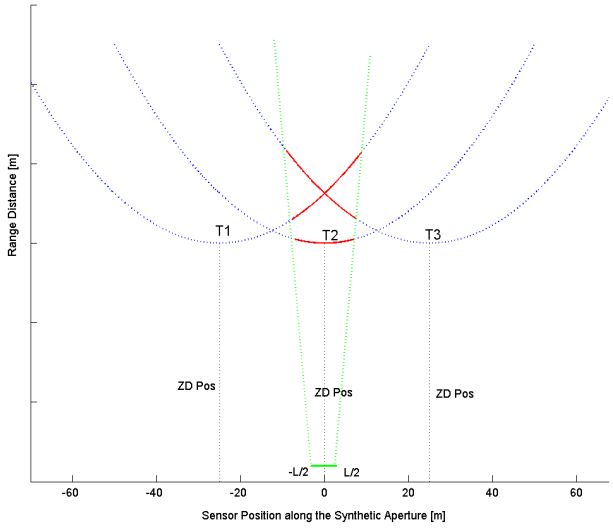

Fig. 3.15: Part of *RCM* curves really sampled in the case of Short Synthetic Aperture (SSA) concerning the three targets at the same zero-Doppler position of Fig. 3.14.

selection of the mid range of the valid data to generate the reference function. Besides, the range-Doppler algorithm is able to carry out an efficient and accurate SAR focusing for reasonable small Doppler centroids and apertures [Prats,05]. On the contrary, the ω-*k* algorithm focuses without assuming any approximation with a computational burden comparable to the range-Doppler. The critical point is the implementation of the interpolation procedure the technique requires in the frequency domain. This step must be performed with a high precision in order to avoid phase artifacts in the final phase image. The same drawback characterizes the range-Doppler algorithm but not the Chirp-scaling focusing technique, which uses only FFTs and phase products to reduce the computational burden. Finally, the three techniques share two main hypotheses. The first one is that the Doppler bandwidth describing azimuth properties are constant for each pixel of the image to be focused. When a satellite or airborne platforms are employed for azimuth sampling, no constraint in terms of observation time is present and this condition can be easily fulfilled. The second one is that the range-compressed raw data is basebanded.

3.3.2. Cross Range Domain: ground-based SAR case

When the synthetic aperture process is carried out using a terrestrial platform, new limitations arise. Owing to the short dimension of mechanical linear units, targets' cross-range properties come to depend on their spatial position with respect to the aperture center. In order to clarify this issue, let three targets be located at the same zero-Doppler position as shown in Fig. 3.14. The two

terms $r_T(0)$ and $\theta_T(0)$ are the radial distance and the *aspect* angle of the generic target *T* when the sensor is positioned in the reference origin, respectively. The green segment describes the aperture synthesized in time by the ground-based sensor while the orange areas account for moving antennas' footprint. It can be observed that $L_{gbSAR} \ll \Delta Y$. Hereinafter, this condition will be referred to as short synthetic aperture (SSA).

The way the gbSAR observes the three targets during the aperture synthesis is sketched in Fig. 3.15. The dotted blue curves describe the corresponding RCM in the case of non-limited aperture while red segments highline the part of the parabolas really sampled during the sensor movement. It can be noticed that the classical zero-Doppler position is not reached for most of the targets within the scenario. Despite the stripmap acquisition mode is considered, only targets aligned along the *boreside* direction are symmetrically sampled. In general, the higher $\theta_T(0)$, the higher the asymmetry of the sampled curve. Asymmetric sampling of RCM curves is typical of squinted SAR observations [Prats,05], i.e., when the *Tx*/*Rx* antennas do not point orthogonally to platform's trajectory. The main difference is that in air/space-borne squinted observations all the targets are described by the same asymmetric sampling whereas in the gbSAR acquisitions the asymmetry of sampled RCM curve becomes a function of target's angular position.

Among the processing techniques described in Section 3.3.1, none of them is suitable for cross-range focusing UPC sensor's acquisitions. The classical range-Doppler and chirp-scaling/extended chirp-scaling algorithms are not capable of handling this spatial-variance. Besides, they do not represent an optimal solution when wide-beam antennas (see Chapter 4) are employed and, consequently, high squinted observations are gathered. Regarding *ω-k*, a different problem must be addressed. Although this technique has been recently applied to VNA-like gbSAR acquisitions [Bernardini,08], *ω-k* is unfit to focus UPC sensor's raw data. In fact, the presence of the term $2\alpha t_n t$ described in Eq. 3.7, which represents the kernel of range focusing process, makes the base-band hypothesis of range-compressed raw data fail.

A general cross-range focusing algorithm with no specific assumption about raw data spectral properties is the Back-Projection (BP) [Soumek,99]. This method makes it possible to carry out the exact inversion of the linear-aperture SAR problem under any observation geometry, either very large (high-resolution SAR) or very short (terrestrial SAR sensor) [Prats,05]. Essentially, it constitutes a generalization of classical beam-forming: for each image pixel the expected signal is used as a reference kernel in a correlation processing. The pulse echo is interpolated at the time-

delay corresponding to the range between the pixel and each position of the antenna and back-projected over spherical shells to the position in the image grid. The pixel-by-pixel sum of the interpolated values directly provides the final focused image. Two main drawbacks of the BP technique must be outlined. The first one is that it is very poor in terms of computational efficiency. The second drawback is that it necessitates a high interpolation rate of the range-compressed raw data for an accurate retrieval of scenario reflectivity map. But if BP is usually discarded for airborne and satellite acquisitions processing, it turns out to be suitable for the UPC sensor's raw data. On the one hand, it takes profit of the high interpolation factor required for the *RVP* error removal discussed in Section 3.4. One the other hand, the small scenario and the fixed observation geometry allow one to remarkably reduce the computational time.

In all this evidences, the BP algorithm will be employed in the frame of this PhD disseration for the raw data cross-range processing.

3.3.2.1. The Back-Projection Focusing Algorithm

Let $P_T\left(x_T, y_T, z_T\right)$ define the position of a generic target *T* in the system reference sketched in Fig. 3.13 and r_{T0} its zero-doppler distance. According to Eq. 3.3, Eq. 3.8 and Eq. 3.68, the RVP-compensated backscattered signal from *T* when the sensor is located at $P_S\left(0,u,0\right)$ can be expressed as

$$S_c^{RVP}\left(\omega,u\right)=\psi\left(r_{T0},y_T\right)e^{j\frac{2\beta}{c}\sqrt{r_{T0}^2+\left(y_T-u\right)^2}}H\left(\omega-\frac{4\alpha}{c}\sqrt{r_{T0}^2+\left(y_T-u\right)^2}\right) \tag{3.78}$$

where $\sqrt{\sigma_n}e^{j\phi_n}$ has been here substituted by the complex reflectivity function $\psi\left(r_{T0},y_T\right)$ defined for any point within the swath. Denoting with *L* the length of the synthetic aperture and R_{ref} the reference distance chosen to carry out the in-phase sum of backscattered echoes, an estimation of $\psi\left(r_T,y_T\right)$ may be obtained as

$$\widehat{\psi}\left(r_{T0},y_T\right)e^{j\frac{4\pi}{\lambda}R_{ref}}=\int_{-L/2}^{L/2}S_c^{RVP}\left(\omega-\frac{4\alpha}{c}\sqrt{r_{T0}^2+\left(y_T-u\right)^2},u\right)\zeta\left(u,r_{T0},y_T\right)du \tag{3.79}$$

where

$$\zeta\left(u,r_{T0},y_T\right)=Ae^{-j[\mathrm{sign}(\alpha)]\frac{2\beta}{c}\left(\sqrt{r_{T0}^2+\left(y_T-u\right)^2}-R_{ref}\left(r_{T0},y_T\right)\right)} \tag{3.80}$$

is usually referred to as *back-projection* kernel. The function sign(α) must be introduced to make the phase of the compensation kernel consistent with the sign of the *chirp-rate*. In classical formulation, R_{ref} corresponds to the zero-Doppler distance r_{T0} [Soumeck,99]. The importance of this term for the cross-range spectral features of gbSAR data will be pointed out in Section 3.8.

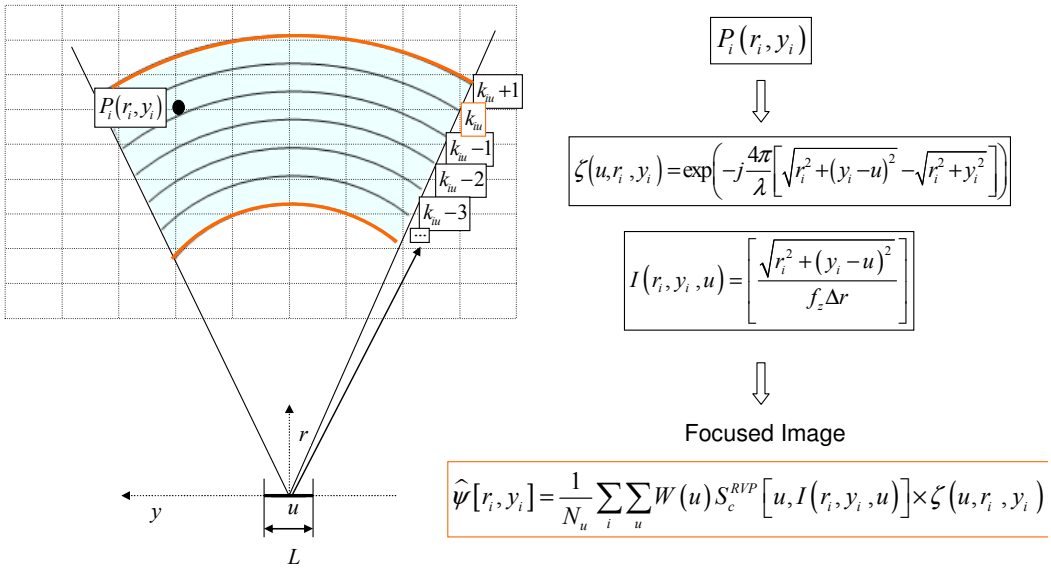

Fig. 3.16: Graphical description of back-projection focusing algorithm. First a regular grid (Cartesian or Polar) is defined. Then the matrices [ζ] and [I] are calculated: [ζ] contains, for each pixel, the values of the kernel compensating for the variations of the target-to-sensor time-delay; [*I*] contains, for each pixel, the position of the useful information in each line of the interpolated range-compressed 2D raw data (the index k_{iu} in the orange frame). The focused image is finally obtained by performing the coherent sum in *u* of the properly compensated $S_c^{RVP}[k_{iu}]$ samples for each pixel of the grid $\hat{\psi}[r,y]$.

The complex reflectivity image is finally obtained by defining a grid $\hat{\psi}[r_{T0},y_T]$ in the (r_{T0},y) 2D domain and solving the integral equation in Eq. 3.79 at each point of the grid. As the range sampling does not follow targets' range migration, the range-compressed data is usually interpolated to obtain a precise computation of Eq. 3.79. Concerning the case of UPC system, the interpolation step is carried out for the removal of the RVP error. Then the signal S_c^{RVP} in Eq. 3.78 can be directly projected onto the image grid.

It is worth noting that no limitation has been introduced on the (r_T,y_T) domain. The reason lies in the physical meaning of the back-projection process, which spreads out the interpolated range-compressed radar echo like a fan each time centered on the proper antenna phase center and sums them coherently. Accordingly, the integral in Eq. 3.79 can be evaluated for an arbitrary image position or size and at any resolution scale. This fact makes it possible to handle any aperture geometry, either very large (high-resolution SAR) or very short (terrestrial SAR sensor). Let's now analyze the computational costs of BP. If *N* positions of the aperture are to be examined for each of the *N*×*N* pixels of the final image, this number is proportional to N^3. The computational cost can be reduced to $N^2\log N$ by multi-stages algorithms operating in the time-domain [Yegulalp,99], which basically exploit the fundamental redundancy between nearby aperture positions for high-frequency reflectivity components in the along-track direction. The rationale of fast back-

projection (FBP) approaches is instead dividing the full-aperture into sub-apertures to be processed in parallel and achieve an efficiency of $N^2\sqrt{N}$ [Urlander,03].

Despite these improvements, the BP technique still remains unattractive for wide-areas processing and it is just employed to obtain reference images for the assessment of faster focusing methods. On the contrary, BP constitutes the optimum solution for gbSAR acquisitions. On the one hand, BP is able to handle the spatial variance of pixels' spectral properties. On the other hand, the computation time becomes more than tolerable due to the small scene that the terrestrial platform can illuminate. Besides, this computational time may be further reduced when a high number of data sets acquired with a fixed geometry are to be processed. In fact, cross-range samples are taken at the same positions along the linear unit during the repeated scanning processes. Then, it is possible to speed up the focusing procedure through the creation of two look-up tables [I] and [ζ] such that [I] contains the position of the useful information in each line of the interpolated range-compressed 2D raw data, and [ζ] provides the value of the kernel compensating for each variation of the target-to-sensor time-delay. Fig. 3.16 briefly explains how the two matrices are filled. Then, Eq. 3.79 can be rewritten for the *discrete* domain as

$$\widehat{\psi}\left[r_{T0i}, y_i\right] = \frac{1}{N_u}\sum_u W(u)\, S_c^{RVP}\left[u, I\left(r_{T0i}, y_i, u\right)\right] \times \zeta\left(u, r_{T0i}, y_i\right) \tag{3.81}$$

where the index i identifies the image pixel, u the position of the sensor along the aperture and $W(u)$ accounts for the filtering window employed for the cross-range side-lobe suppression. Contrary to the range domain, side-lobes generated by the BP focusing are not negligible and their reduction turns out to be mandatory. A description of the different filtering windows that may be employed for this purpose can be found in [Levanon,04].

3.3.2.2. Cartesian vs polar Coordinates

The dimensions of a SAR focused image are usually identified with *range* and *azimuth* dimension, where the first coordinate corresponds to targets' zero-Doppler position and the second one to the synthetic aperture trajectory. In the case of SSA, i.e., when L is much shorter than the azimuth dimension of the scenario to be imaged, this interpretation is not always correct. In order to explain the reason, the four point targets described in Table 3.1 have been simulated. After generating the corresponding gbSAR raw data, two different evenly-spaced pixel grids have been employed for the cross-range imaging: a Cartesian grid and a polar grid. It is worth pointing out that as the BP technique focuses the final image pixel-by-pixel, the spatial distribution of the

	$r_T(0)$ **[m]**	$\theta_T(0)$ **[Deg]**	X **[m]**	Y **[m]**	RCS
T1	400	0	400	0	10
T2	400	5	398.48	34.86	10
T3	600	4	598.53	41.85	10
T4	600	8	594.16	83.50	10

Table 3.1: Cartesian and Polar coordinates of the four simulated targets displayed in Fig. 3.17 and Fig. 3.18.

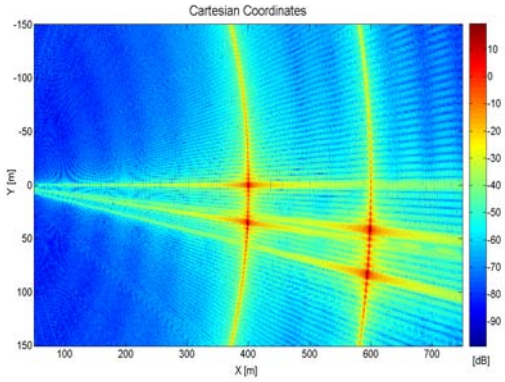

Fig. 3.17: gbSAR amplitude image obtained from a raw data simulating the targets detailed in Table 3.1 focused on a grid of Cartesian evenly-spaced points .

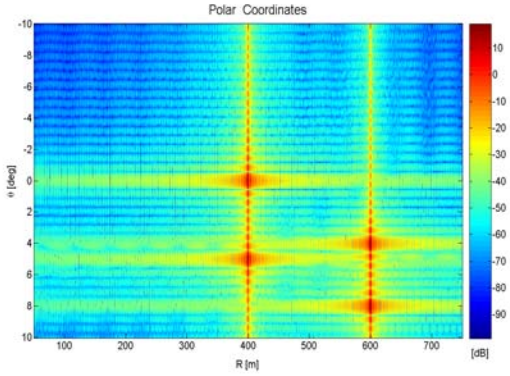

Fig. 3.18: gbSAR amplitude image obtained from a raw data simulating the targets detailed in Table 3.1 focused on a grid of Polar evenly-spaced points.

points is irrelevant. Concerning the Cartesian grid, the vertical axis has been oriented to be parallel to the synthetic aperture (the horizontal is defined by consequence) and the origin *O* has been located at the center of the SSA. The amplitude of the focused image is displayed in Fig. 3.17. It can be observed that *psf*s side lobes do not spread out along orthogonal axis parallel to the reference system. They spatially distribute along the radial direction connecting *O* to the target's position and along circumferences with center *O* and radius equal to $r_T(0)$. The same conclusion can be drawn by observing Fig. 3.18, where *psf*s' side-lobes are shown to stretch out along the two orthogonal axes when polar evenly-spaced points are focused.

This result is extremely useful because it indicates how to separate fast- and slow-time domains and, accordingly, how to carry out a detailed study of gbSAR cross-range imaging features. Nevertheless, when the main concern of the analysis is the interpretation of radar reflectivity image, the use of Cartesian or polar reference must be chosen carefully. Distortion effects induced by polar-distributed pixels often prevent from easily identifying the scatterers within the scene, even when optical images are available. At the same time, Cartesian-distributed points are unsuitable to focus areas with range variation higher than 1km. As the cross-range resolution degrades proportionally to $r_T(0)$ (see Section 3.7), the spatial oversampling factor increases excessively from near to far range. Therefore, the number of Cartesian-spaced pixels required to

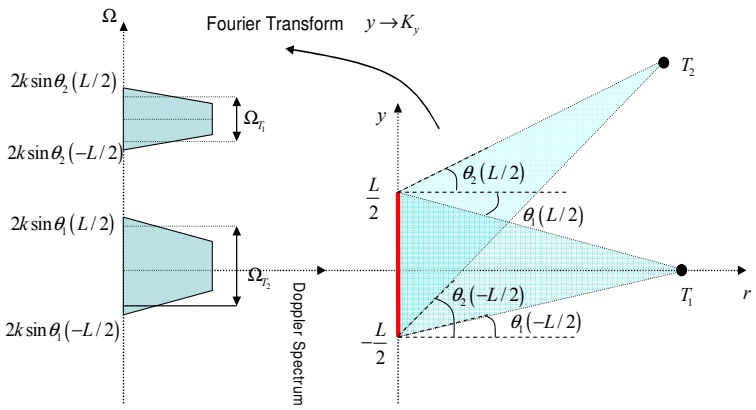

Fig. 3.19: Graphical description of the Doppler band concerning two targets at cross-range position in the case of SSA. The higher the squint angle φ the shorter the support of the corresponding Doppler band, whose limits are defined by the *aspect* angle at the extreme positions of the aperture.

describe the whole scenario becomes much higher than polar-spaced ones', even if the amount of information is exactly the same. It follows that the choice of the image grid must be made in accordance with the extension of the area of interest and the type of analysis to be carried out. In the light of this reasoning, the concepts of *range* and *azimuth* in ground-based and satellite/air-borne SAR images might differ. Since in the frame of this PhD dissertation only gbSAR acquisitions will be studied, these two dimensions coordinates are here redefined. In the following, the term *range* will refer to the targets' distance to the center of the synthetic aperture $r_T(0)$ whereas the *azimuth* or *cross-range* position will denote their angular position $\theta_T(0)$.

3.3.3. Cross-Range Spectral properties

Let T be a generic target located at $P_T\left(x_T, y_T, z_T\right)$. According to the SAR classical formulation [Soumek,99], its maximum cross-range bandwidth Ω_T for an infinite synthetic aperture L and isotropic Tx/Rx antennas is given by

$$\Omega_T = [-2k\sin\theta_T\left(\frac{L}{2}\right), 2k\sin\theta_T\left(-\frac{L}{2}\right)]\Big|_{L\to\infty} = [-2k, 2k] \tag{3.82}$$

where k is the wavenumber and θ_T is the target's *aspect* angle defined in Eq. 3.70. If a real case is now considered, isotropic antennas are replaced by narrow-beam antennas and the azimuth samples that significantly contribute to focus T are limited by the radiation patterns. Denoting with θ_{TMIN} and θ_{TMAX} the minimum and maximum *aspect* angles of T during platform movement, Ω_T becomes

$$\Omega_T = [2k\sin\theta_{TMAX}, 2k\sin\theta_{TMIN}] \tag{3.83}$$

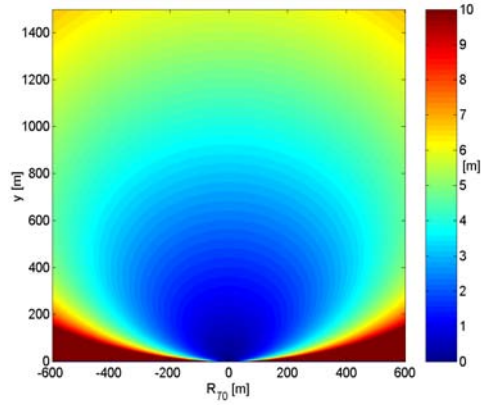

Fig. 3.20: Variation of the azimuth resolution δ_a at X-band on a regular Cartesian grid with a 2 meter long SSA.

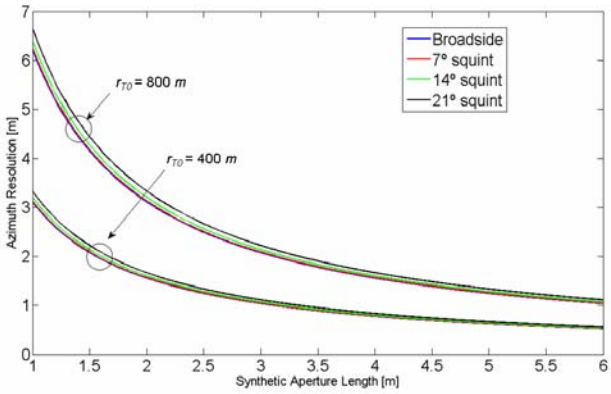

Fig. 3.21: Relationship between δ_a and L at X-band for two groups of four targets at different squint angles θ_{TS} and range distances.

In the case of *stripmap* acquisition mode, Eq. 3.83 simplifies to

$$\Omega_T = \left[-2k\frac{\Delta\Omega_0}{2}, 2k\frac{\Delta\Omega_0}{2}\right] = \frac{4\pi}{d_a} \tag{3.84}$$

where $\Delta\Omega_0$ is the antenna azimuth beam defined in Eq.3.71. A rough estimation of the azimuth resolution δa is then given by the inverse of the cross-range bandwidth as follows

$$\delta a = \frac{2\pi}{\Omega_T} = \frac{d_a}{2}\,. \tag{3.85}$$

Although Eq.3.85 perfectly matches the result obtained in Eq. 3.77, the interpretation in terms of *aspect* angles variation is more general. In fact, it stresses the relationship between δa and the target-sensor extreme positions and not with the speed of the platform. In the case of air-borne or satellite observations, δa is constant over the whole swath since θ_{TMIN} and θ_{TMIN} are independent of targets' position. In case of SSA, the observation conditions change. The *aspect* angles when the sensor is located at the extreme of the SSA strictly depend on both range and azimuth position, as it is sketched in Fig. 3.19. The azimuth bandwidth Ω_T turns from a baseband into a passband signal centered at

$$\Omega_{TC} = 2k\sin\theta_T(0) \tag{3.86}$$

and with a band support given by

$$|\Omega_T| = \frac{4kL}{r_T(0)}\cos^2\theta_T(0)\,. \tag{3.87}$$

where r_{T0} and $\theta_T(0)$ are target's *range* and *azimuth* coordinates, respectively [Soumek,99]. Accordingly, the corresponding cross-range resolution becomes

$$\delta_a = \frac{2\pi}{|\Omega_T|} = \frac{r_{T0}\lambda}{4L\cos^2\theta_T(0)}\,. \tag{3.88}$$

Eq. 3.88 states that the azimuth resolution stops being constant in SSA observations but it decreases proportionally to *range* and *cross-range* distance. As example, the distribution of δ_a obtained with a 2 meter long aperture on a scenario of about 1.5 km^2 is displayed in Fig. 3.20. The radial symmetry of the image with respect to the aperture central point is easily detectable. The dependence of δ_a on parameters such as L, r_{T0} and $\theta_T(0)$ is instead stressed by the plots in Fig. 3.21. It is important to remark that Eq. 3.88 is correct also in case of squinted SSA observations, i.e., when antennas *boreside* direction is not orthogonal to the platform's trajectory. In fact, the different orientation of the antennas' radiation pattern makes the sensor observe a different part of the scene but does not affect the variation of *aspect* angle characterizing targets' resolution, which uniquely depends on their position with respect to SSA central position. Yet, it is easy to understand that a squinted SSA geometry leads to a significant degradation of δ_a within the illuminated area with respect to the stripmap case.

A final comment about Doppler band modulation is in order. According to Eq. 3.86, targets at squinted positions are characterized by modulated cross-range band. The modulation arises when the classical SAR theory is extended to SSA and pixels are focused with respect to r_{T0}, even if most of them are never observed from the corresponding zero-Doppler position. In order to demonstrate this, five targets at the same range distance $r_T(0)$ but different azimuth position $\theta_T(0)$ have been simulated and focused on an evenly-spaced polar grid. The corresponding amplitude image is displayed in Fig. 3.22. The estimation of the targets' Doppler band shown in Fig. 3.23 clearly shows that targets' spectral components shift proportionally to their angular position. The red bulk segment defines the theoretical $|\Omega_T|$ foreseen by Eq. 3.86. The modulation presence makes the azimuth spectral analysis of SSA acquisitions quite uncomfortable. In fact, a high number of samples is required for the correct estimation of all the frequency components and classical interpolation techniques as the zero-padding cannot be applied because the focused image is not band-based. A thicker grid of pixels might be used, but the higher computational time makes this solution inconvenient, especially if several data are to be focused. A way to circumvent this problem is to employ targets' *range* position $r_T(0)$ instead of the classical zero-Doppler position r_{T0}. In other words, the reflectivity of the generic point $P(r_{T0}, y_T)$ is estimated by redefining the term R_{ref} in Eq. 3.79 as

$$R_{ref}(r_{T0}, y_T) = \sqrt{r_T(0)^2 + y_T^2}\,. \tag{3.89}$$

As a result, targets' Doppler band is demodulated. This can be observed in Fig. 3.24, which shows

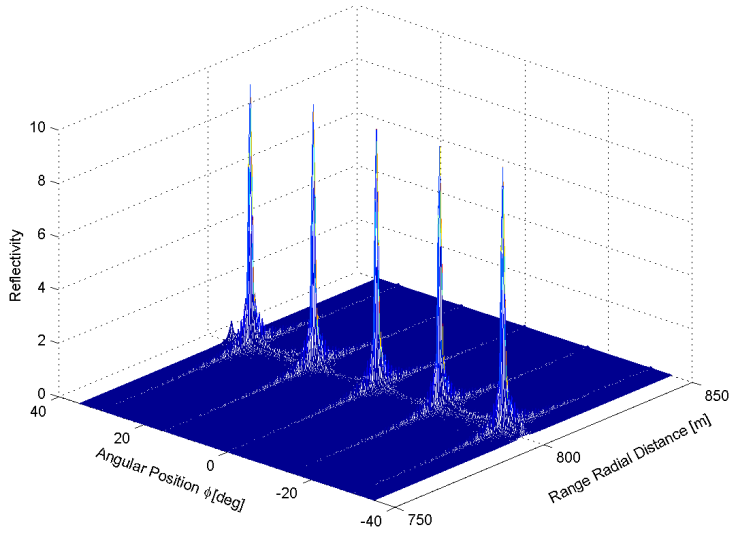

Fig. 3.22: gbSAR amplitude image at X-band of 5 targets at the same range distance form the sensor (800m) but at different aspect angle $\theta_T(0)$ $[0^o, \pm 15^o, \pm 30^o]$ obtained by simulating a 2 meter long aperture.

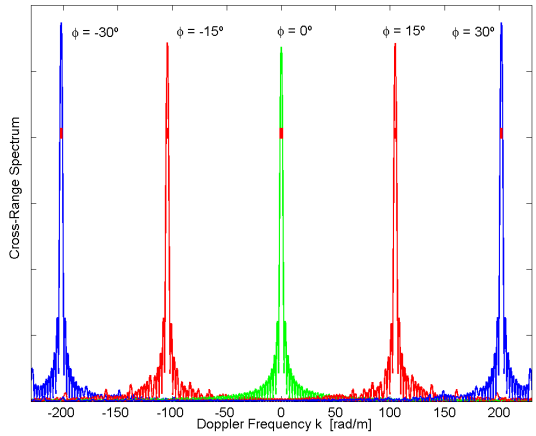

Fig. 3.23: Cut of the cross-range spectrum of the gbSAR simulation described in Fig. 3.22 when raw data are focused with R_{ref} equal to the target's zero-Doppler position r_{T0}.

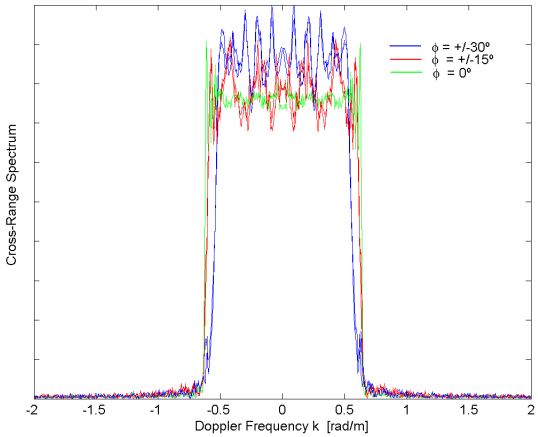

Fig. 3.24: Cut of the cross-range spectrum of the gbSAR simulation described in Fig. 3.22 when raw data are focused with R_{ref} equal to the target's azimuth position $r_T(0)$.

the new *baseband* Ω_T concerning the 5 targets of Fig. 3.22. Since the observation geometry has not changed, the reduction of $|\Omega_T|$ proportional to targets' *azimuth* position is still present. Owing to the advantage of working with base-band complex data, this second criterion has been employed for the cross-range focusing of UPC sensor's raw data.

3.3.4. Cross-range sampling condition

According to Eq. 3.82, the maximum cross-range support band characterizing a target in the case of isotropic antenna and infinite aperture is equal to

$$\Omega_T = [-2k, 2k]. \tag{3.90}$$

For an alias-free cross-range imaging over the whole 2D radar plane, the Nyquist's criterion

states that

$$2k_{MAX} \le \frac{2\pi}{\Delta u} \Rightarrow \Delta u \le \frac{\pi}{2k} = \frac{\lambda}{4} \tag{3.91}$$

where Δu is the cross-range maximum sampling step. Nonetheless, the Nyquist's condition turns out to be too restrictive for real acquisitions where antennas with limited cross-range beam are employed. This means that in order to process real acquisitions just the angular sector $\Delta\Omega_0$ defined in Section 3.5 must be alias-free. Concerning airborne and satellite SAR sensors, very narrow-beam antennas are generally used. For example, *C*-band antennas with an azimuth -3dB beamwidth of about 2.5º are mounted on EMISAR [Christensen,02] and of about 1º are instead used by ERS 1/2 [Partington,98]. As a first approximation, the maximum cross-range sampling step that can be accepted is given by

$$\Delta u \le \frac{\pi}{2k \sin\theta_{MAX}} \simeq \frac{\pi}{k\Delta\Omega_0} . \tag{3.92}$$

Eq. 3.92 has been directly derived from Eq. 3.91 for the *stripmap* acquisition mode. In the case of squinted observation, i.e. when antennas' *boreside* direction is not orthogonal to sensor's trajectory but tilted of an angle θ_c, Eq 3.92 is substituted by a more general expression [Soumek,99] equal to

$$\Delta u \le \frac{\pi}{k \sin\theta_{MAX} - k \sin\theta_{MIN}} = \frac{\pi}{k \sin\left(\Delta\Omega_0/2 + \theta_c\right) - k \sin\left(\Delta\Omega_0/2 + \theta_c\right)} . \tag{3.93}$$

In the case of gbSAR systems, the short synthetic aperture prevents from employing so narrow beam antennas for gathering meaningful observations. Accordingly, wider cross-range illumination cones are usually preferred. In this case, Eq. 3.92 is still valid but θ_{MAX} becomes now the maximum angular position where a target can be clearly detected by the Tx/Rx antennas, which is generally wider than $\Delta\Omega_0 / 2$. The reason is again related to the short dimension of the synthetic aperture. For satellite or air-borne platforms, only the samples obtained when the target passes through the nominal beamwidth (-3dB) are characterized by a useful S/N ratio, while the rest of contributions are too noisy and do not significantly contribute to the focusing process. Contrarily, the short range distance of targets illuminated by gbSAR sensors and the time-average operation performed by the FM-CW radar technology guarantee a high S/N ratio even for angular sectors wider than $\Delta\Omega_0$. It follows that imposing the condition $\theta_{MAX} > \Delta\Omega_0 / 2$ represents the only way to retrieve alias-free information concerning the scene that the sensor is observing efficiently, which turns out to be wider than the area within the -3dB antenna beam. The value of θ_{MAX} should be fixed in accordance with both the system's working parameters and the

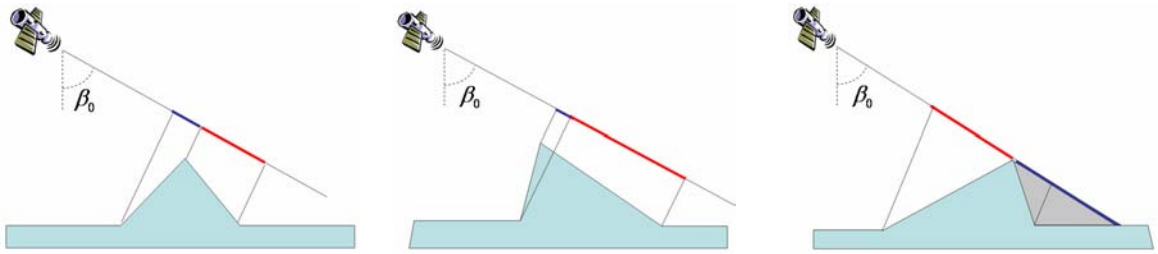

Fig. 3.25: Distortion effects of *foreshortening* (a), *layover* (b) and *shadowing* (c) phenomena in SAR imaging process.

scenario main features. However, angular sectors up to 40º can be fruitfully exploits when a gbSAR is employed for the monitoring activity [Martinez,08].

3.4. Foreshortening, layover and shadowing effect in gbSAR images

Any radar system measures distances in the range direction so that all the ground features are sorted as a function of their distance to the sensor. This leads to some typical phenomena that affect SAR imaging independently of the type of platform employed for the measurement.

The first one is the *foreshortening*, which makes terrain slopes tilted towards the sensor shrink in the SAR image and appear as if they were leaning towards the platform. Contrary, slopes tilted away from the sensor are stretched out. These two effects can be observed in Fig. 3.25a.

When the slope inclination is equal to the look angle β_0, the projection becomes ambiguous. Under this condition, the echoes from the peak might overlap to the ones from the bottom of the slope and the whole slope collapses into few range pixels. For higher inclinations, echoes from higher scatterers get to the sensor before the ones from lower scatterers, as shown in Fig. 3.25b. This effect is usually referred to as *layover*. Finally, terrain slopes with an inclination lower than - β_0 are not illuminated by the radar Fig. 3.25c. As they appear as noisy dark areas in the focused SAR image, this effect is called *shadowing*.

In general, terrestrial sensors work with incidence angles much higher than satellite and air-borne platforms. Foreshortening and shadowing are likely to affect gbSAR acquisitions significantly. Since the observation geometry of ground-based SAR sensors strictly depends on its specific location with respect to the area of interest, its deployment must be chosen cautiously in order to optimize quality of monitoring conditions.

Chapter 4

UPC Ground-Based SAR System

Ground-based SAR sensors represent a cost-effective solution for the continuous monitoring of small scale phenomena. First experiments date back to 90s of the last century, when in-door experiments were carried out to better understand the microwave backscattering characteristic of vegetations and soils [Morrison,96] [Sagues,00] [Cloude,99]. Besides, they were precursor to outdoor systems, designed to be easily deployable at widely separated measurement sites. This new research branch found several followers among the research groups of the remote sensing scientific community. Polarimetric systems were developed mainly for investigation purposes [Morrison,95] [Broquetas,97] [Zhou,04], whereas single-polarization sensors started being used for commercial activities [LiSALab] [IDS]. The kernel of all these solutions is the employment of a Vector Network Analyzer (VNA) for the generation of a bandpass microwave signal. A breakthrough in the SAR community is represented by the polarimetric interferometric ground-based sensor (gbSAR) developed by the Remote Sensing Laboratory (RSLab) at the Universitat Politècnica de Catalunya (UPC). A specific device was projected for optimizing the signal generation and transmission in order to reduce the time required for the scanning process. This Chapter is focused on the analysis of the UPC system architecture. After a brief description of the different strategy implemented at hardware level for the transmitted *chirp* modulation, the whole acquisition process is analyzed in detail. Particular attention is given to the parameters affecting the quality of the retrieved information. The meaningfulness of polarimetric acquisitions when widebeam antennas are employed to illuminate the area of interest is also addressed. In the end, the two test-sites analyzed in the frame of this PhD dissertation are briefly described.

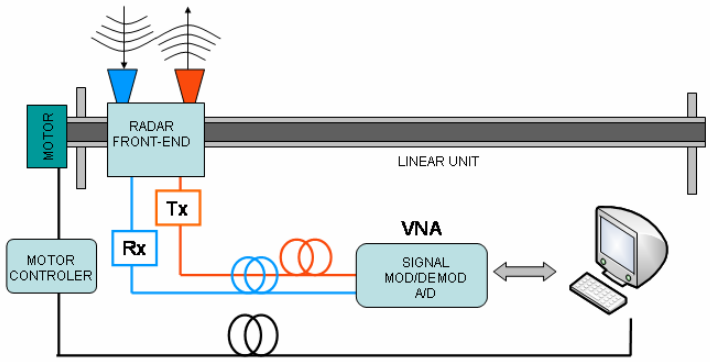

Fig. 4.1: Basic architecture of VNA-based ground-Based SAR systems.

4.1 Architecture of VNA-Based gbSAR Sensors

A ground-based SAR sensor essentially consists of a CW radar system mounted on a sliding support and synthesizing in time an aperture longer than the physical dimension of the real transmitting and receiving antennas. The radio-frequency block is made up of three main parts: the one involved in the generation of the microwave signal, the radar front-end performing the transmission and reception steps, and the part carrying out raw data demodulation, sampling and final storing. The synthetic aperture is instead carried out through the movement of the front-end along a linear rail controlled via computer. This basic structure is resumed in the sketch of Fig. 4.1. The microwave signal generation, demodulation and A/D conversion is usually carried out by a Vector Network Analyzer (VNA). This constitutes the solution mostly adopted in the remote sensing scientific community [Bennet,96] [Pieraccini,00] [Luzi,04] [Zhou,04] [Nico,05] [Noferini,05]. The main reason is the high versatility of VNAs to generate tones from low up to high frequencies and the opportunity to devise a ground-based SAR system without assembling a complex electronic hardware (HW). The two main drawbacks of this approach are the sensitivity to temperature changes and the time required for the scanning process instead. The first problem is caused by the electrical instability the long coaxial microwave lines employed to connect the VNA with the sliding front-end versus flexure and temperature. Changes of atmospheric parameters (mainly the temperature) during the acquisitions process have been observed to induce appreciable phase variations. Moreover, the mechanical deformations of cables during the front-end movement along the linear unit causes phase shifts in the order of several degrees. In order to compensate for these distortion effects, an autocalibration calibration procedure has been designed and proposed in [Noferini,05]. An alternative option is to mount the whole sensor, i.e. VNA plus front-end block, on the moving slide, as it is described in [Martinez,06]. Although effective, this solution is

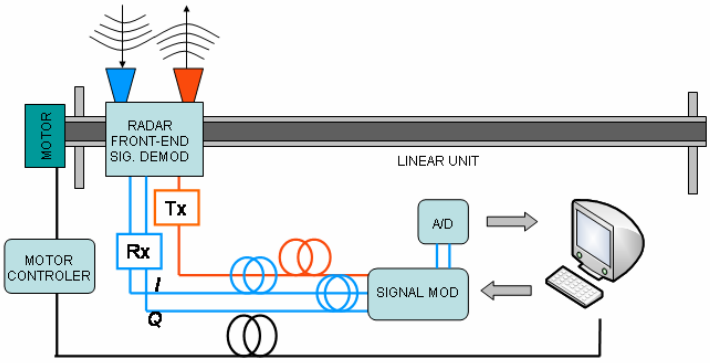

Fig. 4.2: Blocks-Scheme of the (DDS-based) UPC X-band ground-based SAR sensor.

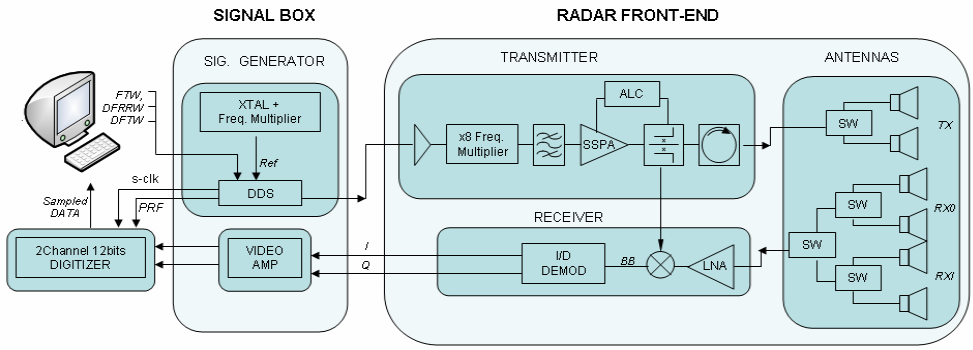

(a)

Fig. 4.3: Internal architecture of the (DDS-based) UPC X-band gbSAR system.

not efficient. Besides requiring a much higher electrical supply to displace a bulky structure, it loses the advantages of portability and the easy deployability that a ground-based SAR sensor is expected to provide. The second drawback is the time VNAs need to sweep the frequency band providing the desired range resolution at each position of the synthetic aperture. This time might turn out to be critical depending on the range/cross-range resolution required for the monitoring application and on the time-scale of the phenomenon to be studied. Finally, it is worth stressing that most of the afore-referenced systems are able to gather single-polarization observation. Being the time required for multi-polarization acquisitions nearly proportional to the number of channels to be measured, VNA-based gbSAR sensors do not constituted a feasible solution for polarimetric observations.

4.2 Architecture of UPC gbSAR Sensor

A new generation of gbSAR sensors conceived as stand-alone systems has been projected and developed by RSLab in the laboratory of the UPC [Aguasca,04]. The basic structure of Fig. 4.1 has been maintained. Yet, significant modifications have been introduced to guarantee measurements quality and to optimize the system's performance. The first step has been to develop

a specific hardware focused on the type of monitoring activity that a gbSAR sensor is expected to carry out. Renouncing to the unexploited wide frequency range that a VNA is able to generate, the system has been devised to work at specific frequency windows and to offer advantages such as portability, reduced size and weight, and, even more important, low power consumption. The radar architecture is based on a FM-CW modulated solid-state transmitter designed to be flexible and adaptable to different frequency bands, such as *L-, C-*, *X-*, and *Ku*-bands. The system is modular and the change of different frequency band is obtained with interchangeable frequency-multiplication modules. Besides, the employment of off-the-shelf components reduces the equipment global costs. Since this PhD dissertation deals with gbSAR data acquired at *X*-band, in the following the analysis is focused on the *X*-band sensor. Its schematic description is given in Fig. 4.2. By comparison with Fig. 4.1, it can be noticed that the VNA has been substituted by two now blocks: the signal-generation box and the A/D converter. I/Q demodulation is now performed inside the sliding box so that a baseband signal travels along the long coaxial cables employed for the sensor movement. It follows that the phase distortions described in [Noferini,05] become here negligible and sophisticated autocalibration procedures are unnecessary.

In order to emphasize the different strategy the UPC gbSAR follows with respect to the VNA-based sensors, a more specific description of the hardware architecture is sketched in Fig. 4.3. The kernel is the frequency generation module, which backs up on a Direct Digital Synthesis (DDS) chipset [Analog]. This device is a programmable high speed D/A converter capable to synthesize analog sine-waves by fast frequency hops and a very fine tune resolution. Its versatility makes it possible to digitally generate analogical and digital modulated signals by loading the configuration parameters into its internal registers. For gbSAR applications, the DDS is set up to generate *chirp*-modulated signals. Details about its configurations can be found in [Calvo,04]. Briefly, the device set-up is carried out through the definition of three parameters:

- the start frequency FTW (**F**requency **T**uning **W**ord)
- the up-dating frequency time-step DFRRW (**D**elta **F**requency **R**amp **R**ate **W**ord)
- the frequency increment DFTW (**D**elta **F**requency **T**uning **W**ord).

An external clock is used as reference to increment output signal frequency without generating phase discontinuities. This is obtained by imposing the first phase value after a frequency hop to be an increment of the last phase value before the change, but at the updated FTW. The output is an *L*-Band FM-modulated signal that must be bandpass-filtered to eliminate spurious replica

generated by the D/A conversion. A final x8 frequency multiplier provides a *chirp* centered at 9.65 GHz. A high temperature-stability versus external temperature variation is obtained through hysteresis cycle-based heating and cooling processes inside the signal generation box. This guarantees a drift of the *chirp* frequency carrier of less than the 0.2 ppm specified in the datasheet of the reference oscillator within the temperature range 0ºC-50ºC [Farnell]. According to intuitive approach proposed in [Luzi,04], the phase variation due to gbSAR instrumental instability is proportional to the range distance. Yet, for scenarios of few square kilometers, a maximum positioning error of less than 0.1 mm can be reasonably assumed at X-band.

The last step before the transmission is the signal amplification. This is obtained using a Solid State Power Amplifier (*SSPA*) controlled by an Automatic Gain Control (AGC), which ensures long term power stability through a feedback loop. At this point of the circuit, a directional coupler extracts and injects to the receiver block a copy of the signal sent to the transmitting antennas for deramping the received signal (see Section 3.3). It is worth noting that there are other two DDS outputs denoted with *s-clk* and the *PRF*: they are employed as sampling and modulation rate references, respectively. Being the former a multiple of the latter, these two time references guarantee a perfect synchronism among the samples belonging to the different FM modulations when the time-averaging operation is performed.

4.3 UPC gbSAR Front-End Analysis

The microwave signal transmission and reception is carried out by the front-end module detailed in Fig. 4.4. The CW architecture requires the simultaneous use of an independent antenna for each of these two tasks [Skolnik,90]. In order to provide fully polarimetric interferometric (PolInSAR) measurements in a single-pass mode, six identical linearly-polarized pyramidal horns (Fig. 4.5) have been mounted on the radar front-end. The two antennas within the yellow circle are used for the horizontal (*h*) and vertical (*v*) transmission, whereas the other four for the zero-baseline and interferometric *h*/*v* reception, respectively. The position of the last two horns is not fixed but it is adapted to the sensitivity required for the In-SAR measurements [Hansenn,01], as it will be explained in Chapter 5. Multi-polarization data are gathered by switching among the selected combinations of transmitting and receiving antennas in the serial scheme detailed in Fig. 4.6.

4.3.1 Polarization Purity

A key parameter indicating the quality of polarimetric measurements is the polarization purity of

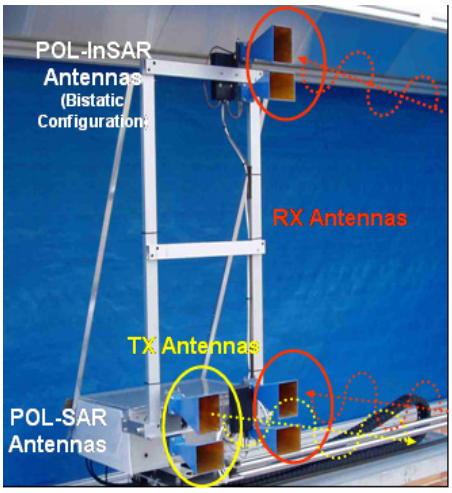

Fig. 4.4: Layout of the X-Band horn antennas mounted on the polarimetric interferometric front-end of UPC gbSAR.

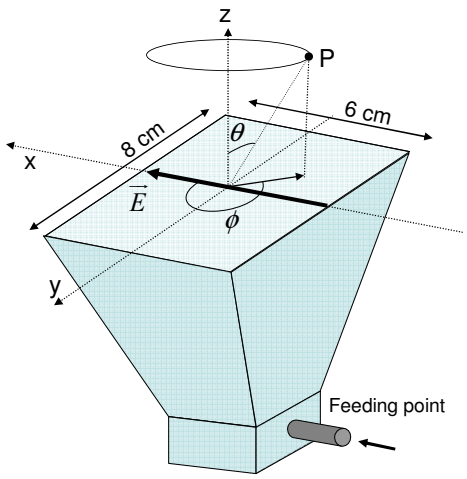

Fig. 4.5: Sketch of the X-band horn antenna mounted on the front-end of the UPC system.

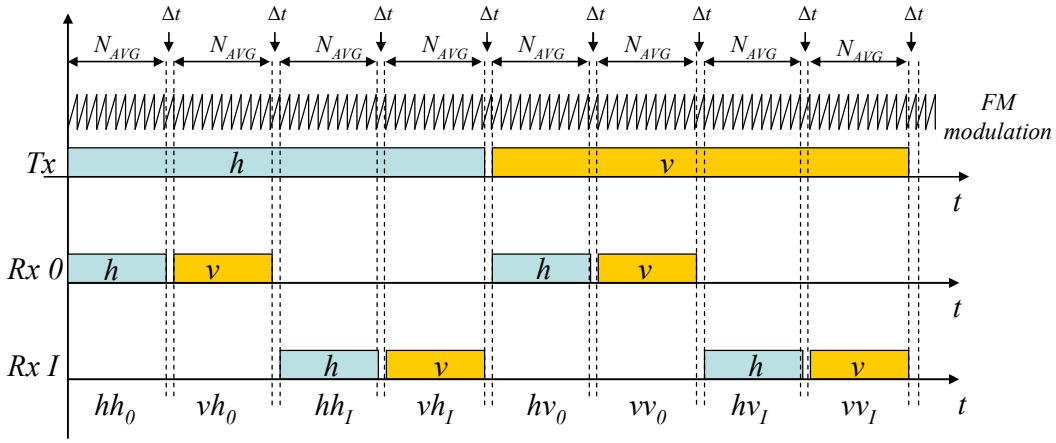

Fig. 4.6: Diagram of serial scheme carried out by UPC gbSAR at each position of the SSA to gather PolInSAR measurements: *Tx* denotes the transmitting antenna, *Rx0* and *RxI* the zero-base and interferometric receiving antennas, N_{AVG} is the number of chirp modulations to be time-averaged for each polarization channel, Δt is the polarization switching time.

the system. In order to understand its physical meaning, the concepts of antenna polarization and cross-polarization must be recalled. As widely known, the distribution of the electromagnetic field $\vec{E}(\vec{r})$ at the antenna aperture determines its radiation pattern and the so-called antenna polarization. The former defines the directivity of the antenna; the latter describes the geometrical orientation of $\vec{E}(\vec{r})$ at any position of the far-field zone [Balanis,89]. Similarly, it is possible to introduce the concept of antenna cross-polarization. Intuitively, it defines an orientation orthogonal to the polarized component of $\vec{E}(\vec{r})$. Still, three different definitions of antenna cross-polarization can be found in the literature. In the framework of this PhD dissertation, the 3rd definition given in [Ludwig,73] is adopted. This is the convention that is usually employed in anechoic chamber measurements.

Let the reference system be oriented as shown in the sketch of Fig. 4.5, and let the direction of the electric field at the antenna aperture be parallel to *x* axis. Being the point P located in the antenna far field zone and $(\hat{u}_{r_a}, \hat{u}_{\theta_a}, \hat{u}_{\phi_a})$ the corresponding spherical unit vectors at P, the co-polar $C(\theta_a, \phi_a)$ and cross-polar $X(\theta_a, \phi_a)$ components of $\vec{E}(\vec{r})$ are given by [Ludwig,73]

$$\begin{aligned} C(\theta_a, \phi_a)\hat{i}_C &= E(\vec{r}) \cdot \left[\sin\phi_a \hat{u}_{\theta_a} + \cos\phi_a \hat{u}_{\phi_a} \right] \\ X(\theta_a, \phi_a)\hat{i}_X &= E(\vec{r}) \cdot \left[\cos\phi_a \hat{u}_{\theta_a} - \sin\phi_a \hat{u}_{\phi_a} \right] \end{aligned} \tag{4.1}$$

where "·" denotes the vector scalar product. The polarization purity of the antenna is hence defined as the power unbalance between co-polar and cross-polar components as follows

$$P(\theta_a, \phi_a) = 20\log_{10}\left(\frac{C(\theta_a, \phi_a)}{X(\theta_a, \phi_a)} \right). \tag{4.2}$$

The co-polar and cross-polar radiation diagram of the antennas mounted of the UPC gbSAR front-end in Fig. 4.4 can be observed in Fig. 4.7a and Fig. 4.7b, respectively. The measurements have been carried out in the anechoic chamber of the UPC. The plots in Fig 4.8 represent the θ_a profiles of the *v*-polarized antenna's co-polar and cross-polar components at $\phi_a = 0$ and $\phi_a = 90^o$. From a brief analysis, it can be drawn that the difference between the two orthogonal cuts is negligible within the -6dB antenna beamwidth, assuring and that the corresponding polarization purity is higher than 40 dB. It is worth noting that the condition $\phi_a = 90^o$ of the *v*-polarized antenna corresponds to $\phi_a = 0$ of the *h*-polarized antenna. Since the polarimetric response of the target passes through the transmitting and receiving horns, the distortion effects introduced by *h* and *v* radiation patterns may be described by the co-polar ratio ρ_{hv} defined as

$$\rho_{hv} = \frac{C_h(\theta_a, \phi_a)}{C_v(\theta_a, \phi_a)} = \frac{C(\theta_a, \phi_a)}{C(\theta_a, \phi_a \pm \pi/2)}. \tag{4.3}$$

The modulus of ρ_{hv} is displayed in Fig. 4.9 and shows that the power unbalance between *h* and *v* radiation patterns can be approximated to an offset in the whole area of the central lobe, extending the results of Fig. 4.7 to all the possible values of ϕ_a. The distortion of the absolute phase is given by the argument of ρ_{hv}, which is displayed in Fig. 4.10. Also for this phase term, it is possible to affirm that the combination of *h*- and *v*-polarized antennas' radiation pattern introduces just an offset within the beam area delimited by the condition $\theta_a \le \theta_{6dB}$. This result is very important because it allows one to simplify significantly the polarimetric calibration procedure of gbSAR acquisitions, as it will be explained in Section 4.4. Another importance issue to be stressed is the

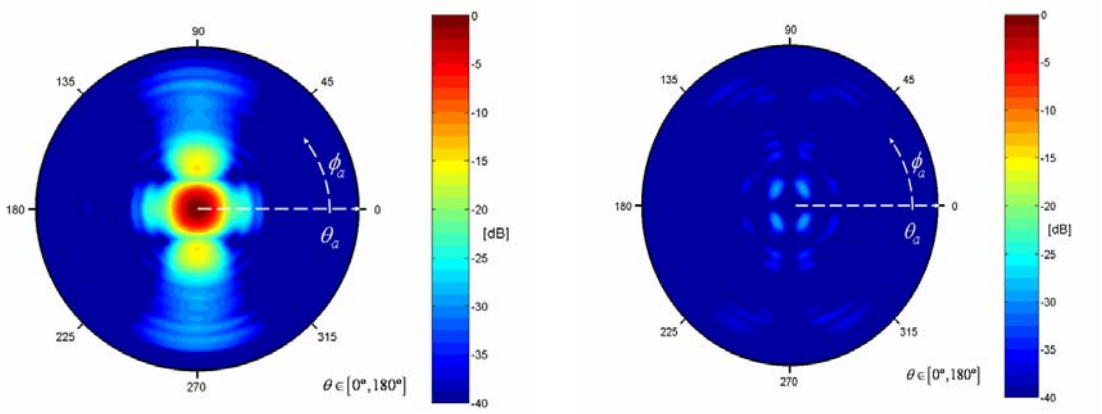

(a) (b)

Figs. 4.7: Co-polar $C(\theta_a, \phi_a)$ (a) and cross-polar $X(\theta_a, \phi_a)$ (b) radiation diagrams of the antennas mounted on the UPC system.

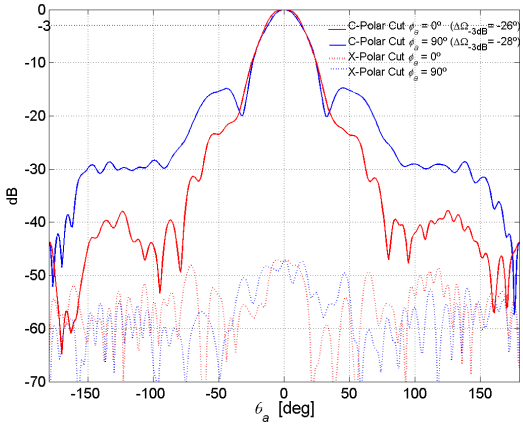

Fig. 4.8: Cuts of the co-polar and cross-polar radiation diagrams of the X-Band horn antennas mounted on the UPC gbSAR Sensor at $\phi_a = 0°$ and $\phi_a = 90°$. The -3dB antenna beam are respectively 26º and 28º.

antennas' feeding point orientation. The front-end layout of the UPC system has been devised to minimize the antenna-to-switch cable length. As shown in the sketch depicted in Fig. 4.11, the orientation of feeding points is the same for the vertical but not for horizontal polarized antennas. Their orientation must be taken into account for each configuration of the switches in order to avoid a phase offset equal to π among the different polarimetric channels and, accordingly, to properly compensate the effects of *Tx* and *Rx* antenna radiation patterns.

4.3.2 Cables and equivalent phase-centers compensation

Few comments about the spatial location of the antennas and the length of cables used for the connections are in order. For the sake of simplicity, let each couple of transmitting and receiving horns providing a different polarimetric measurement be substituted by an equivalent fictitious antenna. This new antenna accomplishes the two functions and it is equidistant from the two real ones. Hereinafter, its position is denoted with *equivalent phase center* (EPC). The EPCs

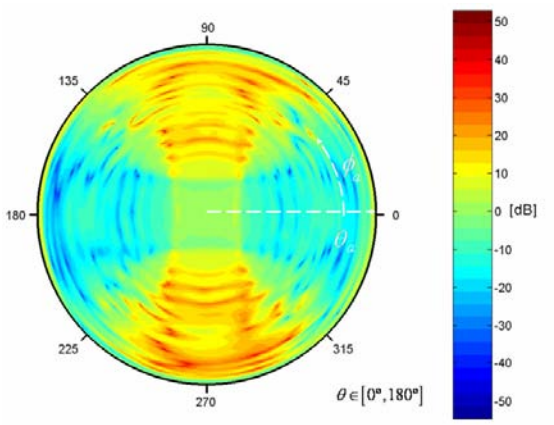

Fig. 4.9: Amplitude of the co-polar ratio ρ_{hv} in Eq. 4.3 of the UPC gbSAR antennas in dB.

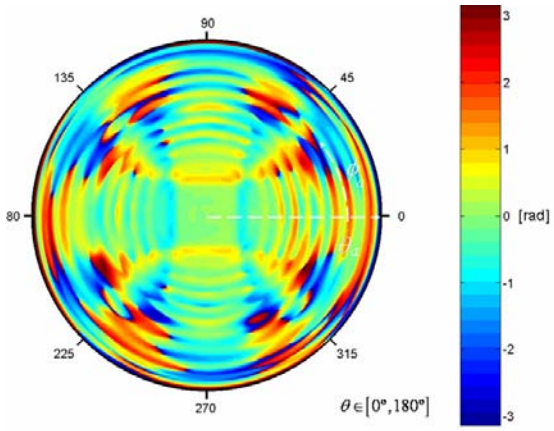

Fig. 4.10: Phase of the co-polar ratio ρ_{hv} in Eq. 4.3 of the UPC gbSAR antennas in radians.

corresponding to all the possible combinations of the antennas mounted on the UPC sensor front-end are depicted as colored circles in Fig. 4.11.

Two EPCs located at two different positions introduce a coregistration mismatch between corresponding focused SAR images, corrupting both amplitude and phase information. An efficient way to solve this problem without employing time-consuming interpolation procedures is to compensate for EPCs' different location during the cross-range focusing process.

First, a phase center denoted with EPC_M is chosen as reference. Then, all the remaining EPCs are referred to EPC_M. To do this, the distance vector of each slave EPC to EPC_M is decomposed into a horizontal component Δy_{EPC} parallel to the synthetic aperture trajectory and a vertical component Δz_{EPC}. For geometrical reasons, Δy_{EPC} turns out to affect the azimuth dimension while Δz_{EPC} the range dimension. Once EPCs' position is measured with submillimetric precisions, this information can be directly introduced in the formulation of the back-projection focusing algorithm (see Section 3.6). Defining the position of the i*th* EPC with respect to EPC_M as

$$P_{EPC}^{i}\left(0,\Delta y_{EPC}^{i},\Delta z_{EPC}^{i}\right)=\left(0,y_{EPC}^{i}-y_{EPC}^{0},z_{EPC}^{i}-z_{EPC}^{0}\right), \tag{4.4}$$

the kernel function of Eq. 3.79 is redefined as

$$\zeta_i\left(u,r_T,y_T\right)=Ae^{-j[sgn(\alpha)]\frac{2\beta}{c}\left(\sqrt{r_T(0)^2+2z_T\Delta z_{EPC}^{i\,2}+\Delta z_{EPC}^{i\,2}+\left(y_T-(u-\Delta y_{EPC}^{i})\right)^2}-\sqrt{r_T(0)^2+2z_T\Delta z_{EPC}^{i\,2}+\Delta z_{EPC}^{i\,2}+y_T^{\,2}}\right)}. \tag{4.5}$$

From the second column of the table in Fig. 4.11 it can be observed that just two values are available for Δz_{EPC}. Then, the effect of Eq. 4.5 is essentially to compensate for any horizontal baseline generated by the antennas layout and to define two equivalent phase centers: EPC_M for the zero-baseline and EPC_S for the interferometric measurements, being the latter horizontally aligned to the former but with a vertical separation equal to Δz_{EPC}. The subscripts M and S stand for

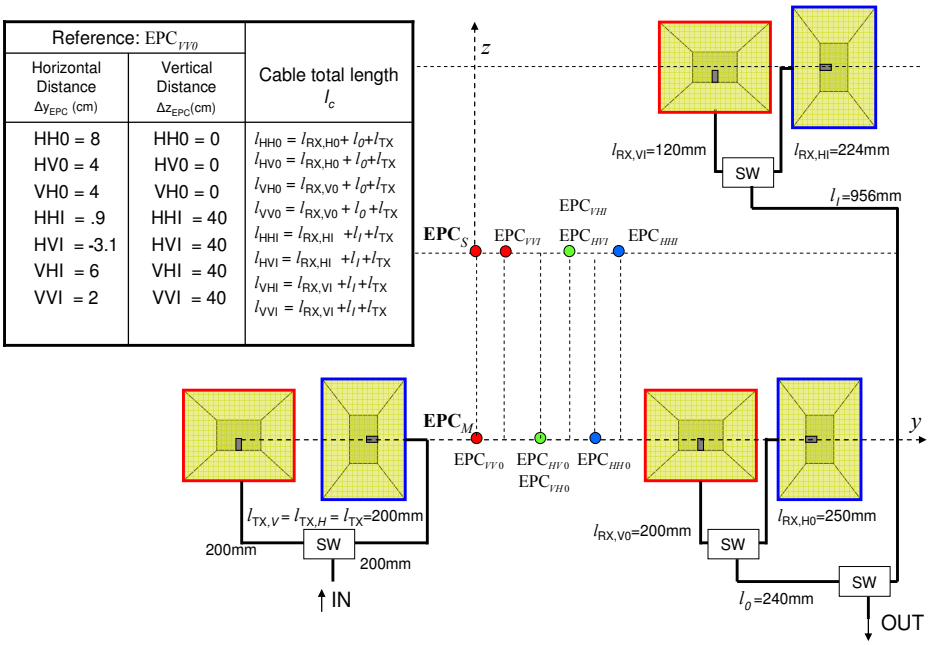

Fig. 4.11: Layout of UPC gbSAR front-end and spatial position of the *Equivalent Phase Center* (EPC) corresponding to each combination of transmitting and receiving antennas; EPC$_M$ and EPC$_S$ indicate the position of the zero-baseline and interferometric polarimetric measurements after the correction described in Eq. 4.5, respectively.

master and *slave*, respectively. These are the two names usually employed for the reference and secondary antennas when interferometric measurements are gathered.

Finally, the effect of the different length of feeding-points-to-switches cables must be analyzed. In pulsed-radar measurements, the length of the cable affects just the absolute phase information by adding an offset term. In the UPC gbSAR measurements, the effect changes significantly as any time-delay turns into a frequency shift after the deramping and range-compression steps. Being l_c the length of a cable and ε_r its dielectric constant, the time-delay of the microwave signal traveling along l_c is given by

$$t_c = \frac{l_c \sqrt{\varepsilon_r}}{c}. \tag{4.6}$$

In order to keep into account the propagation through each cable, Eq. 3.4 can be reformulated by substituting the term t_n with $t_n + t_c$. After some mathematics, Eq. 3.8 becomes

$$S_c(\omega) = F\left[S_c(t)\right] = \sum_{n=1}^{N} \sqrt{\sigma_n} e^{j\phi_n} H\left(\omega - 2\alpha\left[t_n + t_c\right]\right) e^{j\beta t_n + j\alpha t_n^2 - j\omega t_n} e^{j\beta t_c + j\alpha t_c^2} e^{j(2\alpha t_n - \omega)t_c}. \tag{4.7}$$

At any position of the radar along the rail, the *psf* defining the target's position in the range-compressed profile is $2\alpha t_c$ shifted from its real location. As in the short synthetic apertures (SSA) geometry the range corresponds to the target radial distance from the aperture center, a *post*-focusing compensation might turn out to be troublesome. In fact, if under polar coordinates it

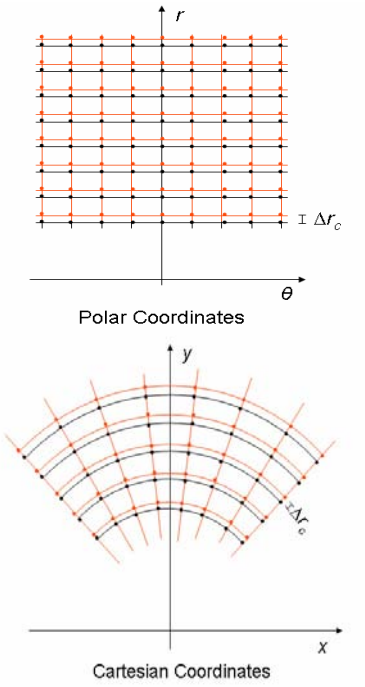

Fig. 4.12: Examples of range coregistration errors along the range dimension caused by different values of the cable length l_c.

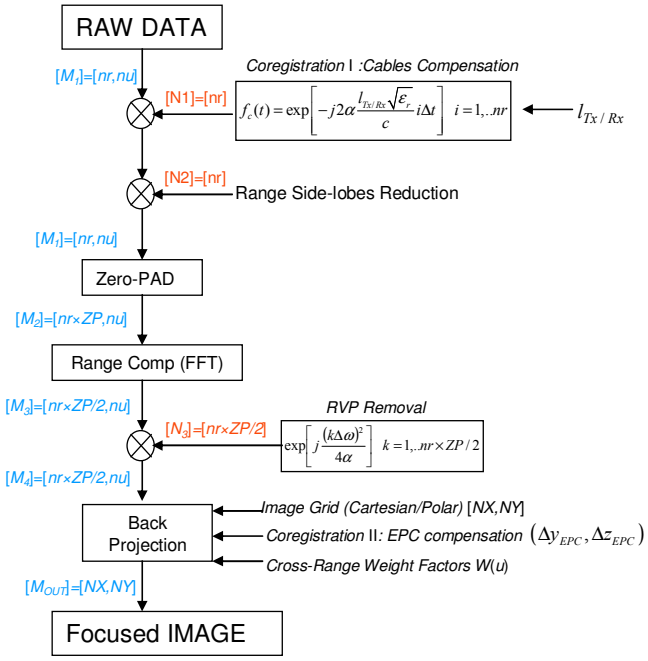

Fig. 4.13: Processing scheme of UPC gbSAR raw data. Range and cross-range coregistration is performed by compensating the terms $l_{Tx/Rx}$ and $(\Delta y_{EPC},\Delta z_{EPC})$. Red and blue expressions specify the data matrix dimensions at each step of the chain.

causes a simple shift in one dimension, the compensation of a Cartesian-focused image entails a 2D interpolation on a non-regular domain. The two situations are sketched in Fig. 4.12. The problem can be nicely avoided by multiplying the deramped signal in the time domain by the correction function $f_c(t)$ defined as

$$f_c(t)=e^{-j2\alpha t_c t}=e^{-j2\alpha\frac{l_c\sqrt{\varepsilon_r}}{c}t} \tag{4.8}$$

just before performing the raw data range compression. In order to carry out an efficient compensation, the length of all the cables within the front-end hardware must be measured with high accuracy. The values of l_c to be substituted in Eq. 4.8 for the different polarization channels are reported in the table of Fig. 4.11. Since the cables used for transmitting antennas have the same length, l_{Tx} contribution might be neglected. The deployment of calibrators within the illuminated scene allows one to refine the correction parameters estimate through amplitude spatial correlation analysis [Sheiber,00]. For instance, a 45º tilted active calibrator can be successfully employed for this purpose [Freeman,90]: as the power answer is theoretically equal in the four polarimetric channels and the corresponding phase-centers' locations is identical, a high sub-pixel coregistration precision in the range and cross range directions is possible. If now the new phase

contributions to $S_c(\omega)$ with respect to Eq. 3.8 are considered, it can be seen that βt_c and αt_c^2 introduce a constant offset that will be compensated for by polarimetric calibration. Concerning the last term, it is of interest to analyze its value around the angular frequency of *psf* maximum, which indicates the real location of the target. According to the mathematical formulation of Section 3.4, the sampled angular frequency closest to *psf* maximum is given by $k_{MAX}\Delta\omega$, being k_{MAX} the index identifying the target's location is the range-compressed profile and $\Delta\omega$ the sampling step. Then, it is possible to round up the aforementioned phase term as

$$(2\alpha t_n - \omega)t_c\Big|_{\omega_n} = \left(2\alpha tn - k_{MAX}\Delta\omega\right)t_c \leq \Delta Q_{MAX} \,. \tag{4.9}$$

As the quantization error ΔQ_{MAX} for high interpolation rate is very small and t_c is in the order of 10^{-9}, it follows that the phase distortion caused by $(2\alpha t_n-\omega)t_c$ is perfectly negligible.

4.4 UPC gbSAR raw data processing

In order to properly focus raw data acquired by the UPC gbSAR, a specific sequence of operations must be followed. This Section summarizes the whole processing chain by passing through the main steps pointed out in Chapter 3 and integrating the compensation procedures proposed in Section 4.3. The first step is to compensate for the coregistration error introduced by the difference length of the cables. Denoting with l_c the total length of the cables accounting for any combination of *Tx* and *Rx* antennas, the range correction function f_c(t) is obtained from Eq. 4.8 and multiplied by each range profile in the time domain. Afterwards, data are filtered using a Hanning window for optimizing the zero-padding interpolation performance, and focused in range using an FFT-based compression. Being the signal $s_c(t)$ a combination of cosines (Eq. 3.18) and then an odd function, the estimated spectrum is perfectly symmetric. Then, just the positive components are considered for the Residual Video Phase (*RVP*) error compensation (see Section 3.5), in agreement with IEEE propagation convention [IEEE,79].

At this point, the absolute phase of the range-compressed data linearly depends on the target range position and the back-projection algorithm can be successfully applied. The azimuth focusing step needs three inputs. The first one is the grid of points where to perform the coherent sums of back-propagated echoes. The second one is the position of the EPC describing the specific combination of antennas involved in the acquisition process with respect to the reference phase center EPC_M. Usually, EPC_{VV0} is selected for this purpose. The last input is the cross-range filtering widow $W(u)$ for the side lobes reduction. The entire process chain is resumed in the block-diagram sketched in

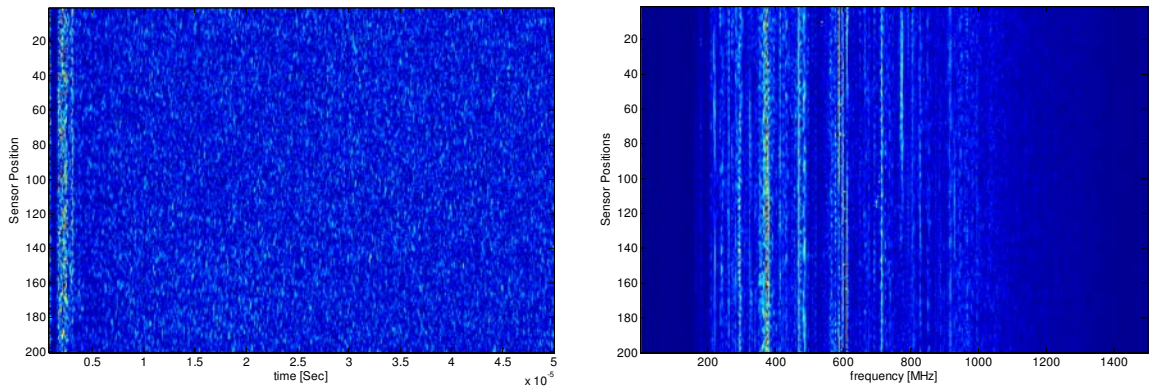

(a) (b)

Fig. 4.14: Example of UPC X-band gbSAR raw data amplitude in the time domain (a) and after the range-compression (b). The SSA is 2 meters long and the sampling step Δu is 1cm.

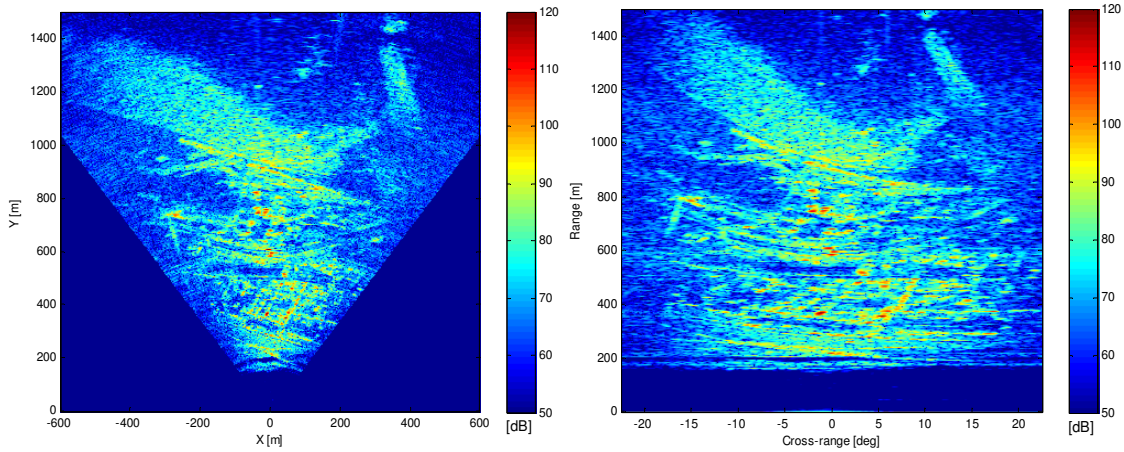

(a) (b)

Figs. 4.15: Example of gbSAR raw data focused on a grid of Cartesian (a) and polar (b) even-spaced points stressing the distortion effects caused in the second case on the near-range targets.

Fig. 4.13. An example of the gbSAR raw data is shown in Fig. 4.14a while the amplitude of the corresponding range-compressed data is displayed in Fig.4.14b. Finally, Fig. 15a and Fig. 15.b show the amplitude of the final focused image using Cartesian and polar evenly-spaced pixels, respectively.

4.5 UPC gbSAR polarimetric data calibration

In order to ensure the extraction of reliable quantitative information from focused PolSAR acquisitions, data must be polarimetrically calibrated. In fact, the transmission and reception blocks of any radar system alter the scattering information concerning the area under observation. Distortion effects can be reduced by increasing the quality of the hardware requirements but they can never be neglected [Zyl,90]. An assessed description of this process linearly relates the real scattering matrix [S] of a target to the matrix [M] measured by the radar as follows

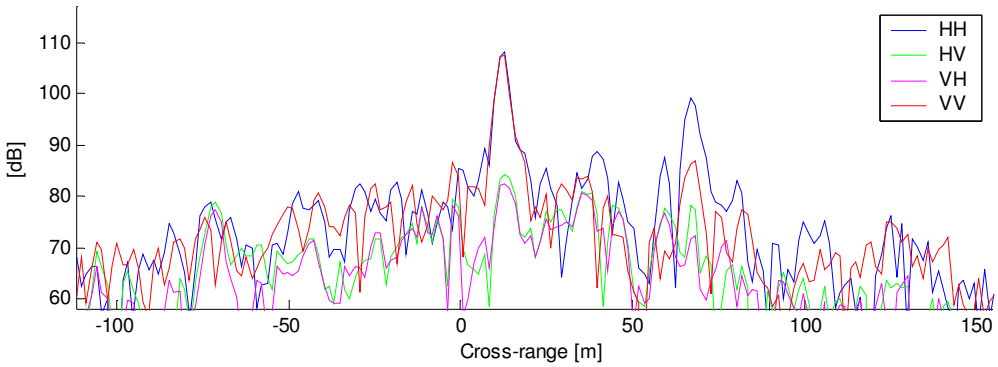

Fig. 4.16: Amplitude cross-range cut of an uncalibrated UPC gbSAR polarimetric data set at 300m from the sensor. The highest peak corresponds to a trihedral with leg length a = 45 cm.

$$[M]=\begin{bmatrix} M_{hh} & M_{hv} \\ M_{vh} & M_{vv} \end{bmatrix}=\begin{bmatrix} R_{hh} & R_{hv} \\ R_{vh} & R_{vv} \end{bmatrix}\begin{bmatrix} S_{hh} & S_{hv} \\ S_{vh} & S_{vv} \end{bmatrix}\begin{bmatrix} T_{hh} & T_{hv} \\ T_{vh} & T_{vv} \end{bmatrix}+[N]=[R][S][T]+[N] \qquad (4.10)$$

where the 2×2 complex matrices [R] and [T] describe the distortion introduced in each polarimetric channel by the receiver and the transmitter, respectively, and [N] is a 2×2 complex matrix taking into account the additive noise contribution [Ulaby,90] [Carlson,86]. Any polarimetric calibration procedure essentially aims at inverting Eq. 4.10 and estimating [S]. A brief analysis reveals that Eq. 4.10 contains just 4 equations but 12 unknown quantities: 4 (complex) scattering matrix elements and 8 (complex) radar system unknowns. Further equations are then required to achieve a reliable solution. To do this, three main approaches may be pursued [Freeman,92]: the first is to use man-made targets with known scattering matrices; the second is to make assumptions regarding the general properties of the scatterers being measured; and the third is to make assumptions about the radar system parameters. Depending on the monitoring conditions, the three approached may be also combined to work out an appropriate solution. Without entering into details, it must be mentioned that the most assessed techniques applied to space- and air-borne SAR acquisitions split the calibration problem into two steps: the *cross-talk unbalance* compensation and the *radiometric* calibration. The former problem may be coped with through the detection of homogeneous areas [Quegan,94] [Papathanassiou,98] [López,07] or the formulation of an iterative solution [Ainsworth,06]; the latter one is solved using co-polar pure targets [Gray,90] [Urlander,90] [Zebker,90]. When the polarimetric data are acquired by a gbSAR sensor, the extension of the observed scene is rarely higher than 2-3 km^2. Depending on the features of the illuminated area, the air-borne/satellite approach might turn out to be inappropriate. For example, the presence of homogeneous zones providing sufficient samples for the estimation of the

unknown terms might not be assured. Similarly, the observation of an urban environment implies the presence of several saturated pixels that might affect the convergence of iterative solutions.

Concerning the specific case of the UPC sensor, it has been shown (see Section 4.3) that a polarization purity of about 40 dB is guaranteed for the -6dB antenna radiation beam. Besides, real data show that a separation of about 30 dB is provided between co-polar and cross-polar channels before any calibration technique is applied. As example, the uncalibrated polarimetric response of a corner reflector is shown in Fig. 4.16. Under these conditions, the off-diagonal terms of both [*R*] and [*T*] may be neglected, i.e.

$$R_{hv} = R_{vh} = T_{hv} = T_{vh} \simeq 0 \,. \tag{4.11}$$

The cross-talk effects reduce to a cross-polar unbalance that does not extend to the co-polar channels. Accordingly, Eq. 4.10 may be rewritten in a vectorial form as follows

$$\begin{bmatrix} M_{hh} \\ M_{hv} \\ M_{vh} \\ M_{vv} \end{bmatrix} = \begin{bmatrix} R_{hh}T_{hh} & 0 & 0 & 0 \\ 0 & R_{hh}T_{vv} & 0 & 0 \\ 0 & 0 & R_{vv}T_{hh} & 0 \\ 0 & 0 & 0 & R_{vv}T_{vv} \end{bmatrix} \begin{bmatrix} S_{hh} \\ S_{hv} \\ S_{vh} \\ S_{vv} \end{bmatrix}. \tag{4.12}$$

A polarimetric calibration technique tailored to radar system with good polarization isolation has been proposed in [Sarabandi,90]. The linear equations system in Eq. 4.12 may be solved using just one reference target with known scattering matrix, namely a trihedral, and a strong cross-polarized scatterer. Denoting with the subscripts "*t*" and "*x*" all the quantities associated with the trihedral and the cross-polar calibration target, respectively, the polarimetric behavior characterizing a generic target within the scenario is estimated as follows

$$\begin{aligned} S'_{hh} &= \frac{M_{hh}}{M_{hh,t}} S_t = S_{hh} e^{j2kr_t} e^{-j2kr} & S'_{hv} &= \frac{M_{hv}}{\sqrt{K_1 K_2}} S_t = S_{hv} e^{j2kr_t} e^{-j2kr} \\ S'_{vh} &= M_{vh} \sqrt{\frac{K_1}{K_2}} S_t = S_{hv} e^{j2kr_t} e^{-j2kr} & S'_{vv} &= \frac{M_{vv}}{M_{vv,t}} S_t = S_{vv} e^{j2kr_t} e^{-j2kr} \end{aligned} \tag{4.13}$$

where

$$\begin{aligned} K_1 &= \frac{M_{hv,x}}{M_{hv,x}} \\ K_2 &= M_{hh,t} M_{vv,t} \end{aligned} \tag{4.14}$$

and S_t and r_t are the trihedral amplitude and range position, respectively. It is worth pointing out that the retrieved scattering information does not exactly correspond to the elements of [*S*] in Eq.

4.10 and previously defined in Eq. 2.34, since two phase terms are added. The first one is constant within the whole scene and it is related to trihedral's range distance r_t. The second one accounts for signal propagation from the transmitting antenna to the target and back to the receiving antenna, or equivalently for the EPC-target round-trip delay. As these two contributions are constant, they do not affect the polarimetric properties of the observed scatterers. Still, they constitute the rationale of interferometric applications, as it will be discussed in Chapter 5. The term S_t can be analytically calculated as [Freeman,92]

$$S_t = \sqrt{\frac{a^3}{3\lambda^2}} \tag{4.15}$$

where a is the leg length of the trihedral. On the contrary, the amplitude and phase information of the complex terms M_{hh}^t and M_{vv}^t are estimated using the integral and peak method described in [Gray,90], respectively. Regarding the cross-polar target "x", no information about its theoretical response is required. As the term K_1 in Eq. 4.14 is given by the ratio between its two cross-polar measurements, any strong cross-polarizing scatterer can be employed. Yet, it is important to stress that real scenarios might lack of such a scatterer. For example, this is quite common in SAR acquisitions concerning natural environments. Then, it has been essential to work out a solution for being able to calibrate gbSAR data whatever the features of the area to be monitored.

The usage of Polarimetric Active Radar Calibrators (PARC) [Brunfeldt,84] [Freeman,90] has been excluded at once. Its active nature does not fulfill the conditions for the Reciprocity Theorem applicability and the cross-polar channels equality is verified only when orientated at exactly 45º with respect to the line of sight of the target. The high sensitivity of its response to alignment errors and the fluctuations in the signal amplification process make active calibrators unsuitable for long-time calibration purpose [Freeman,90] [Freeman,91]. The possibility to use of a strong cross-polar passive target has been hence checked. Theoretically, a dihedral calibrator 45º tilted along the radar line of sight (*LOS*) represents an optimum solution. In fact, its back-scattering response in the $\{\vec{h},\vec{v}\}$ polarization basis (see Section 2.3) is

$$\left[S_{DH}^{45^\circ}\right] = c\begin{bmatrix} 0 & 1 \\ 1 & 0 \end{bmatrix}. \tag{4.16}$$

The passive nature of the calibrator assures the perfect symmetry of the real scattering matrix. In practice, the dimension necessary to be easily detectable at range-distance higher than 400 m makes the dihedral extremely directive and its correct positioning critical [Freeman,92].

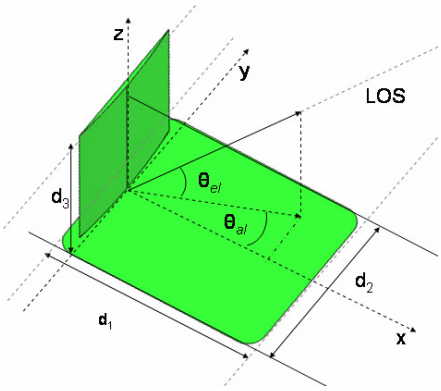

Fig. 4.17: Geometry of a bruderhedral and its orientation relative to the radar line of sight (LOS) in terms of θ_{al} and θ_{el}

Fig. 4.18: Picture of the Bruderhedral constructed in the laboratory of the UPC (d_1=65 cm, d_2=55cm, d_3=45cm r=2m). The optical pointer is used to achieve the correct alignment with the sensor location.

In order to overcome this limitation, the employment of a *bruderhedral* [Bruder,92] has been taken into consideration. This reflector is essentially a finite cylinder-segment of a top [Silverstein,97], as it can be seen in the sketch of Fig. 4.17. Its back-scattering properties are almost identical to a dihedral but it offers the advantage of being much less directive. The condition of maximum backscattering is obtained when θ_{al} and θ_{el} in Fig. 4.17 are equal to 0º and 45º, respectively. To guarantee a high backscattered answer, the bruderhedral has been dimensioned to have approximately the same nominal RCS of the trihedral in Fig. 4.16. Unlike corner reflectors, there is no analytical expression of the bruderhedral RCS. Then, an advanced electromagnetic solver, the GRECO [Rius,93], was employed to properly choose the dimensions of the calibrator before its physical construction in the Antennas' Laboratory of the UPC (Fig. 4.18). The results obtained with real data in terms of polarization purity perfectly match the prediction of the simulation, as it can be noticed by briefly comparing the plots in Fig. 4.19 and Fig. 4.20.

Resuming, the correction of the cross-talk unbalance is performed by a 45º tilted bruderhedral (in the case no strong cross-polar target is detectable within the scenario) whereas the radiometric calibration is carried out using a corner reflector. The calibration process of PolInSAR data sets is obtained by applying the described technique to the polarimetric acquisitions gathered in the zero-baseline and interferometric configurations separately, but using the same calibrators. Afterwards, the common offset present between the two PolSAR data sets is compensated using a second corner reflector, a homogenous flat area [Papathanassiou,98] or an external DEM. Finally, two important issues must be addressed. The first one is related to the scattering phase information retrieved by the calibration procedure resumed in Eq. 4.13. With respect to Eq. 2.34, the elements

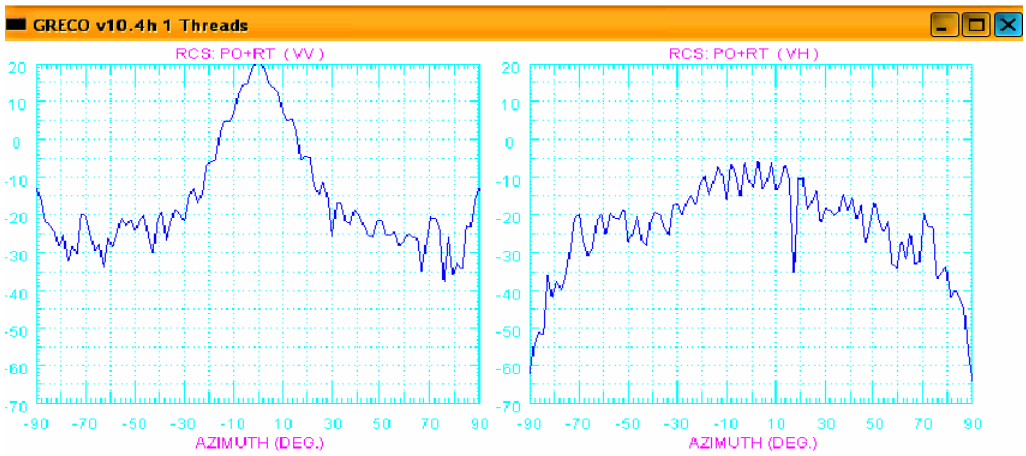

Fig. 4.19: Co-polar and cross-polar azimuth RCS of the Bruderhedral simulated by the GRECO©. The polarization purity is about 25 dB when the reflector is perfectly oriented towards the sensor and the tilt angle is 0º.

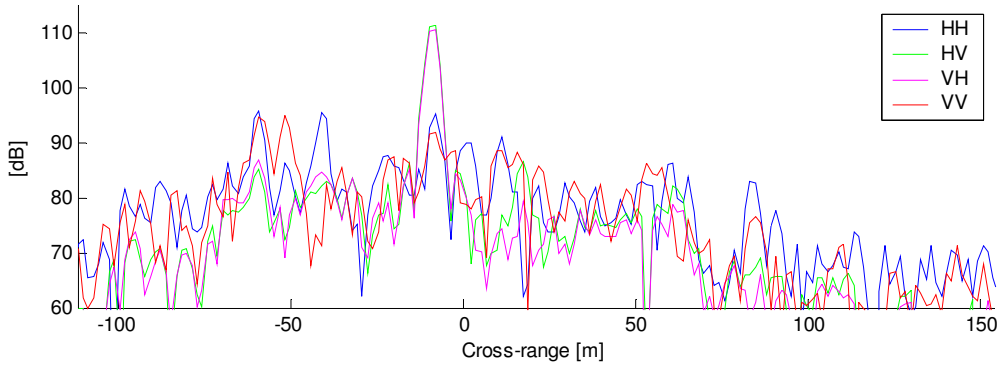

Fig.4.20: Amplitude cross-range cut of an uncalibrated UPC gbSAR polarimetric data set. The peak corresponds to the response of the bruderhedral of Fig. 4.18. The orientation angle of the reflector with respect to the radar LOS is 45º and the corresponding backscattering behavior matches with the features of $\left[S_{DH}^{45^\circ}\right]$. The separation between the cross-polar and co-polar channels in the peak is about 20 dB.

of the calibrated scattering matrix [S'] contain two additional phase terms. One accounts for the target's round-trip delay. As a first approximation, the position of the scattering phase center associated to each polarization is identical. In Chapter 8, this hypothesis is relaxed and a simplified scattering model is proposed for advanced differential interferometric studies. The second contribution is related to the position of the trihedral employed for calibration purposes. As this term is common to all the polarization channels, it does not alter the polarimetric properties of the observed scene. Yet, it becomes of key-importance in long-time monitoring activities: if the calibrator position changes between a set of acquisitions and the successive, the corresponding variation of r_t must be taken into account.

The second issue deals with the position of the two calibrators. In order to guarantee the meaningfulness of orthogonal polarization states, the co-polar and cross-polar reference targets must be located at the center of the antenna beam, as it is explained in the next section.

4.6 Polarimetry in ground-based SAR observation geometry

Air-borne and space-borne SAR sensors are characterized by very narrow-beam antennas. Typical values of the -3dB illumination cone both in range and cross-range are 2º/3º for the first platform [Christensen,02] and 1º or even less for the satellite sensors [Partington,98] [Mittermayer,03]. It is worth recalling that the antenna beamwidth in range is trade-off between the velocity of the platform and the minimum cross-range sampling step to be guaranteed in order to avoid aliasing phenomena. As a matter of fact, these two quantities limit the maximum size of the *swath* that can be observed without range ambiguities. Concerning the azimuth dimension, the main limitation is the maximum power that can be provided in transmission in order to fulfill S/N ratio requirements. In terms of polarization, the use of so narrow beam antennas allows to approximate the signal transmitted by the SAR sensor to a plane wave within the -3dB footprint. Therefore, it is possible to state that the direction of the incident electrical field $\vec{E}(\vec{r})$ within the illuminated scene is exactly the same.

In the case of gbSAR sensors, the platform velocity is not a constraint since it can be adapted to the extension of the area to be monitored. Either the S/N ratio requirements represent an issue: the use of CW architecture gives the opportunity to reduce the noise level by increasing the time-averaged factor applied to the backscattered signal instead of the power in transmission. As a consequence, terrestrial sensors are able to exploit a wider part of the central lobe with respect to conventional SAR system. Antennas with illumination beams up to 35º/40º in range and azimuth dimensions are often employed for continuous monitoring purpose [Aguasca,04] [Martinez,07] [Bernardini,08].

At this point, it is important to study the consequences of working with so wide antenna beam in terms of polarization of the incident wave. For this purpose, let us consider a linear polarized antenna whose electric field is parallel to the *x* axis, as shown in Fig. 4.5. According to Eq. 4.1, the co-polar component *C* of the transmitted field $\vec{E}(\vec{r})$ in the *boreside* direction is oriented as $\hat{u}_{\theta_a}$, which is parallel to $\hat{u}_x$. The cross-polar component *X* is instead oriented as $\hat{u}_{\phi_a}$, which is consequently parallel to $\hat{u}_y$. It follows that, when a narrow beam centered along the *boreside* direction of the *Tx*/*Rx* antenna is considered, the *C* and *X* components of the electric field are directly given by the polarization of the transmitting antenna and its orthogonal polarization, respectively. But as the antenna beam widens, this condition stops being fulfilled. This can observed in Fig. 4.21a and Fig. 4.21b, where the different orientation that the vectors ($\hat{u}_C, \hat{u}_X$) and

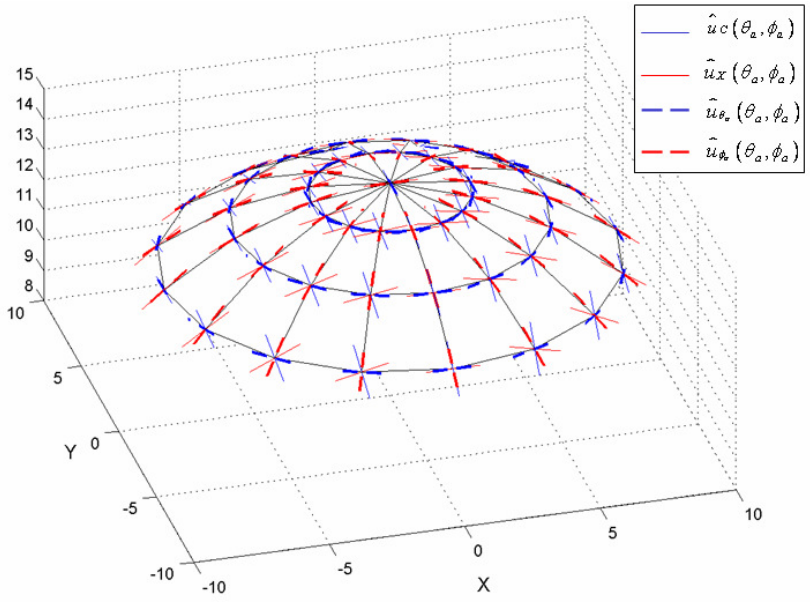

(a)

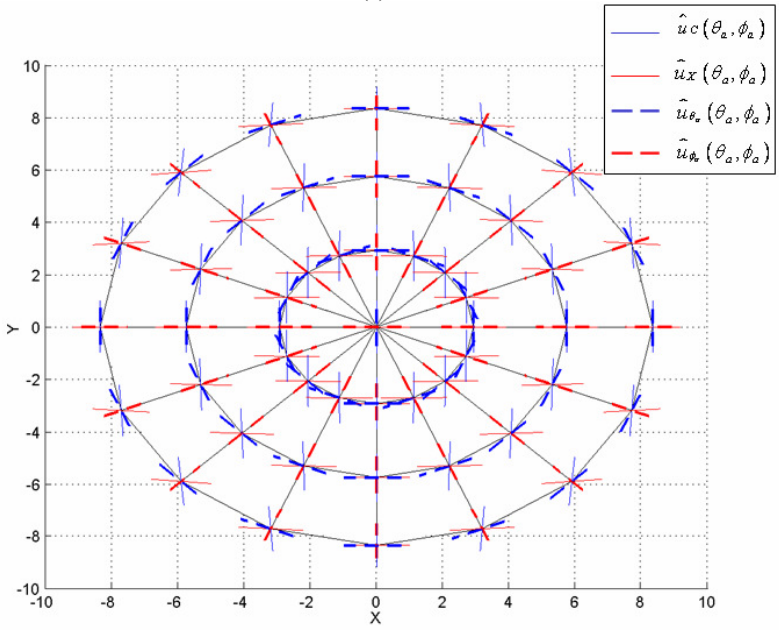

(b)

Fig. 4.21: Spatial orientation of the co-polar $\hat{u}_C$ and cross-polar $\hat{u}_X$ unitary vectors of the electric field generated by a linear polarized antenna vs spherical unitary vectors $\hat{u}_{\theta_a}$ and $\hat{u}_{\phi_a}$. The four vectors have been projected on a spherical surface delimitated by the condition $\theta_a \leq 32^\circ$. The result is shown in a 3D (a) and a 2D (b) views.

$(\hat{u}_{\theta_a}, \hat{u}_{\phi_a})$ assume over a spherical surface is easy detectable. For the sake of clearness, just an angular sector equal to 32º around axis *z* has been depicted. It is now necessary to work out an efficient way to describe the distortion effects introduced by a wide antenna beam in terms of polarimetric description of the scenario. As linear polarized antennas are usually employed for gbSAR measurements, it is reasonable to carry out this study using two orthogonal dipoles $\hat{u}_{d_1}$ and $\hat{u}_{d_2}$ with normalized RCS. Let the first dipole be parallel to the co-polar component of the

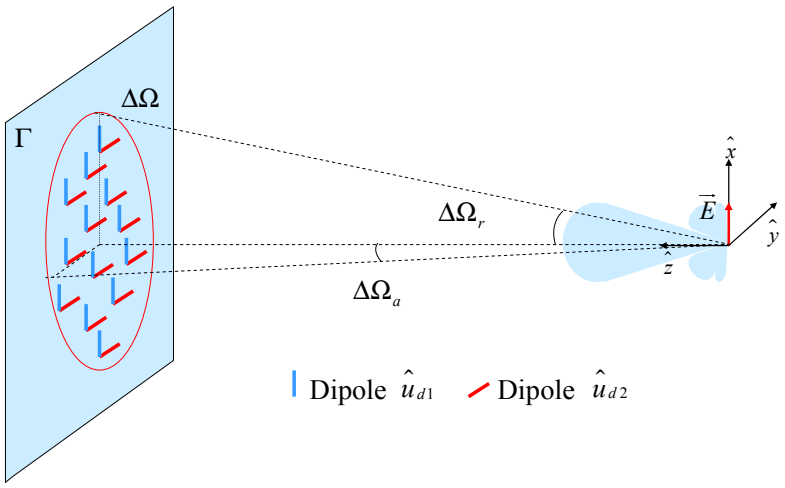

Fig. 4.22: Distribution of orthogonal dipoles within the antenna beam ΔΩ oriented according to the direction of co-polar (blue) and cross-polar (red) components of the incident electric field in the boreside direction. The transmitting antenna is linear polarized as indicated by $\vec{E}$.

transmitted field in the direction of maximum radiation. The second one is defined by consequence. Mathematically, their orientation may be described by the condition

$$\begin{aligned} \arccos\left(\hat{u}_{d_1}\cdot\hat{u}_C(0,0)\right)&=0 \\ \arccos\left(\hat{u}_{d_2}\cdot\hat{u}_X(0,0)\right)&=0 \end{aligned} \tag{4.17}$$

where "$\cdot$" denotes the vector scalar product [Mirsky,90]. A pictorial description of the spatial orientation of $\hat{u}_{d_1}$ and $\hat{u}_{d_2}$ with respect to the antenna radiation pattern is given in Fig. 4.22. Let now the position but not the orientation of the two dipoles change on the plane Γ, and, hence, within the antenna footprint $\Delta\Omega$. The two reference scatterers and the co-polar and cross-polar component of the field do not lie on the same plane anymore. In order to compare their spatial orientation, $\hat{u}_{d_1}$ and $\hat{u}_{d_2}$ must be first projected on the plane orthogonal to the propagation direction of the wave $\hat{u}_r$. This step is carried out by the following equations

$$\begin{aligned} \vec{u}_{d_{1t}}(\theta_a,\phi_a)&=\left[\hat{u}_{d_1}\cdot\hat{u}_{\theta_a}(\theta_a,\phi_a)\right]\hat{u}_{\theta_a}+\left[\hat{u}_{d_1}\cdot\hat{u}_{\phi}(\theta_a,\phi_a)\right]\hat{u}_{\phi_a} \\ \vec{u}_{d_{2t}}(\theta_a,\phi_a)&=\left[\hat{u}_{d_2}\cdot\hat{u}_{\theta_a}(\theta_a,\phi_a)\right]\hat{u}_{\theta_a}+\left[\hat{u}_{d_2}\cdot\hat{u}_{\phi}(\theta_a,\phi_a)\right]\hat{u}_{\phi_a} \end{aligned}. \tag{4.18}$$

It possible to describe the orientation of $\hat{i}_{d_{1t}}$ with respect to $\hat{i}_C$ and of $\hat{i}_{d_{2t}}$ with respect to $\hat{i}_X$ through the definition of two functions f_1 and f_2 equal to

$$\begin{aligned} f_1(\theta_a,\phi_a)&=\arccos\left(\hat{u}_{d_{1t}}(\theta_a,\phi_a)\cdot\hat{u}_C(\theta_a,\phi_a)\right) \\ f_2(\theta_a,\phi_a)&=\arccos\left(\hat{u}_{d_{2t}}(\theta_a,\phi_a)\cdot\hat{u}_X(\theta_a,\phi_a)\right) \end{aligned}. \tag{4.19}$$

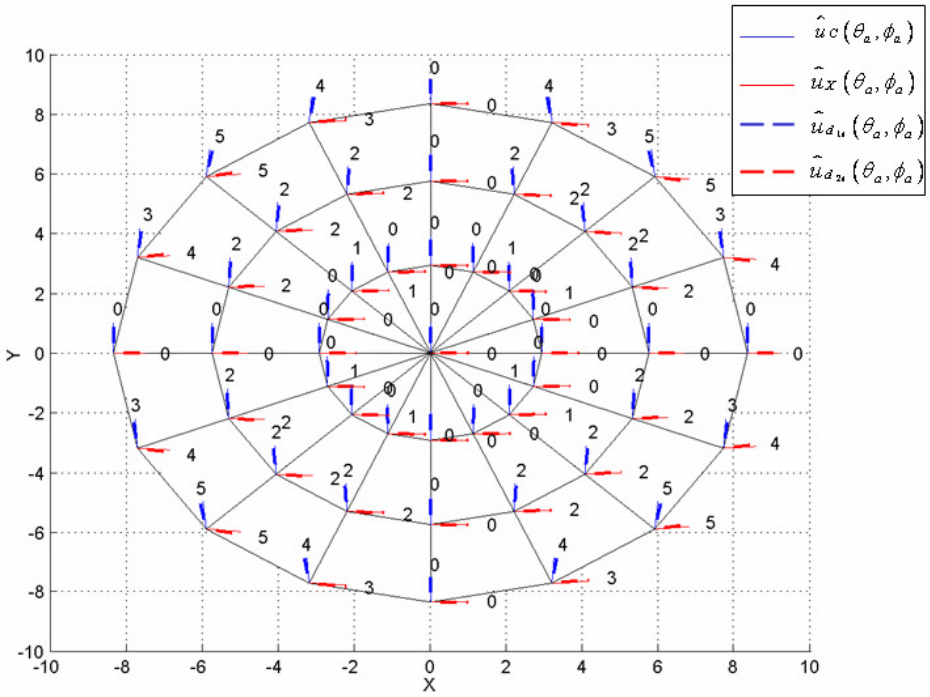

Fig. 4.23: Spatial distribution of f_1 and f_2 functions within a symmetric antenna beam. The displayed circles correspond to θ_a equal to 11.5º, 23ºand 32 º, respectively.

Note that Eq. 4.17 can be obtained from Eq. 4.19 by imposing the *boreside* condition. If no distortion effect is introduced, the scattering properties of the dipoles must not change at every point within the illumination cone. In other terms, it must be fulfilled the condition

$$f_1(\theta_a,\phi_a) = f_2(\theta_a,\phi_a) = 0 \quad \forall(\theta_a,\phi_a) \subset \Delta\Omega\,. \tag{4.20}$$

The result obtained for f_1 and f_2 considering a symmetric antenna beam ($\Delta\Omega_r = \Delta\Omega_a = 70º$) is shown in Fig. 4.23. The displayed circles correspond to θ_a equal to 11.5º, 23º and 32º, respectively. It can be observed that as the value of θ_a increases, the changes in the description of the polarimetric properties of the reference targets become more significant. The dipole oriented as $\hat{u}_C(0,0)$ starts generating a cross-polar component at the antenna, as well as the dipole oriented as $\hat{u}_X(0,0)$ starts contributing to co-polar measurement. Moreover, this effect shows also a dependence on the angle ϕ_a. The main consequence of this distortion is that the response of identical scatterers located at different positions in the footprint, and, hence, at different (θ_a,ϕ_a) within the antenna radiation pattern, might be different. Besides, the sign of the rotation shown by $\hat{u}_{d_{1t}}(\theta_a,\phi_a)$ and $\hat{u}_{d_{2t}}(\theta_a,\phi_a)$ with respect to $\hat{u}_C(\theta_a,\phi_a)$ and $\hat{u}_X(\theta_a,\phi_a)$ might be different too. This effect can be observed only graphically, being the cosine performed by the scalar product an odd function. Nonetheless, it is sufficient to state that wide beam antennas do not always guarantee the description of the same orthogonal scattering mechanisms through orthogonal polarization

properties. An equivalent interpretation is that two antennas generating orthogonal polarization states do not provide at high squint angles an orthogonal polarization basis for the description of illuminated targets, which constitutes the basic assumption to polarimetrically characterize a scatterer. In all these evidences, it is essential to define a maximum beamwidth where polarimetric measurements are meaningful. An error of 2º corresponds to a polarization mixing of about 3% and represents a reasonable maximum threshold for any polarimetric study. As shown in Fig. 4.23, this condition is obtained for $\Delta\Omega_r = \Delta\Omega_a \approx 45º$. Since the -6dB beamwidth of the antennas mounted on UPC sensor's front-end is approximately 38º, the distortion effects characterizing its polarimetric measurements within this angular sector can be perfectly neglected.

4.7 Test-sites description

In the framework of this PhD dissertation, two main test sites will be studied: the area of Collserola, in the outskirts of Barcelona, and the Station district of the Sallent village, in northeastern Spain. The first scene was selected for testing purposes: owing to its closeness to the UPC campus, the first scenario constituted a suitable area to check the sensor's hardware as well as the software managing the whole acquisition process. The second test site was instead chosen to demonstrate the UPC gbSAR sensor capability to monitor slow-time deformation process. Remanding to the successive Chapters for a detailed description of each measurement campaign, this last section gives an overall view of the two areas and the corresponding observation geometry imposed by the sensor's location.

4.7.1 The Collserola test-site

Collserola is a protected hilly area surrounding the city of Barcelona. Its southern part is about one kilometer far from the Signal Theory and Communications (TSC) department of the UPC, where the laboratory of the RSLab is located. The satellite picture displayed in Fig. 4.24 shows the position of the department, indicated by the flag "gbSAR", with respect to the closest part of Collserola park. The sensor was periodically located on the roof of the TSC building for testing purposes. The orientation of the -3dB antennas' beamwidth, which is defined by the yellow dotted line in Fig. 4.24, was selected to minimize the range distance of the area of interest as well as the shadowing effects. A picture of the sensor in the operative configuration is shown in Fig. 4.25 whereas a view of the scenario from the gbSAR location is detailed in Fig. 4.26. The test-site is a heterogeneous environment. It mainly contains low– to medium-density vegetated areas. Yet, a

Fig. 4.24: Satellite photo of the Collserola test-site, in the outskirts of Barcelona.

Fig. 4.25: Photo of the gbSAR UPC sensor located on the roof of the TSC department at the UPC.

Fig. 4.26: Photo of the Collserola test-site observed from the UPC sensor's location

UPC gbSAR System	
Frequency Carrier f0	9.65 *GHz*
Chirp duration	50e-6 *sec*
Chirp Sampling Frequency	81.92 *MHz*
Chirp PRF	20 *Khz*
Chirp Bandwidth	[60:120] *MHz*
Deramped Signal Bandwidth	40 *MHz*
Transmitted Power	27 *dBm*
3dB Antenna Beamwidth	27º
Range Time-Average Factor	128
Synthetic Aperture Length	2 *m*
Cross-Range Samples	1 *cm*
Acquisition Duration: Single-Pol / PolSAR / PolInSAR	1 min / 2 min 40 sec / 4 min 30 sec

Table 4.1: UPC gbSAR measurement parameters during the campaign in Collserola.

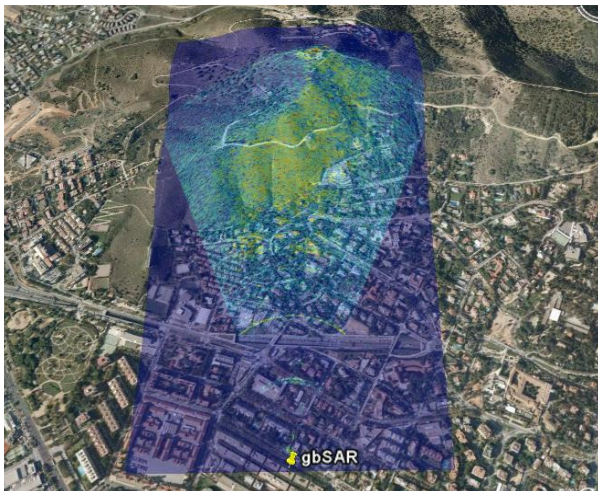

Fig. 4.27: Geocoded reflectivity image (*hh* polarization) of the Collserola test-site overlapped to the Google-Earth© ortophoto.

pine covered area can be detected in the top-left corner of the hill slope. Urban structures are present too, although they are sparsely distributed at short range distances. The geocoded reflectivity information provided by the gbSAR sensor in the *hh* polarization is displayed as

example in Fig. 4.27. The geocoded-image has been overlapped to the Google Earth© ortophoto to stress the fact that the main scattering contribution comes from the low-vegetated hill slope. Despite the apparent proximity between the hill and the sensor, more than 1 km separates the two points: an entire district of the city and a highway stay in between. This complex metropolitan environment, together with the proximity of the sea, generates instable atmospheric conditions which might come to affect the quality of gbSAR data. In order to study the effects of the atmosphere instability on gbSAR polarimetric zero-baseline acquisitions, several experiments were carried out using the test-site of Collserola between the end of 2004 and the first half of 2005. The most interesting results were obtained during the two measurements campaigns carried out in June 2005: the first one from June 15th to June 18th, and the second one from June 27th to July 3rd. Accordingly, just these last two experiments will be described in detail in Chapter 6. The measurement parameters employed for the acquisition process are reported in Table 4.1: a 120 MHz chirp bandwidth provided a nominal range resolution of 1.25 m whereas a 1 cm cross-range sampling guaranteed an alias-free angular sector of about ± 50º, which is fairly wider than the -6 dB limit described in Section 4.6. Finally, it worth recalling that the chirp sampling frequency f_c is given directly by the DDS device and corresponds to a multiple of the PRF signal. This fact assures a perfect synchronization of the chirp modulations that are continuously transmitted and received by the sensor. It follows that the backscattered signal SNR is increased by splitting the raw data lie acquired at each SSA position in frames of f_c/PRF samples and then averaging the obtained collection of chirp-modulations. The averaging factor reported in Table 4.1, namely 128, represents the best trade-off between the sensor scanning time and the backscattered signal SNR for a maximum range distance of about 1.5 km, as in the case of the Collserola test-site.

4.7.2 The Sallent test-site

The second test-site is the village of Sallent, in northeastern Spain, where the RSLab of UPC carried out a one-year measurement campaign using its X-band gbSAR sensor. The field experiment was funded by the Institut Geològic de Catalunya (IGC) and aimed at studying the subsidence phenomenon affecting the district known as Barri de l'Estació, close to the Llobregat river. The deformation process is a consequence of the salt mining activity carried out until 1954, when a natural cavity of about 120 meters high and 40 meters wide was found during mining works under this area. Although this part of the mine stopped being exploited immediately, it was closed only after the water floods in 1957 and 1962, which filled it up with saturated salty water.

Fig. 4.28: Picture of the cliff close in Sallent chosen for the installation of the UPC gbSAR sensor.

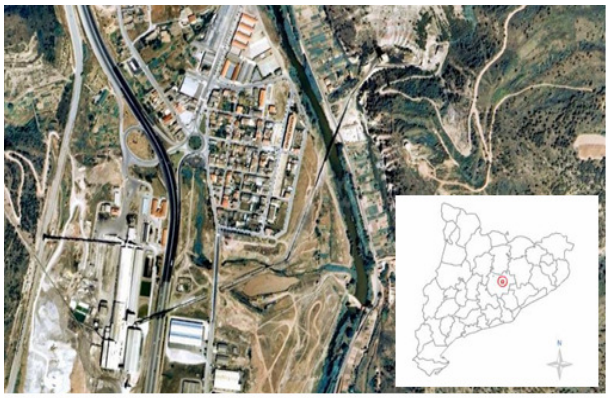

Fig. 4.29: Satellite picture of the Sallent test-site (Barri de l'Estació), northeastern Spain

During the 90s, heavy damages appeared in man-made structures built in the district area. As a response, the Catalan Administration started an investigation program to identify, quantify and model the still ongoing subsidence phenomena [ICC,03] [Marturia,05]. The collaboration between the IGC and RSLab institutions aimed at assessing the capability of gbSAR sensors to improve the spatial accuracy and temporal sampling of the deformation process with respect to satellite SAR acquisitions [Marturia,05] [Blanco,03]. When a terrestrial radar solution is adopted for monitoring a specific area, the most critical issue is the location of the sensor: the higher the incidence angle, the higher the reduction of the shadowing effects (see Section 3.4). Accordingly, the top of the cliff at the east side of the Llobregat river shown in Fig. 4.28 was selected for this purpose. Located at 84 m above the village level area, this position provided an observation angle within the area of interest varying from 72º up to 82º. It is worth pointing out that the steep slope of the chosen hill made it possible to avoid any radar front-end saturation problem which might be caused by close targets. A satellite picture of the Barri de l'Estació and the view from the sensor's location are detailed in Fig. 4.29 and Fig. 4.30, respectively.

In order to guarantee the repeatability of the observation conditions with submillimetric positioning error, the system was deployed on the concrete basement with an iron screws grid shown in Fig. 4.31. A picture of the sensor in the operative configuration is displayed in Fig. 4.32 whereas Fig. 4.33 shows an example of the geocoded *hh* reflectivity information of the scenario projected on the Google Earth© ortophoto. The measurement campaign started in June 2006 and finished in July 2007. Data were acquired on ten different days, as it is reported in Table 4.2: red color denotes the diurnal monitoring activities, the blue color the nocturnal ones, whereas the last three columns describe the actual part of the day selected for the acquisition process, the amount of data sets daily gathered by the sensor, and the time span of consecutive data sets, respectively. As

Fig. 4.30: Picture of the Barri de l'Estació observed from the UPC sensor's location.

Fig. 4.31: Picture of the concrete basement guaranteeing the observation of the Sallent test-site under a fixed geometry.

Fig. 4.32: Photo of the UPC gbSAR in the operative configuration in Sallent. The usage of a wide-angle lens makes it possible to stress the observation geometry of the Sallent test-site from the sensor's location.

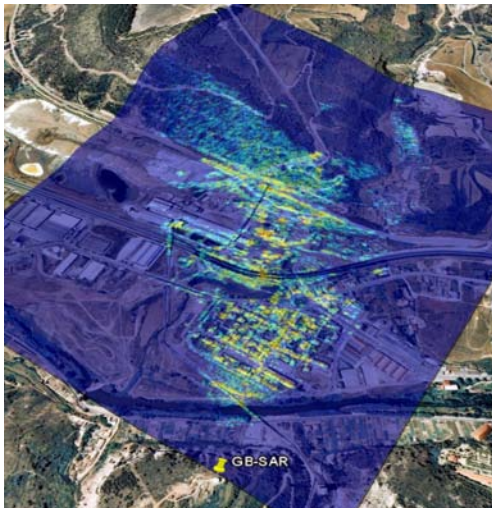

Fig. 4.33: Geocoded reflectivity image (*hh* polarization) of the Sallent test-site overlapped to the Google-Earth© ortophoto.

	Date	Time	# of Scans	Time-Delay
DAY 1	29/06/06	11:00 - 16:00	27	10 min
DAY 2	26/07/06	08:00 - 11:30	30	13 min
DAY 3	19/09/06	10:40 - 16:00	39	8 min
DAY 4	20/10/06	09:40 - 15:00	31	7 min
DAY 5	14/11/06	12:30 - 16:30	41	8 min
DAY 6	28-29/11/06	19:00 - 08:40	44	20 min
DAY 7	18-19/12/06	20:45 - 05:00	99	10 min
DAY 8	13-14/02/07	22:00 - 09:55	37	25 min
DAY 9	14-15/03/07	20:00 - 09:50	41	25 min
DAY 10	04-05/07/07	22:00 - 10:50	45	25 min

Table 4.2: Timetable of the measurements campaign. Red and blue colors denote the diurnal and nocturnal monitoring activities, respectively.

the observation geometry limited the maximum range distance of the scenario to about 1.5 km, the Sallent test site was monitored using the same configuration employed for the Collserola campaign (see Table 4.1). A complete description of the system's measurement parameters and the comprehensive list of gbSAR data sets gathered during the experimental campaign in Sallent can be found in *Appendix C*. After each day of measurements, the system was removed and placed again at the same position after about one month. Data calibration was carried out as explained in

Section 4.5 using a corner reflector located in a near-range bare area and a strong cross-polar urban target. Owing to the high number of data sets regularly acquired during one-year and to the reduced shadowing effect, the experimental results presented in the frame of this PhD dissertation mainly deals with the Sallent test-site. In Chapter 5, interferometric gbSAR acquisitions of Sallent will be employed for the assessment of an innovative technique proposed in this PhD dissertation for the retrieval of topography information. In Chapter 6, zero-baseline acquisitions will be instead used to demonstrate the main properties of the atmospheric phase artefacts under the hypothesis of wave propagation through a spatial homogeneous troposphere. In Chapter 7, the one-year collection of polarimetric gbSAR data of Sallent will give the opportunity to look into the temporal stability of the scattering process within an urban scenario. Finally, the problem of estimating the deformation process of the observed scene from gbSAR polarimetric zero-baseline acquisitions will be addressed in Chapter 8.

Chapter 5

Ground-based SAR Interferometry, DEM Retrieval and Data Geocoding

SAR Interferometry (InSAR) is an established technique for topographic map retrieval [Massonet,93] [Coltelli,96] [Lanari,96] based on combining two SAR images of the same scene acquired from two slightly different viewpoints [Balmer,98]. In this Chapter, the basic formulation of InSAR is adapted to ground-based SAR (gbSAR) sensors. The geometrical relation between the scatterers' interferometric phase and height information is carried out for the specific case of Short Synthetic Aperture (SSA). The general concept of interferometric coherence as a quality descriptor of the estimated interferometric phase is then introduced. Particular emphasis is given to the simplification of many decorrelation factors affecting air- and space-borne SAR data but negligible in gbSAR acquisitions. In the last part, the problem of DEM retrieval and radar images geocoding is addressed. The classical approach proposed in the literature, which deals with the two issues separately, is briefly described. Afterwards, an alternative iterative method solving the two problems at once is put forward and assessed using real gbSAR data. In the end, the special case of zero-baseline measurements is briefly analyzed and the possibility to employ terrestrial SAR sensors to successfully monitor deformation phenomena is highlighted.

5.1 gbSAR Interferometry

According to the processing chain described in Section 4.5, the zero-baseline and interferometric backscattering information provided by the UPC gbSAR sensor is represented by two calibrated scattering matrices $\left[S'_M\right]$ and $\left[S'_S\right]$ equal to

$$\begin{aligned}\left[S'_M\right] &= \begin{bmatrix} S'_{hhM} & S'_{hvM} \\ S'_{hvM} & S'_{vvM} \end{bmatrix} = \begin{bmatrix} S_{hhM} & S_{hvM} \\ S_{hvM} & S_{vvM} \end{bmatrix} e^{j2kr_t} e^{-j2kr_{TM}} \\ \left[S'_S\right] &= \begin{bmatrix} S'_{hhS} & S'_{hvS} \\ S'_{hvS} & S'_{vvS} \end{bmatrix} = \begin{bmatrix} S_{hhS} & S_{hvS} \\ S_{hvS} & S_{vvS} \end{bmatrix} e^{j2kr_t} e^{-j2kr_{TS}}\end{aligned} \tag{5.1}$$

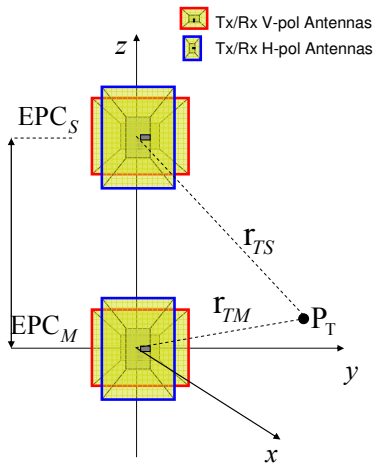

Fig. 5.1: Location of zero-baseline and interferometric EPCs in the UPC gbSAR data.

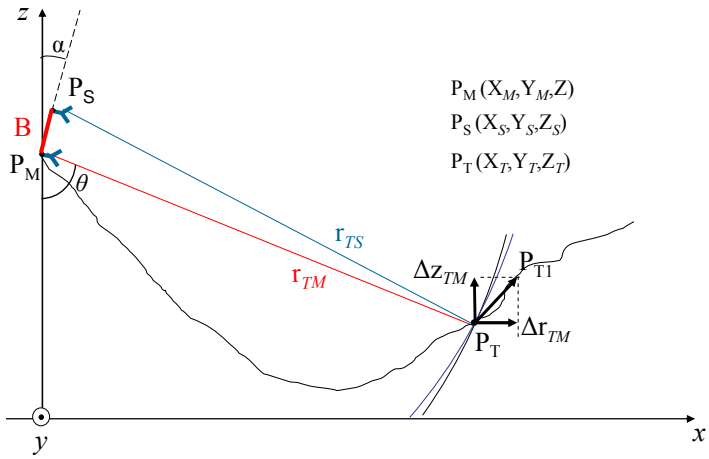

Fig. 5.2: Typical observation geometry of a ground-based SAR sensor for interferometric acquisitions.

where the subscripts *M* and *S* refer to zero-baseline (*master*) and interferometric (*slave*) measurements, respectively. The terms r_{TM} and r_{TS} denote the target's radial distance from the corresponding equivalent phase center EPC_M and EPC_S, respectively; r_t accounts for the radial position of the trihedral employed for data calibration with respect to EPC_M. The sketch in Fig. 5.1 describes the equivalent phase centers associated the two measured scattering matrices with respect to a generic target positioned at P_T. In general, the elements of $\left[S'_M\right]$ and $\left[S'_S\right]$ depend on several parameters such as the polarization of the transmitting and receiving antennas, the radar wavelength λ, the time and the viewing geometry [Freeman,92]. Nonetheless, when a scatterer is simultaneously observed from two slightly different positions, its polarimetric response may be assumed to be the same, that is

$$\left[S_M\right] \simeq \left[S_S\right]. \tag{5.2}$$

Under this hypothesis, which constitutes the underlying assumption of the SAR Interferometry [Lanari,96], it is possible to relate the phase difference between the master and slave acquisitions in the same polarimetric channel to geometrical parameters. Denoting with *i* the generic polarization channel of the two calibrated matrices in Eq. 5.1, it results

$$\left(S_{iM}\right)\left(S_{iS}\right)^* \simeq \left|S_{iM}\right|^2 e^{-j2k(r_{TM}-r_{TS})} = \left|S_{iM}\right|^2 e^{j2k\Delta r} = \left|S_{iM}\right|^2 e^{j\phi} \tag{5.3}$$

where * stands for the conjugate operation. According to this geometrical model, the term ϕ depends on the wavenumber *k* and on the range distance between target, and the two EPCs and is usually referred to as *interferometric phase*. When a different transmitting antenna is employed for the two acquisitions, the measurement configuration is referred to as *ping-pong*. This is the case of satellite interferometric data, which are usually gathered during two repeated passes of the sensor along very close orbits. When a common transmitting antenna is instead employed, as in UPC

system observations, the two data sets are gathered in a single-pass mode and the configuration is defined as non-*ping-pong* or *bistatic* [Soumek,99]. The main difference between *ping-pong* and non-*ping-pong* modes is the separation between the two EPCs, which usually halves passing from the first to the second situations. Yet, both configurations can be described by Eq. 5.3.

Taking into account the measurement geometry, it is possible to estimate the topographic information of the illuminated scene from the phase term ϕ. An example of the typical observation geometry of ground-based SAR sensors is depicted in Fig. 5.2. The points P_M and P_S define the position of the EPC_M and EPC_S, respectively; B, namely the *baseline*, describes the spatial separation between the two EPCs and corresponds to half the vertical separation between the two receiving antennas [Soumek,99]. According to Fig. 5.2, it is possible to express the term ϕ in Eq. 5.3 as a function of B, yielding

$$\phi = \frac{4\pi}{\lambda} r_{TM} \left[1 - \sqrt{1 - \frac{2\mathrm{B}}{r_{TM}} \sin(\theta - \alpha) + \frac{\mathrm{B}^2}{r_{TM}^2}} \right] \tag{5.4}$$

where α takes into account a possible inclination of the gbSAR front-end necessary to point directly towards the area of interest, and θ is the look angle equal to

$$\theta = \cos^{-1}\left(\frac{z_T - z_M}{r_{TM}} \right). \tag{5.5}$$

In order to avoid angular changes of the target's complex reflectivity, the baseline is normally kept small compared to the range distance, allowing one to assume that $B/r_{TM} \ll 1$. This hypothesis is usually referred to as *parallel-ray* assumption [Zebker,92].

By approximating the expression within the square root of Eq. 5.4 with the first order Taylor series expansion, the expression converts into

$$\phi = \frac{4\pi}{\lambda} \mathrm{B} \sin(\theta - \alpha). \tag{5.6}$$

Owing to the short wavelength of radar systems relative to the imaging geometry and to the circular nature of phase measurement, the term ϕ in Eq. 5.6 is ambiguous within integer multiples of 2π. This means that only its values in the range $(-\pi, \pi]$ are known, but not the integer number of cycles required to define its absolute value. Therefore, the analysis of a single pixel of the image does not permit to solve this ambiguity and to retrieve the absolute interferometric phase. In order to circumvent this problem, the relation between two adjacent pixels may be considered. According to Eq. 5.6, the interferometric phase increment between two close pixels P_T and P_{TI} can be approximated using the first order of Taylor series expansion to

$$\Delta\phi(r_{TM}, z_{TM}) = \frac{\partial\phi}{\partial r_{TM}} \Delta r_{TM} + \frac{\partial\phi}{\partial z_{TM}} \Delta z_{TM} \tag{5.7}$$

where $z_{TM} = z_T - z_M$ is the vertical height with respect to sensor elevation while Δr_{TM} and Δz_{TM} are the corresponding range and height separations. A visual interpretation of these two components is shown in Fig. 5.2. The two derivatives in Eq. 5.7 represent the range and z change-rate of the interferometric phase increment, respectively. The first quantity describes the linear interferometric phase pattern generated by the Earth surface in absence of topography. It is commonly defined as *flat-earth* component and is equal to

$$\frac{\partial \phi}{\partial r_{TM}} = \frac{4\pi}{\lambda} B\cos(\theta - \alpha) \frac{\partial \theta}{\partial r_{TM}} = \frac{4\pi}{\lambda} \frac{B\cos(\theta - \alpha)}{r_{TM} \tan\theta}. \tag{5.8}$$

The second term defines the *height sensitivity* of the interferometric measurements and may be mathematically expressed as

$$\frac{\partial \phi}{\partial z_{TM}} = \frac{4\pi}{\lambda} \mathrm{B}\cos(\theta - \alpha) \frac{\partial \theta}{\partial z_{TM}} = \frac{4\pi}{\lambda} \frac{\mathrm{B}\cos(\theta - \alpha)}{r_{TM} \sin\theta}. \tag{5.9}$$

Hence, the total increment of the interferometric phase $\Delta\phi$ between two adjacent pixels is obtained as sum of the flat-earth and the topographic phase and Eq. 5.7 becomes

$$\Delta\phi = \Delta\phi_{flat-earth} + \Delta\phi_{topography} = \frac{4\pi}{\lambda} \frac{\mathrm{B}\cos(\theta - \alpha)}{r_{TM} \tan\theta} \Delta r_{TM} + \frac{4\pi}{\lambda} \frac{\mathrm{B}\cos(\theta - \alpha)}{r_{TM} \sin\theta} \Delta z_{TM}. \tag{5.10}$$

Therefore, if the goal is to obtain just a phase term proportional to the scene topography, the *flat-earth* component must be carefully estimated and removed. At this point, an important issue characterizing the observation geometry of any ground-based SAR must be addressed. The mathematical formulation of the interferometric problem depicted in Fig. 5.2 assumes that the two EPCs and the target T lie on the same plane orthogonal to the x-axis. In other words, the underlying premise is that target is always aligned in the sensor's *boresight* direction. This condition is always fulfilled by a pixel of an air- and space-borne focused SAR image. In fact, no physical constraint limits the size of the aperture that these platforms are able to synthesize in time. The main contribution of the backscattered power from each scatterer is obtained when it is illuminated through the main lobe of the antenna radiation pattern. Accordingly, each pixel can be focused with respect to its zero-Doppler position. In gbSAR focused data, only a minority of the imaged pixels are really observed in such a way, as explained in Section 3.7. In fact, the points P_M, P_S and P_T lie now on a plane that is not always orthogonal to x. It follows that the baseline B is not constant over the whole scenario, as well as its inclination angle α in Eq. 5.10. As it can be observed in Fig. 5.3, these quantities become a function of the target's aspect angle φ defined in Eq. 3.70. Decomposing B into its z and z-orthogonal ($\perp z$) components [Nico,04], Eq. 5.10 becomes

$$\Delta\phi = \frac{4\pi}{\lambda} \frac{\mathrm{B}(\varphi)\cos(\theta - \alpha(\varphi))}{r_{TM} \tan\theta} \Delta r_{TM} + \frac{4\pi}{\lambda} \frac{\mathrm{B}(\varphi)\cos(\theta - \alpha(\varphi))}{r_{TM} \sin\theta} \Delta z_{TM} \tag{5.11}$$

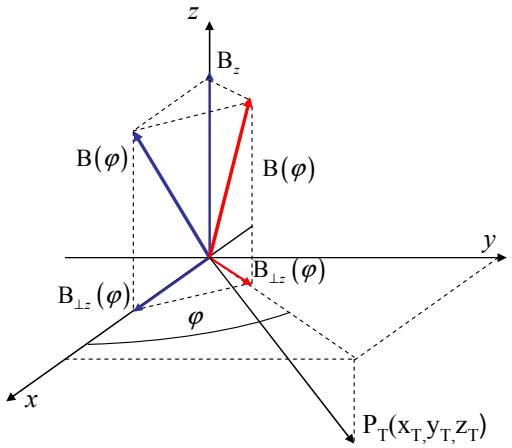

Fig. 5.3: Description of the horizontal and vertical components of the gbSAR interferometric baseline B as a function of target squint φ.

where

$$\mathrm{B}(\varphi)=\sqrt{\mathrm{B}_z^2+\mathrm{B}_{\perp z}^2(\varphi)}=\sqrt{\mathrm{B}_z^2+\mathrm{B}_{\perp z}^2(0)\cos^2\varphi} \tag{5.12}$$

and

$$\alpha(\varphi)=\arctan\left(\frac{\mathrm{B}_{\perp z}(\varphi)}{B_z}\right)=\arctan\left(\frac{\mathrm{B}_{\perp z}(0)\cos\varphi}{B_z}\right). \tag{5.13}$$

Finally, two considerations are in order. First, Eq. 5.10 is valid for absolute phase differences, and not for the wrapped version of it. The interferometric phase map (*interferogram*) obtained from Eq. 5.4 contains multiple 2π variations, called fringes, due to complex exponential periodic nature. The number of fringes is related to the topography of the observed scene and to the *height ambiguity* of the measurement, defined as the height information contained in a 2π cycle of phase and equal to

$$\Delta h_{2\pi}=\frac{\lambda r\sin\theta}{2\mathrm{B}\cos(\theta-\alpha)}. \tag{5.14}$$

It follows that interferometric phase must be first unwrapped before retrieving any topographic information. A description of the alternative approaches that may be pursued to cope with the phase-unwrapping problem can be found in [Ghiglia,98]. It must be stressed that the complexity of the unwrapping process is related to the fringes density. In order to reduce this complexity, a Digital Elevation Models (DEM) of the observed area is often used. Without entering into details, the fringes pattern due to the known topography can be calculated from Eq. 5.5 using the so co-called back-geocoding process (see Section 5.4 for more details) and subtracted from the wrapped phase. The fringes rate of the residue becomes lower and, hence, easier to unwrap. The total phase is finally obtained as the sum of the unwrapped residual and the DEM's subtracted interferogram [Carrasco,98]. The second point deals with the relative and not absolute topographic information the interferometric phase contains. Since Eq. 5.10 has been obtained by linking adjacent pixels and

that the measurement is sensitive to the sensor's position, the unwrapped phase as well as the retrieved height information may present an offset. The absolute position of at least one pixel of the image, called *tie-point*, is required to compensate for this offset.

5.2 Interferometric Coherence

The relationship between topography and interferometric phase stressed by Eq. 5.10 has been obtained through a geometrical study of the positions of the illuminated area with respect to the master and slave EPCs. Accordingly, the accuracy in the estimation of the topography is directly determined by the accuracy in the estimation of ϕ.

Depending on the nature of the observed scatterers, this estimation at pixel level might turn out to be misleading due to the speckle phenomenon. In Section 2.3.1, it has been explained that speckle is due to the high ratio between the SAR sensors' resolution and transmitted signal's wavelength [Goodman,76]. Although it is generate generated by deterministic reflection mechanisms, the high number of interactions within each resolution cell makes the scattering from homogeneous areas a noise-like random process [Lopez,03]. In the case of point targets (see Section 2.3), the speckle effects are negligible and the backscattering process may be assumed deterministic. It follows that when Eq. 5.2 is fulfilled and a high signal-to-noise ratio is guaranteed, the interferometric phase information of the single pixel may be directly related to the targets' elevation.

On the contrary, in the case of distributed targets as natural surfaces, the scattering process becomes non-deterministic: the interferometric phase values of the pixels belonging to the same distributed target become samples of a stochastic process. Accordingly, statistical descriptors are required to properly estimate ϕ. An assessed estimator used for this purpose is the cross-correlation complex coefficient ρ between two SAR acquisitions S_0 and S_1, which may be calculated as

$$\rho = \gamma e^{j\tilde{\phi}} = \frac{E\left\{S_0 S_1^*\right\}}{\sqrt{E\left\{|S_0|^2\right\} E\left\{|S_1|^2\right\}}} S \tag{5.15}$$

where $E\{.\}$ expresses the ensemble average operation in the realizations space [Papoulis,84]. The phase of ρ denoted with $\tilde{\phi}$ corresponds to the estimation of the true interferometric phase ϕ in Eq.5.3; the amplitude of ρ, denoted with γ, is usually referred to as the *interferometric coherence* and describes quantitatively the resemblance between the two SAR images. The value of γ varies in the range [0,1] and the two extremes account for the two limit situations of data total uncorrelation and total correlation, respectively.

Under the hypothesis of ergodicity and spatial homogeneity of the processes S_0, S_1 and $S_0 S_1^*$, the expectation E{.} may be replaced by a space average and Eq. 5.15 becomes

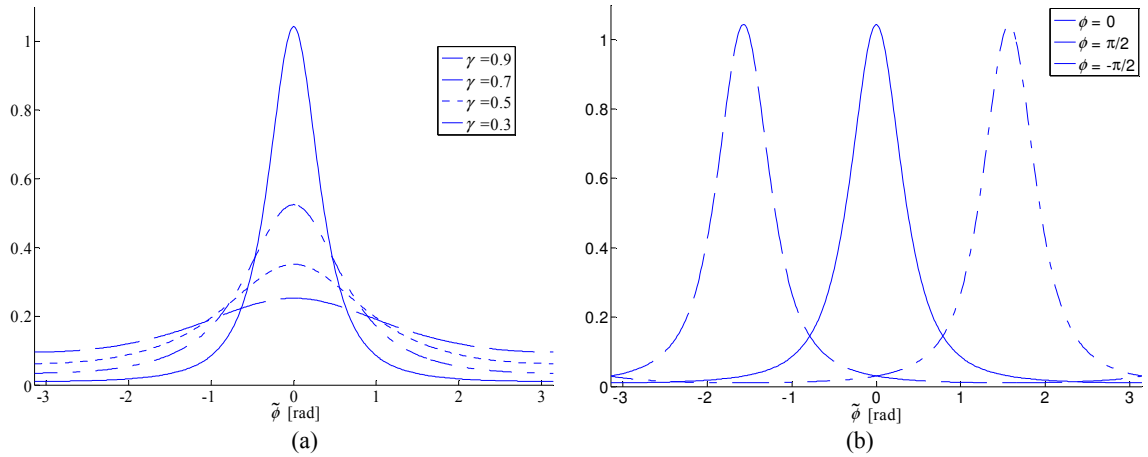

Fig. 5.4: Examples of the probability density function (*pdf*) of the estimated interferometric phase $\tilde{\phi}$ for different values of the coherence γ (a) and the real interferometric phase ϕ when $\gamma = 0.9$ (b).

$$\rho = \gamma e^{j\tilde{\phi}} = \frac{\sum_{n=1}^{ENL} S_0 S_1^*}{\sqrt{\sum_{n=1}^{ENL} |S_0|^2 \sum_{n=1}^{ENL} |S_1|^2}} \tag{5.16}$$

where *ENL* is the number of independent samples or *equivalent number of looks* within the averaged area. This number may be non-integer if the pixels being averaged are correlated, as it is explained in [Oliver,98] [Gierull,02]. Generally, a boxcar filter or *multilook* is employed for calculating ρ and the coherence estimator is indeed the maximum likelihood estimator [Seymour,94]. The higher the *ENL,* the higher the quality of the retrieved phase information but the worse the spatial resolution. This behavior is described by the following Cramer-Rao bound [Rodriguez,92]

$$\sigma_{\tilde{\phi}} = \frac{1}{\sqrt{2ENL}} \frac{\sqrt{1-\gamma^2}}{\gamma} \tag{5.17}$$

stating that the phase standard deviation $\sigma_{\tilde{\phi}}$ of the estimated interferometric phase $\tilde{\phi}$ approaches asymptotically to zero as the equivalent number of looks increases. Finally, it is worth recalling two problems affecting the accuracy of coherence estimation [Tough,95] [Touzi,,99] [Lee,02]: overestimation, due to an insufficient number of samples associated with the window size [Hanseen,01], and underestimation, which occurs when samples come from different distributions and the homogeneous hypothesis turns out to be unfulfilled. It follows that the size of the boxcar used to estimate γ must be chosen as a trade off amongst the statistical confidence of the estimator, the meaningful of the homogeneity assumption within of the block used in the calculation, and the maximum loss of resolution that can be accepted. In the following, the estimation of the true interferometric information will be directly indicated with the term ϕ.

5.3 Interferometric decorrelation factors

When real scenarios are observed, several factors might introduce a decorrelation among the two interferometric SAR acquisitions, yielding a drop of the overall coherence and to a consequent worsening of ϕ estimation.

5.3.1 Air- and Space-borne SAR sensors

The most general expression of the interferometric coherence γ formulated for the satellite/airborne SAR sensor is [Mora,04]

$$\gamma = \gamma_t \gamma_{vol} \gamma_{\Delta x} \gamma_{\Delta y} \gamma_v \gamma_{fD} \gamma_{th} \gamma_p \tag{5.18}$$

where each subscript identifies a different decorrelation source, namely

- t : changes in the backscattered signal due to different acquisition instants
- vol : the penetration of the radar wave in the scattering medium combined with a different look angle
- $\Delta x/\Delta y$: residual coregistration errors in the two radar image's dimensions
- v/f_D : non-overlapping parts of the two images bidimensional spectrum
- th : losses of system components
- p : processing errors related to sensor trajectory's uncertainties, focusing algorithm approximations and interpolation inaccuracies.

It is important to note that the coherences given by γ_{vol} and γ_t are inherent to the measuring conditions and they might be improved only in case of polarimetric interferometric data, as it is proposed in [Sagues,00] [Cloude,98].

The term v, also known as *wavenumber* shift [Galtelli,94], affects the range spectral domain and is related to the slightly different observation angles the interferometric geometry imposes. The different mapping of the ground-to-slant range makes the spectrum of the two images differ. Therefore, the effects of v may be reduced by filtering out the non-overlapping portions of two range spectra. The term f_D derives from cross-range spectral shift [Schwäbisch,95] between the two images when the Doppler centroid is different [Franceschetti,99] [Hansenn,01]. This might be caused by a different squint angle of the sensor or by not perfectly parallel trajectories followed by the platform during the two acquisition processes. Both situations turn into different observation geometries and cause effects similar to the ones described for the range domain. Again, filtering the non-common parts of the spectra allows one to improve the interferometric data set correlation. γ_{th} is related to the signal-to-noise ratio [Just,94] so that it depends on the losses and gains of the system components. Finally, γ_p can be maximized using proper processing algorithms and accurate interpolators.

5.3.2 UPC gbSAR sensor Interferometric Coherence

Concerning the UPC gbSAR interferometric acquisitions, several decorrelation effects become negligible or even null by construction, and, consequelty, the corresponding terms in Eq. 5.18 may be assume unitary. The capability of the sensor to acquire the two interferometric data sets in a single-pass mode excludes coherence drops due to different Doppler centroids as well as to temporal decorrelation effects. This means that the value of γ_t and γ_{fD} is 1. Besides, the mechanical displacement of the radar guarantees a perfect knowledge of the sensor position at each point of the synthetic aperture. This fact, along with the high interpolation factor used for the range compression and time-domain algorithm used for cross-range focusing, makes it possible to disregard coherence decreases due to γ_p. Owing to the short range distance and to the high S/N ratio the FM-CW radar system is able to provide, even the thermal noise contribution might be neglect in a first approximation. Concerning the *wavenumber* shift, the line of reasoning of [Galtelli,94] can be adapted to the gbSAR interferometric configuration. An estimate of range spectral shift effect is provided by the expression

$$\Delta f_r = -\frac{\mathrm{B}c}{\lambda_0 r_{TM}} \cos(\theta - \alpha) \tan(\theta - \varepsilon) r_{TM} \tag{5.19}$$

where θ is the look angle measured with respect to the master EPC horizontal plane, ε the local terrain slope, B the baseline, c the speed of the light in the vacuum, λ_0 the radar wavelength in the vacuum of the transmitted chirp's central frequency, r_{TM} the range distance from the master antenna. The term r_{TM} might vary from a few hundred meters to a few kilometers, whereas θ and ε strictly depend on the scene topography. Near and far range behavior might be very different, being the look angle variations generally relevant. Yet, maximum spectral shifts of a few hundred kHz are observed even in the worst cases [Nico,04]. This can be seen in Fig. 5.5, where the Δf_r dependence on the terrain slope ε for different height positions of the sensor is shown. The chirp-signal bandwidth transmitted by the X-band UPC sensor varies from 60 MHz up to 120 MHz [Aguasca,04], guaranteeing a range spectral overlapping of at least 99% between the two gbSAR images for Δf_r lower than 600 kHz. Moreover, the filtering window applied in range to enhance the quality of the zero-padding interpolation narrows the effective bandwidth of the signal. According to [Martinez,08], it is possible to state that the common band pre-filtering step in the UPC gbSAR interferometric acquisitions becomes unnecessary. In all these evidences, for the UPC gbSAR case Eq. 5.18 reduces to

$$\gamma = \gamma_{\Delta x} \gamma_{\Delta y} \gamma_{vol} \tag{5.20}$$

At this point, a last comment about the spatial averaging introduced in Eq. 5.16 for the estimation of the interferometric coherence γ is in order. The presence of topographic phase, whose fidelity is

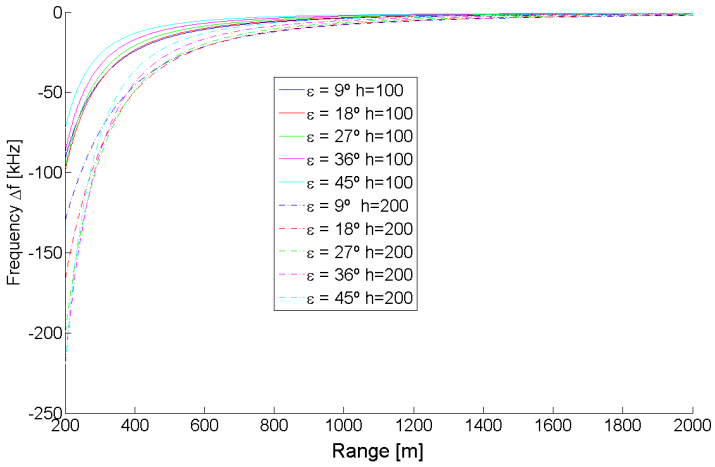

Fig. 5.5: Range spectral shift as a function of the terrain slope ε and the gbSAR sensor height.

theoretically described by γ, constitutes an inhomogeneity component within the area to be averaged. Depending on the tool chosen to perform the estimation, the obtained result underestimates the real value of γ. This is the case of the multi-look boxcar, which is widely employed in the SAR community as well as in the frame of this work. The reason lies in the spectral properties of this filter, which is essentially a bidimensional sinc function equal to

$$H(\omega_x,\omega_y)=\frac{1}{MN}\frac{\sin(\omega_x M/2)}{\sin(\omega_x/2)}\frac{\sin(\omega_y N)}{\sin(\omega_y/2)}e^{-j\omega_x\frac{M-1}{2}}e^{-j\omega_y\frac{N-1}{2}} \tag{5.21}$$

where M and N respectively define the two dimensions of the rectangular averaging window in pixels. The estimator works properly if the spectrum of the area used for the estimation is basebanded. In presence of topographic fringes, the homogeneity condition is not fulfilled and the obtained result underestimates the real value of γ [López,07]. A solution widely adopted is to use an external DEM to generate a synthetic interferogram of the area (see Section 5.7) or, if it is not available, to remove at least the flat-earth component in order to reduce their amount.

5.4 Digital Elevation Model (DEM) retrieval

The existence of a mathematical relationship between the SAR interferometric phase and scatterers' vertical elevation makes it possible to carry out an accurate description of the observed scene topography. This procedure is referred to as Digital Elevation Model (DEM) retrieval and deals with projecting (*geocoding*) the height information extracted from Eq. 5.10 onto a convenient *geodetic* reference. Among the various types of projections employed in cartography, it is worth mentioning the World Geodetic System 1984[1] (WGS84) and the Universal Transverse

[1] WGS84 is employed by Global Positioning System (GPS) devices and is suitable for global scale localizations and comparisons. Each point is identified by its latitude and longitude above the geocentric ellipsoid chosen as absolute reference while its height is the point-to-ellipsoid distance.

[2] UTM is generally employed for topographic mapping purposes and geological analysis. The ellipsoid is divided into different zones (namely 60) and each zone is conformal projected onto a plane *XY* tangent at its central meridian. The axis direction is chosen in such a way that it is parallel to the central meridian and points to the North; the x direction is obtained by consequence. The height information corresponds to the point-to-geoid distance along the so-called plumb line.Reference transformations exist to easily pass from WGS84 to UTM and vice versa.

Mercator[2] (UTM) [Schreier,93]. Two different approaches to the DEM retrieval problem can be found in literature. The first one is basically a two-step procedure. First, terrain heights are computed from range and interferometric phase difference through geometrical approximations. Then, the height information in the slant range-azimuth geometry is transformed into the UTM or WSG84 space coordinate to obtain the DEM. The second approach employs the information of sensor position and interferometric phase at once to generate the DEM directly without any geometrical approximation. The coordinates of each pixel within the interferograms are defined in a 3D Cartesian reference and a non-linear equations system is solved to invert the $\Delta\phi - \Delta z$ relationship in Eq. 5.7.

In the case of satellite or airborne SAR sensors, the first solution is generally adopted: simple geometrical approximations permit to express Δz as a linear function of $\Delta\phi$ [Madsen,98]. Concerning gbSAR sensors, this linearization process is not straightforward because the baseline depends on targets' squint angle φ, as stressed by Eq. 5.11. Approximations are then needed to work out a practical expression [Nico,04] unless specific hypotheses on the observation geometry are assumed [Pieraccini,00], [Noferini,07]. Yet, it is worth recalling that the observation geometry of terrestrial sensors is sensitive to its specific location with respect to the area of interest. The possibility to exploit the portability of these terrestrial devices to select the opimum observation geometry turns into a high variety of monitoring conditions the geocoding procedure has to deal with. Geometrical simplifications applied in [Nico,04] [Noferini,07] [Pieraccini,01] are usually consistent with satellite or airborne observations but might be inappropriate to describe ground-based observations.

In all this evidences, the second approach mentioned before seems to be more suitable to handle the geometry diversity of the terrestrial platforms. In the next Section, an innovative procedure for the retrieval of DEMs from gbSAR interferometric acquisitions pursuing this alternative strategy is put forward.

5.4.1 Geocoded DEM retrieval

Let the points P_M (x_M,y_M,z_M) and $P_S(x_S,y_S,z_S)$ denote the position of master and slave EPCs in a Cartesian reference system $(\hat{x},\hat{y},\hat{z})$, respectively. Since a Short Synthetic Aperture (SSA) is considered, the position of the gbSAR front-end is assumed to be fixed at the middle point of the linear unit. As it has been shown in Fig. 4.5 and sketched in Fig 4.11 and Fig. 5.1, the front-end antennas as well as their equivalent phase centers lie on the same plane. It follows that the baseline B connecting P_M to P_S is, by construction, orthogonal to the master and slave radar planes hereinafter denoted with Γ_M and Γ_S, respectively.

In general, a plane Γ is uniquely defined in Cartesian reference $(\hat{x},\hat{y},\hat{z})$ by the expression

$$\Gamma : A_x x + A_y y + A_z z + \left(A_x x_0 + A_y y_0 + A_z z_0 \right) = 0 \tag{5.22}$$

where $\left(A_x, A_y, A_z \right)$ are the components of any vector orthogonal to Γ and (x_0,y_0,z_0) are the coordinate of a generic point lying on Γ. Accordingly, the two parallel planes Γ_M and Γ_S may be described as

$$\begin{aligned} \Gamma_M &: B_x x + B_y y + B_z z - \left(B_x x_M + B_y y_M + B_z z_M \right) = 0 \\ \Gamma_S &: B_x x + B_y y + B_z z - \left(B_x x_S + B_y y_S + B_z z_S \right) = 0 \end{aligned} \tag{5.23}$$

where

$$\mathrm{B}\left(B_x, B_y, B_z \right) = \left(x_S - x_M, y_S - y_M, z_S - z_M \right) \tag{5.24}$$

Let now consider the master image as reference. The energy backscattered by a generic target T located at P_T (x_T,y_T,z_T) is focused on a point T' of Γ_M. This point is obtained as the intersection between Γ_M and the unique arc $\widehat{\mathrm{P_T T'}}$ orthogonal to the radar plane and lying on the spherical wavefront centered at P_M with radius r_{TM}. A schematic description of this projection is given in Fig. 5.6. The problem of DEM retrieval deals with estimating the Cartesian coordinates of P_T using master and slave gbSAR images information.

Let the aspect angle of T' described in Eq. 3.70 be redefined as φ in order to avoid any confusion. Three geometrical relations link the two EPCs and the projection of P_T on Γ_M each pixel of the focused image, yielding the equations system

$$\begin{cases} \left(x_M - x_T \right)^2 + \left(y_M - y_T \right)^2 + \left(z_M - z_T \right)^2 = r_M^2 \\ \left(x_S - x_T \right)^2 + \left(y_S - y_T \right)^2 + \left(z_S - z_T \right)^2 = r_S^2 \\ \vec{v}_S \cdot \overrightarrow{\mathrm{P_M T'}} = \left| \vec{v}_S \right| \left| \overrightarrow{\mathrm{P_M T'}} \right| \cos\left(\pi / 2 + \varphi \right) \end{cases} \tag{5.25}$$

where "$\cdot$" and "$|\cdot|$" stand for the vector scalar product and modulus operation, $\vec{v}_S$ is the unitary vector defining the sensor linear trajectory, and r_{TM} and r_{TS} are the target's radial distance from *master* and *slave* EPCs, respectively. It is worth pointing out that the main difference between ground-based and satellite or airborne SAR acquisitions geocoding is represented by the third equation. For the latter platforms, all the pixels within the interferometric data set are focused with respect to the zero-doppler position. This means that φ is always zero and the equation reduces to

$$\vec{v}_S \cdot \overrightarrow{\mathrm{P_M T'}} = 0 \,. \tag{5.26}$$

In order to admit a unique solution, the non-linear equations system must be well-determined. The first two equations are related by the absolute interferometric phase ϕ as follows

$$r_{TS} = r_{TM} + \frac{\lambda}{2\pi} \phi \,. \tag{5.27}$$

Concerning the third equation, it is necessary to express T' and φ as functions of P_T. To do this, a non-linear equations system providing the (x,y,z) coordinates of T' should be first solved. Yet, just

the angular relation between the vectors $\vec{v}_S$ and $\overrightarrow{\mathrm{P_M T'}}$ is actually required to solve Eq. 5.25. In Fig. 5.6, it can be observed that the same information may be obtained by considering an alternative, but mathematically simpler, projection of $\mathrm{P_T}$ denoted with T": T" is given by the intersection between Γ_M and the line *l* orthogonal to Γ_M, that is parallel to the baseline B, passing through $\mathrm{P_T}$. Then, it is possible to replace the third equation of Eq. 5.25 with

$$\vec{v}_S \cdot \overrightarrow{\mathrm{P_M T''}} = \left|\vec{v}_S\right| \left|\overrightarrow{\mathrm{P_M T''}}\right| \cos\left(\pi/2 + \varphi\right). \tag{5.28}$$

As the new equations system is still non-linear in the variables (x_T,y_T,z_T), a closed-form solution is not available and iterative methods must be employed. The Newton-Raphson's algorithm [Press,92] is simple to implement and guarantees a quite fast convergence to the solution. Details about its mathematical formulation can be found in [Celma, 07] and, for the sake of handiness, in *Appendix B*. Once the absolute position of $\mathrm{P_T}$ is obtained, the final DEM in UTM coordinates is retrieved into two-steps. First, the Cartesian coordinates are transformed into ellipsoidal coordinates (latitude ς_{lt}, longitude ς_{ln} and elevation *h*) by the transformation [Schreier,93]

$$\begin{aligned} \varsigma_{lt} &= \arctan \frac{z_T + e'^2\, b \sin^3 \kappa}{p - e^2 a \cos^3 \kappa} \\ \varsigma_{\mathrm{ln}} &= \arctan\left(y_T / x_T\right) \\ h &= \frac{\sqrt{x_T^2 + y_T^2}}{\cos \varsigma_{lt}} - N \end{aligned} \tag{5.29}$$

where *a* and *b* are the reference ellipsoid semiaxes, *N* is the curvature radius given by

$$N = \frac{a^2}{\sqrt{a^2 \cos^2 \varsigma_{ln} + b^2 \sin^2 \varsigma_{ln}}}. \tag{5.30}$$

and κ and e' are auxiliary quantities equal to

$$\kappa = \arctan \frac{z_T a}{b\sqrt{x_T^2 + y_T^2}} \qquad e' = \frac{a^2 - b^2}{b^2}. \tag{5.31}$$

A geometrical interpretation of the different quantities is sketched in Fig. 5.7. Finally, plane coordinates (x_{UTM},y_{UTM}) are obtained from latitude and longitude using the Gauss-Krüger projection [Schreier,93].

Few last comments are in order. Owing to the reduced area observed by the gbSAR sensor, the same initial guess can be used to iteratively solve in Eq. 5.25 for all the pixels of the radar image to be geocoded. In general, the same *tiepoint* used for the determination of the absolute interferometric phase ϕ after the interferometric phase unwrapping step (see Section 5.1) is employed for this purpose. In section 4.3, it has been stressed that gbSAR data might be focused on polar or Cartesian grids of pixels, depending on the reference system that turns out

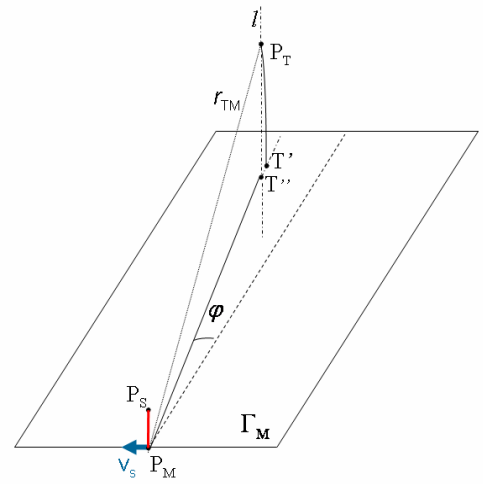

Fig. 5.6: Geometrical projections T' and T'' of the target at P_T onto master antenna's radar plane Γ_M.

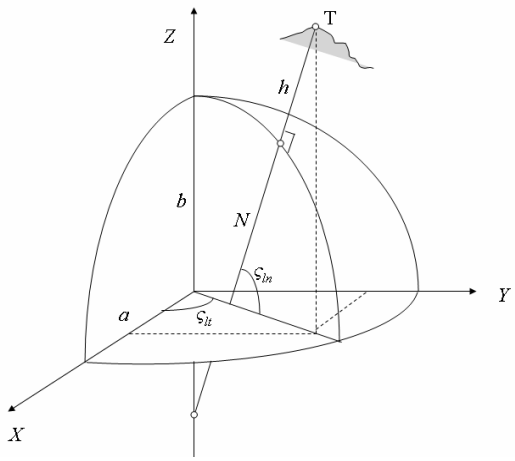

Fig. 5.7: Cartesian (x,y,z) and geodetic$(\varsigma_{lt},\varsigma_{ln},h)$ coordinates of a target T on the Earth surface.

to be more suitable for the specific monitoring case. Since the problem has been formulated at pixel level, the proposed technique is able to geocode interferometric information whatever the spatial grid of points gbSAR raw data have been focused on.

5.4.2 Back-Geocoding

The reverse or back-geocoding is the opposite process to geocoding and basically consists in mapping a ground-range DEM in a reference coordinates frame to a slant range radar image. This information turns out to be useful in order to reduce problem complexity, as for the phase unwrapping process (see Section 5.1), or to improve the estimation of parameters sensitive to topographic fringes, such as the interferometric coherence (see Section 5.3).

In general, DEMs are available in UTM coordinates whereas the Cartesian coordinates system is required to apply the Euclidean geometrical concepts of distances and angles. This conversion is performed in two steps. First, UTM information is transformed into latitude ς_{lt}, longitude ς_{ln} and elevation h by the inverse Gauss-Krüger projection [Carrasco,98] after choosing an ellipsoidal reference (for instance the WGS-84). Then, the relation between ellipsoidal and Cartesian coordinates is provided by the following set of equations

$$\begin{aligned} x &= (N+h)\cos\varsigma_{ln}\cos\varsigma_{lt} \\ y &= (N+h)\cos\varsigma_{ln}\sin\varsigma_{lt} \\ z &= \left(\frac{b^2}{a^2}N+h\right)\sin\varsigma_{ln} \end{aligned} \quad . \tag{5.32}$$

The range coordinates of each points of the DEM in the *master* and *slave* radar image, as well as the squint angle φ are directly given by the equations system in Eq.5.25. At this point, calculating the synthetic interferometric phase becomes straightforward. A final interpolation on a regular grid

defined on the radar reference plane provides the DEM in the radar slant-range domain. Parameters as the maximum range-distance and the antenna radiation pattern may be taken into account to filter out zones invisible to the sensor. Besides, the knowledge of topography and targets' absolute position allows one to estimate the incidence angle of the transmitted wave as

$$\alpha_{inc} = \pi - \arccos \frac{\overrightarrow{P_M P_S} \cdot \overrightarrow{P_M P_T}}{\left|\overrightarrow{P_M P_S}\right| \left|\overrightarrow{P_M P_T}\right|} . \tag{5.33}$$

The positive and negative variations of α_{inc} along *iso-squint* cuts make it possible to work out a shadow-mask filtering out not-illuminated areas, as it is shown in Fig. 5.8. Although it is not strictly necessary for the purposes mentioned before, this procedure is extremely helpful in order to find the optimum location of the sensor minimizing the shadowing effects within the area of interest.

5.4.3 DEM retrieval technique assessment

In terms of geocoding accuracy, it has been already mentioned that the proposed technique does not perform any geometrical approximation. Moreover, the iterative solution makes it possible to reduce the error in the estimation of pixels' absolute position to the appropriate precision. The main source of errors affecting the retrieved DEM are instead related to the quality of the unwrapped interferometric phase, which depends on targets' coherence and shadowing effects, and to the accuracy in the estimation of observation geometry parameters, i.e. the absolute position of the *master* antenna and the trajectory vector $\vec{v}_S$. Owing to the short dimension of the linear unit and to the limited precision of commercial GPS devices, the direct measurement of such parameters is unfeasible. In fact, even when a differential GPS is employed, an error of about 0.5 meter for the plane coordinates over the reference ellipsoid and at least 2 meters for the elevation must be assumed.

A possible solution to the problem is the use of reference or tie points (*TPs*). The procedure is based on measuring *TPs*' position using commercial GPS devices and converting this information into the ellipsoidal Cartesian reference *xyz*. The ground-truth *squint* of the *i*th tie-point TP_i is then given by

$$\varphi_{TP_i}^{GPS} = \arcsin \frac{\vec{v}_S \cdot \vec{r}_{\mathrm{TP_iM}}}{\left|\vec{r}_{\mathrm{TP_iM}}\right|} - \frac{\pi}{2} \tag{5.34}$$

where $\vec{r}_{\mathrm{TP_iM}}$ is the vector connecting the *master* antenna to its projection onto the radar plane Γ_M. Since the deployment of the linear unit is perfectly horizontal, $\vec{v}_S$ lies on Γ_M and is orthogonal to the baseline B as well as to the gravity direction. Then, it may be expressed as

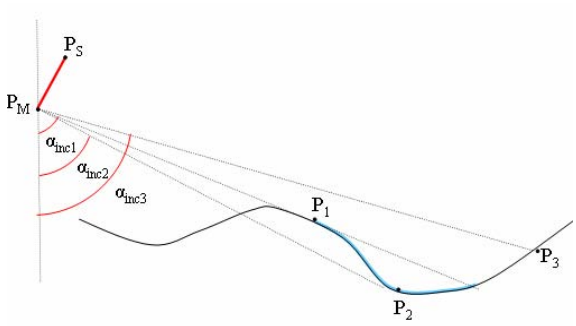

Fig. 5.8: Shadowing effects in back-geocoding process using the negative gradient of the incident angle α_{inc}.

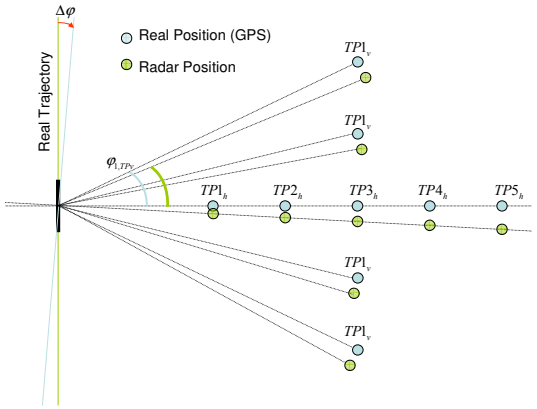

Fig. 5.9: Correction of gbSAR trajectory orientation ξ using a range and a cross-range alignments of *tie-points*.

$$\vec{v}_S = \Im\left(\begin{bmatrix} x_{M,UTM} \\ y_{M,UTM} \\ h_{M,UTM} \end{bmatrix} + \begin{bmatrix} \cos\xi \\ \sin\xi \\ 0 \end{bmatrix}\right) - \Im\left(\begin{bmatrix} x_{M,UTM} \\ y_{M,UTM} \\ h_{M,UTM} \end{bmatrix}\right) \tag{5.35}$$

where ξ is its orientation with respect to the North direction and $\Im$ defines the UTM-to-Cartesian conversion function. It can be easily noticed that an error in the estimation of ξ directly affects $\vec{v}_S$, introducing a common squint offset $\Delta\varphi$. Accordingly, the relation between $\varphi_{TP_i}^{GPS}$ in Eq. 5.35 and the real squint position φ_{Ri} may be expressed as

$$\varphi_{TP}^{GPS} = \varphi_{R_i} + \Delta\varphi + \Delta\zeta_i \tag{5.36}$$

where $\Delta\zeta_i$ indicates the error of GPS measurements. Denoting with $\varphi_{TP_i}^{M}$ the squint position retrieved from the *master* reflectivity image, $\Delta\varphi$ can be directly compensated by minimizing the error function

$$\varepsilon_\varphi = \sqrt{\sum_{i=1}^{N_{TP}} \left(\varphi_{TP_i}^{M} - \varphi_{TP}^{GPS}\right)^2} \tag{5.37}$$

with respect to synthetic aperture orientation ξ. An iterative method may be employed for this purpose. It has been observed that just a few iterations are needed for the convergence of the algorithm to the absolute minimum ε_φ.

In order to analyze the sensitivity of this technique to *TPs* and sensor location errors, the scenario sketched in Fig. 5.9 has been considered. To stress the different dependence of Eq. 5.37 on range and cross-range dimensions, 5 reference targets have been aligned along the *boreside* and other four ones orthogonally to this direction. The corresponding UTM coordinates are reported in Table 5.1. These positions have been selected within the test-area of Sallent described in Section 4.7.2.

As a first approximation, the standard deviation of UTM coordinates has been assumed constant, i.e. $\sigma_x = \sigma_y = \sigma_h = \sigma$. The behavior of the standard deviation σ_ξ, which essentially describes the

	X_{UTM} [m]	Y_{UTM} [M]	h [m]
Sensor Position	408940	4630352	354
$TP1_H$	408688	4630251	269
$TP2_H$	408609	4630223	269
$TP3_H$	408534	4630193	270
$TP4_H$	408437	4630154	268
$TP5_H$	408305	4630105	270
$TP1_V$	408422	4630027	273
$TP2_V$	408400	4630098	273
$TP4_V$	408360	4629234	272
$TP5_V$	408338	4629299	272

Table 5.1: UTM coordinates of the tie-points (*TPs*) sketched in Fig. 5.9.

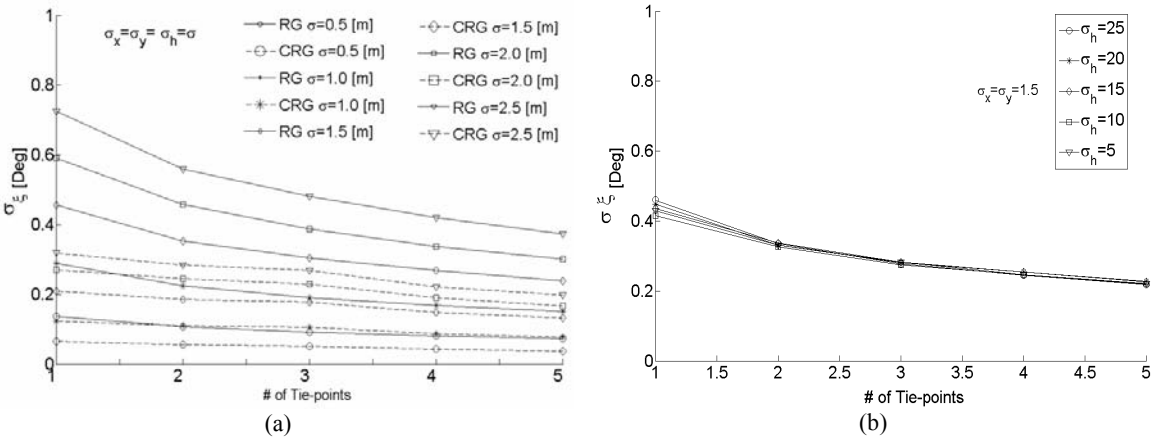

Fig. 5.10: Standard deviation of the gbSAR trajectory orientation ξ as a function of UTM coordinates (x_{UTM},y_{UTM},h) uncertainty for different numbers of tie-points. In (a) it is assumed (σ_x=σ_y=σ_h) while in (b) σ_x=σ_y<<σ_h. For each case, 500 estimates of the orientation angle ξ have been carried out.

uncertainty in the gbSAR trajectory orientation, is displayed in Fig. 5.10a as a function of the number of tie-points N_{TP}. The cross-range array (dotted lines) turns out to be more reliable than the range alignment (continuous lines): the value of σ_ξ is always much lower for the first lay-out. Moreover, the decrease of σ_ξ for the cross-range case is almost negligible, showing that a few squinted *TPs* are sufficient for ξ estimation. Since the accuracy of the latitude and longitude measurements provided by commercial GPS devices is higher than the accuracy of height estimation, it is reasonable to look into the effects of a higher uncertainty of h. To this end, a second simulation with fixed value of σ_x and σ_y and σ_h varying from 5 up to 25 meters has been carried out. The results are shown in Fig. 5.10b for the range alignment. It is easy to observe that σ_ξ is nealy independent of the height information and its decrease seems to be insensitive to N_{TP}. Resuming, ξ is sensitive to error in the x and the y dimensions but it slightly changes for even high uncertainties in the h dimension. Squinted tie-points must be preferred for a more precise estimate of the SSA orientation $\vec{v}_S$ but even commercial GPS sensor can be used for the measurement of their absolute position.

UPC gbSAR System	
Frequency Carrier f_0	9.65 *GHz*
PRF	20 *KHz*
Chirp Bandwidth	120 *MHz*
Baseband Bandwidth	40 *MHz*
A/D Sampling Rate	100 *Ms/sec*
Transmitted Power	27 dB*m*
3dB Antenna Beamwidth	128
Cross-range Sampling	1 *cm*
Aperture Length	2 *m*
Polarization	*vv*
Scan time-duration	1 *min* 20 *sec*
Antennas Vertical Separation	*0.8 m*
Inclination angle α	*12.5º*

Fig. 5.11: Picture of the Sallent test-area from sensor's location.

Table 5.2: UPC gbSAR measurement parameters.

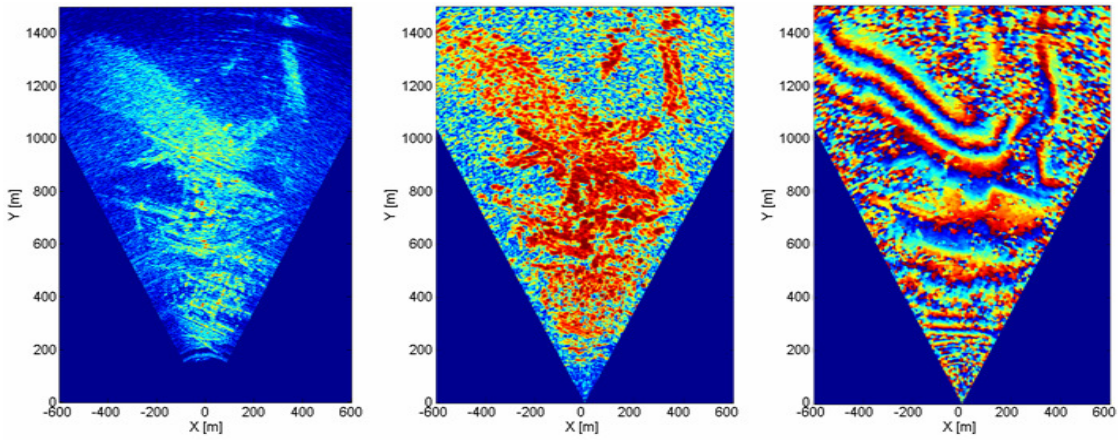

(a) (b) (c)

Fig. 5.12: *Master* reflectivity image (a), single-pass interferometric coherence γ (b) and wrapped interferometric phase ϕ (c) concerning the Sallent test-site. The Pixel dimension is 1.5m×1.5m and a 10×10 boxcar has been used for the estimation of γ and ϕ.

Concerning the quality of the retrieved DEM, an uncertainty of ξ turns into an error proportional to the same topography and for this reason strictly depends on the scenario and on the sensor location. Nevertheless, as far as σ_ξ is lower than the 0.4º, geocoding errors have been observed to be negligible. This will be shown in Section 5.4.5, where the distortion effects introduced by incorrect estimations of observation geometry parameters are analyzed in detail. In the end, maximum uncertainty thresholds for a reliable DEM retrieval from gbSAR interferometric acquisitions are also drawn.

5.4.4 Real DEM Retrieval

In order to provide a comprehensive description of the processing chain developed for retrieving geocoded DEMs from gbSAR real data, the area of the Station district of Sallent described in Section 4.7.2 is examined closely. A view of the test-site from the sensor position is detailed in Fig. 5.11. Information concerning the measurement parameters is reported in Table 5.2, while an

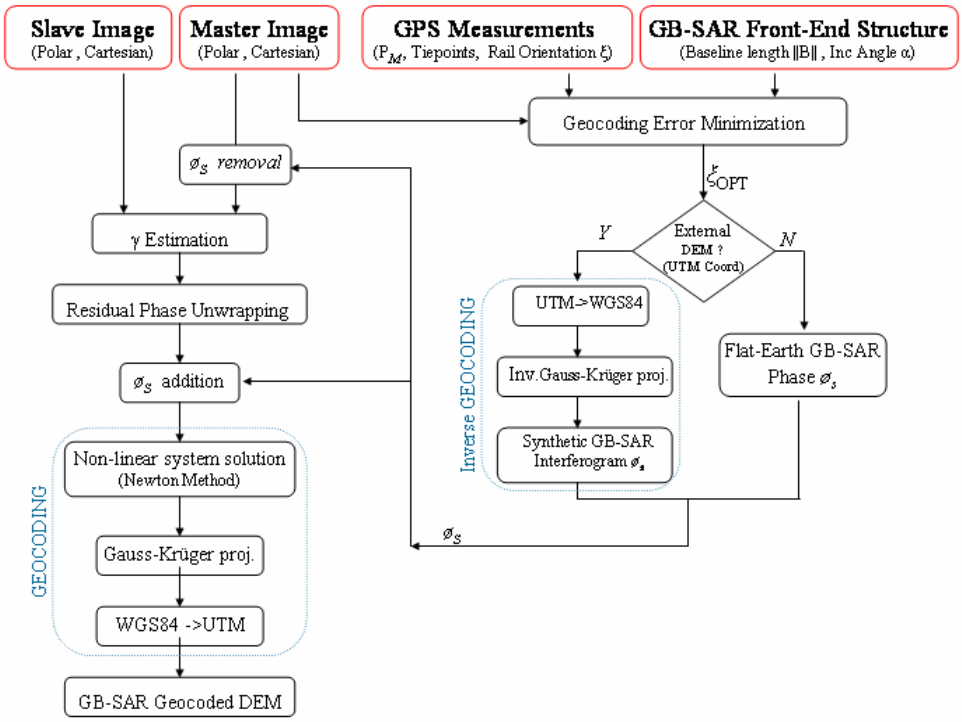

Fig. 5.13: Processing chain of the DEM retrieval technique using UPC gbSAR interferometric acquisitions. The red boxes define the input information required to start the process.

example of the *master* reflectivity image, the single-pass interferometric coherence γ and the wrapped interferometric phase ϕ in the radar coordinate system are shown in Fig. 12a-c. The interferometric data set was acquired on September 19th 2006 at 22:10.

A block- diagram resuming the main steps of the DEM retrieval procedure is sketched in Fig. 5.13. The red frames contain the input information that technique needs to carry out the geocoding process. First, the position of the tie-points in the *master* image reflectivity is matched with the GPS ground-truth information to estimate ξ and hence $\vec{v}_S$ (see Section 5.5.3). To this end, the four points shown in the satellite photo of Fig. 5.14 have been employed. Since the GPS measurements are given in ellipsoidal coordinates with respect to the WGS-84 ellipsoid, *TPs* position is converted into a Cartesian xyz system before performing the minimization step described in Eq. 5.35. Then, an external Digital Terrain Model (DTM) is used to obtain the interferometric synthetic phase ϕ_{syn} of the scenario in radar coordinates. This step is carried out by applying the inverse geocoding procedure described in Section 5.4.2. Regarding the Sallent test-area, the external DTM was provided by Institut Cartogràfic de Catalunya (ICC). Nonetheless, if no external DEM is at disposal, at least the flat-earth component in Eq. 5.13 may be employed to generate ϕ_{syn}. This synthetic phase component is subtracted from the master complex data to improve the estimate of the interferometric coherence γ and the corresponding residual phase ϕ_{res} (see Section 5.1). Afterwards, ϕ_{res} is unwrapped using a Weighted Least Mean Square

Fig. 5.14: Location of the four tie-points used for the estimation of UPC gbSAR's trajectory ξ in the Sallent test-site.

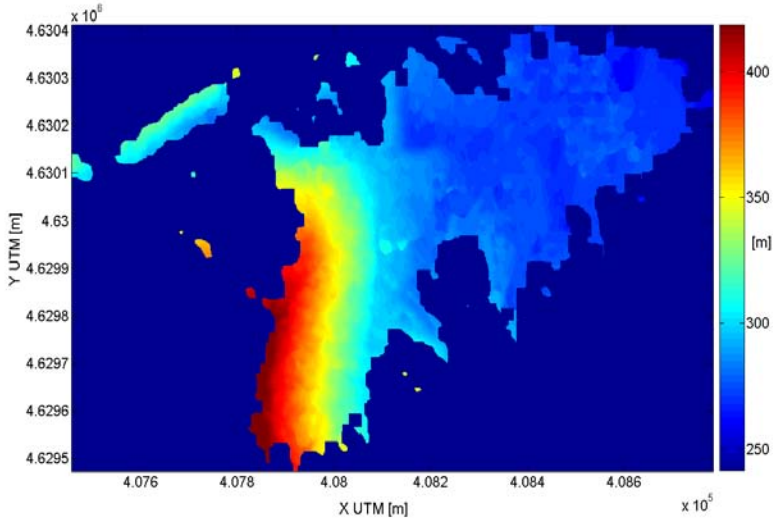

Fig. 5.15: Retrieved DEM in UTM coordinates concerning the test-site of Sallent obtained as output of the processing chain sketched in Fig. 5.13.

(WLMS) technique [Carrasco,98] [Ghiglia,98], added again to ϕ_{syn} and finally offset-compensated using one of the tie-points. At this point, the absolute interferometric phase is available and the non-linear equations system in Eq. 5.25 is solved, pixel by pixel, as explained in Appendix B. The Cartesian coordinates of each pixel are than transformed into ellipsoidal coordinates ($\varsigma_{lt}, \varsigma_{ln}, h$) by the Gauss-Krüger projection, and finally into Ed50 UTM reference ($x_{\mathrm{UTM}}, y_{\mathrm{UTM}}, h$) using the *Helmert* Transformation [Hoffman,97]. The final result is the DEM of the observed scene shown in Fig. 5.15. An estimation of the topographic estimation error is given by the difference, pixel by pixel, between the DTM (employed as ground-truth) and the retrieved DEM shown in Fig. 5.16; the corresponding histogram is displayed in Fig. 5.17. It can be seen that the topographic errors are centered at zero. That is, the retrieved topography is not biased, guaranteeing that the estimation

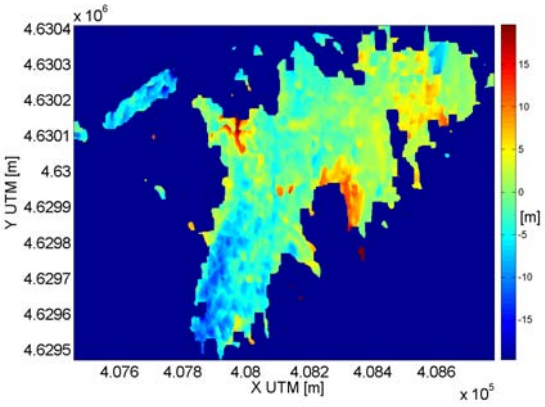

Fig. 5.16: 2D distribution of the topographic error of the DEM retrieved by interferometric UPC gbSAR data sets using the ICC DTM as ground-truth.

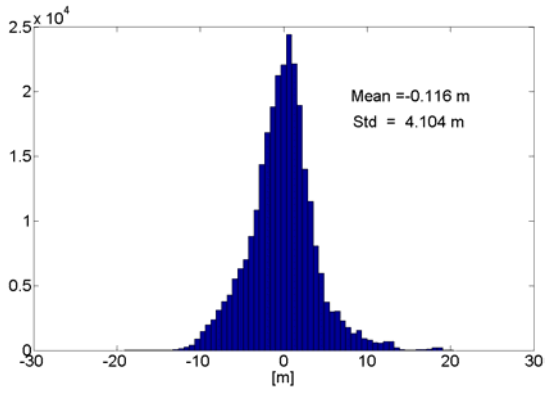

Fig. 5.17: Histogram of the topographic error of the DEM retrieved by interferometric UPC gbSAR data sets using the ICC DTM as ground-truth.

of the measurements parameters such as the sensor's position and baseline's orientation is correct. Concerning the error standard deviation, it is worth pointing out that the value of 4 meters is in the order of the results obtained by the alternative two-step geocoding techniques compared in [Martinez,08] when a set of 32 interferograms is employed for the estimation of ϕ. On the contrary, just one UPC gbSAR interferograms has been employed for the DEM retrieval in Sallent. Indeed, the quality of the retrieved DEM underestimates the potentials of the geocoding technique here proposed. As a DTM and not a DEM has been used as ground-truth, the presence of buildings, structure and man-made objects has not been taken into account. The 10×10 averaging boxcar filter employed for the estimate of γ is supposed to mitigate the corresponding phase differences, but it can be noticed that the incorrect pixels in Fig. 5.16 are mostly concentrated within the urban area (the red spots in *near* range). Possible errors arising from the phase unwrapping of sparse coherent pixels should be also allowed for. Shadowing areas due to the gbSAR observation geometry might make WLMS technique unsuitable to successfully handle these situations. More suitable techniques described in [Ghiglia,98] might be employed to unwrap the interferometric phase over a sparse grid of trustful pixels or badly connected areas. Finally, the canopy in the top left side of the scenario (Fig. 5.11 and Fig. 5.12a-c) is likely to affect the two-way wave propagation from the sensor to the ground. This justifies the poorer quality of the retrieved height information concerning this area. Indeed, lower standard deviation values are expected to be obtained over bare or low vegetated environment.

5.4.5 Retrieved DEM Sensitivity Analysis

In this section, a brief analysis of the sensor sensitivity with respect to observation geometry parameters uncertainty is carried out. In particular, the effects of the SSA orientation ξ, the baseline inclination α, and the platform height h incorrect estimation are analyzed in terms of

overall error of the retrieved DEM. In order to separate these geometrical effects from possible phase unwrapping errors due to low coherent pixels, the synthetic interferometric phase ϕ_{syn} obtained by back-geocoding the ICC DTM is employed. The parameters used to calculate ϕ_{syn} are reported in Table 5.3 while the synthetic DEM in the radar reference is shown in Fig. 5.18. Concerning the gbSAR orientation ξ, the existence of a relation between the number of reference points used for its estimation and the retrieved value uncertainty has been proven in Section 5.5.3. As four tie-points located at different cross-range positions have been employed for the DEM retrieval of Section 5.4.4, the effects of an incorrect ξ might be overestimated by assuming a maximum error $\Delta\xi = 0.5°$. Then, the topographic error at pixel level is given by

$$\Delta h_{UTM} = h_{UTM}(\xi) - h_{UTM}(\xi \pm \Delta\xi) \tag{5.38}$$

where the term $h_{UTM}(\xi)$ is the ground-truth DTM and $h_{UTM}(\xi + \Delta\xi)$ is the elevation obtained by geocoding ϕ_{syn} with respect to a $\xi \pm \Delta\xi$ oriented SSA. The 2D distribution of the error in the worst case and the corresponding histogram are displayed in Fig. 5.19a and Fig. 5.19b, respectively. It can be observed that the error depends on the topographic gradient and varies in [-10m,10m] with a standard deviation of about 2.6 m. These values are in the order of the results shown in Fig. 5.15. Besides, the two error patterns resemble each other. Any attempt to reduce the real data standard deviation by slightly varying ξ generates an error offset but no improvement in terms of error dispersion. Moreover, the study of amplitude images shows that higher geocoding errors are introduced for ξ different from the nominal value in Table 2.3., confirming the efficiency of the approach described by Eq. 5.38.

Regarding the second parameter, an analogical inclinometer was used to measure the baseline inclination α with respect to the gravity direction. According to instrument specifications, an error of $\Delta\alpha$ equal to 0.5° is by far higher than the real uncertainty. Following the idea described for ξ, it is possible to overestimate this height error contribution as

$$\Delta h_{UTM} = h_{UTM}(\alpha) - h_{UTM}(\alpha \pm \Delta\alpha) \tag{5.39}$$

The results in terms of 2D distribution and error histogram are shown in Fig. 5.20a and Fig.5.20b, respectively. In this case, an error of α turns into an undesired height range-ramp and generates ramp-like histogram error. It is worth noting that the histogram mean value is different from zero. A brief comparison between Fig. 5.20a and Fig. 5.16, as well as between Fig. 5.20b and Fig. 5.17, allows one to exclude that this type of error is affecting the height information retrieved in Section 5.5.4. Finally, it is possible to describe the effects of platform elevation uncertainty by studying the function

$$\Delta h_{UTM} = h_{UTM}(h_{UTM}^{GBSAR}) - h_{UTM}(h_{UTM}^{GBSAR} \pm \Delta h)\,. \tag{5.40}$$

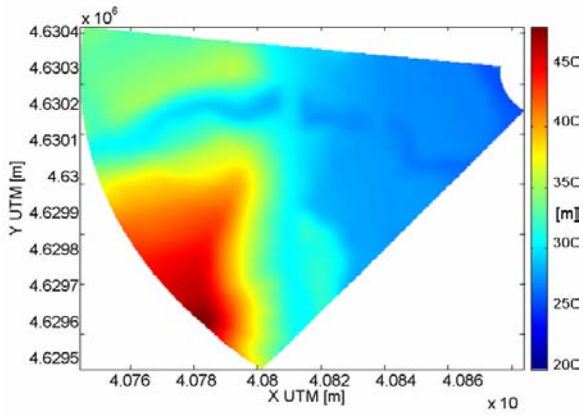

Back-Geocoding Parameters	
Longitude Zone(Huso)	31
Datum	ed50
Vertical Baseline B	0.4 m
Inclination Angle α	12.5º
North Orientation ξ	-22.7º
Sensor Position (UTM)	[408939, 4630350,355]
Angular Mask (deg)	[-30º,30º]
Min Range	200 m
Max Range	1500m

Fig. 18: Geocoded DTM of Sallent retrieved from the synthetic interferogram ϕ_{syn} given by inverse-geocoding the ICC DTM.

Table 5.3: List of back-gecoding parameters used to calculate ϕ_{syn} from the ICC DTM.

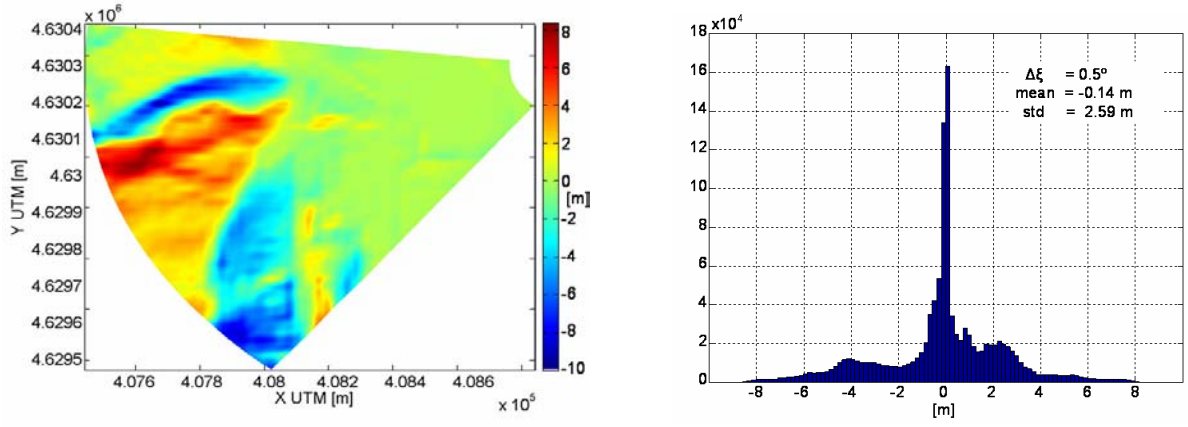

(a) (b)

Fig. 19: 2D distribution (a) and histogram (b) of the topographic error obtained by geocoding the synthetic interferogram ϕ_{syn} and assuming a maximum uncertainty $\Delta\xi$ equal to 0.5º in the SSA orientation.

A maximum error Δh equal to 3 m can be reasonably assumed for the Differential GPS measurements. The spatial distribution and the statistical behavior of the corresponding error are displayed Fig. 5.21a and Fig. 21b, respectively. As expected, an offset in the estimation of height is introduced. Concerning the proportionality to the topography profiles that the error seems to show, this effect is due to the double interpolation step required to project the UTM information to the radar reference and then again to UTM reference system. These numerical errors are generated by the interpolation of the non-regular distribution of points on a regular grid. Yet, they are negligible with respect to the offset component. As the error histogram of Fig. 5.17 is zero-mean, any significant error component due to platform height uncertainty can be excluded. In all these evidences, it is possible to state that the overall error characterizing the real DEM retrieved in Section 5.4.4 is not related to the incorrect estimation of the observation geometry parameters. Even if an orientation angle uncertainty $\Delta\xi$ cannot be excluded, the result of Fig. 5.19b is likely to overestimate this component. Contrarily, the main contributions are likely to come from the phase

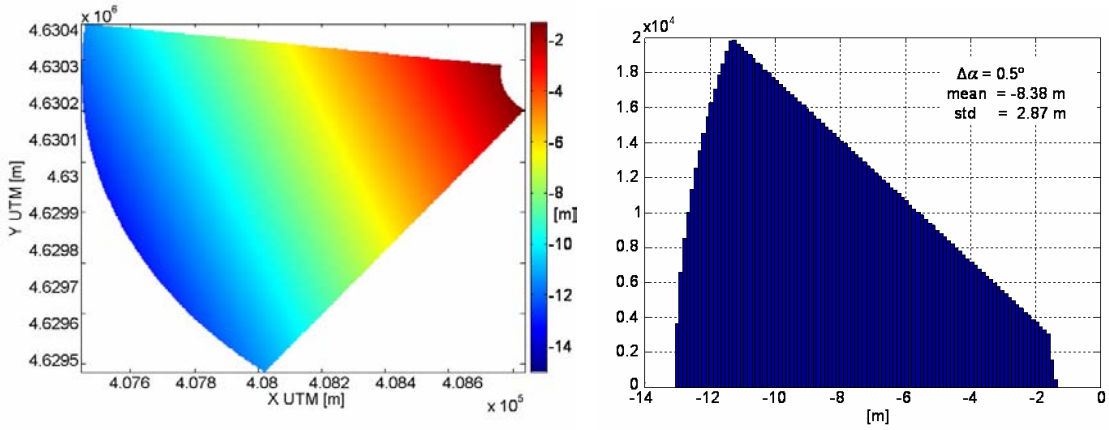

(a) (b)

Fig. 20: 2D distribution (a) and histogram (b) of the topographic error obtained by geocoding the synthetic interferogram ϕ_{syn} and assuming a maximum uncertainty $\Delta\alpha$ equal to 0.5º of the baseline inclination.

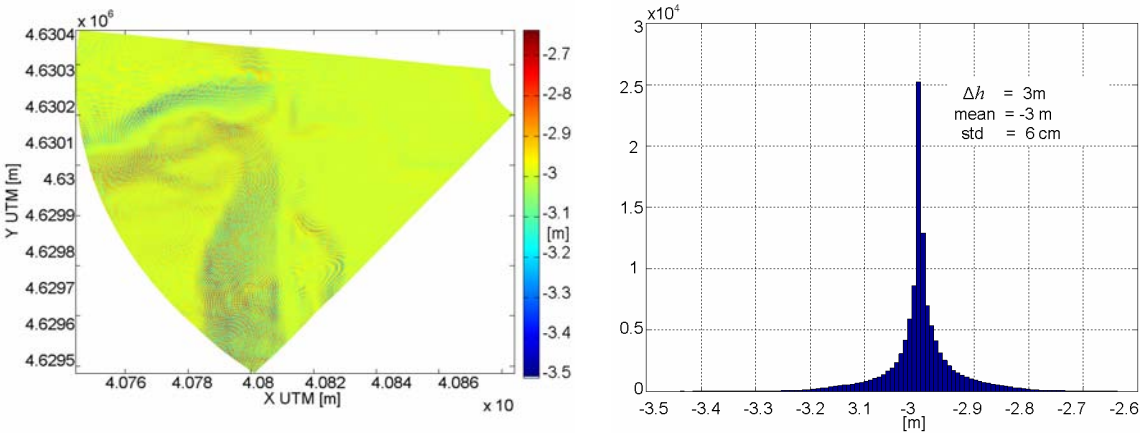

(a) (b)

Fig. 21: 2D distribution (a) and histogram of the topographic error obtained by geocoding the synthetic interferogram ϕ_{syn} assuming a maximum uncertainty Δh equal to 3m of the platform elevation.

unwrapping procedure, which in some part of the scene becomes critical due shadowing effects and to the presence of man-made structure that are not taken into account by the ground-truth DTM. Indeed, better results are expected to be carried out in case a different scenario is observed. However, the accuracy of the DEM retrieved in Section 5.5.4 demonstrates the reliability of both the geocoding technique here proposed and the quality of UPC gbSAR interferometric measurements.

Finally, it must be pointed out that once a mathematical relation between the points of an external or retrieved DEM and the pixels of radar plane are established, any kind of information available in radar coordinates can be easily geocoded. To do this, the information imaged on the evenly distributed grid of pixels in radar coordinates is simply interpolated onto the unevenly distributed grid obtained from back-geocoding procedure. The geocoded reflectivity image of Sallent scenario overlapped to a GoogleEarth's orhophoto is shown as example in Fig. 5.22.

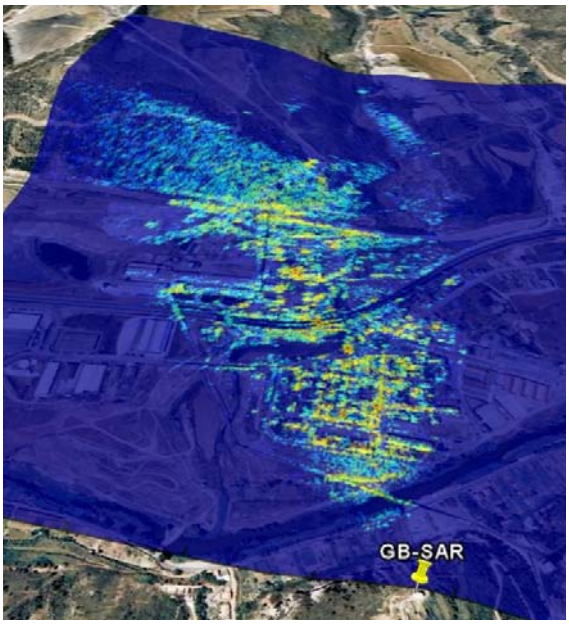

Fig. 5.22: Geocoded reflectivity image (*hh* polarization) of the Sallent test-site overlapped to GoogleEarth© 's orthophoto.

5.5 gbSAR differential Interferometry

The interferometric formulation which has been presented in the previous sections mainly deals with the estimation of topographic information. Its basic assumption is the temporal and geometrical stability of the scenario when it is observed from two slightly different positions; its rationale is the sensitivity of the interferometric phase to spatial elevation changes as an effect of baseline modulation. If longer time-spans separate the *master* and *slave* acquisitions, the possibility that modifications occur in the scenario must be taken into account. In these cases, an additional contribution is introduced in Eq. 5.10 as follows

$$\Delta\phi = \Delta\phi_{flat-earth} + \Delta\phi_{topography} + \Delta\phi_{def} \,. \tag{5.41}$$

where the new term $\Delta\phi_{def}$ accounts for the phase variation introduced by a relative movement between two adjacent pixels. In the case the scattering properties of the linked pixels do not change, $\Delta\phi_{def}$ may be directly converted in terms of LOS displacement Δr by

$$\Delta r_{def} = \frac{\lambda}{4\pi}\Delta\phi_{def} \,. \tag{5.42}$$

The accuracy of this new component is in the order of a fraction of wavelength, that is much higher than the accuracy of height estimation given by Eq. 5.14. When the main concern is the estimate of the deformation process affecting the area under observation, topographic terms in Eq. 5.42 turn out to be useless and must be eliminated. In this case, the SAR interferometry is commonly renamed differential SAR Interferometry (DInSAR). The observation of the same area from exactly the same position automatically makes the baseline B in Fig. 5.2 equal to zero and the

topographic contribution to the interferometric phase null. It is easy to understand that in the case of air- and space-borne SAR sensors, this is unfeasible. Flight and orbit trajectories can be very similar, but never identical. This means that topographic phase components cannot be neglected in Eq. 5.42 and must be carefully compensated for. For their estimation and successive correction, an external DEM or and third acquisition is generally employed [Carrasco,98]. Without entering into details, the typical approach deals with estimating first the topography using an external DEM or two SAR acquisitions whose time-span is short enough to assure that no deformation has occurred within the scene. After being scaled to the proper baseline value, the topographic phase is removed from the interferogram and the displacement information is extracted from the residual term. In this process, DEM errors, uncertainties in the description of sensor's trajectory, and residual motion-compensation errors, directly degrade the quality of the retrieved displacements. Contrarily, when a gbSAR sensor is employed for the monitoring activity, different constraints arise. The system performs a SSA construction mechanically. Being the radar mounted on a sled moving along a linear unit, repeated scans are obtained by illuminating the scenario from exactly the same cross-range positions. It follows that the zero-baseline interferometric phase is insensitive to scene topography by construction and the error sources characterizing air- and space-borne SAR sensors are not present. At the same time, Eq. 5.20 is unfit to describe the acquisitions' correlation: coregistration errors and volumetric decorrelation effects become negligible. A new expression for the zero-baseline interferometric coherence (or differential coherence) γ_{0B} tailored to gbSAR systems is then

$$\gamma_{0B} = \gamma_t \gamma_{atm} \tag{5.43}$$

where γ_t and γ_{atm} account for the target's temporal decorrelation due to scatterer changes and propagation medium changes in between the two scans, respectively. Note that γ_{atm} is rarely mentioned in classical DInSAR formulations. The reason is twofold. On the one hand, the time required for the observation of a target during the aperture synthesis is in the order of few seconds. During this time, the propagation properties of the target-to-sensor atmospheric layers are reasonably constant so that they affect the backscattered echoes the same way. On the one hand, the observation geometry of flying platforms makes the changes of the propagation medium turn into a very low spatial-frequency component (some kilometers scale). It follows that the atmospheric modifications in DInSAR data sets mainly introduce phase offsets which almost never yield interferometric coherence decreases.

The situation changes significantly in gbSAR measurements. The different acquisition geometry makes the propagation effects generate more complex artefacts. Besides, the time required for the scanning process is much higher, in the order of a few minutes. The medium time-stationary

hypothesis might fail under atmospheric turbulent conditions and a non-negligible decorrelation due to propagation changes might affect the zero-baseline coherence [Pipia,08]. Remanding to Chapter 6 for a detailed analysis of the atmospheric artefact affecting *0B* gbSAR acquisitions, a simplified factorization of the gbSAR differential phase ϕ_{0B} becomes

$$\phi_{0B} = \phi_{def} + \phi_{atm} + \phi_{t,i} \qquad i \in \{hh, hv, vv\} \tag{5.44}$$

where ϕ_{def} accounts for target's displacement, ϕ_{atm} for atmosphere instability and $\phi_{t,i}$ for the scatterer's temporal decorrelation in the *i* polarization channel. It is worth pointing out that the first two quantities are polarization-independent: the first one is generated by a change in the position of the two adjacent targets but it does not assume any scattering property variation; the second one is a function of the propagation properties of the medium, which affects the different polarization channel the same way if rain events are excluded [Bringi,01].

5.6 Summary

In this Chapter, the classical formulation of SAR interferometry for the estimation of the illuminated scenario's topography has been adapted to the short-synthetic aperture case. In gBSAR observation geometry, the normal baseline is not a constant term but becomes a function of targets' squint position. Accordingly, customized procedures keeping into account the targets' squint variation within the scene has been formulated for the retrieval of Digital Elevation Models (DEM) from gbSAR interferometric acquisitions and gbSAR images geocoding. The techniques available in the literature essentially split the problems into two main steps. Firstly, the interferometric phase in the radar reference system is transformed into height through geometrical approximations. Secondly, the topography information is mapped onto a geodetic reference system to obtain the final geocoded DEM. The main limitation of these approaches is that they do not account for the high variety of observation geometries that the use of a terrestrial platform might entail. The geometrical approximations that are applied to work out a linear relationship between interferometric phase and height are consistent with air- and space-borne SAR sensors but might reveal inappropriate to describe ground-based observations. For this reason, in the framework of this PhD dissertation a different strategy avoiding any geometrical simplifications and, hence, suitable to any type of monitoring condition, has been looked into. The rationale of the method is the definition of a non-linear equations system relating the absolute position of the master and slave antennas (known terms) and of the target (unknown term) to the interferometric phase and the targets' aspect angle. The employment of an iterative algorithm makes it possible to estimate the location of the targets at once and to obtain the geocoded DEM through simple geodetic coordinate transformation. The technique has been assessed using real data and very promising

results have been shown. The standard deviation of the retrieved DEM is in the order of the results obtained by the alternative two-step geocoding techniques [Martinez,08] when a set of 32 interferograms is employed for the estimation of the interferometric phase. However, the presence of an urban environment within the scene is supposed to underestimate the real performance of the technique. A more suitable scenario is now required in order to assess the real potentials of the UPC sensor for DEM retrieval purposes.

Chapter 6

Atmospheric Artefacts in Zero-Baseline gbSAR Measurements

One of the benefits of ground-based SAR sensors is the opportunity to gather zero-baseline repeated scans for differential measurements. Thanks to the employment of a terrestrial platform, the revisiting time is not an issue for this type of sensors. For the same reason, many terms usually affecting the differential coherence such as coregistration approximations, baseline construction uncertainties and DEM removal residual errors become here negligible. This has been shown in Chapter 5, where the main factors affecting the coherence between two zero-baseline gbSAR acquisitions have been reduced to two: the target temporal decorrelation $(1-\gamma_t)$ and the atmosphere decorrelation $(1-\gamma_{atm})$. In fact, the short range distance generally covered by gbSAR systems and the high time-average performed by the CW radar at each position of the rail make it possible to neglect the noise decorrelation $(1-\gamma_{th})$. In this Chapter, the way the atmospheric changes affect the gbSAR differential coherence and phase is analyzed in detail. First, the simplest condition of propagation through a homogeneous medium is discussed. The main properties of the atmospheric artefacts which are usually observed in zero-baseline data sets are described. Then, a linear propagation model is introduced to work out a coherence-based technique for the atmospheric phase artefact compensation. In the end, some examples of unpredictable artefacts arising from atmosphere turbulent behaviors are shown. The need to reduce as much as possible the acquisition time in order to guarantee the reliability of the information retrieved from gbSAR acquisitions is finally emphasized.

6.1 Refractive index in the troposphere medium

The *troposphere* is the lower part of the atmosphere, extending from ground level to an altitude of about 9 km at the earth's poles and 17 km at the equator. It is in the troposphere that changes of

temperature, pressure and humidity, as well as clouds and rain, influence the radiowaves propagation. Ionization of atmospheric gases becomes appreciable at heights of 60 to 1000 km, i.e., in the *ionosphere*. Being the scope of this Chapter to describe the propagation of electromagnetic waves in the frame of ground-based SAR observations, the analysis is limited to the *troposphere* in absence of any rain event. Under this hypothesis, the medium can be assumed insensitive to the polarization state of the propagating wave at X-band [Bringi,01]. In Chapter 2, the solution of the Maxwell's equations in the case of *free-source* and lossless homogeneous isotropic medium has led to the concept of electromagnetic plane waves. According to Eq. 2.1-3, the propagation properties of these waves is described by the following analytical signal

$$\vec{E} = \vec{E}_0 e^{-j\vec{k}\cdot\vec{r}}. \tag{6.1}$$

where $\vec{E}$ is the electrical field. It is worth reminding that the vector $\vec{k}$ defines the propagation direction of the plane wave and its modulus fulfills the equation

$$k = \omega\sqrt{\varepsilon_0\varepsilon_r\mu_0\mu_r} \tag{6.2}$$

where ω is the angular frequency, ε_0 and μ_0 are the electric permittivity and magnetic permeability in free space, respectively, while ε_r and μ_r keep into account the specific properties of the medium. As the troposphere is not a magnetic material, $\mu_r = 1$ and Eq. 6.2 may be hence rewritten as

$$k = k_0\sqrt{\varepsilon_r} = k_0 n \tag{6.3}$$

where k_0 is called *wavenumber* in the vacuum whereas n is usually referred to as medium refractive index. In the case the medium is the troposphere, an accepted semi-empirical formula relates n to the temperature T(K), the pressure P(mb) and water vapor pressure w_p(mb) as follows [Bye,89]

$$n = 1 + 10^{-6}\left(77.6\frac{P}{T} + 3.73\frac{10^5 w_p}{T^2}\right). \tag{6.4}$$

While pressure and temperature are directly measurable, the water pressure is usually derived from the relative humidity (H). Defining the maximum possible (saturated) vapor pressure at the temperature T as w_{ps}, w_p it given by

$$w_p = w_{ps}H = 6.11e^{\left(19.7\frac{T-273}{T-2.273}\right)}H. \tag{6.5}$$

As it is demonstrated in [Hall,79], Eq. 6.4 is correct within 0.5% for atmospheric pressures between 200 and 1100 *mb*, air temperatures between 240 and 310 K, water vapor pressures less than 30 *mb,* and for radio frequencies less than 30 GHz. Changes in refractive index of only a

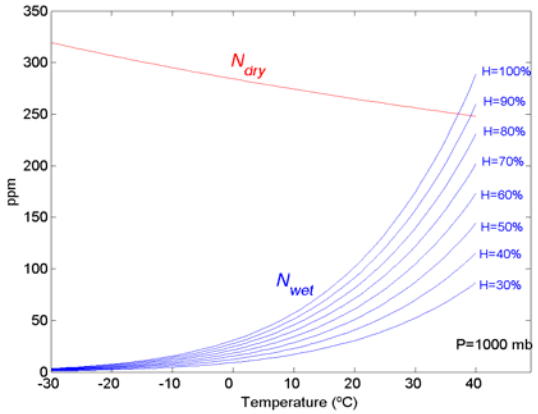

Fig. 6.1: Comparison between N_{dry} and N_{wet} as a function of temperature T and relative humidity H for a fixed value of pressure P (1000 mb).

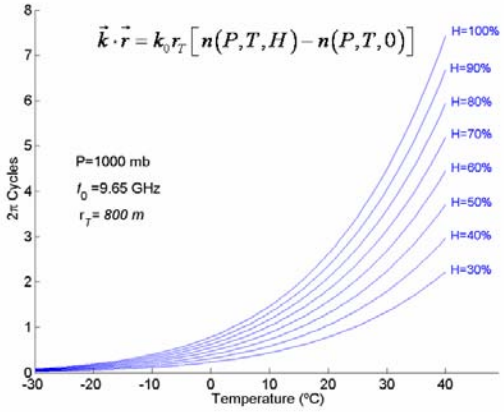

Fig. 6.2: Phase variations (2π cycles) at $r_T = 800$ induced by the changes of refractive index n described in Fig. 6.1 at X-band.

few parts per million have an important effect on electromagnetic wave propagation. For this reason, it is usual to work in parts per million (ppm) by redefining the quantity within parenthesis in Eq. 6.4 as

$$N = (n-1)10^{-6} = N_{dry} + N_{wet} \,. \tag{6.6}$$

where the two terms N_{wet} and N_{dry} strictly depend on the temperature T but separate the effect of the relative humidity. For example, at very low temperature N_{wet} becomes very small even for saturated air and N is almost independent of H. As the temperature rises, there is a slow decrease of N_{dry} but a rapid increase of N_{wet}. The behavior of the two components as a function of T for different value of H is shown in Fig. 6.1. The corresponding variations of the phase term in Eq. 6.1 with respect to the case $H = 0$ are plotted in Fig. 6.2 for r equal to 800 m. As the scalar quantities T, P and H may vary both in space and time, the refractive index n in absence of rain events may be expressed as a scalar space-time function as follows

$$n = n\left(T(\vec{r},t), P(\vec{r},t), H(\vec{r},t)\right) = n(\vec{r},t) \,. \tag{6.7}$$

The phase term of Eq. 6.1 in the case of propagation through the troposphere must be hence considered as the result of the integration process of n along the traveling path. The propagation phase of the monochromatic wave in the far-field zone at the time t should be hence described as

$$\vec{k} \cdot \vec{r} = k_0 \int n\left(\vec{r},t\right) d\vec{r} \tag{6.8}$$

where r is the radial distance from the sources' position. Careful studies carried out in [Hall,66] showed that the refractive index n decreases along the first kilometers of troposphere with a median gradient of about -40 ppm/km, whereas variations in the horizontal are negligible by

(a) (b)

Fig. 6.3: Pictures of the Collserola test-site, in the outskirts of Barcelona, from the satellite (a) and the UPC sensor's location (b) on the roof of the Signal Theory and Communication (TSC) department.

comparison. This result was assessed in most temperate regions of the planet [Bye,89]. By denoting with h the height above the ground, the distribution of N through the whole troposphere is hence modeled as a multi-layer medium and its decrease is described as

$$N(h,t) = N_s(t)e^{-\frac{h}{h_0}} \tag{6.9}$$

where N_s is the surface value of the refractive index at h_0.

6.2 Atmospheric artefacts description in gbSAR acquisitions

In the previous Chapters, it has been pointed out that the dimensions of the area that can be monitored by a ground-based SAR system are strictly related to its location. Since it rarely exceeds few squared kilometers and few hundred meters in height, the portion of troposphere involved in the measurement can be reasonably assumed spatially homogeneous. This means that the value of n depends on the time the measurement is performed but its variations with h may be neglected. It is worth noting that this hypothesis must be fulfilled not just during the few milliseconds the wave needs to go from the sensor to the target and back[1], but also during the synthetic aperture construction, which might take up to several minutes. For this hypothesis to hold, the modifications introduced for the description of plane wave propagation through the troposphere may be now extended to gbSAR acquisitions. Assuming that the transmitted wave illuminating a generic target T at the range distance r and the back-scattered wave at the receiving antenna are locally plane, the calibrated scattering matrix given by the gbSAR system may be expressed as

[1] Note that the round-trip delay for a maximum range distance of 3 km is in the order of tens of *microseconds* (μs). The few milliseconds take into account the time-averaging performed by the CW radar system usually employed by a gbSAR sensor.

$$[S'] = \begin{bmatrix} S'_{hh} & S'_{hv} \\ S'_{hv} & S'_{vv} \end{bmatrix} = \begin{bmatrix} S_{hh} & S_{hv} \\ S_{hv} & S_{vv} \end{bmatrix} e^{-j2k_0 \int n(\bar{r},t) d\bar{r}} . \quad (6.10)$$

and, invoking the spatial homogeneity of the medium, Eq. 6.10 simplifies to

$$[S'] = \begin{bmatrix} S_{hh} & S_{hv} \\ S_{hv} & S_{vv} \end{bmatrix} e^{-j2k_0 r n(t)} . \quad (6.11)$$

where $n(t)$ is the mean value of the refractive index from the sources' location to the distance r at the time t. At this point, let T be observed at the time instants t_1 and t_2 under different homogenous atmospheric conditions. If the target is motionless ($\Delta r = 0$ in Eq. 5.42) and its scattering behavior does not change between the two acquisitions ($\gamma_t = 1$ in Eq.5.43), the zero-baseline interferometric phase becomes

$$\phi_{0B} = \phi_{atm} = 2k_0 r \left(n(t_2) - n(t_1) \right) . \quad (6.12)$$

It can be easily noticed that ϕ_{0B} increases linearly with range, independently of the polarization of the EM wave. Moreover, the phase difference is proportional to the carrier frequency in such a way that larger shifts are obtained for higher frequencies. Owing to the different properties of near- and far-range in gbSAR images and to the high frequency generally employed (C-band [Noferini,07], X-band [Aguasca,04], K-band [Antonello,04]), these effects cannot be neglected. In order to demonstrate the need to compensate for the atmospheric phase artefacts before retrieving any meaningful differential gbSAR information, the results of a one-dimensional measurements campaign held in the test-site of Collserola are first presented. The heterogeneity of the scenario has been already stressed in Section 4.7.1: it contains low– to medium-density vegetated, forested and urban areas. From the satellite picture of Fig. 6.3a and in the photo of Fig. 6.3b, it can be observed that a pine covered area and medium vegetated zone are detectable in the top-left corner of the hill slope, whereas urban structures are sparsely distributed at short ranges. Despite the apparent proximity, more than 1 km separates the hill and the sensor and an entire district of the city and a highway stay in between. The gbSAR sensor acquired a raw data line at X-band every 2.5 minutes from 10 am on 15th to 8 am 17th June 2005 at a fixed position of the linear unit. Each line was obtained using a time-average factor equal to 1024, range-compressed and finally stored. It is worth reminding that each point of a range-compressed profile corresponds to the coherent superimposition of the signals backscattered from all the illuminated targets located at the same range distance from the sensor. Afterwards, the zero-baseline coherence evolution was estimated by Eq. 5.15 using the first acquisition as master and all the successive ones as slaves.

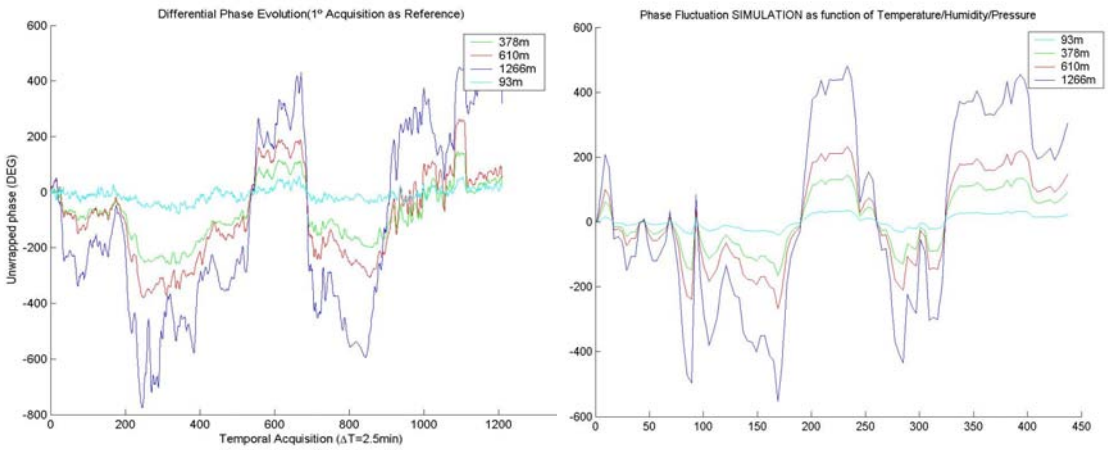

(a) (b)

Fig. 6.4: Temporal evolution of the real (a) and simulated (b) zero-baseline interferometric phase concerning 4 high-coherence pixels ($\gamma \geq 0.8$) selected within the 1D dataset collection.

The study of the 1D profiles made it possible to detect four high-coherence peaks at different range distance: the time evolution of the corresponding differential phase is shown in Fig. 6.4a. The cyan line describes the behavior of the closest target, about 100 m far from the sensor; the blue line account for the most distant one, at 1266 m. An unwrapping phase step has been also introduced for the far-off targets. The linear dependence of phase-shifts' amplitude and targets' range distance is clearly visible.

During the whole experiment, temperature, pressure and relative humidity were measured every ten minutes. The atmospheric parameters were then substituted in Eq. 6.4 and Eq. 6.5 for the estimation of the refractive index *n*. The differential phase variations induced by *n* changes at the four range distances specified in Fig. 6.4a was then reproduced using a gbSAR simulator [Pipia,05a]. The simulations were obtained under the assumption of propagation through a homogeneous medium. The result is shown in Fig. 6.4b. A rough comparison of the two images points out a strong similarity between simulated and real phase profiles in terms of shape of the curves, magnitude of the differential phase fluctuations and proportionality to the range distance. Since no deformation took place within the test-site during the observations, the observed variations are ascribed to changes of the troposphere medium.

6.3 One-dimensional atmospheric artefacts compensation technique

After having demonstrated the relation between atmospheric changes and differential phase fluctuations in the 1D case, the case of 2D focused gbSAR images is here analyzed. For this purpose, a new measurement campaign was carried out from June 27th to July 3rd 2005: zero-

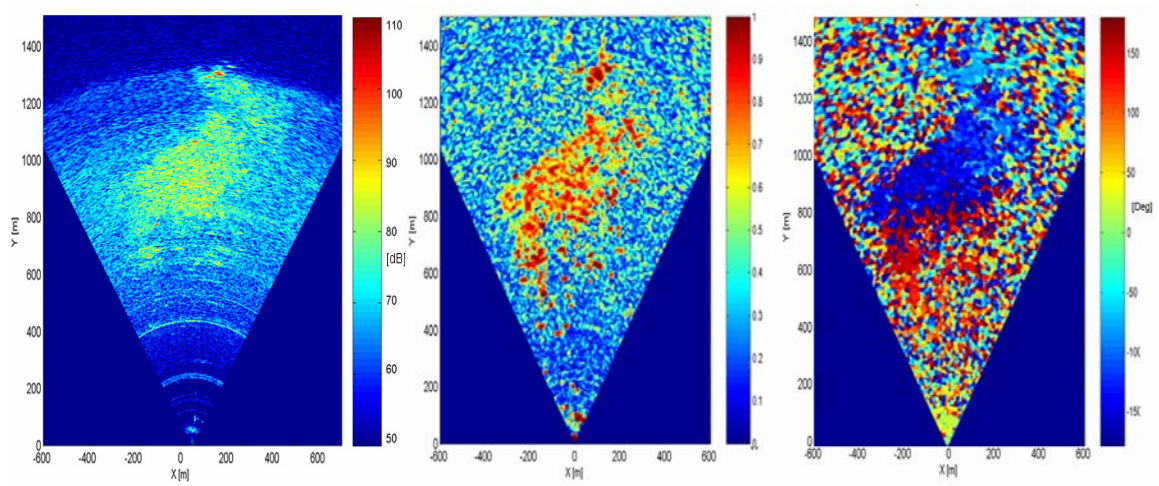

(a) (b) (c)

Figs. 6.5: Examples of UPC gbSAR reflectivity (a), zero-baseline coherence (b) and differential phase (c) concerning the test area of Collserola in the *hh* polarization. The time delay between the two differential acquisitions is about 6 hours.

baseline polarimetric gbSAR data sets of Collserola were acquired during almost one week with a time sampling step of about 90 minutes. An example of the test-site reflectivity image taken at 11 a.m on June 29th is given in Fig. 6.5a whereas Fig. 6.5b and Fig. 6.5c show the zero-baseline coherence and the corresponding differential phase in the *hh* polarization of two data sets acquired on the same day with a time separation of 6 hours. The limitation introduced by the radiation pattern of the antennas as well as the strong angular geometry due to the short synthetic aperture is easily detectable in the three images.

According to Section 3.3.2.2, the SSA geometry makes it necessary to introduce a new concept of range dimension with respect to air- and space-borne platforms, which becomes the distance between the target and the center of the synthetic aperture. Taking into account this fact, the phase-ramp in Fig. 6.5c provides an example of the typical zero-baseline atmospheric artefact induced by a variation of n when the troposphere fulfills the spatial homogeneity hypothesis.

In order to compensate for the undesired phase contribution, the method proposed in [Noferini,05] was first considered. Its rationale is the detection of two stable points for the solution of a linear equations system describing the atmospheric artefact. Yet, this approach presented two main limitations. The first one is related to the criterion employed for the selection of the two trustworthy pixels, which deals with the analysis of the amplitude stability [Ferretti,01] and requires that a collection of at least 30 acquisitions be at disposal. In the case just a few data sets are available, the estimation turns out to be unreliable and the method cannot be applied. The second problem dealt with the properties of the Collserola test-site. The detection of reference

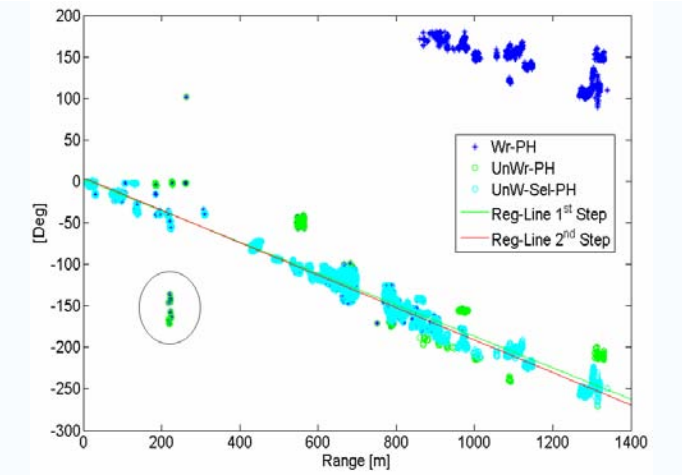

Fig. 6.6: Distribution of the pixels' wrapped (blue) and unwrapped (green/cyan) differential phase of high-coherent pixels ($\gamma_{TH} = 0.97$) in Collserola projected on a single range-cut. The red and green lines are the 1st and 2nd (without outliers) linear-fitting tests, respectively.

Regression Coefficients : $\hat{\phi}(r) = a_1 r + a_0$

	a_1	a_0
HH	-3.29e-3	0.057
HV	-3.17e-3	0.069
VV	-3.20e-3	0.032

Table 6.1: Regression-line coefficients estimating the atmospheric phase artefact provided by *hh*, *hv* and vv polarization channels.

point scatterers that were close enough to avoid phase unwrapping but sufficiently far to estimate correctly the artefact model coefficients turned out to be troublesome, leading to poor results.

Accordingly, an alternative technique was worked out to cope with the removal of atmospheric artifacts from zero-baseline gbSAR interferograms. Its rationale is the selection of reliable pixels through a coherence-based approach. It is worth pointing out that, under the hypothesis of propagation through a homogeneous troposphere, the atmospheric artefact essentially introduces a low-spatial frequency component in the differential interferogram. That is, ϕ_{atm} is constant within the area employed to estimate the coherence γ (see Section 5.2) and it can be pull out of $E\{\cdot\}$. Then, it is possible to state that γ_{atm} in Eq. 5.43 is practically one. In the light of this reasoning, if a high-coherence threshold γ_{TH} is fixed, the condition $\gamma \geq \gamma_{TH}$ filters out the unreliable points corrupted by temporal decorrelation effects, i.e., pixels belonging to targets that modified their scattering properties between the two acquisitions, and selects just the stable targets. Besides, the homogeneity assumption makes the variation of refractive index Δn constant within the illuminated scene so that targets at the same range-distance are equally affected by atmospheric changes. It follows that, from a theoretical point of view, a single range-cut is sufficient for the estimation of the 2D phase ramp. The unwrapping step simplifies because it reduces to a one-dimensional problem and a linear-fitting procedure may be employed to estimate the unknown coefficients of the artefact. In practice, this approach is not efficient: the acquisition geometry of gbSAR sensors usually increases the shadowing effects and the number of useful pixels detectable in a single cut may be very low. If the pixels selected along the range cut are too few or they are

concentrated in a short range interval, the estimation turns out to be unreliable. A possible work-around to this eventuality is to order the high-coherence pixels of the whole image by their range distance and to project their differential phase onto a unique cut. This strategy offers several advantages: it provides more samples for additive noise suppression; it reduces the extension of areas masked by closer targets with respect to a single range-cut; finally, it turns out to be more robust than searching for the best range-cut. The result obtained by projecting the differential phase of pixels in Fig. 6.5b with a coherence value higher than 0.97 is shown in Fig. 6.6. The green and blue points represent the wrapped and unwrapped differential phase ordered along the range direction, respectively. In order to describe the atmospheric artefact, the distribution of points may be fit to the linear model

$$\hat{\phi}(r) = a_1 r + a_0 . \tag{6.13}$$

The two coefficients a_1 and a_0 can be calculated in the least square sense through the minimization of squared residuals sum

$$\varepsilon = \sum_{i=1}^{N_P} \left(\phi(r) - \hat{\phi}(r) \right)^2 \tag{6.14}$$

where N_P is the number of pixels fulfilling the coherence minimum threshold γ_{TH}. The regression line coefficients [Papolulis,84] are calculated by setting the gradient of ε to zero, as follows

$$\frac{\partial \varepsilon}{\partial a_0} = 0 \Rightarrow a_0 = \frac{1}{N_P} \sum_{i=1}^{N_P} \phi_i \tag{6.15}$$

$$\frac{\partial \varepsilon}{\partial a_1} = 0 \Rightarrow a_1 = \frac{\sum_{i=1}^{N_P} 2 r_i \left(\phi_i - a_0 \right)}{\sum_{i=1}^{N_P} 2 r_i^2} . \tag{6.16}$$

It can be easily observed that the behavior of the projected differential phase follows a linear trend, confirming that the homogeneous medium hypothesis is fulfilled. Yet, the presence of outlier pixels deviating from this tendency is worth being discussed. They correspond to man-made targets that have slightly changed their scattering behavior despite their high coherence value. For these pixels, an additional polarization-dependent phase term sums to the atmospheric phase artefact and Eq. 6.12 becomes

$$\phi_{0B,i} = \phi_{atm} + \phi_{t,i} \quad i = hh, hv, vv . \tag{6.17}$$

For instance, the points inside the black circle in Fig. 6.6 correspond to the backscattering from a

tower crane within the scenario that is likely to have varied its spatial alignment with respect to the gbSAR sensor between the two acquisitions. For atmospheric compensation purposes, they become outliers and must be discarded because their differential phase information is heavily corrupted by $\Delta\phi_{i,t}$. This filtering operation is performed through a two-steps procedure. All the pixels fulfilling the minimum coherence condition are first employed for a rough estimation of the regression line coefficients and, even more important, of the standard deviation of the fitting error, here denoted with σ_{mod}. Afterwards, the condition

$$\left|\phi_i - \hat{\phi}(r_i)\right| \leq \sigma_{\text{mod}} \tag{6.18}$$

is imposed to filter out high-coherence but phase-instable targets. A better description of the phase artefact is finally achieved by carrying out a second regression-line estimation using the remaining trustworthy pixels. In the example of Fig. 6.6, the pixels fulfilling Eq. 6.18 selected by have been plotted in cyan whereas the first and second line-fitting steps are described by the red and green lines, respectively. As it has been previously mentioned, troposphere is not an ionizing medium. Therefore, the propagation properties, and consequently the atmospheric phase artefacts, are expected to be independent of the polarization state of the traveling wave. As a proof, the coefficients of the linear model obtained using the different polarimetric channels are reported in Table 6.1. It can be noticed that the term a_1, which defines the gradient of the regression line, is almost constant: *hh* and *vv* estimate is practically identical whereas it slightly differs in the case of *hv* channel. This is due to the lower number of high coherent pixels at disposal for the cross-polarization line fitting test. Nevertheless, the result proves the atmospheric phase artefact independence of the polarization state of the propagating wave. Besides, it validates the employment of the channel providing the higher number of coherent pixels for the compensation of the whole polarimetric data set. On the contrary, the differences among the terms a_0 are due to the difference length of the cables used for the PolSAR measurements and are compensated when data calibration is performed (see Section 4.5). Finally, the atmosphere-compensated polarimetric differential interferograms $\Delta\phi_{ci}$ are obtained as

$$\phi_{ci}(r_i) = \phi_i(r_i) - \hat{\phi}(r_i) \tag{6.19}$$

where $i = hh, hv, vv$. As example, the interferograms obtained from the zero-baseline PolSAR data sets acquired on June 29th are displayed in Fig. 6.7a-f before and after applying the compensation technique. If the whole collection of acquisitions gathered during the one-week measurements

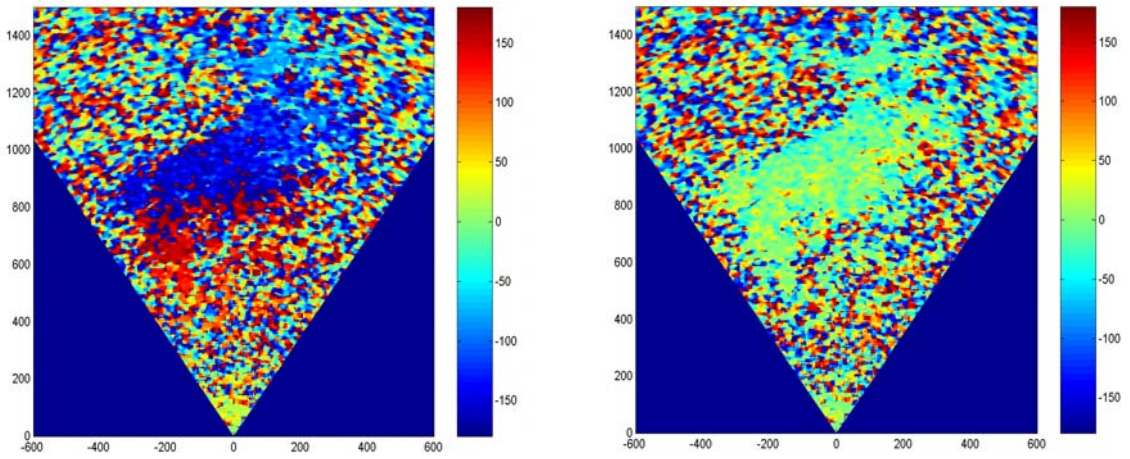

(a) Uncompensated *hh* Interferogram

(b) Compensated *hh* Interferogram

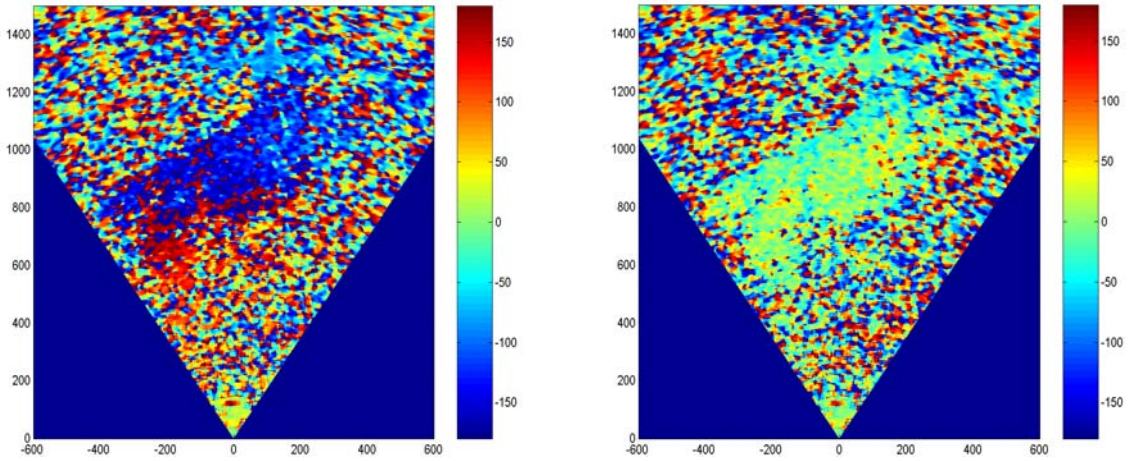

(c) Uncompensated *hv* Interferogram

(d) Compensated *hv* Interferogram

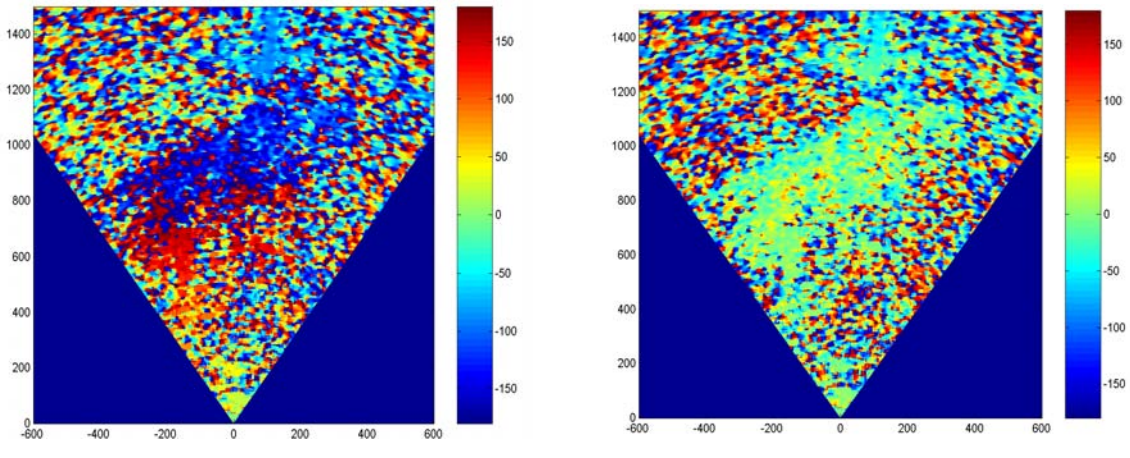

(e) Uncompensated *vv* Interferogram

(f) Compensated *vv* Interferogram

Fig. 6.7: Polarimetric zero-baseline interferometric phase before and after compensating for the atmospheric artefact: $\hat{\phi}$ has been estimated using the *hh* polarization and substituted in Eq. 6.19 for the compensation of the whole polarimetric data set. The differential coherence has been estimated by an averaging boxcar of 10×10 pixels. Yet, no significant variations have been observed in $\hat{\phi}$ estimation for window size up to 30×30.

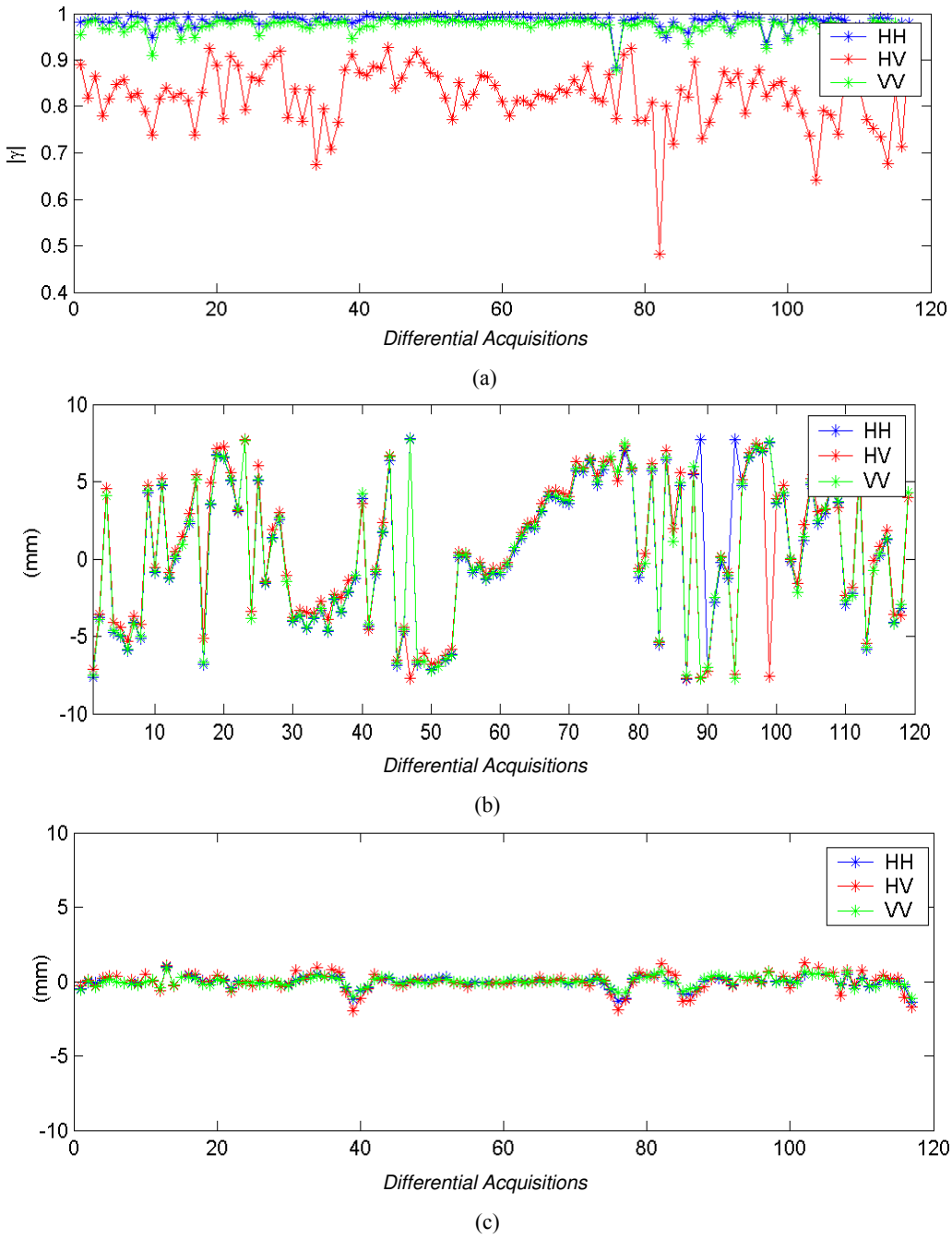

Fig. 6.8: Temporal evolution of the polarimetric differential coherence (a) and radial displacement before (b) and after (c) the atmospheric phase artefacts compensation concerning an urban pixel within the scenario portrayed in Fig. 6.3b. The time sampling-step is approximately 90 minutes.

campaign is analyzed, the differential phase presents very high fluctuations that can be only related to the changes of the index *n*. This is shown by the plots in Fig. 6.8, which describe the behavior of an urban target selected within the illuminated area. The time-evolution of the polarimetric differential coherences is shown in Fig. 6.8a; the information in terms of equivalent radial displacement (see Eq. 5.42) of the uncompensated and compensated differential phases is displayed in Fig. 6.8b and 6.8c, respectively. The vertical polarization has been used for the

estimation of $\hat{\phi}$. Again, the result proves that the phase distortion introduced by *n* variations affects the same way all the different terms of the scattering matrix [*S*]. Besides, it corroborates the meaningfulness of employing the polarization channel providing the higher stability for the compensation of the whole polarimetric interferometric data set.

6.3.1 Compensation technique assessment

In order to assess the compensation technique described in the previous Section, the response of reference targets is here examined. Active and passive calibrators were located within the Collserola scenario at different cross-range positions about 1km far from the sensor. A parc P1 in the Vertical-Vertical configuration [Freeman,90] was employed as motionless control point for differential polarimetric monitoring activity. A second parc P2, in this case in the Vertical-Horizontal configuration, was instead used to simulate a real displacement: the device was mounted on a micrometric positioner and moved during the experiment. To obtain an equal answer in the four polarimetric channels, the two parcs were 45º tilted with respect to the radar line of sight (*LOS*). The corresponding theoretical scattering matrices are given by

$$[S_{P1}] = \begin{bmatrix} 0 & 0 \\ 0 & 1 \end{bmatrix} \Rightarrow [S_{P1}^{45^\circ}] = \frac{1}{2}\begin{bmatrix} 1 & 1 \\ 1 & 1 \end{bmatrix} \tag{6.20}$$

$$[S_{P2}] = \begin{bmatrix} 0 & 0 \\ 1 & 0 \end{bmatrix} \Rightarrow [S_{P2}^{45^\circ}] = \frac{1}{2}\begin{bmatrix} -1 & -1 \\ 1 & 1 \end{bmatrix}. \tag{6.21}$$

A set of 16 images was collected in approximately of 6 hours. During this perod, the temperature fluctuation was about 4ºC around a mean value of 21ºC, whereas the maximum variation of relative humidity was 15% (min 44%- max 59%). The time-evolution of the zero-baseline interferometric phase concerning the two reference points has been calculated by fixing the first data set as master and all the successive as slaves. The plots in Fig. 6.9 show the behavior of P1 in terms of radial displacement before and after the artefacts removal. In this case, the *hh* polarization has been selected for the phase ramp estimation, proving again that the phase distortion introduced by *n* variations affects the different terms of [*S*] the same way. The last experiment presented in this section deals with the retrieval of the time position sequence of the Parc P2. Although the 45º orientation of P2 with respect to the radar line of sight guarantees a significant answer in all the polarimetric channels, for the sake of clarity just the *vv* channel has been considered. The retrieved profile is plotted in Fig. 6.10 versus the real sequence of displacements performed with high

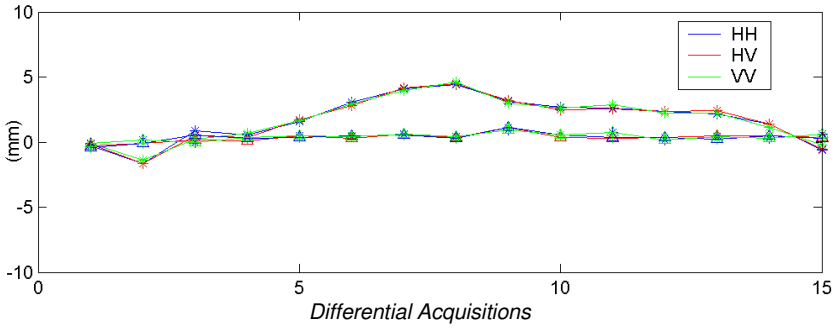

Fig. 6.9: Time evolution of the polarimetric differential phase of the 45º-tilted Parc P1 before (*) and after (Δ) the atmospheric artefacts compensation using the 1D linear-fitting technique.

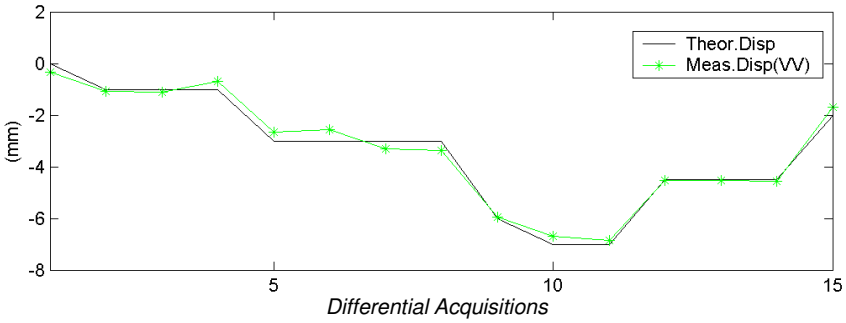

Fig. 6.10: Real and estimated sequences of displacements characterizing the 45º-tilted Parc P2 retrieved after compensating for the atmospheric phase artefacts using the 1D linear-fitting technique.

precision using the micrometric positioner. Despite only one polarimetric zero-baseline data set was collected for each position of P2, the two plots match almost perfectly. It must be taken into account that the response of P2 cannot be considered as stable as a corner reflector due to its active nature [Freeman,90] and to small fluctuations of the amplification process. The movement estimation is expected to be further reduced if more acquisitions are gathered and a temporal filtering is applied. Yet, the experiment provides evidence that a phase correction is necessary to retrieve displacement profiles with millimetric precision even when the atmosphere is subjected to slight changes.

6.4 Two-dimensional and spectral atmospheric artefacts compensation techniques

Two alternative coherence-based strategies have been also looked into for the estimation of the atmospheric phase artefacts affecting zero-baseline gbSAR acquisitions. The first one deals with unwrapping the 2D differential interferogram before applying the line-fitting test. Although in the optimal case it leads to almost identical results, this technique turns out to be less robust than the 1D solution described in Section 6.3. The reason is that the differential coherence of a scenario generally decreases at X-Band (or at higher frequency) even a after few hours. The interferogram

obtained by filtering out the low coherence pixels often reduces to a sparse matrix of points, which constitute a critical condition for any 2D unwrapping algorithm [Ghiglia,98]. On the contrary, this problem is mitigated by the 1D approach: the projection of the whole information onto a one-dimensional space makes it possible to fill up the possible shadowed areas arising in the 2D approach. The second strategy is based on the spectral analysis of the atmospheric phase artefacts [Pipia,06]. From a spectral point of view, the variation of the propagation refractive index n introduces a very-low frequency tone in the two-dimensional interferogram (Fig. 6.5c). The spatial resolution of gbSAR sensors and the limited size of the observed area prevent from estimating correctly the value of the atmospheric carrier by means of DFT analysis.

A way to overcome the constraints of classical spectral analysis is to employed the two-dimensional Chirp-Z transform (CZT) [Proakis,98]. The basic idea is to move along a spiral contour instead of using the unitary circle of FFT and to linearly vary the basis frequency in arbitrarily small steps. This makes it possible to compute the spectrum component with any desired resolution and hence to zoom on the desired spectral interval. Details about the mathematical formulation of CTZ and its digital implementation can be found in [Proakis,98]. Since very low frequency components are expected to be caused by n changes, this technique is theoretically capable of estimating with high precision the atmospheric artefacts. Yet, two conditions must be guaranteed. Firstly, a sufficiently wide high-coherence homogeneous motionless area is required to effectively apply the CZT. Depending on the scenario and the time span between acquisitions, detecting this type of distributed target might reveal troublesome. Secondly, the radial symmetry of the atmospheric phase ramp prevents the CZT from estimating correctly the 2D spatial carrier on a grid of Cartesian evenly-spaced points. In fact, the 2D CZT is implemented via two orthogonal 1D transforms: any spectral component is then expressed as a combination of orthogonal plane wave component, i.e., k_x and k_y. In the case of a pure radial function, which usually describes gbSAR atmospheric artefact under homogeneous medium assumption, the approximation

$$e^{jk_{atm}\sqrt{x^2+y^2}} = e^{jk_{atm}r} \approx e^{j\hat{k}_x x + j\hat{k}_y y} \tag{6.22}$$

leads to an incorrect estimation of the range phase-ramp. Accordingly, gbSAR acquisitions must be focused on a polar grid of points to successfully employ the CZT-based technique. As example, the result obtained for the Parcs P1 and P2 using the spectral estimation is displayed in Fig. 6.11 and Fig. 6.12, respectively. Although a good agreement with the profiles of Fig. 6.9 and Fig. 6.11

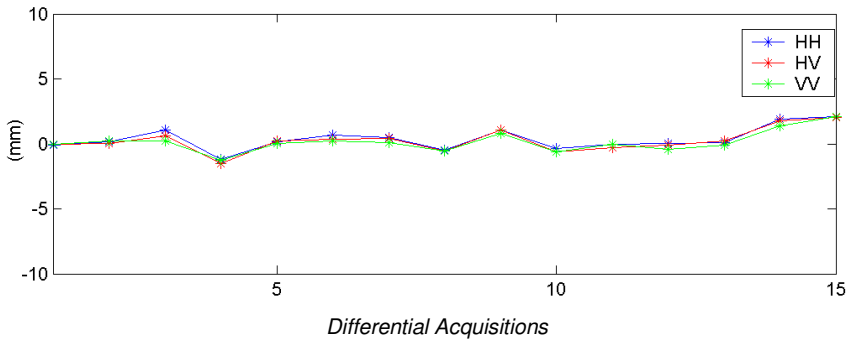

Fig. 6.11: Time evolution of the polarimetric differential phase of the 45º-tilted Parc P1 after the atmospheric artefacts compensation using the CZT transform.

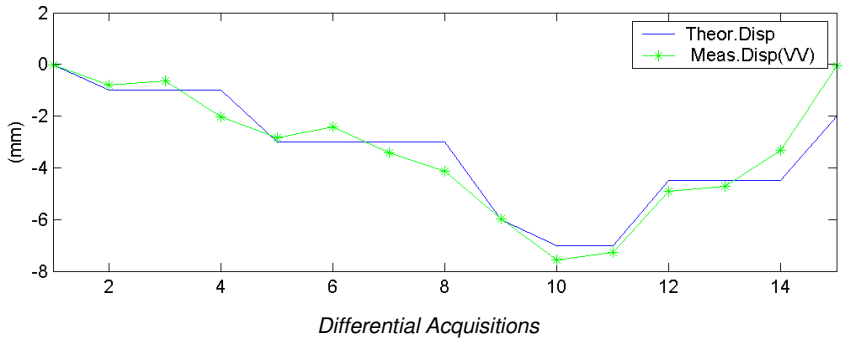

Fig. 6.12: Real and estimated sequences of displacements characterizing the 45º-tilted Parc P2 retrieved after compensating for the atmospheric phase artefacts using the CZT transform.

is detectable in both cases, the spectral technique turns out to be less efficient than the 1D method. This result, which apparently points out a higher reliability of the first method, must not to be related to a theoretical limitation of CZT approach but to the main features of the observed scene. In fact, the two techniques are based on a linear description of the atmospheric phenomenon and are expected to bring to similar results when the hypotheses for their correct employment are fulfilled. Owing to the reduced scene illuminated by the gbSAR sensor, the homogeneous area needed by CZT had to be selected in the low/medium vegetated part of the hill slope, where decorrelation effects caused by atmosphere instability become significant. Nonetheless, nor the 1D neither the spectral approach constitutes a technique able to compensate for gbSAR atmospheric artefacts in any situation. They must be though as alternative procedures giving the opportunity to compensate for the atmospheric distortion effects in a wider set of scenarios.

6.5 Homogeneous atmosphere hypothesis assessment

The basic assumption of the compensating technique described in Sections 6.3 is that the transmitted and backscattered wave propagates through a homogeneous medium. This hypothesis

has been proved by projecting the differential phase of the whole scenario onto a single range cut and showing that the distribution fits a linear model. Although it demonstrates the linearity of the atmospheric artefacts with respect to range direction, it gives no information about the variance of this behavior in the cross-range dimension. In order to carry out this study, the significant angular sector $\Delta\Phi$ of the gbSAR interferogram may be expressed as

$$\Theta = \bigcup_{i=-N/2}^{N/2} \Delta\Theta_i = \bigcup_{i=-N/2}^{N/2} \left[i\Theta_s \pm \Delta\Theta_s \right] \tag{6.23}$$

where $\cup$ denotes the union set operation, $\Delta\Theta_i$ is the i*th* sub-area of angular width $\Delta\Theta_s$ and centered at $i\Theta_s$. The phase-ramp slope a_{1i} describing the atmospheric artefact in each sector may be estimated by projecting the differential phase of high-coherence pixels within $\Delta\Theta_i$ onto a single range-cut. Being a_{10} the artefact gradient estimated with the whole image, that is using $\Delta\Theta$, the error arising from approximating the troposphere to a homogenous medium may be calculated as

$$\varepsilon = \frac{\left(\frac{1}{N} \sum_{i=-N/2}^{N/2} \left(a_{1i} - a_{10} \right)^2 \right)^{1/2}}{a_{10}}. \tag{6.24}$$

Such a study cannot be carried out using the test-site of Collserola. If the scenario is divided as described by Eq. 6.23, the shadowing phenomena caused by the upwards observation geometry make the total amount of coherent pixels within each sector insufficient to perform a meaningful analysis, even for a small *N*. For this purpose, the test-site of Sallent, which has been already introduced in Section 4.7.2 and Section 5.4.4, turns out to be more suitable. For the sake of handiness, the photo of the observed environment is again shown in Fig. 6.13. An example of the corresponding *hh* reflectivity image is displayed in Fig. 6.14, whereas the differential coherence and phase obtained using two 10-hours-delayed gbSAR acquisitions are shown in Fig. 6.15 and Fig. 6.16, respectively. The data sets correspond to the measurements 10 (20:51 on November 11th 2006) and 40 (7:41on November 12th 2006) acquired on DAY 6 of Table 4.2. The three images allow one to appreciate that the shadowing effects are notably reduced with respect to the Collserola scenario, confirming that the angular study described by Eq. 6.23 can be successfully applied to Sallent data sets. It is worth noting that the useful angular sector at disposal in the reflectivity image is wider than the -3dB antenna beam specified in Chapter 4. Polar coordinates have been preferred to Cartesian axes to better emphasize the angular independence of the

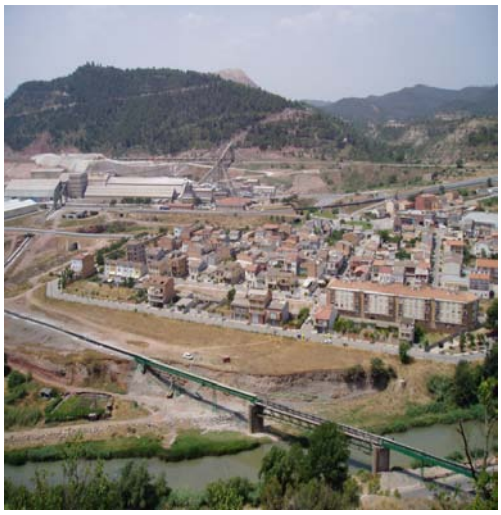

Fig. 6.13: Picture of the Sallent test-area from the UPC sensor's location.

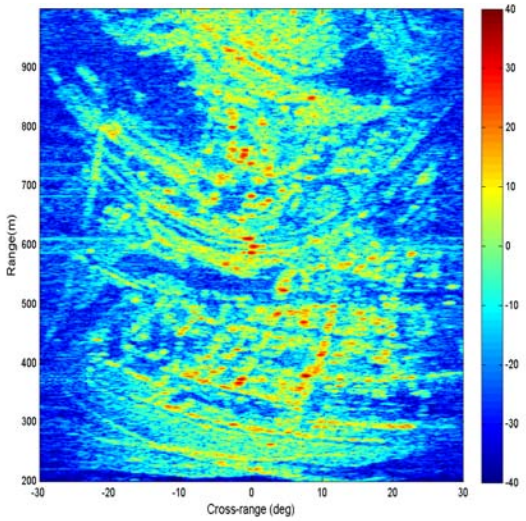

Fig. 6.14: UPC gbSAR reflectivity image of the scenario focused on a polar grid of pixels in the *hh* channel.

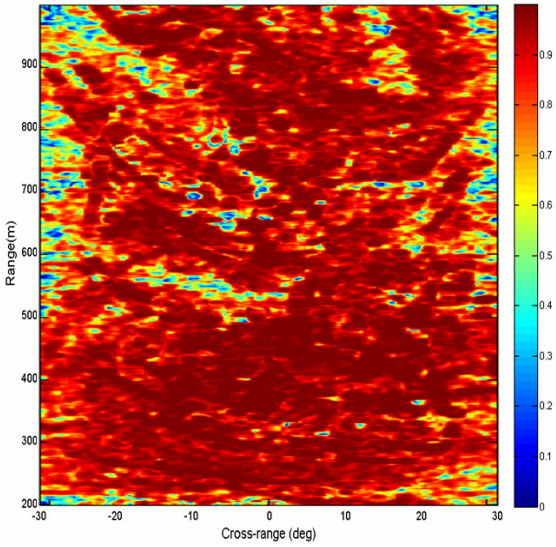

Fig. 6.15: Differential coherence of two zero-baseline gbSAR *hh* data acquired in Sallent with a time span of 10 hours and focused on a polar grid.

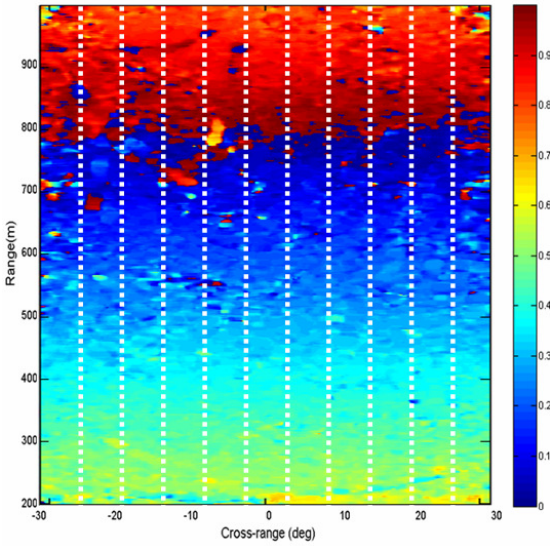

Fig. 6.16: Differential phase of two zero-baseline gbSAR *hh* data acquired in Sallent with a time span of 10 hours and focused on a polar grid.

atmospheric phase artefact. The results obtained for $\Delta\Theta_s = 5º$, $\Theta_s = 5º$ and $\Delta\Theta = [-27.5º, 27.5º]$ are reported in Table 6.2. The error ε given by Eq. 6.24 is approximately 0.01, demonstrating that the cross-range homogeneity hypothesis assumed for the atmospheric artefact phase-ramp in Section 6.3 is fulfilled. The last column shows a gross estimation of the phase difference between the artefact estimation carried out from each sector and using the whole scenario at 1km. It can be observed that the error is always very low, less than 3º, with the exception of the three angular sectors in blue. For these areas, far range zone shadowing effects reduces the number of useful pixels at disposal for the atmospheric artefact analysis and the estimate is less reliable. Yet, it is worth pointing out that the incorrect estimation is due to the illumination geometry and not to

Angular Sector Center Θ_s	a_{1i} [rad/m]	a_{1i}-a_{10} [rad/m]	Error at 1000 m [deg]
	1e-3 ×	1e-5 ×	
0	6.09	6.67	2.0
-5	5.98	3.97	0.4
5	6.00	6.17	1.7
-10	5.92	-1.11	-2.4
10	5.94	0.22	-1.6
-15	5.84	-0.20	-7.6
15	5.87	-6.76	-5.6
-20	5.92	-1.42	-2.6
20	5.99	4.71	0.9
-25	5.86	-7.44	-6.0
25	5.99	5.14	1.1

Table 6.2: Estimation of the atmospheric phase artefact in Fig. 6.16 for different angular sectors using the 1D technique of Section 6.3. The mean value a_{10} and standard deviation σ of the angular coefficients a_{1i} are $a_{10} = 5.94\text{e-}3$ and $\sigma = 5.96\text{e-}005$, respectively.

troposphere inhomogeneous behaviors. Indeed, the overall error estimation given by Eq. 6.24 is $\varepsilon = 1\%$, which confirms that employing all the pixels within $\Delta\Theta$ at once to overcome shadowing critical conditions and carry out the artefact compensation is perfectly correct.

6.6 Limits of the atmospheric artefact compensation technique

Up to now, particular importance has been given to the spatial homogeneity hypothesis that the troposphere must fulfill to linearly model the gbSAR atmospheric phase artefacts. Yet, another condition is implicitly assumed by the approximation of the refractive index *n* to a constant value: the propagation properties of the troposphere must maintain constant during the time required for the aperture synthesis. As the antennas movement is performed through a mechanical displacement of the RF block along the linear unit, the duration of the scanning process is in the order of minutes. The exact time is related to the dimension of the aperture to be synthesized, the frequency defining the minimum cross-range sampling step Δu, and the specific hardware implementation (See Chapter 4). A comparison between the performance of two VNA-based gbSARs [Martinez,07] [Noferini,07] described in the literature and the UPC sensor is reported in Table 6.3. Depending on the time required for the complete scanning process and on the atmosphere instability of the environment under observation, this second hypothesis might not be fulfilled.

GBSAR System	Carrier Frequency	Bandwidth	Acquisition Mode	SSA Length (L)	Scanning Time (Δt)
LiSA [1]	C K	60MHz 100 Mhz	*Single* Pol (VV)	3.5 m 2 m	12 min
Uni-Fi [2]	C	20MHz	*Single* Pol(VV)	1.8 m	19 min
UPC gbSAR	X	[60:144] MHz	*Single* Pol *PolSAR* *PolinSAR*	2 m	1 min 2min 20 sec 4 min 30sec

Table 6.3: Performance of VNA-based gbSAR sensors available in the remote sensing scientific community versus the DDS-based UPC system.

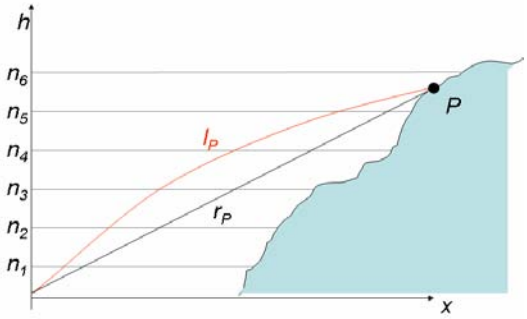

Fig. 6.17: Ray-bending effect in a 2D space due to n vertical layered distribution: r_P and l_P are the real range distance of P and the estimation given by the gbSAR.

6.6.1 Anomalous artefacts simulation

Under turbulent conditions, the troposphere stops behaving as a homogeneous medium and is better described by a multi-layer model. In general, propagation of electromagnetic plane waves through a multilayer medium generates phenomena known as ray-banding [Hall,87]. An example in a 2D space is sketched in Fig. 6.17. The real range position of the target P is r_P whereas the term l_P indicates the distance measured by gbSAR sensor as an effect of n vertical gradient. Owing to possible variations of refractive index distribution, l_P might change not just between two different scans but even during the same acquisition process. Normally, the apparent displacements are shorter than the resolution cell size, so that only the differential phase is noticeably affected. Yet, in the worst cases cell-jumps might occur, causing significant decreases of the differential coherence. An accurate description of these atmospheric phenomena requires the knowledge of the time-space distribution of temperature, pressure and relative humidity at any position between sensor and scenario. Since this measurement is unfeasible, it is almost impossible to foresee what kind of artefact will affect the differential interferogram in the case of turbulent troposphere. Three main situations might be pointed out:

I. n is vertically layered but time-constant
II. n is spatially constant but changes in time during the aperture synthesis
III. n is vertically layered and changes in time.

In the first case, the distortion effect is strictly related to the specific topography of the scenario. In fact, the curvature of the ray trajectory will be related to the number of layers the wave travels through during its round-trip propagation. In the second case, n is assumed to be different at each position of the sensor but spatially homogeneous. This situation might correspond to a cold or

warm mass air swiftly entering the area of interest. To understand the way the backscattering information might be distorted, a linear variation of n equal to 5ppm along a 2 m SSA has been considered. It is worth pointing out that this variation corresponds to a short-term excursion of temperature and relative humidity equal to 2ºC and 10%, respectively, i.e. to a realistic atmosphere change. The propagation phase in Eq. 6.11 associated to a generic target at the real range-position r_T during the aperture synthesis may be described as

$$2kr_P\left(m\Delta u\right) = 2k_0 r_P\left(n_{(0)} + K_n m\Delta u\right) \quad m = [0 : N_u - 1] \tag{6.25}$$

where Δu is the SSA sampling step and m the index that makes it possible to describe the whole synthetic aperture, N_u is the number of azimuth samples, $n_{(0)}$ is the refractive index when the measurement starts, and K_n is the variation gradient. Then, a scenario consisting of three boreside-aligned targets at different range positions (500m, 1000m, 1500m) have been simulated. The reflectivity image focused on a Cartesian grid is shown in Fig. 6.18. It can be observed that the targets are cross-range shifted with the respect to their real position. As a matter of fact, they have rotated around the SSA centre proportionally to their range distance as well as to their squint angle φ. This second dependence is better stressed in Fig. 6.19, where the rotation angle $\Delta\varphi$ is plotted against target's real squint position φ: the amount of rotation is proportional to target's range distance whereas its sign depends on both the sign of n gradient and the direction of sensor movement. Concluding, a linear modulation of n entails not a simple rotation but a real distortion of the scenario spatial proportions. If non-linear modulations of n are finally analyzed, the rotation comes with defocusing effects. The third case is finally given by a mixture of the first two: the targets information is expected to be distorted in a way proportional to their range and cross-range position as well as to their topographic height.

6.6.2 Anomalous artefacts in gbSAR Real Data

When real gbSAR data are gathered under instable atmospheric condition, the coherence parameter is usually robust to distortion effects and just the differential phase information is unpredictably corrupted. In order to show different examples of anomalous artefacts arising from troposphere inhomogenity, the test-site of Collserola is selected. The main reason is that the combined effect of the complex metropolitan environment surrounding this area and the proximity to the sea often causes high variations of atmospheric parameters during short time intervals. An experiment held in May 2005 was mainly focused on evaluating how troposphere turbulences

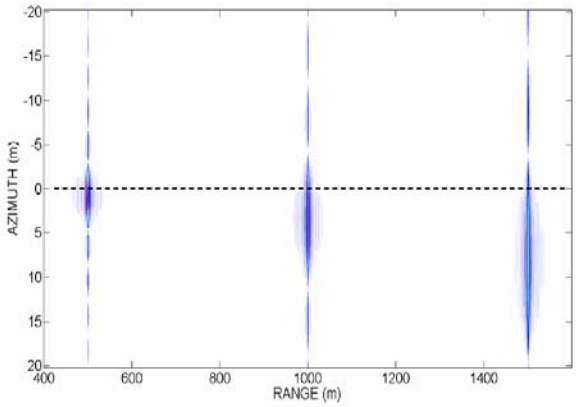

Fig. 6.18: Rotation of *boreside*-aligned targets caused by a linear variation of the refractive index *n* during the short aperture synthesis.

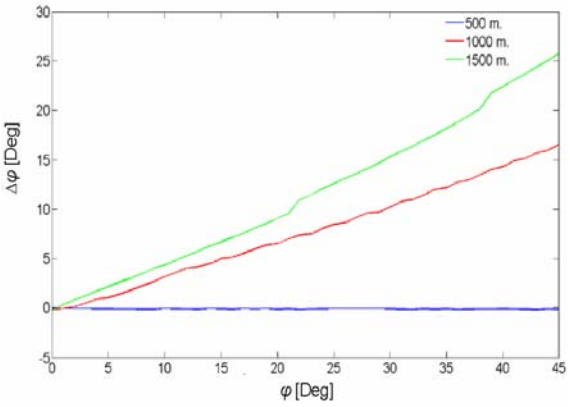

Fig. 6.19: Cross-range rotation $\Delta\varphi$ due to a linear variation of *n* during the SSA construction as a function of target's squint position φ.

might affect the gbSAR measurements at X-Band. On May 26th, strong gusts of wind blew from the sea during approximately 5 hours. On order to emphasize the distortion effects, the measurement parameters of the UPC sensor were chosen so that the acquisition process took approximately 12 minutes for synthesizing a 2 meters long aperture. It is worth recalling that this is the typical duration of the scanning process carried out by VNA-based terrestrial SAR sensor. Single-polarization measurements in the *hh* channel were acquired every 30 minutes during approximately 12 hours, giving the opportunity to observe different examples of anomalous atmospheric artefacts.

The first example is displayed in Fig. 6.20a-b. Although little distortions can be observed in far range, the value of zero-baseline coherence is high in the central part of scenario (Fig. 6.20a). It can be seen that the coherence pattern is quite similar to the one in Fig. 6.5b, which was obtained under stable troposphere condition. On the contrary, the differential phase in Fig. 6.20b shows that the artefact corrupting differential information is no longer a range phase-ramp. Accordingly, the compensation technique proposed in Section 6.3 cannot be successfully used. Neither an equivalent cross-range approach might be pursued. A careful analysis reveals that, fixing the azimuth position, close and far-off targets are not affected the same way. Indeed, a cross-range rotation as well as a dependence on targets' range/height position is detectable. According to the case study described in the Section 6.6.1, this artefact could be classified as type 3.

When apparent displacements get higher, the distortion might come to compromise also the coherence. A significant mismatching between master and slave reflectivity images makes differential coherence decrease dramatically. As it has been pointed out for the distortion effects described in Fig. 6.19, this phenomenon cannot be dealt with as a sort of co-registration error

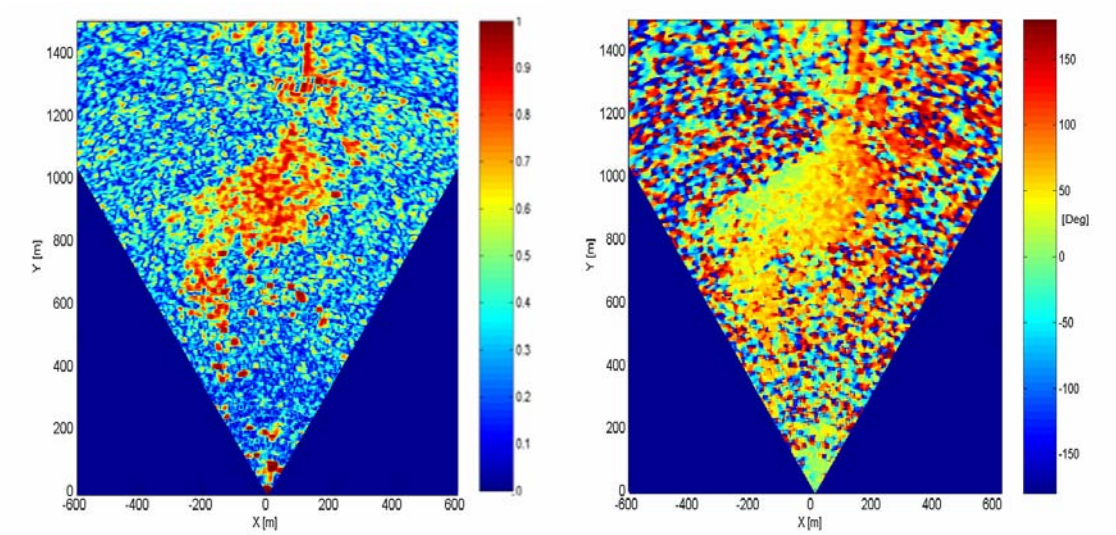

(a) (b)

Fig. 6.20: Example of anomalous atmospheric artefacts affecting differential phase (b) but not the differential coherence (a). The time span between the two *hh* data acquired on May 26th 2005 is about 30 minutes while the duration of the 2 meter aperture synthesis is 12 minutes.

[Scheiber,00]. In fact, it is not caused by a rigid shift of slave-image upon the master acquisition. It arises from the lack of atmospheric homogeneity within the scenario and introduces a real distortion of the amplitude information. As example, the far range area of Collserola corresponding to two successive 30 minutes delayed acquisitions is displayed in Fig. 6.21a and Fig. 6.21b. A white grid has been overlapped to the images in order to emphasize the rotation effect of bright pixels within the scenario. In the top-left part of the second image it is possible to observe ghost targets. They are not generated by aliasing but by *anomalous* constructive interference. The image rotation has been better stressed in Fig. 6.22a and Fig. 6.22b by zooming the two amplitude images on the backscattering from a cylindrical metal structure close to the communication tower. The target position shifts more than 7 meters in cross-range dimension whereas no significant variation occurs in range, in perfect agreement with the simulation results. Besides, in both images the target is well focused, demonstrating that the coherent echoes of the synthetic aperture sum constructively even if they are characterized by different propagation properties (linear modulation of n). If it is possible to retrieve some common features from the amplitude analysis, no useful information can be instead extracted from the differential coherence and phase. These two quantities are displayed in Fig. 6.23a and Fig. 6.23b and appear completely noisy. When atmospheric conditions became even more instable, the correlation among the echoes collected during the aperture synthesis dramatically decreases. The coherent sum performed by the azimuth focusing procedure leads to unpredictable results (n non-linear modulation). An example

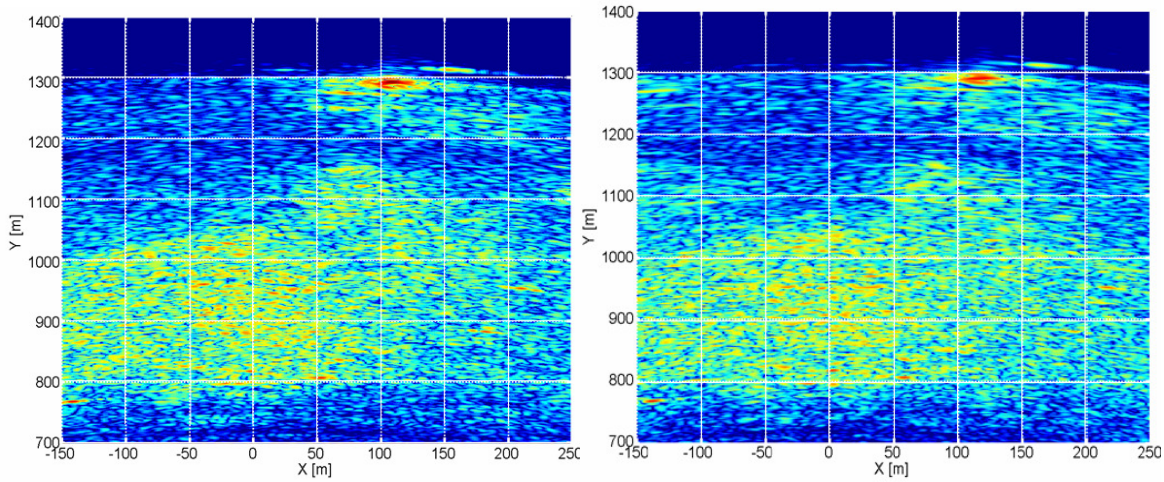

Fig. 6.21: Examples of the effects of *n* variations during the aperture synthesis process on gbSAR images. The two *hh* data were acquired on May 26th 2005 with a time separation of 30 minutes. The white grid has been overlapped to stress the different cross-range position of the deterministic targets in far range zone.

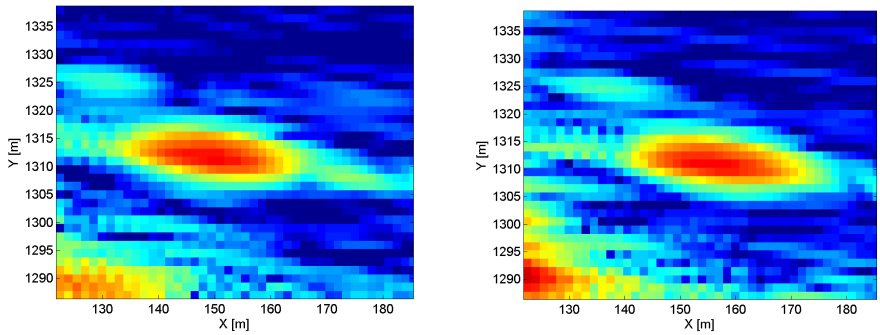

Fig. 6.22: Zoom of the amplitude images in Fig. 6.21a (a) and Fig. 6.21b (b) on a deterministic target in the far-range zone showing a cross-range shift of about 7 meters.

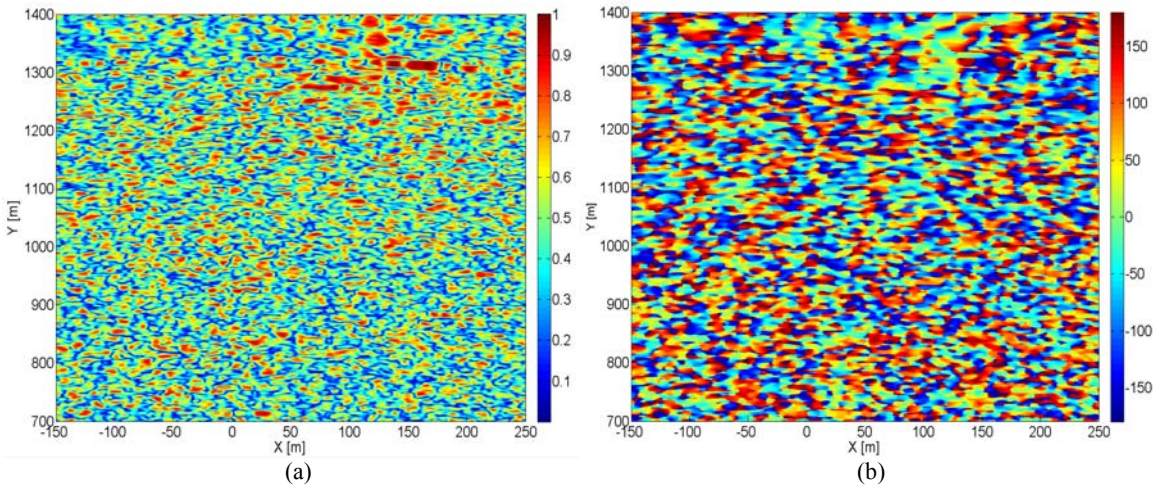

Fig. 6.23: Zero-baseline interferometric coherence (a) and phase (b) of the two *hh* data sets displayed in Fig. 6.21. The two images are completely noisy as a consequence of *n* modulation distortion.

is given in Fig. 6.24: it can be noticed that the reflectivity image stretches along the azimuth dimension and targets farther than 1 km shift up to 100 m. Besides, defocusing and aliasing effects

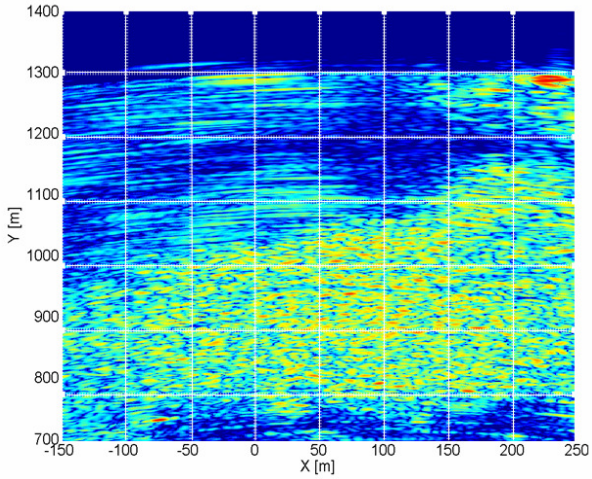

Fig. 6.24: Anomalous effects introduced by non-linear modulation of *n* during the aperture synthesis. The distortion is so high that the far-range amplitude information image shows no relation with the real geometry of the scenario.

are also observable in the upper part of Fig. 6.24. As it has been previously pointed out, the amount of distortion a turbulent troposphere can induce on gbSAR acquisitions is unpredictable because the perfect knowledge of *n* in time and space is unfeasible. In the case of propagation through non-homogeneous media, no reliable information can be extracted and data are generally rejected. In all these evidences, it is clear that the problem cannot be solved through the employment of advanced compensation techniques. The key-point is to avoid the atmosphere decorrelation by reducing the duration of the acquisition process as much as possible.

Finally, it is important to remark that these atmospheric effects become even more critical when reliable PolSAR or single-pass PolInSAR data are to be gathered, being the time required for the aperture synthesis proportional to the number of polarization channels. The maximum tolerable time must take into account factors like spatial resolution constraints, number of polarizations and specific atmospheric properties of the scenario. For instance, concerning the test-site of Collserola, no significant alterations were observed in gbSAR zero-baseline acquisitions even under very turbulent atmospheric conditions when the measurement took less than 3 minutes. Fulfilling this time restriction, even for single polarization observations, is not possible if a VNA-based sensor is employed. The development of faster sensors, as it is the case of the UPC gbSAR system, indeed constitutes the unique solution for gathering reliable data sets in almost any weather conditions.

6.7 Summary

In this Chapter, the time required by gbSAR systems for the aperture synthesis has been indicated as the key parameter affecting the quality of amplitude and phase information. Slow scanning processes performed under turbulent troposphere conditions have been shown to lead to low-

quality interferometric data. In the worst cases, focused reflectivity images might come to have no correspondence to real scenario geometry and had to be rejected. Contrary, when fast gbSAR acquisitions are gathered, it is possible to approximate the troposphere to a homogeneous medium: the atmospheric distortions turn into regular polarization-independent phase ramps which are generated by refractive index variations among successive scans. In these cases, a simple coherence-based technique may be successfully applied to cope with the phase artefacts compensation. Concerning the two test-sites considered in the frame of this thesis, homogeneous medium hypothesis was always fulfilled as long as scanning time lower than 3 minutes were performed. Still, it cannot be excluded that in different environment or climate, unpredictable phase artifacts might appear under very instable troposphere conditions, even for faster scanning time.

Chapter 7

Polarimetric Temporal Analysis of Urban Environments

Revisiting time constitutes a fundamental constraint for continuous monitoring activities based on satellite and airborne SAR acquisitions. On the contrary, the employment of a terrestrial platform overcomes this limitation and makes it possible to perform a time-continuous observation of small space-scale phenomena. New research lines of SAR dealing with the backscattering evolution of different types of scenarios becomes hence possible through the analysis of gbSAR data collections. The RSLab of the UPC drove a one-year measurements campaign using its X-Band gbSAR sensor in the village of Sallent, in northeastern Spain. The field experiment was funded by the Institut Geològic de Catalunya (IGC) and aimed at studying the subsidence phenomenon induced by the salt mining activity carried out in this area during the past decades. In this Chapter, the Sallent test-site and the measurements campaign is first described. Then, the analysis is focused on the problem of urban targets polarimetric stability in short and long time scales. The PolSAR data monthly acquired from June 2006 to July 2007 are employed to stress the presence of non-stationary backscattering processes within the urban scene and to propose a filtering procedure aiming at reducing its randomness in one-day and long-time data collections. Finally, the improvements provided by the novel filtering procedure are assessed in terms of polarimetric time-entropy decrease over the whole area of interest.

7.1 Sallent Measurements Campaign

The Conca Potàssica Catalana (the Catalan potassic salt basin) is located in the so-called Central Catalan Depression, within the Ebre River Depression in northeastern Spain. This basin is made of a great saline unit, composed by an alternation of potash salts (sylvinita and carnalita mainly)

Fig. 7.1: Picture of the Sallent test-area from the UPC sensor's location.

	Date	Time	# of Scans	Time-Delay
DAY 1	29/06/06	11:00 - 16:00	27	10 min
DAY 2	26/07/06	08:00 - 11:30	30	13 min
DAY 3	19/09/06	10:40 - 16:00	39	8 min
DAY 4	20/10/06	09:40 - 15:00	31	7 min
DAY 5	14/11/06	12:30 - 16:30	41	8 min
DAY 6	28-29/11/06	19:00 - 08:40	44	20 min
DAY 7	18-19/12/06	20:45 - 05:00	99	10 min
DAY 8	13-14/02/07	22:00 - 09:55	37	25 min
DAY 9	14-15/03/07	20:00 - 09:50	41	25 min
DAY 10	04-05/07/07	22:00 - 10:50	45	25 min

Table 7.1: Timetable of the measurements campaign. Red and blue colors denote the diurnal and nocturnal measurements, respectively.

Fig. 7.2: Wide-angle lens picture stressing the observation geometry of the ground-based SAR sensor in Sallent.

layers. The potash salts were traditionally exploited since ancient times and are still an important mining activity in Catalonia. The Enrique mine, located in the village of Sallent, was under exploitation until 1974. In 1954 a natural cavity of about 120 meters high and 40 meters wide was found during mining works. This cavity, caused by water circulation, is located under the south-east part of Sallent, in the neighborhood known as Barri de l'Estació, close to the Llobregat River. Water floods in 1957 and 1962 forced to abandon this part of the mine, filling up the cavity with saturated salty water.

During the 90s, heavy damages appeared in man-made structures built within the district. As a response, the Catalan Administration started a research program to identify, quantify and model the phenomena subsidence in this area [ICC, 03]. In the framework of that program, a multiple set of techniques such as topographic leveling, geological mapping, geophysic prospection, extensometric measurements, drilling, and orbital DInSAR, were employed to evaluate the risk of structure collapse [Marturia,05]. In 2003 the SAR group of the UPC, jointly with the Institut Cartografic de Catalunya (ICC), studied the geological behavior of the district applying DInSAR techniques to ERS1/2 acquisitions [Blanco,03].

A new collaboration between the two institutions started at the end of June 2006 as an attempt to improve both the spatial accuracy and temporal sampling of the deformation process using the UPC gbSAR sensor. A picture of the Barri de l'Estació observed from sensor's location is detailed

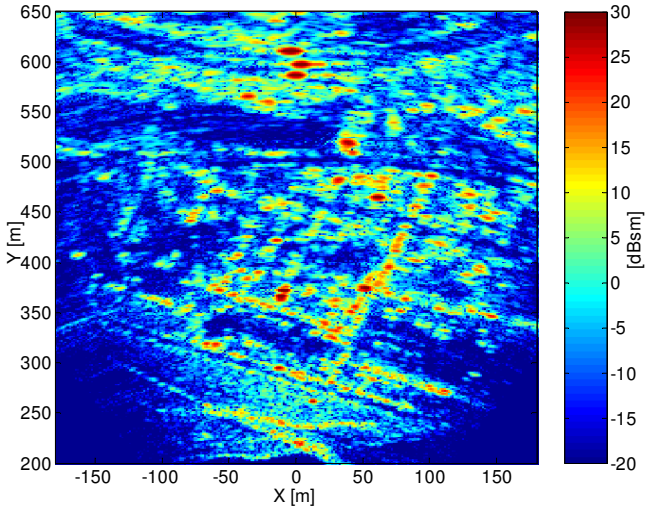

Fig. 7.3: Reflectivity image of the Station district of Sallent in the *hh* polarization in dBsm.

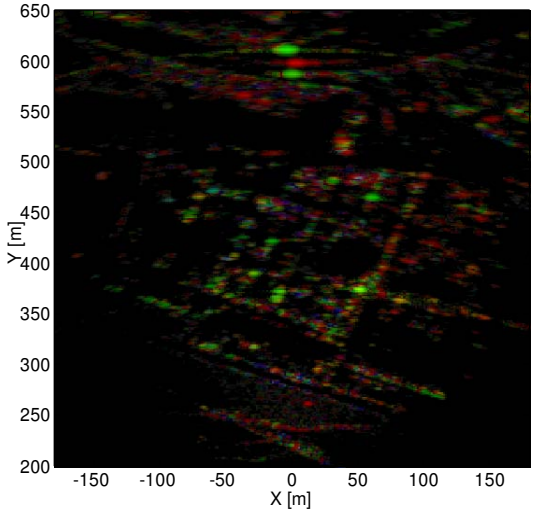

Fig. 7.4: RGB composition of Pauli's components within the Station district of Sallent weighted by span.

in Fig. 7.1, while a photo of the system in the operating configuration is displayed in Fig. 7.2. Data were acquired on ten different days from June 2006 to July 2007,as it is reported in Table 7.1: red and blue colors denote the diurnal and nocturnal collections, respectively.

7.2 Urban environment polarimetric main features

A minimum of 30 PolSAR data sets were acquired at X-band during each day of measurements with a span varing from the 7/8 minutes employed for diurnal acquisitions to the 20/25 minutes mostly characterizing the nocturnal ones (*Appendix C*). An example of the district reflectivity response in the *hh* polarization is displayed in Fig. 7.3. Data calibration was carried out as explained in Section 4.5 using a corner reflector located in a near-range bare area and a strong cross-polar urban target. A brief description of the main scattering mechanisms characterizing the urban environment can be performed using one of the coherent techniques in Section 2.2.2. Owing to its direct physical interpretation, the Pauli's decomposition has been preferred. Then, the calibrated scattering matrix [*S*] measured in the $\{\vec{h},\vec{v}\}$ polarization basis is decomposed in a trihedral-like, a dihedral like and a volumetric/45º tilted dihedral-like components as follows

$$[S]=\begin{bmatrix} S_{hh} & S_{hv} \\ S_{hv} & S_{vv} \end{bmatrix}=\sqrt{span}\left(a_T \begin{bmatrix} 1 & 0 \\ 0 & 1 \end{bmatrix}+a_D \begin{bmatrix} 1 & 0 \\ 0 & -1 \end{bmatrix}+a_V \begin{bmatrix} 0 & 1 \\ 1 & 0 \end{bmatrix}\right) \tag{7.1}$$

where a_T, a_D and a_V are the normalized complex coefficients whose modulus describes the way the total power of [*S*] splits up among the three elementary mechanisms. A simultaneous description of these three quantities is obtained by defining each component as the additive primary color of an RGB image. The result is shown in Fig. 7.4. The red, green and blue colors

correspond to single-bounce (a_T), double-bounce (a_D) and volumetric (a_V) power contributions to backscattering process, respectively. Additionally, the *span* has been used as weight factor to stress the position of high-reflectivity urban scatterers. It can be noticed that one dominant mechanism characterizes most of the pixels. Red and green pixels are mainly detectable. Few yellow points, describing the concurrent presence of both single and double bounces, are observable too. Blue points, which are quite rare, are generated by multiple-reflections phenomena. The polarimetric features of the monitored scenario perfectly agree with the results obtained with other SAR platforms. In [Schneider,06] [Moriyama, 05], it is pointed out that man-made structures are mainly characterized by strong dihedral-like scattering generated by the interaction between vertical elements, i.e. walls, and the ground. These studies were based on the analysis of L-band and X-band air-borne SAR acquisitions. The analogies shown by gbSAR observations make it possible to extend these general considerations to terrestrial platforms. Yet, the weight that the dielectric constant might assume at high incidence (>70º) in terms of geometrical interpretation of the Pauli's components will be carefully looked into in Section 7.4.1.

7.3 Urban environment daily instability

According to Eq. 6.11, the scattering matrix measured by the UPC sensor under hypothesis of propagation through a homogenous medium may be defined as

$$[S'] = \begin{bmatrix} S_{hh} & S_{hv} \\ S_{hv} & S_{vv} \end{bmatrix} e^{-j2k_0 n(t) r} + [N_T] \tag{7.2}$$

being r the target range position, $n(t)$ the refractive index, k the wavenumber and the new term $[N_T]$ the 2×2 complex matrix accounting for the additive noise contribution. Note that in Eq. 7.2 the time-dependence of $n(t)$ points out that the refractive index is assumed constant only during the acquisition process of a single PolSAR data sets.

Let w define one of the measurement dates reported in Table 7.1 and N_w the corresponding number of zero-baseline data sets gathered by the gbSAR system in that day. The expression describing the ith scattering matrix of the collection may be rewritten as

$$[S']_i^w = \begin{bmatrix} S_{hh}^{i,w} & S_{hv}^{i,w} \\ S_{hv}^{i,w} & S_{vv}^{i,w} \end{bmatrix} e^{j2k_0 \left(n_{1,w} + \Delta n_{i,w}\right) r} + [N_T]_i^w \quad i = 1,..,N_w \tag{7.3}$$

where n_1 is the refractive index of the first acquisition (master) and Δn_i describes the variation of the propagation properties due to changes of the troposphere in data set i with respect to the master image. It is worth recalling that the term Δn_i generates the atmospheric artefacts analyzed in

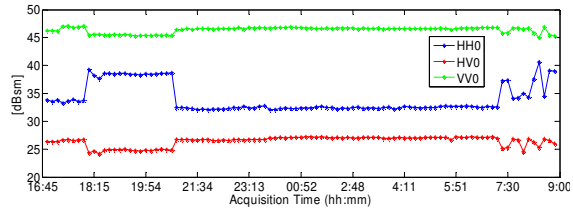

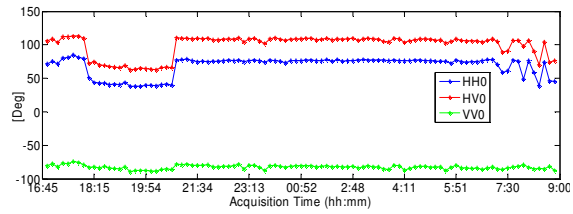

(a)

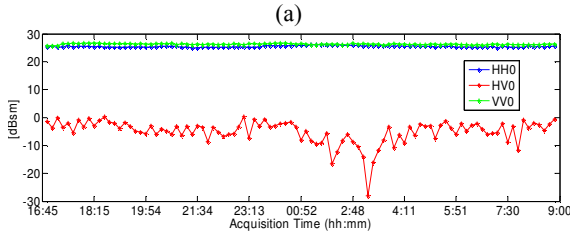

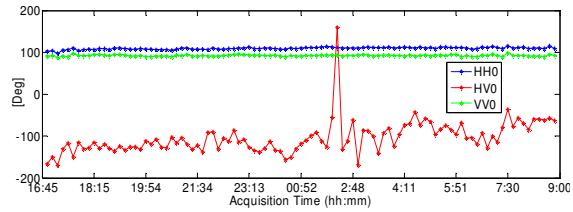

(b)

Fig. 7.5: Time evolution of the amplitude A [dB] and absolute phase φ [deg]concerning the target P_1 (a) and the corner reflector C_1 (b) from 5 pm on December 18th 2006 to 9am next day. The time sampling step is 10 minutes.

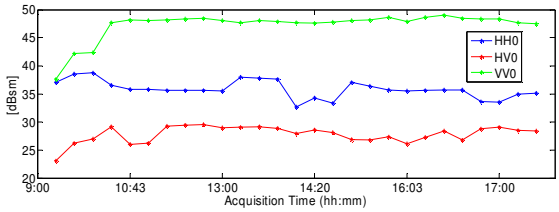

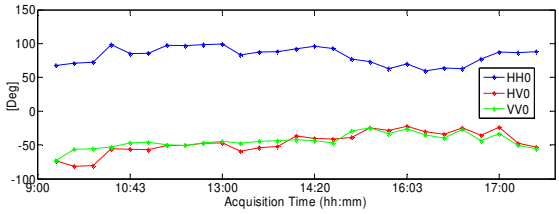

(a)

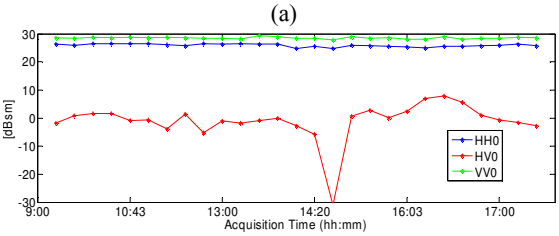

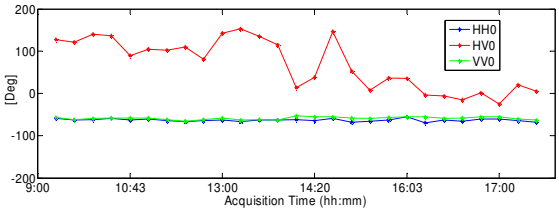

(b)

Fig. 7.6: Time evolution of the amplitude A [dB] and absolute phase φ [deg]concerning the target P_1 (a) and the corner reflector C_1 (b) from 9am to 3 pm on 20th October 2006. The time sampling step is 20 minutes.

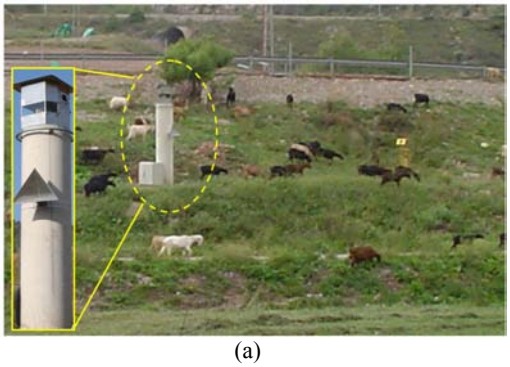

(a)

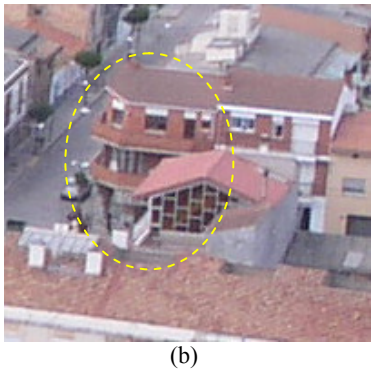

(b)

Fig. 7.7: Picture of the trihedral C_1 mounted on a concrete pillar (a) and of the target P_1 (b). The range distance of the two targets is about 650m and 300m, respectively.

Section 6.3. After compensating for the corresponding atmospheric-induced phase ramps, the ith scattering matrix of the gbSAR daily collection becomes

$$\left[\widehat{S'}\right]_i^w = \begin{bmatrix} S_{hh}^{i,w} & S_{hv}^{i,w} \\ S_{hv}^{i,w} & S_{vv}^{i,w} \end{bmatrix} e^{j2k_0 n_{1,w} r} + \left[N_T\right]_i^w \quad i = 1,..,N_w . \tag{7.4}$$

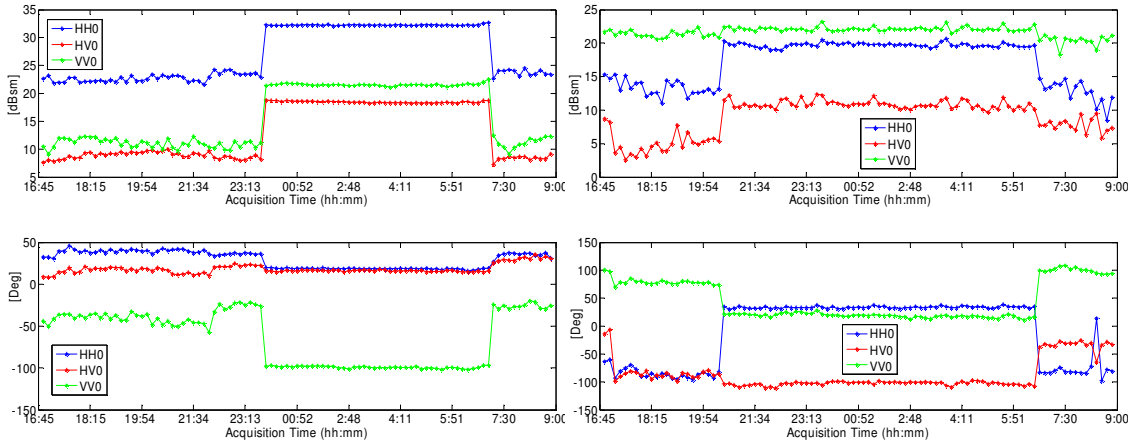

(a) (b)

Fig. 7.8: Time evolution of the amplitude A [dB] and absolute phase φ [deg]concerning two targets P_2 (a) and P_3 (b) located at less than 30 meters from P_1 in Fig. 7.5 during the monitoring activity carried out on December 18th 2006.

In the case of time-invariant deterministic scatterers, $[\widehat{S'}]_i^w$ is constant over time and it depends only on their position with respect to the sensor. This behavior is typical of speckle-free scatterers and is generally associated to pixels belonging to urban structures [Lopez,03]. Despite this is a widely shared assumption in the SAR remote sensing community, the following analysis of real X-band gbSAR data will reveal that this hypothesis might be unfulfilled. That is, the evolution of the amplitude A and absolute phase φ of the different polarimetric channels within the Sallent urban environment turns out to depend on the part of the day data are acquired. In order to stress this unexpected behavior, the collection of December 18th is first taken into consideration. The monitoring process was carried out with a 10 minutes time-sampling between consecutive scans, giving the opportunity to look into the temporal evolution of targets' time response in great detail. The plots of Fig. 7.5a describe the polarimetric behavior of a high reflectivity pixel, hereon denoted with P_1, at 400 m from the sensor. A stable answer characterizes the first 9 acquisitions. The samples correspond to the time interval from 4:45 pm to 6 pm. Then, a jump affects both polarimetric amplitudes and phases, leading to a new but still stable polarimetric behavior that keeps constant for the next 17 acquisitions, until approximately 9 pm. Afterwards, a new modification seems to restore the previous scattering properties. In the last part of the profile, from 7 am to 9 am, it is possible to observe significant fluctuations. The suspicion of any system failure is excluded by the stable answer of a corner reflector displayed in Fig. 7.6. This calibrator, shown in Fig. 7.7 and hereon denoted with C_1, was mounted on a concrete pillar at a range distance of about 650 m. The slightly difference between the two co-polar channels is due to the reflectivity of the metallic structure on the top of the pillar in the *hh* and *vv* polarizations. When a diurnal

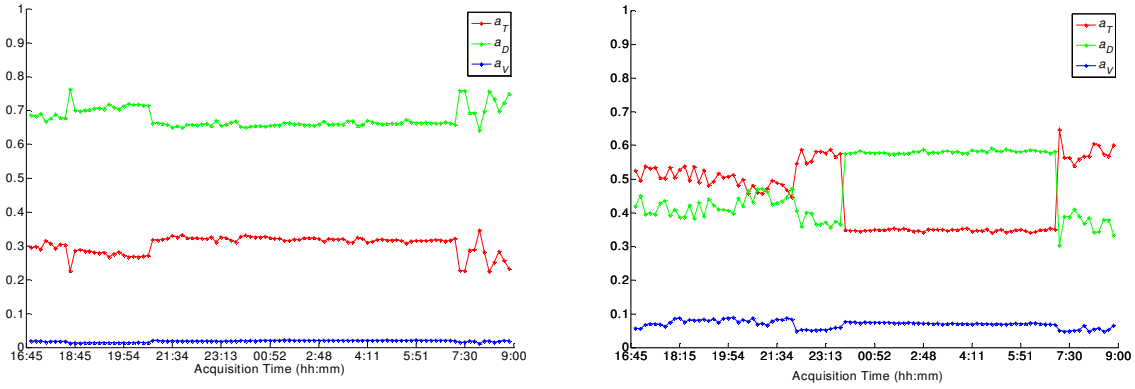

(a) (b)

Fig. 7.9: Time evolution of normalized-to-span Pauli's components concerning the targets P_1 (a) in Fig.7.5 and P_3 (b) in Fig. 7.8b during the monitoring activity carried out on December 18th 2006.

collection is instead analyzed, the fluctuations of P_1 profiles generally increase whereas the answer of C_1 keeps stable, guaranteeing that no system failure occurred. As example, the behavior of these two targets on October 20th 2006 is shown in Fig. 7.6a and Fig. 7.6b. The absolute phase difference of the co-polar channels in the two days is due to the different location of the corner reflector employed for the polarimetric calibration of each set of daily acquisitions. It follows that the explanation of these irregular profiles in terms of atmospheric artifact residual errors or coregistration procedure uncertainties must be also excluded. In fact, the high spatial correlation length characterizing these error sources should make close pixels present similar trends. Careful analyses have revealed that this does not occur. This can be observed in Fig. 7.8a and Fig. 7.8b, which show the evolution of two pixels P_2 and P_3 located at about 30 meters from P_1. Finally, it must be pointed out that working out a relation between polarization temporal changes and backscattering mechanism modifications is not straightforward. In fact, different polarization trends of a pixel do not necessarily turn into different backscattering processes within the resolution cell. This is stressed by the nocturnal evolution of the normalized-to-span Pauli's components concerning P_1 and P_3 shown in Fig. 7.9a-b. The two images reveal that the stability of one polarimetric channel is not sufficient to state that the scattering mechanism within the resolution cell maintains constant along the time axis. In all these evidences, these anomalous temporal profiles cannot be related to possible processing chain errors. On the contrary, an explanation must be looked for at pixel level. For this purpose, alternative approaches based on coherent and incoherent analyses of the gbSAR daily collection are now proposed.

7.3.1. Classical Permanent Scatterers approach

According to the results commented in the previous section, the stability of urban targets'

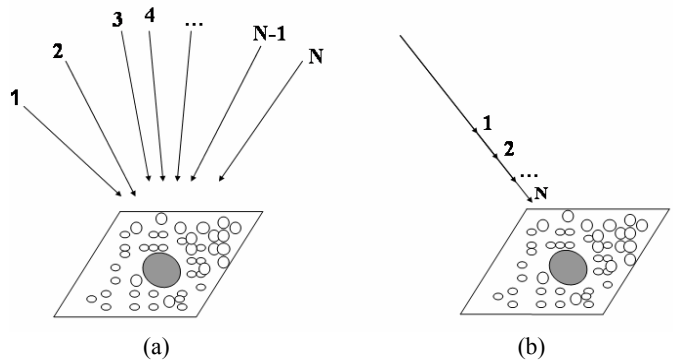

Fig. 7.10: Multi-temporal SAR observations of a PS using satellite (a) and terrestrial (b) platforms. For the sake of clarity, the illuminated target has been modeled as a Swerling target of type 1. Yet, the emphasis is given to variable versus constant observation geometry entailed by the two platforms more than to the hypotheses concerning the statistical distribution of scatterers inside the resolution cell.

response at X-bands might vary with polarization. Then, it is meaningful to analyze the temporal evolution of each channel of the scattering matrix separately. At the same time, it is reasonable that the description procedure employed for this purpose agrees with the main properties of gbSAR acquisition geometry. An assessed method for the discrimination of stable pixels within urban scenarios in long-time collections of single-polarization satellite data is the Permanent Scatterers (PSs) [Ferretti,01]. This technique is based on the estimation of the parameter D_A, which is referred to as *Dispersion* index, defined as

$$D_A = \frac{\sigma_A}{m_A} \tag{7.5}$$

being m_A and σ_A the mean value and the standard deviation of the amplitude samples of the pixel along the image set, respectively. Precise statistical hypotheses allow one to relate D_A to the dispersion of the absolute phase. Essentially, the resolution cell is modeled as a Swerling target of type 1 [Skolnik,90]. When it is illuminated from a wide set of incidence angles, the amplitude of the backscattered signal from a PS is Rice distributed [Papoulis, 84]

$$f_A(a) = \frac{a}{\sigma_n^2} I_0\left(\frac{aA_0}{\sigma_n^2}\right) e^{-\left(a^2+A_0^2\right)/2\sigma_n^2} \tag{7.6}$$

where I_0 is the modified Bessel function of the first order, σ_n^2 is the variance of the additive complex circular Gaussian noise of real and imaginary parts of the signal, and A_0 is the PS complex reflectivity. It can be demonstrated that for high signal-to-noise ratio (SNR), namely higher than 15 dB, the Rice distribution approaches a Gaussian distribution and the pixel's phase stability can be associated to its amplitude dispersion as follows

	D_A^{hh} / D_A^{vv}	$\sigma_\varphi^{hh} / \sigma_\varphi^{vv}$
Day	0.056 / 0.038	0.055 / 0.054
Night	0.031 / 0.024	0.046 / 0.031

Table 7.2: Co-polar estimate of D_A and σ_φ [rad] concerning the target C_1 in the case of diurnal and nocturnal monitoring activity.

	$D_A^{hh} / D_A^{hv} / D_A^{vv}$	$\sigma_\varphi^{hh} / \sigma_\varphi^{hv} / \sigma_\varphi^{vv}$
P_1	0.35 / 0.09 / 0.05	0.25 / 0.28 / 0.05
P_2	0.18 / 0.25 / 0.28	0.06 / 0.23 / 1.30
P_3	0.52 / 0.53 / 0.65	0.17 / 0.09 / 0.56

Table 7.3: Polarimetric estimate of D_A and σ_φ [rad] in the case of nocturnal monitoring activity concerning the targets P_1, P_2 and P_3. Red numbers indicate the anomalous cases.

$$D_A \simeq \frac{\sigma_n}{A_0} \simeq \sigma_\varphi \tag{7.7}$$

where σ_φ stands for the absolute phase dispersion. The larger the number of images, the more reliable the statistical analysis, being the desirable minimum number of scenes around 30. According to simulation described in [Ferretti,01], Eq. 7.6 is valid for D_A lower than 0.25 and it implies a maximum σ_φ of 14°. Although time scales longer than one day are generally considered, this parameter might be useful for the detection of reliable pixels also in gbSAR acquisitions. It is worth pointing out that the different observation geometry of terrestrial and satellite platforms, which are compared in Fig. 7.10, does not represent an issue since the statistical hypotheses are exactly the same.

Concerning the area of the Station district in Sallent, a minimum SNR of 30 dB is guaranteed for pixels belonging to man-made targets. Then, the expected value for D_A is in the order of 0.04. With respect to the classical *PS* formulation, a further comment is in order. Residual errors related to the atmospheric phase-artefacts compensation procedure might also affect σ_φ. Theoretically, this contribution to phase uncertainty is statistically independent of the additive noise and the absolute phase dispersion can be expressed as

$$\sigma_\varphi = \sqrt{\sigma_n^2 + \sigma_{atm}^2(r)} \tag{7.8}$$

where the subscript *atm* denotes the artefacts residual errors contribution. Note that the term σ_{atm} has been modeled as a range-dependent parameter (see Section 6.4). The farther the target, the higher the uncertainty introduced by artefact residual errors. The estimation of D_A and σ_ϕ over the co-polar responses of C_1 in the diurnal and nocturnal cases are reported in Table 7.2. It can be noticed that despite the presence of this second term, the condition in Eq. 7.7 is fulfilled. As C_1 is located beyond the area of interest, it can be also stated that the effect of atmospheric residual errors onto the estimation of PSs absolute phase dispersion is negligible within the whole district

area. Once demonstrated that the PSs technique can be meaningfully applied to gbSAR acquisitions, it is worth recalling the main hypothesis behind this model. The time-samples employed for estimating D_A must belong to the same statistical process, i.e. the target backscattering process must be *stationary* in time. If now the sudden transitions shown in Fig. 7.5a, Fig. 7.6a and Fig. 7.10a-b are considered, an explanation of this variability in terms of additive noise effects is not possible. The reason is twofold. On the one hand, very low values of SNR should be assumed. On the other hand, the statistical properties of the AWGN noise [Papoulis,84] [Carlson,86] make the probability to obtain such regular discontinuities null. These effects are instead caused by the non-stationary behavior of the targets. In order to show this, the values of D_A and σ_φ concerning the targets P_1, P_2 and P_3 are reported in Table 7.3. For the estimation, the whole time-samples profiles have been used. It is easy to observe that amplitude and absolute phase dispersions in red do not satisfy Eq. 7.7. The reason is that the term A_0 describing the response of the PS cannot be assumed constant along the observation period. It follows that using the *PS* technique for detecting stable targets might lead to select unreliable pixels, as for P_1 in the *hv* polarization, or to cast out pixels carrying stable phase information, as for P_3 in *hh* and *hv* polarizations.

In conclusion, the statistical model proposed in [Ferretti,01] cannot be directly employed to deal with the urban pixels non-stationary behaviors shown up by the gbSAR data sets. A modified approach based on the PS idea but tailored to the properties of the terrestrial continuous monitoring must be hence worked out.

7.3.2. Modified Permanent Scatterers approach

The response of a time-invariant deterministic target in an atmosphere-compensated collection of gbSAR daily acquisitions is mainly affected by additive noise. This scattering condition may be modeled as a random walk plus a constant phasor process [Goodman,75] [Ferretti,01]. Despite urban scatterers are generally included in this category, in the previous sections it has been shown that sudden changes might affect the temporal stability of polarimetric amplitude and phase components within the man-made environment of Sallent. The plots in Fig. 7.5a and Fig. 7.8a give a clear example of the different backscattering patterns which might alternate in the description of urban pixels under fixed observation geometry. In the case of anomalous transitions, the stationarity hypothesis of the scattering process fails and any statistical analysis based on this

assumption turns out to be unsuitable. For this reason, an alternative technique is here proposed to cope with the description of urban environments' daily scattering behavior.

The rationale is to split the whole set of daily samples concerning a deterministic target into non-overlapping subsets where the variations of amplitude and phase quantities are always lower than fixed thresholds, i.e., where the scattering process may be assumed stationary in time. The final result is a set of disjoint subsets ordered by cardinality that described the different time-stationary behaviors that the target shows during one-day. The main assumption is that the subset with the highest cardinality provides the most reliable description of the target. As it has been shown in Section 7.3.1, amplitude and absolute phase are not related by Eq. 7.7 under the non-stationarity assumption so that their stability must be studied separately. In [Ferretti,01], it is pointed out that the amplitude parameter is generally more robust to targets modifications. For this reason, the amplitude information is analyzed first.

Let $a_{k,i}^{w}$ denote the i*th* amplitude sample in dB of the *k* polarization channel of $\left[\widehat{S'}\right]_i^w$ measured by the gbSAR sensor during the day *w*. In addition, let Th_A define a generic maximum amplitude discontinuity threshold. The daily information of each pixel of the image may be expressed as

$$A_k^w = \left\{ a_{k,1}^w, .., a_{k,N_w}^w \right\} = \bigcup_{i=1}^{N_k} A_{k,i}^w \tag{7.9}$$

where $A_{k,i}^w = \left\{ a_{k,m}^w \in A_k^w \,/\, \left| a_{k,i}^w - a_{k,m}^w \right| \le Th_A \right\}$ and $\cup$ denotes the set union operator. Note that the term $A_{k,i}^w$ essentially contains all the elements of A_k^w that present whose absolute distance from the reference sample $a_{k,i}^w$ is lower than Th_A. It follows that the subsets $A_{k,i}^w$ are non-disjoint subsets of A_k^w and some of them might be even equivalent. Denoting with # the cardinality set operation and with $I_{w,1} = \left\{ 1, ..., N_w \right\}$ the set containing the indices of day *w* samples, subset useless repetition are eliminated by defining the first stationary subset $B_{k,1}^w$ of A_k^w as

$$B_{k,1}^w = A^w_{k,\min\left\{ i \in I_{w,1} / \# A_{ki}^w = \max_{j \in I_{w,1}} \# A_{k,j}^w \right\}} . \tag{7.10}$$

where "max" operator makes it possible to detect the subset A_{ki}^w with the highest number of elements while "min" operator is introduced to solve possible ambiguous equal-cardinality cases. Denoting with "\" the set difference operator, the complementary set of $B_{k,1}^w$ in A_k^w is given by

$$F_{k,1}^w = A_k^w \setminus B_{k,1}^w , \tag{7.11}$$

the other disjoint subsets $B_{k,m}^w$ of A_k^w are iteratively provided by the conditions here below

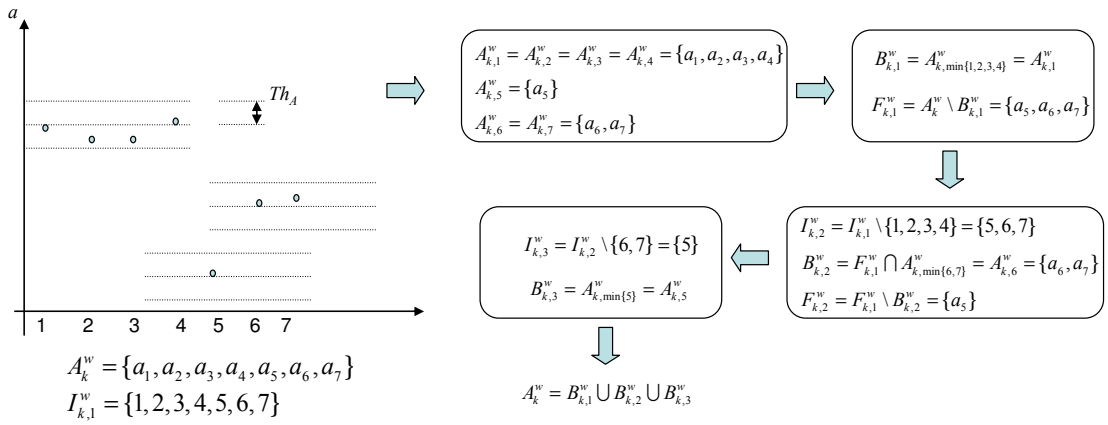

Fig. 7.11: Sketch of the selection procedure splitting the pixel's collection of gbSAR amplitude samples $A_{k,1}^w$ acquired on day w in the polarization channel k into regular disjoint subsets $B_{k,i}^w$ fulfilling the time-stationary condition derived from the PS formulation.

$$\begin{cases} I_{w,m} = I_{w,m-1} \setminus \left\{ j \in I_{w,m-1} \,/\, a_{k,j}^w \in B_{k,m-1}^w \right\} \\ B_{k,m}^w = F_{k,m-1}^w \cap A^w_{k,\min\left\{ i \in I_{w,m} / \#\left(A_{k,i}^w \cap F_{k,m-1}^w \right) = \max\limits_{j \in I_{w,m}} \#\left(A_{k,j}^w \cap F_{k,m-1}^w \right) \right\}} \\ F_{k,m}^w = F_{k,m-1}^w \setminus B_{k,m}^w \end{cases} . \tag{7.12}$$

The iterative procedure continues until it is fulfilled the condition

$$\bigcup_{i=1}^{M_k} B_{k,i}^w = A_k^w \tag{7.13}$$

where $\cup$ denotes the disjoint union set operator. This formulation joins all the samples describing a specific amplitude behavior of a target that have repeated during the whole observation period, even inconsecutively. The sub-segment $A_{k,1}^w$ containing the highest number of samples is assumed to represent the pixel more likely behavior. A simple example resuming the basic steps carried out by the iterative selection technique is shown in Fig. 7.11 for a group of seven acquisitions.

After selecting the samples guaranteeing a stable amplitude profile in the k polarization channel, their phase information is considered. In order to filter out significant phase discontinuities, a maximum threshold for phase jumps, Th_ϕ, is introduced.

Denoting with $\Phi_{k,1}^w$ the set containing the phase information of the samples defined by $B_{w,1}$, it results

$$\Phi_{k,1}^w = \bigcup_{n=1}^{N} \Phi_{k,1,n}^w \tag{7.14}$$

where each subset $\Phi_{k,1,n}^w = \left\{ \varphi_{k,1,m}^w \in \Phi_{k,1}^w \,/\, \left| \varphi_{k,1,m}^w - \varphi_{k,1,n}^w \right| \le Th_\varphi \right\}$. The process described for the amplitude parameter can be now applied to the absolute phase, yielding

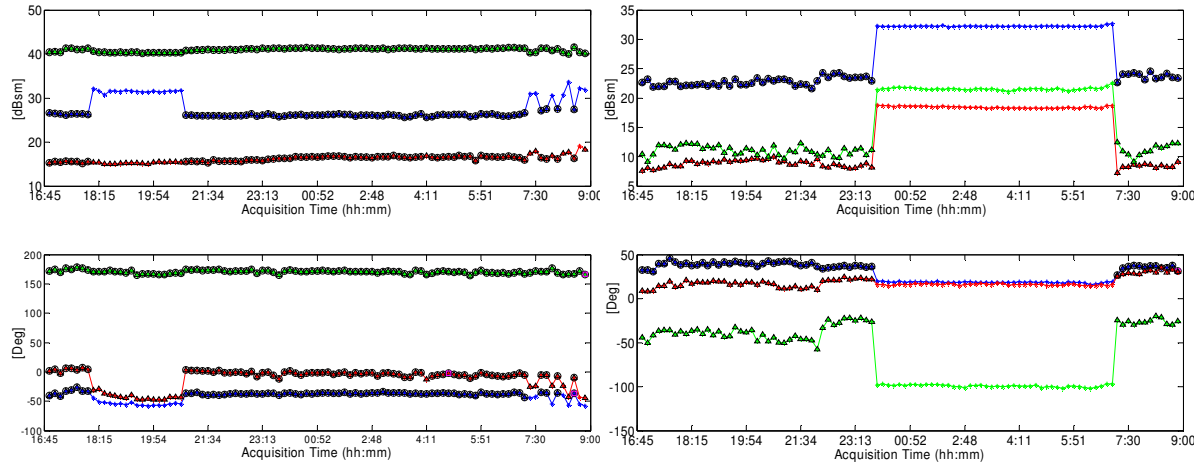

(a) (b)

Fig. 7.12: Time-stationary amplitude ($B^7_{hh,1}$, $B^7_{hv,1}$, $B^7_{vv,1}$) and absolute phase ($C^7_{hh,1,1}$, $C^7_{hv,1,1}$, $C^7_{vv,1,1}$) subsets selected within the temporal polarimetric profiles of the targets P_1 (a) and P_2 (b). The Δ and O label a sample fulfilling the amplitude and phase stability criteria, respectively. $Th_A = 2dB$ and $Th_A = 10^o$ have been used for the selection. Note that in for P_2 it results $\#C^7_{hh,1,1} = \#C^7_{hv,1,1} = 0$

$$\bigcup_{i=1}^{M_k} C^w_{k,1,i} = \Phi^w_{k,1} \tag{7.15}$$

where $C^w_{k,1,i}$ define the disjoint subsets of $\Phi^w_{k,1}$ ordered by cardinality. Similarly, the phase stability procedure can be applied to the rest of $I_{w,m}$ indices subsets. At the end of the process, the time samples of the analyzed pixel are described as the union of disjoint regular subsets. A specific subset $C^w_{k,1,i}$ is finally labeled as reliable if its cardinality is higher than $N_w / 2$.

In order to interpret each subset in terms of an idependent backscattering stationary process, the values of Th_A and Th_ϕ must be physically meaningful. For this purpose, the regularity condition defined in [Ferretti,01] may be employed to calculate amplitude and absolute phase thresholds. Taking into account the high SNR characterizing man-made targets within the gbSAR acquisitions, a more restrictive constraint than 0.25 can be chosen for D_A. In the following, these two stability conditions are fixed to

$$\begin{aligned} Th_A &= 2dB \\ Th_\phi &= 10^o \end{aligned} \quad . \tag{7.16}$$

where Th_A has been obtained by transforming Eq. 7.7 into a dB relationship. It is worth pointing out that the criterion works at single pixel level, preserving the image space resolution. Moreover, the algorithm is independent of the wave polarization and can be successively applied to all the elements of [*S*] separately. An example of the results provided by the described technique concerning the targets P_1 and P_2 is shown in Fig. 7.12. Regarding P_1, for each polarimetric channel it is possible to select a useful subset. But since the profiles regularity is

polarization-dependent, the samples corresponding to each stationary subset might be different. For instance, the whole *vv* profile gets through the amplitude and phase stability criterion, meaning that the projection of the dominant scattering behavior within the pixel on this polarization is time-stationary ($\#C^7_{vv,1,1} = N_7$). Contrarily, its projection on the other two channels reveals a time-instability of the scattering process that leads to reduce the number of useful samples ($\#C^7_{hh,1,1}, \#C^7_{hv,1,1} < N_7$). Concerning P_2, just the *vv* channel is considered stable. In fact, despite $\#B^7_{hh,1}, \#B^7_{hv,1} > 0$, it results $\#C^7_{hh,1,1}, \#C^7_{hv,1,1} = 0$. As a matter of fact, the *hh* profile of P_2 shows an example of a significant absolute phase discontinuity that cannot be detected through the analysis of target's amplitude carried out by PS technique.

The study can be now extended to the whole area of interest.. The result obtained for the three polarimetric channels within the Station district during the diurnal and the nocturnal monitoring activity are displayed in Fig. 7.13a and Fig. 7.13b, respectively. As it has been pointed out by the Pauli's decomposition, the total backscattered power is mainly distributed among the diagonal of [*S*]. This is due to the buildings orientation with respect to the synthetic aperture alignment. For this reason, a specific category, the blue one, has been used for describing the pixels meeting the amplitude and phase regularity conditions in both co-polar channels. The red, green and yellow colors indicate the case the stability conditions are fulfilled just in the *hh*, *hv* or *vv* channel, respectively. Grey points fulfill only the amplitude criterion at least in one channel. Finally, the white background is made up of pixels that do not get through the amplitude test in any polarimetric channel or that show a too low amplitude mean value. As the *hv* generally shows a very low backscattering power level, the minimum power requirement was fixed 7 dB below the co-polar threshold. A quantitative description of the same result is given in the Table 7.4. For each co-polar channel, it is reported the number of pixels selected by amplitude criterion (black) and of pixels that also got through the phase condition (blue). The use of the union and intersection set operations demonstrates that the combination of *hh* and *vv* channels makes the number of stable points increase about 50% with respect to the selection obtained with just one of them. Besides, the information each co-polar channel carries is complementary. The number of stable pixels selected just in the *hv* polarization is significantly lower than the results of the two diagonal terms of [*S*]. Yet, this channel might be exploited in order to enhance the quality of the district description by recovering pixels that turn out to be instable in the *hh* and *vv* polarizations. Another important conclusion that can be drawn from both qualitative and quantitative analyses is the

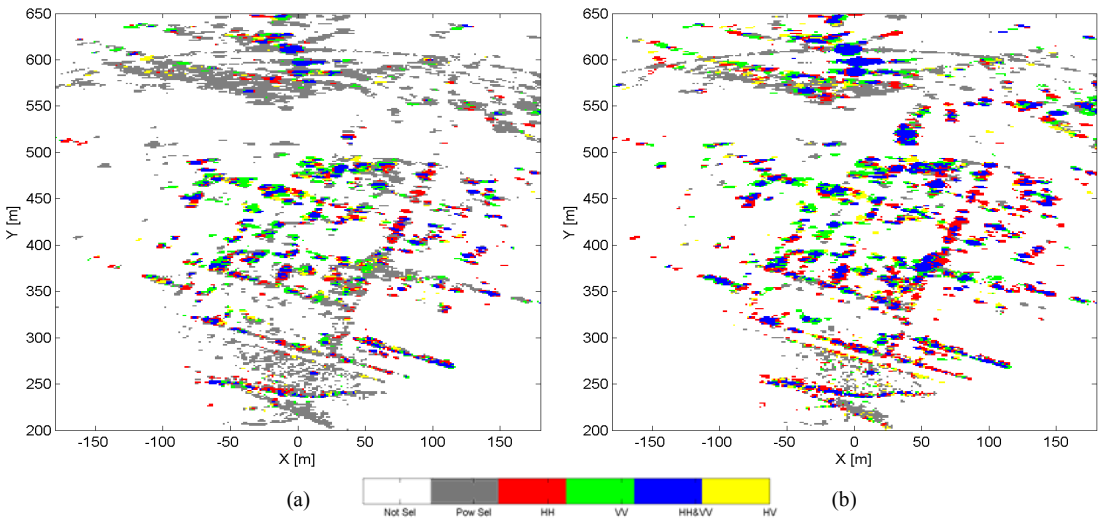

Fig. 7.13: Polarimetric analysis of pixels fulfilling the condition $\#C^{w}_{k,1,1} \geq N_w / 2$ in the diurnal (a) and nocturnal (b) monitoring activities carried out on 20/10/06 and 18/12/06, respectively. Grey color indicates the pixels fulfilling only the amplitude stability criterion at least in one channel, blue color the pixels fulfilling both amplitude and phase criteria in the two co-polar channels, red, green and yellow colors denote the pixels getting though the two criteria just in the *hh*, *vv*, or *hv* channel, respectively. The selection thresholds are $Th_A = 2dB$, $Th_\varphi = 10°$. Minimum amplitude thresholds of 5dB for *hh* and *vv* and -2dB for *hv* have been also used to stress the man-made structures.

the different behavior of the urban area in the case of nocturnal and diurnal observations. Concerning the amplitude quantity, the number of pixels fulfilling the stability condition is approximately the same in both cases. Contrary, the absolute phase behavior turns out to be significantly different. During the night, a percentage of only 15% of amplitude stable pixels is filtered out by the phase condition. A decrease of about the 50% of pixels is instead observed when the diurnal collection is analyzed. This trend has been confirmed by the rest of day and night acquisitions. Finally, the diurnal versus nocturnal results lead to infer that the polarimetric instability shown by urban targets is explainable in terms of dynamic configuration that this type of scenario may assume during a whole day. Since its scattering properties have turned out to be more mutable during the day than the night, the daily human activity turns out to be the most plausible cause for non-stationary urban backscattering process.

7.3.3. Temporal entropy H_T

The study of the daily evolution of scatterers within the Station district of Sallent has made it possible to stress the night/day contrasting properties of the observed test-site. Polarization channels have turned out to be differently affected by targets' changes. Besides, the quantitatively analysis reported in Table 7.4 has shown the complementary information that the different elements of [*S*] are able to provide. It is important to recall that these results have been obtained by

	hh *A* / φ	*hv* *A* / φ	*vv* *A* / φ	*hh*∩*vv* *A* / φ	*hh*∪*vv* *A* / φ	*hv**hh*∪*vv* *A* / φ
DAY	6629 3098	3513 1731	7268 3108	3812 1552	10085 4654	1404 535
NIGHT	7206 6023	4610 3543	6478 5322	3838 3126	9946 8219	1722 1342

Table 7.4: Pixels Selection:Diurnal vs Noctural Measurements. The amplitude is threshold $Th_A = 2dB$ whereas the phase threshold is $Th_\varphi = 10^o$.

studying each polarimetric channel separately. To make out if the instability of the polarimetric temporal profiles induces a modification of the dominant scattering mechanism within the resolution cell, the information carried by the full scattering matrix must be considered at once. A general and assessed descriptor for the degree of randomness of the signal backscattered by an illuminated target is the polarimetric entropy *H* [Cloude,96], defined in the monostatic case as

$$H = \sum_{i=1}^{3} -P(\lambda_i)\log P(\lambda_i) \quad P(\lambda_i) = \frac{\lambda_i}{\sum_{j=1}^{3}\lambda_i} \tag{7.17}$$

where the terms λ_i are the eigenvalues of the Coherency and Covariance matrices, usually indicated as [*T*] and [*C*] (see Section 2.3.2). By construction, *H* varies in the range [0,1]. Owing to the lack of temporal sequence of satellite or airborne zero-baseline PolSAR data, the estimation of *H* has been always performed in the spatial domain under the hypotheses of ergodicity and spatial stationarity of the scattering process. A widely shared interpretation relates *H* to the spatial presence of multiple and orthogonal scattering mechanisms. Very low values denote areas characterized by the presence of a dominant mechanism. As its value increases, it is usually inferred that more mechanisms spatially coexist in the area the average operation is extended to. For these reasons, the statistical meaning of *H* makes this descriptor especially suitable to deal with natural targets. When urban zones are observed, the deterministic nature of this type of environment provides very low values for entropy. At least, this is expected as far as the stationarity hypothesis is fulfilled within the estimation window. When low-medium *H* values are obtained over urban areas, it is generally assumed that the spatial average has been likely extended to pixels belonging to different deterministic targets. Therefore, the information mixing makes the entropy global value increase. In contrast to this classical approach, the collection of data sets acquired by the UPC sensor provides a new dimension to play with: the time. Then, it is possible

to estimate this polarimetric descriptor in the time domain without degrading the resolution of the image. Let's consider the collection of N_w scattering matrices describing the behavior of a pixel during the day w. Denoting with $[\Psi_P]$ the Pauli's set of orthogonal 2x2 complex matrices, it is possible to estimate a *time* coherency matrix $[T_t]$ as

$$[T_t]_w = \sum_{i=1}^{N_w} V\left(\widehat{[S']}_i^w [\Psi_P]\right) \cdot V\left(\widehat{[S']}_i^w [\Psi_P]\right)^{\dagger} \tag{7.18}$$

where V and † stand for the matrix trace and the vector transpose-conjugate operators, respectively. As $[T_t]_w$ is a hermitian semipositive matrix by construction, it can always be decomposed as

$$[T_t]_w = \sum_{i=1}^{3} \lambda_i^t \overrightarrow{u_i^t} \overrightarrow{u_i^t}^{\dagger} \ . \tag{7.19}$$

Then, the temporal entropy H_T is directly obtained by substituting the terms λ_i^t in Eq. 7.17. Taking into account the perfect zero-baseline configuration of the gbSAR sensor, possible spatial inhomogeneities are excluded. It follows that under the hypotheses of ergodicity and time stationarity, the matrix $[T_t]_w$ describing the scattering process from an urban environment is expected to present a rank close to 1 and, consequently, a value of H_T close to zero. In Section 7.3.2, it has been stressed that irregular one-day profiles often characterize the urban scatterers' response. The sudden changes have been justified in terms of non-stationary behaviors of the targets that make the dominant scattering mechanism within the resolution cell vary along the time axis. When this occurs, the rank of $[T_t]_w$ increases and H_T turns into a polarimetric descriptor sensitive to non-stationary properties of the backscattering process.

In order to demonstrate this, simulated data are first analyzed. Observing the sudden transition in Fig. 7.7a, it is clear that each polarization might change independently. According to Section 2.3, the maximum number of degrees of freedom of [*S*] associated to a point-target in the monostatic case is six, corresponding to the three amplitude and three absolute phase quantities. For the sake of clarity, a simplified case where only a sudden discontinuity affects one phase term is here examined. The phase jump varies in the [0°:180°] range within a set of 30 scattering matrices. This corresponds to the minimum number of data sets usually at disposal for each day of measurements in Table 7.1. The sample where the transition occurs is not fixed in the sequence, but changes from the first to last position. The corresponding values of H_T are displayed in Fig. 7.14a. The position of the maximum describes the condition of power equality between the two polarimetric

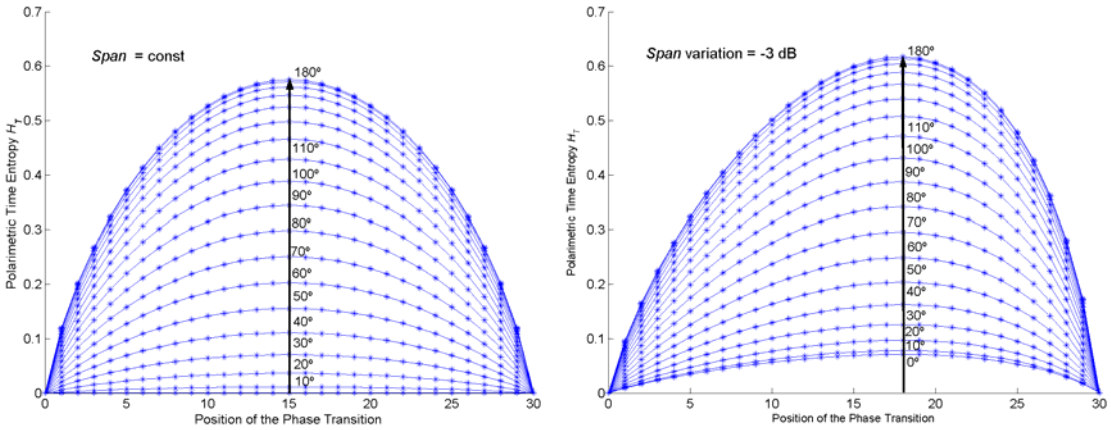

(a) (b)

Fig. 7.14: Study of the variation of the time entropy H_T induced by a phase jump $\Delta\varphi = 10^{\circ}$ affecting only one polarization channel (a) and by a combination of amplitude and phase jumps (b) over a set of 30 samples. In the two images, the phase discontinuity goes from 0º to 180º and its position varies form the first to the last samples along the *x* (*time*) axis. Contrarily, the amplitude discontinuity in (b) is fixed and equal to -3dB.

behaviors. As the sudden change affects absolute phase terms, the *span* of [*S*] keeps constant. Then, it is just the number of samples before and after the transition that determines the weight each scattering mechanism has in the average operation described by Eq. 7.18. This explains the perfect symmetry of the curves in Fig. 7.14a. In the case the span changes too, i.e., the phase discontinuity comes along with an amplitude jump ΔA, the curves becomes asymmetric and the maximum moves to a new equilibrium position. As example, the H_T behavior in the case a fixed ΔA equal to -3dB sums to the above-described phase discontinuity is shown in Fig. 7.14b. In both images, the worst condition is defined by the 180º phase variation. This is reasonable, since it corresponds to the case the first scattering mechanism turns into a new orthogonal one ($H_T \sim 0.6$,). When two polarizations are affected the same way, the maximum value of H_T decreases. Finally, it becomes negligible when the same discontinuity involves all the polarimetric elements. The reason is that H_T increases only if the transition alters the reciprocal relations among the terms of [*S*]. On the contrary, it is insensitive to any kind of common discontinuity due to span modifications or common phase offsets, which do not induce any change in the scattering mechanism characterizing the pixel. This type of behavior can be observed by comparing the plots in Fig. 7.5a and 7.10b: discontinuities in target's amplitude and phase profiles do not necessarily provoke significant discontinuities of the Pauli's normalized components, demonstrating that non-stationary behaviors of a target do not always turn into a significant change of its dominant scattering mechanism.

If more complex configurations are considered, H_T can reach very high values. Keeping into account the results provided by simulations, it is now possible to interpret correctly the meaning of

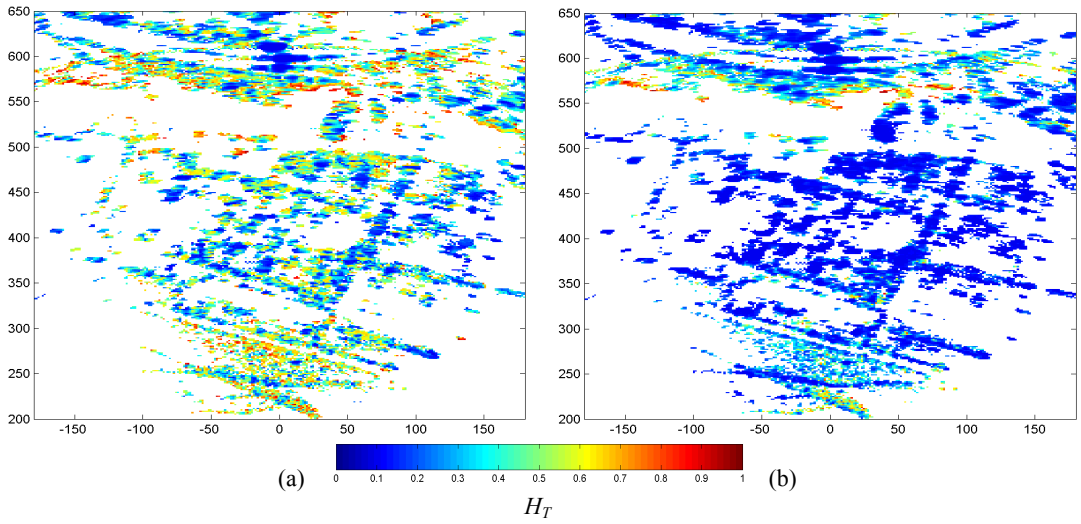

Fig. 7.15: Distribution of the polarimetric temporal entropy H_T within the Station district of Sallent in the diurnal (a) and nocturnal (b) monitoring activities carried out on 20/10/06 and 18/12/06, respectively. 30 temporal samples, acquired in about 8 hours have been employed for the estimation of the Coherency matrix $[T_t]$ in both cases.

H_T when it is estimated, pixel by pixel, over real gbSAR zero-baseline time collections. The resut obtained with the diurnal and nocturnal measurements analyzed in Section 7.3.2 are shown in Fig. 7.15a and Fig. 7.15b, respectively. In order to carry out a meaningful comparison, a set 30 PolSAR acquisitions selected in a period of about 6 hours have been employed. Besides, a common *span* mask has been applied to focus the attention only on pixels belonging to man-made structures.

In accordance with the results of the coherent analysis, the H_T distribution reveals that a much higher number of low-entropy pixels are detectable during the night than the day. This conclusion is corroborated by the time-entropy histograms displayed in Fig. 7.16, which correspond to the 10 days of measurements reported in Table 7.1. Diurnal and nocturnal collections are plotted in red and blue, respectively. The two bulk lines indicate the two days displayed in Fig. 7.15a (20/10/06) and Fig. 7.15b (18/12/06). For the night case, about the 70% of the high-reflectivity pixels show a value of H_T lower than 0.1. During the day this percentage decreases to the 18%. The deterministic nature of the main scatterers within the area makes H_T maintain around medium values, although a non-negligible number of pixels (about 20%) shows a value higher than 0.6. Again, the results induce to identify the human activities, which are supposed to be more frequent during the day than the night, as the predominant cause of the urban scatterers' instability. At the same time, the histograms confirm the sensitivity of the polarimetric temporal entropy H_T to detect temporal changes in the polarimetric behavior of the deterministic targets.

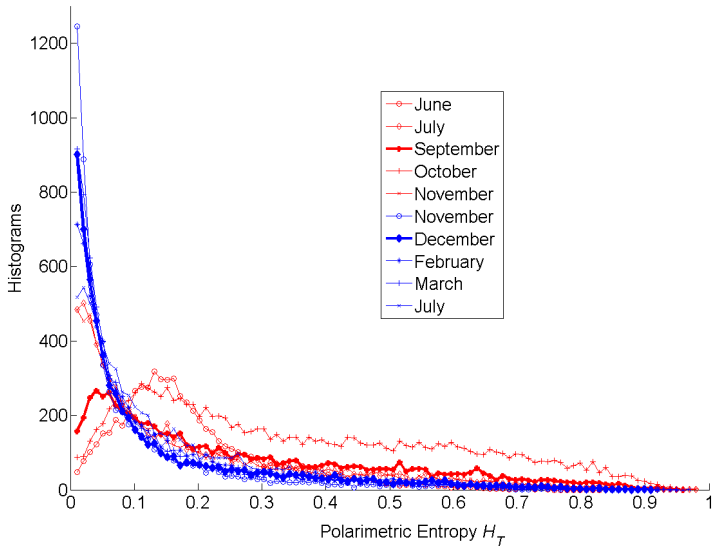

Fig. 7.16: Histograms of the polarimetric entropy H_T distribution concerning the 10 days of measurements reported in Table 7.1. Red and blue lines denote the diurnal and nocturnal monitoring activities, respectively. The two bulk lines correspond to the two days displayed in Fig. 7.15a (20/10/06) and Fig. 7.15b (18/12/06).

7.4 Urban environment long-time instability

The study carried out in the previous section has dealt with the behavior of the high-reflectivity deterministic scatterers in a short-time scale. The daily collections of gbSAR data have been analyzed separately to prove that the backscattering process within an urban environment may be non-stationary. Some conclusions about the different trends of nocturnal and diurnal acquisitions have been also drawn. It is now reasonable to extend the analysis to the whole collection of measurements at disposal. But before doing this, some comments are in order. As explained in Section 4.5, the procedure employed to polarimetrically calibrate the sets of one-day acquisitions introduces a common phase offset equal to

$$\varphi_{0,w} = 2kr_{t,w} \tag{7.20}$$

being $r_{t,w}$ the calibrator's range distance on day w and k the wavenumber. Moreover, the radiometric absolute calibration is related to the precision of the alignment of the co-polar calibrator with respect to the center of the SSA. As the corner reflector used for this purpose was positioned within the scenario before starting the acquisition process and removed at the end of the day, a different phase and amplitude offsets must be assumed for each daily collection. From a theoretical point of view, the corner reflector C_1 mounted on the concrete pillar detailed in Fig. 7.7 was expected to provide a long-time stable reference to compensate for them. Nevertheless, its long-time answer, which is displayed in Fig. 7.17, shows that the relation between the two

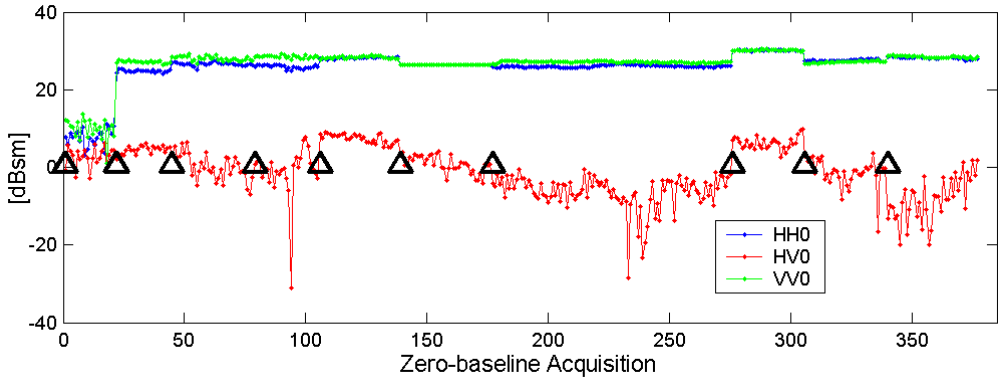

Fig. 7.17: Polarimetric amplitude profiles of C_1 during the 10 days of measurements reported in Table7.1. The triangles indicate the first measurements of each day reported in Table 7.1. Note that the reference point is available from the day2 (July 26th 2006) on.

co-polar channels did not keep constant during the one-year campaign. Since neither C_1 nor urban targets can be employed to compensate for these offsets, the technique introduced in Section 7.3.2 cannot be directly applied to the one-year gbSAR data collection: non-compensated offsets might lead to misinterpret discontinuities due to calibration errors as targets backscattering changes and to filter out useful time-samples. Then, a different strategy has been pursued.

The problem of amplitude and phase offsets can be circumvented by studying the temporal evolution of the normalized-to span Pauli's components (NPCs) at pixel level. In fact, this coherent decomposition is insensitive to absolute phase offsets. Besides, the normalization to the span makes it possible to nicely solve the problems related to the amplitude offsets through the study of the percentages of the total backscattered power dividing up among the three elementary mechanisms.

Following this idea, the long-time analysis of the urban targets' stability is split into three steps, each one described in a specific subsection. In Section 7.4.1, the high complexity of urban targets time-instability is stressed through the analysis of a few representative pixels. In Section 7.4.2, the time entropy H_T is employed to provide a comprehensive description of the whole area of interest in terms of long-time backscattering randomness. In Section 7.4.3, a procedure to detect stable stationary patterns repeating along the one-year collection is proposed.

7.4.1. Long-Time Real Data Analysis

In order to demonstrate the high complexity of long-time instability study, three high reflectivity pixels have been selected as example. The photos in Fig. 7.18a and Fig. 7.18b detail the deterministic targets the three pixels belong to. The first one is a part of a concrete wall (T_1) separating the two lanes of a highway close to the district; the other two targets, T_2 and T_3, are two

(a) (b)

Fig. 7.18: Pictures of the three high reflectivity scatterers selected for the long-time analysis: T_1 (a) is a part of a concrete wall separating the two lanes of the highway close to the urban area; T_2 and T_3 (b) are two close buildings located in the center of the Station district of Sallent.

close buildings located in the center of the urban area. The temporal evolution of their corresponding normalized Pauli's components is plotted in Fig. 19a-c. The triangles indicate the first sample of each daily collection reported in Table 7.1. It can be observed that T_1 exhibits a pure single-bounce backscattering behavior that maintains stable during the whole year. Regarding T_2 and T_3,, a different behavior arises in the diurnal and nocturnal sequences of gbSAR data sets. Let T_2 be studied first. While during the day a dominant dihedral-like reflection can be only inferred, during the night this scattering mechanism becomes clear and its stability increases. Nevertheless, a careful analysis shows that the weight of the two dominant components is not constant but slightly varies along one-day samples. As a matter of fact, the way the total power dividing up between the two components varies linearly, as indicating that a slow-time change is taking place. Owing to the gradualness of the process, these changes are likely to be induced by the atmospheric temperature and humidity daily gradients. In general, it is known that these two physical parameters directly affect the value of targets dielectric constant ε [Ulaby,90]. The effects of this modulation on the reflection mechanism are negligible at medium incidence angles, i.e. for satellite and airborne SAR acquisitions, but they may become significant in gbSAR observation geometries.

Concerning the measurements campaign in Sallent, the observation angle θ (see Fig. 5.2) ranges in [72º,82º] within the area of interest. Then, it is reasonable to assume that the double-bounce mechanism sketched in Fig. 7.20 mostly dominates the backscattering from the urban targets. Let ε_A and ε_B be the dielectric constants characterizing the surfaces A and B, respectively. The scattering matrix associated to the reflection process in the *BSA* convention may be expressed as

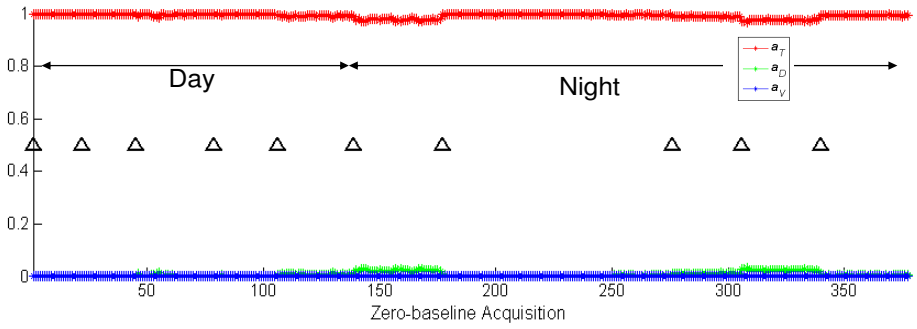

(a)

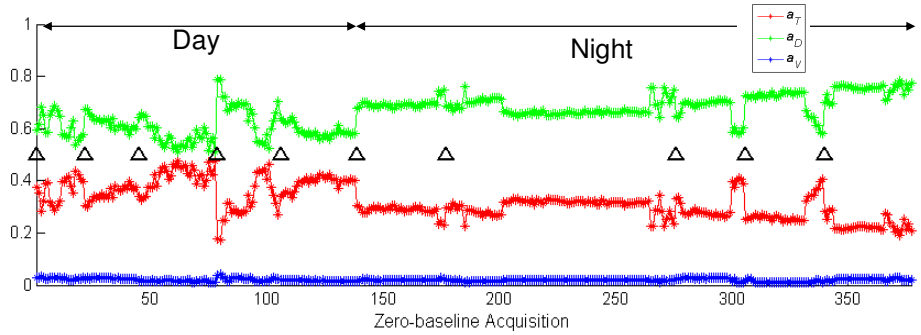

(b)

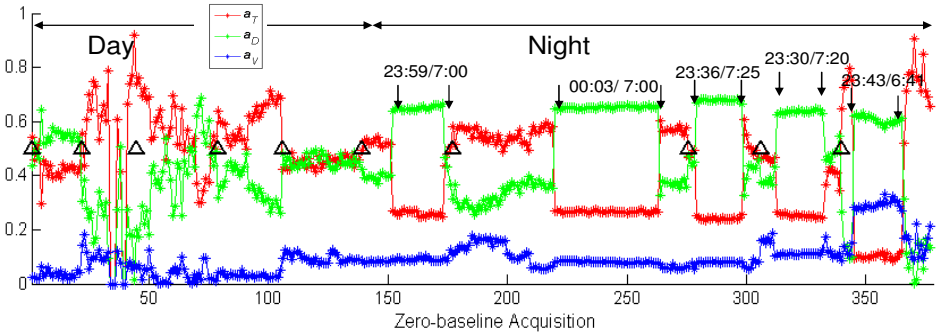

(c)

Fig. 7.19: Long temporal profiles of the normalized-to-span Pauli's components (*NPCs*) concerning the targets T_1 (a) , T_2 (b) and T_3 (c) detailed in Fig. 18a and Fig. 18b. The triangles indicate the first sample of the collection gathered during each day of measurements reported in Table 7.1. The black arrows in (c) indicate the time-samples delimiting the repeated pattern that T_3 showed during the nocturnal acquisitions.

$$[S]=\begin{bmatrix} Shh & 0 \\ 0 & Svv \end{bmatrix} = A \begin{bmatrix} R_{hhA}R_{hhB} & 0 \\ 0 & R_{vvA}R_{vvB} \end{bmatrix} \tag{7.21}$$

where the terms

$$R_{hhA} = \frac{\cos\theta_{inc} - \sqrt{\varepsilon_A - \sin^2\theta_{inc}}}{\cos\theta_{inc} + \sqrt{\varepsilon_A - \sin^2\theta_{inc}}} \qquad R_{hhB} = \frac{\sin\theta_{inc} - \sqrt{\varepsilon_B - \cos^2\theta_{inc}}}{\sin\theta_{inc} + \sqrt{\varepsilon_B - \cos^2\theta_{inc}}} \tag{7.22}$$

are the Fresnel coefficients describing the surface scattering process of *hh* and *vv* polarized incident waves [Cloude,96] [Ulaby,90]. Despite the geometry of the problem always generates a double-bounced reflection, it is not guaranteed that the term a_D in Eq. 7.1 is the main component.

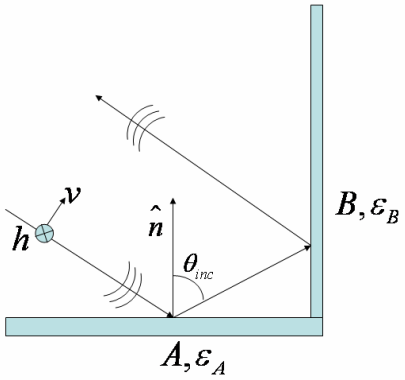

Fig. 7.20: Sketch of the double-bounce reflection geometry. ε_A and ε_B are the dielectric constant of surfaces A and B, respectively.

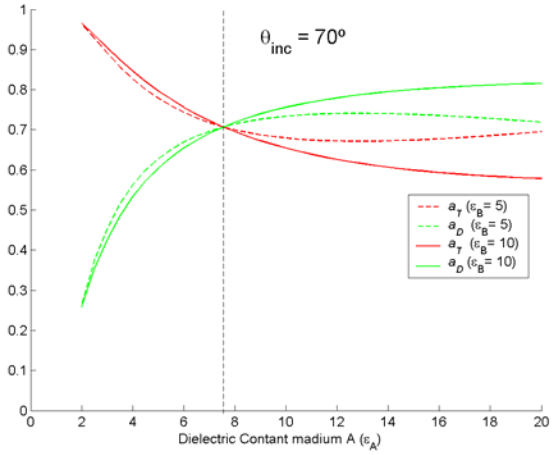

Fig. 7.21: Behavior of the normalized single-bounce a_T and double-bounce a_D Pauli's components concerning the reflection geometry in Fig. 7.20 as a function of ε_A and ε_B for $\theta_{inc} = 70°$.

	Dielectric Constant ε	
Material	Dry	Wet
Asphalt	[2:4]	[6:12]
Clay	[2:10]	[4:40]
Granite	5	7
Limestone	7	8
Sand	[4:6]	[10:30]
Concrete	[4:10]	[10:20]
Sandy Soil	[4:6]	[15:30]
Clay soil	[4:6]	[10:15]

Table 7.5: Examples of the relative dielectric constant ε of common materials.

In fact, the way the total power shares between the trihedral-like and dihedral-like channels at high incidence angle strictly depends on ε_A and ε_B. This can be observed in Fig. 7.21, where the behavior a_T and a_D is plotted as a function of the two dielectric constants. As a matter of fact, it is mainly ε_A that modulates the power distribution. The same intersection between the two curves, which indicates the changeover point between the two mechanisms, does not depend on ε_B but it changes just with the incidence angle θ. Denoting its corresponding value ε_A with ε_{ACO}, it can be shown that

$$\tan\theta_{Br} = \sqrt{\varepsilon_{ACO}} \tag{7.23}$$

where θ_{Br} is generally referred to as Brewster angle. Examples of the relative dielectric constant values concerning different types of materials in dry and wet conditions are reported in Table 7.5. In the light of this reasoning, the gradual exchange of energy between the first two Pauli's components of T_2 can be explained in terms of modulation of the dielectric constant induced by temperature and humidity gradients. This explanation is confirmed by the fact that in real

observation, as well as in simulation, the span quantity is nearly constant. Finally, it is worth pointing out that at high incidence angle the concept of trihedral-like and dihedral-like mechanisms loses a direct geometrical interpretation. This is the case of T_1,: its very stable trihedral-like mechanism is likely to be generated by a double-bounce reflection but, due to the particular observation geometry, it appears as an odd-bounce scattering. Concerning the target T_3, the plots in Fig. 7.19c clearly shows that no stable behavior can be detected in the diurnal observations. The first two components often invert their rule passing from being dominant to being secondary following a linear gradient (Day 3 and Day 4). In other cases the response of the pixel is completely chaotic (Day 2). When night measurements are instead analyzed, the polarimetric profiles of T_3 become very stable and the presence of a repeated stable pattern is also detectable. The time this change occurs turned out to be almost the same, as pointed out in Fig. 7.19c. This situation can be hardly explained in terms of dielectric constant variations. First of all, the transition is too abrupt. Besides, the gradient of atmospheric temperature and humidity strictly depends on the season. The last five days of measurements cover a period of about 7 months, from December 2006 to July 2007. Moreover, contrary to what happened for T_2, the span information is not preserved. This effects are likely to be caused by a human habit that periodically modifies some property of the target within the resolution cell and hence its polarimetric scattering response.

7.4.2. Long-time temporal entropy H_T analysis

The estimation of the time entropy H_T in the one-day collections of gbSAR data sets has made it possible to stress higher stability of urban targets during the night than the day. In other words, the probability that the dominant scattering from a high-reflectivity urban scatterer endures unchanged during a period of some hours turns out to be much higher during the night than the day. At this point, it is meaningful to extend this analysis to longer time-scales. According to the conclusions drawn in the short-time study, a low entropy distribution might be expected when H_T is estimated over the union of all the nocturnal measurements. Similarly, the set of all the diurnal collections is expected to present higher scattering randomness. The result obtained in the two cases is imaged in Fig. 7.22a and Fig. 7.22b, respectively. It can be seen that, despite the different behavior that the two monitoring condition show in the one-day analysis, the long-time diurnal and nocturnal H_T distribution is almost identical. Very few low-entropy pixels are detectable. Besides, their location is approximately the same in the two images. The target T_1 described in Fig. 7.19a and marked

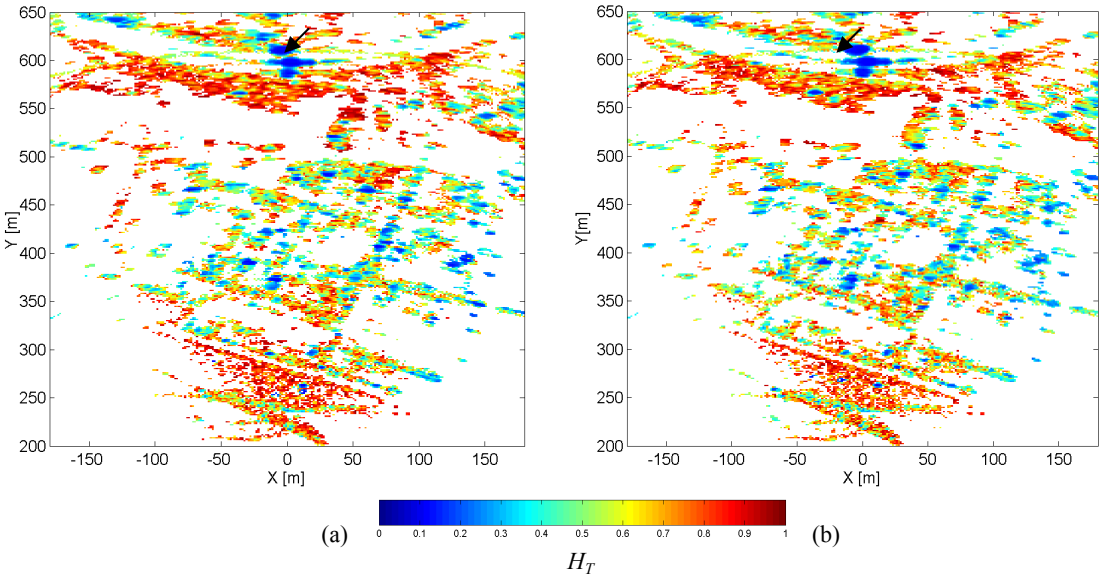

Fig. 7.22: Time entropy H_T estimated over six-month diurnal (a) and nocturnal (b) gbSAR acquisitions in Sallent.

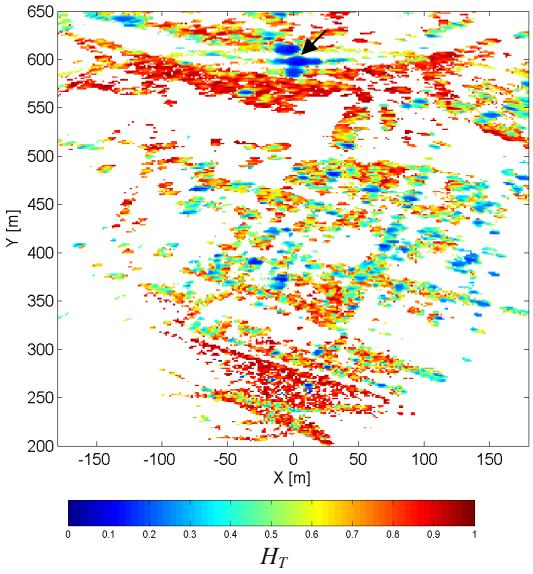

Fig. 7.23: Time entropy H_T estimated over the one-year collection of gbSAR acquisitions in Sallent.

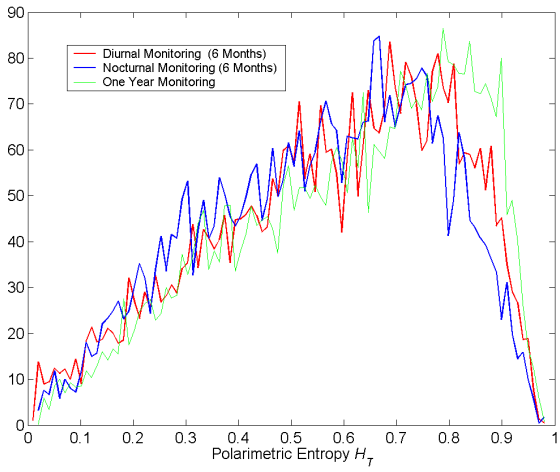

Fig. 7.24: Histograms of H_T distribution in Fig. 7.22a (red), Fig. 7.22b (blue) and Fig. 7.23 (green).

by a black arrow constitutesa representative example. For the sake of completeness, H_T has been estimated over the whole one-year PolSAR data collection and displayed in Fig. 7.23. The histograms of the long-time H_T distributions in Fig. 7.24 quantitatively confirm that no significant difference is detectable in terms of targets stability concerning the three cases. In order to understand the reason for which night and day collections show a so similar behavior, it is worth reminding the physical and mathematical meaning of the time entropy descriptor. In essence, H_T is sensitive to the presence of mathematically orthogonal scattering mechanisms in the estimation of $[T]$ and $[C]$ (see Eq.7.18). Being m and n two time-samples of the long-time PolSAR collection,

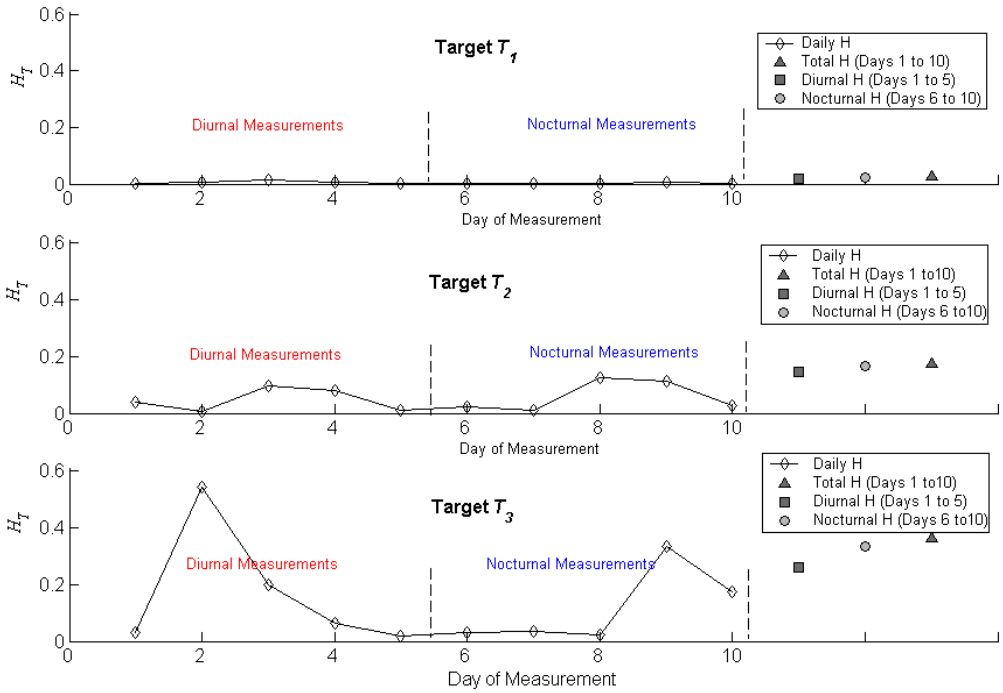

Fig. 7.25: Time entropy H_T concerning the targets T_1, T_2 and T_3 calculated using each daily collection of gbSAR acquisitions in Sallent separately, the whole sets of diurnal and nocturnal acquisitions, and all the measurements.

they contribute to increase the value of H_T if fulfilling the condition

$$\vec{k}_P^{\,n} \cdot \vec{k}_P^{\,m} \ll 1 \tag{7.24}$$

where $\vec{k}_P$ is the Pauli's scattering vector defined in Eq. 2.47. The higher the number of samples satisfying Eq.7.24, the higher the randomness of the scattering process, i.e. H_T. It follows that the irregularity that mainly characterizes the diurnal polarimetric profiles does not necessary make H_T increase. Similarly, the very stable but discontinuous profiles characterizing the nocturnal response of the urban targets are likely to increase the overall value of H_T. The behavior of the three targets analyzed in Section 7.4.1 might come in handy to better understand this issue. The sequence of their corresponding one-day and long-time entropy values is displayed in Fig. 7.25. As T_1 always shows an almost pure trihedral-like behavior, H_T keeps always very low. T_2 presents fluctuations in time that seem to be independent of the part of the day data are gathered. In fact, an anomalous value is obtained for Day 3, Day 4, Day 8 and Day 9. Observing the corresponding profile of Fig. 7.19b, it can be seen that in the first case a steep linear modulation between single and double bounce is present. For the other three days, the increment is caused by a sudden discontinuity introducing a different scattering behavior that keeps constant for several time samples. When the one-year information is finally merged, the total entropy increases even more. Anyway, it never exceeds the value of 0.2. Concerning T_3, very different results are obtained for the one-day estimation. The measurements of Day 2 and Day 9 show the highest level of

backscattering randomness. In both cases, the high value of H_T is not caused by response fluctuations but by the separation that the Pauli's components suddenly assume with respect to a previous trend. If the six months information is now considered, the nocturnal collection shows a level of total entropy higher than the diurnal one, even if the one-day analysis contains more low entropy samples. The reason is that although the changes make the diurnal profiles seem very instable, a single scattering behavior affected by significant fluctuations turns out to be less entropic than two different but quite stable mechanisms alternating in time.

Although H_T seems to indicate that for T_3 the information of the first six months should be preferred, the comparison among subsets of nocturnal acquisitions with similar polarimetric properties is intuitively more correct. In all these evidences, H_T becomes a useful descriptor of the degree of time stationarity of targets' polarimetric response. Yet, a specific filtering procedure is now required to carry out an effective selection of time samples belonging to the same stationary process and, accordingly, lowering the value of temporal entropy H_T.

7.4.3. Long-time regular patterns detection

As long as the polarimetric analysis of urban scatterers' long-time evolution is concerned, it is fundamental to guarantee that just samples belonging to the same stationary backscattering process are compared. The study of the Station district in Sallent during a period of approximately one year has shown that non-stationary behaviors might characterize the response of pixels. In order to cope with the separation of different stationary processes that might alternate in time, a three-step selection methodology is here proposed.

The first step is based on the study of the time evolution of the normalized Pauli's components (NPCs) at pixel level, which are insensitive to the amplitude and phase offsets described in Section 7.4. Then, a filtering procedure able to select time-samples exhibiting a stable polarimetric behavior in the three Pauli's profile has been developed. In order to avoid gaps in the pixels' temporal description, this procedure also guarantees a minimum number of acquisitions for each day of measurements. Following the idea described in Section 7.3.2, the sets of long-time NPCs concerning an illuminated target may be expressed as

$$\begin{aligned} A_T &= \bigcup_{w=1}^{N} A_T^w = \bigcup_{w=1}^{N} \left\{ a_{T,1}^w, \ldots, a_{T,N_w}^w \right\} \\ A_D &= \bigcup_{w=1}^{N} A_D^w = \bigcup_{w=1}^{N} \left\{ a_{D,1}^w, \ldots, a_{D,N_w}^w \right\} \\ A_V &= \bigcup_{w=1}^{N} A_V^w = \bigcup_{w=1}^{N} \left\{ a_{V,1}^w, \ldots, a_{V,N_w}^w \right\} \end{aligned} \tag{7.25}$$

where N defines the number of days at disposal, N_w indicates the corresponding number of data sets acquired on day w, and $\cup$ stands for disjoint-union set operation. Note that the subsets A_T^w, A_D^w and A_V^w essentially contain the Pauli's components of all the samples acquired during the day w. Let $I=\{1,...,N\}$ be the set of the indices defining the measurement days reported in Table 7.1. Denoting with Th_P the maximum discontinuity threshold along the NPC profiles, A_T may be expressed as

$$A_T = \bigcup_{w=1}^{N} \bigcup_{i=1}^{N_w} A_{T,i}^w \tag{7.26}$$

where $\bigcup$ indicates the set union operator and each subset $A_{T,i}^w$ is given by

$$A_{T,i}^w = \left\{ a_{T,i}^k \in \underline{A}_T \,/\, \left| a_{T,i}^w - a_{T,m}^k \right| < Th_P \right\} \qquad \forall k, w \in I \,. \tag{7.27}$$

Essentially, each subset $A_{T,i}^w$ contains all the elements of the trihedral-like one-year profile whose absolute distance from the reference sample $a_{T,i}^w$ is lower than Th_P. Note that $A_{T,i}^w$ are non-disjoint subsets of A_T and some of them might even be equivalent. Let $B_{T,1}$ define the most likely fraction of pixel's total span characterized by an odd-bounce backscattering behavior. According to Eq. 7.26 and Eq. 7.27, $B_{T,1}$ corresponds to the subset $A_{T,i}^w$ which shows the maximum cardinality and at the same time guarantees the selection of a minimum number of samples $n_{\min}$ for each day of measurements. These two conditions may be mathematically described as follows

$$B_{T,1} = A_{T,j}^w \,/\, \left[\#A_{T,j}^w = \max \#A_{T,i}^k \wedge \#\left(A_{T,j}^w \cap A_T^k \right) \geq n_{\min} \right]. \tag{7.28}$$

where $\wedge$ indicates the "and" logical operator. The complementary set of $B_{T,1}$ in A_T is given by

$$F_{T,1} = A_T \setminus B_{T,1} \,. \tag{7.29}$$

In order to check the existence of other useful subsets fulfilling the condition the requirement imposed $n_{\min}$, the selection process may be iteratively applied to the remaining elements of the trihedral-like temporal profile as follows

$$\begin{cases} F_{T,n} = F_{T,n-1} \setminus B_{T,n} \\ A_{T,i}^w = \left\{ a_{T,i}^k \in F_{T,n} \,/\, \left| a_{T,i}^w - a_{T,m}^k \right| < Th_P \right\} \\ B_{T,n+1} = A_{T,j}^w \,/\, \left[\#A_{T,j}^w = \max \#A_{T,i}^w \wedge \#\left(A_{T,j}^w \cap A_T^k \right) \geq n_{\min} \right] \end{cases} . \tag{7.30}$$

The iterative process stops when $B_{T,n+1} = \{0\}$. If the study is now applied to A_D and A_V, the three Pauli's profiles in Eq. 7.26 may be expressed as

$$A_T = \left(\bigcup_{k=1}^{N_T} B_{T,k} \right) \cup F_{T,N_T} \qquad A_D = \left(\bigcup_{k=1}^{N_D} B_{D,k} \right) \cup F_{D,N_D} \qquad A_V = \left(\bigcup_{k=1}^{N_V} B_{V,k} \right) \cup F_{D,N_V} \tag{7.31}$$

where N_T, N_D and N_V denote the number of disjoint subsets each Pauli's component has been split into by the iterative algorithm. Note that these numbers might be different. For instance, the stability of the dihedral-like component cannot assure that no power is being exchanged among the other two mechanisms. Accordingly, the stability of all the three components must be analyzed at once. The indices of the elements acquired on day *w* and contained in the subsets $B_{T,n}$, $B_{D,n}$ and $B_{V,n}$ are given by the following expressions

$$I^w_{B_{T,k}} = \left\{ i / a^w_{T,i} \in B_{T,k} \right\} \quad I^w_{B_{D,k}} = \left\{ i / a^w_{D,i} \in B_{D,k} \right\} \quad I^w_{B_{V,k}} = \left\{ i / a^w_{V,i} \in B_{V,k} \right\}. \tag{7.32}$$

Then, the collection of samples describing the most frequent backscattering process characterizing the pixel under study is given by the indices set $I_{A_{TDV}}$ defined as

$$\begin{aligned} I_{B_{TDV}} &= \bigcup_{w=1}^{N} \left(I^w_{B_{T,m_1}} \bigcap I^w_{B_{D,m_2}} \bigcap I^w_{B_{V,m_3}} \right) \Big/ \left[\#\bigcup_{w=1}^{N} \left(I^w_{B_{T,m_1}} \bigcap I^w_{B_{D,m_2}} \bigcap I^w_{B_{V,m_3}} \right) = \right. \\ &= \left. \max_{\substack{k_1 \in \{1,..,N_T\} \\ k_2 \in \{1,..,N_D\} \\ k_3 \in \{1,..,N_V\}}} \#\bigcup_{w=1}^{N} I^w_{B_{T,k_1}} \bigcap I^w_{B_{D,k_2}} \bigcap I^w_{B_{V,k_3}} \wedge \#\left(I^w_{B_{T,m_1}} \bigcap I^w_{B_{D,m_2}} \bigcap I^w_{B_{V,m_3}} \right) \geq n_{\min} \right] \end{aligned} \tag{7.33}$$

where the "$\wedge$" condition guarantees that at least $n_{\min}$ samples are selected for each day of measurements. In essence, Eq. 7.33 looks for the three subsets of NPC components which maximize the cardinality of their intersection and at the same time guarantee a number of daily common samples higher than $n_{\min}$. The sketch of Fig. 7.26 shows the subsets $B_{T,1}$, $B_{D,1}$ and $B_{V,1}$ selected by the proposed approach in the simple case of three days of measurements.

At this point, it is worth pointing out that the samples of the three subsets selected by Eq. 7.33 are characterized by very similar polarimetric properties. Yet, the normalized Pauli's components are not sensitive to possible common discontinuities or fluctuations along the amplitude/phase daily profiles, which anyway accounts for a change in the pixel's backscattering process. If these discontinuities might be neglect for a polarimetric study, they turn out to be critical for any SAR technique based on the reliability of the absolute phase information, as the differential SAR interferometry. After performing the polarimetric analysis, it is hence necessary to analyze the stability of amplitude and phase profiles of each polarimetric channel during each day of measurements. To do this, the algorithm described in Section 7.3.2 may be applied to the samples of each daily collection identified by the subsets $I^w_{B_{TDV}}$. For each day of measurement *w*, the study

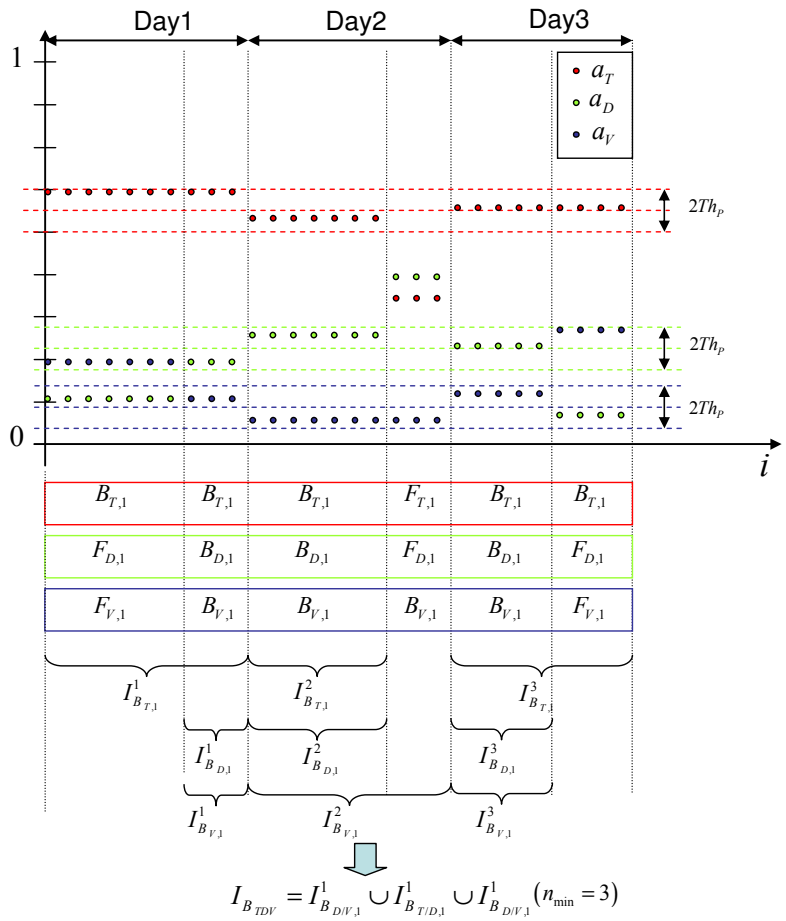

Fig. 7.26: Sketch of the long-time polarimetric selection based on the simultaneous stability of the three Pauli's normalized components. For the sake of simplicity, just three daily collections and $n_{\min} = 3$ have been considered.

study provides three subsets of $I^w_{B_{TDV}}$ denoted with I^w_{hh}, I^w_{vh} and I^w_{vv}. These subsets contain the indices of the time-samples getting through the daily amplitude- and phase-stability criteria in the *hh*, *hv* and *vv* polarization, respectively. It follows that their intersection gives the indices of the samples showing a stable polarimetric amplitude and phase behavior during the day *w* of the collection. At the same time, these samples are characterized by the same backscattering behavior since their indices also belong to $I^w_{B_{TDV}}$. Finally, the subset of $I_{B_{TDV}}$ defining the reliable long-time polarimetric samples concerning each pixel of the scenario is given by the expression

$$I^{Tot}_{B_{TDV}} = \bigcup_{w=1}^{N} \left(I^w_{hh} \bigcap I^w_{hv} \bigcap I^w_{vv} \right) = \bigcup_{w=1}^{N} I^w_{[S]} . \tag{7.34}$$

Resuming, the filtering procedure performs a multi-scale analysis. The long-time scale analysis employs the NPCs to guarantee the stability of the scattering mechanism during the whole observation period. The short-time scale analysis filters out the unreliable samples within each daily collection indicated by the long-time scale processing to preserve the absolute phase

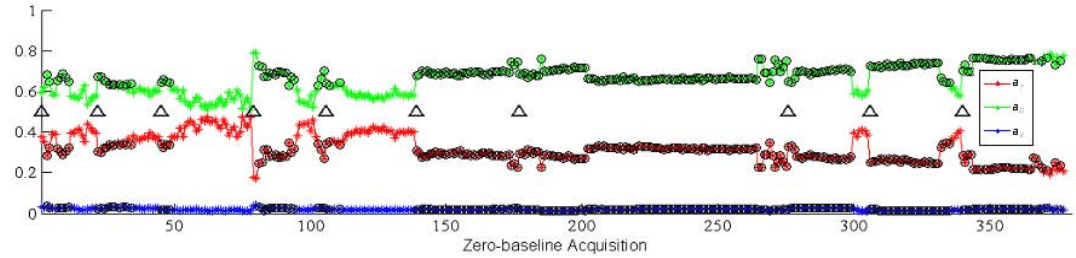

(a)

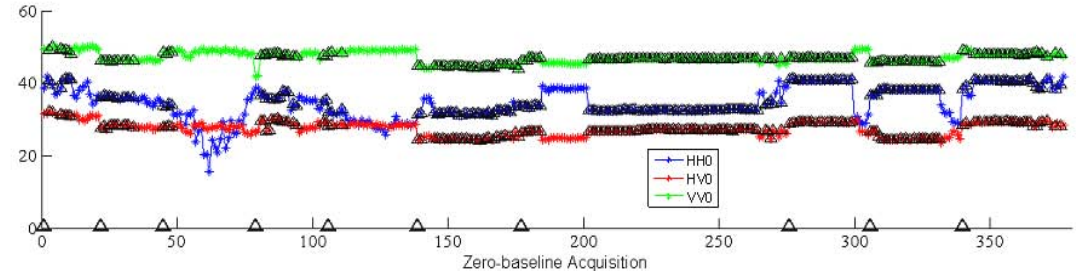

(b)

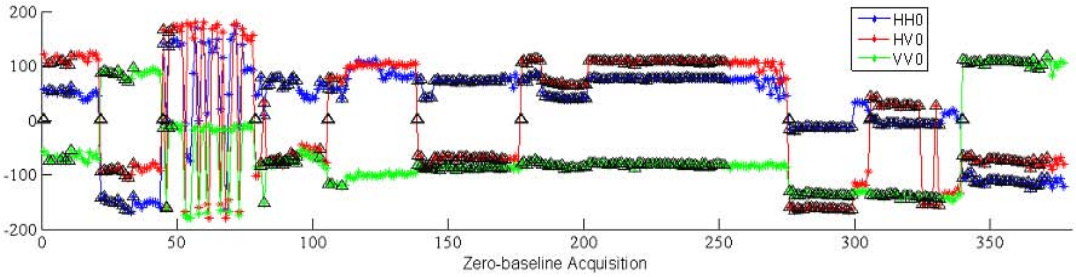

(c)

Fig. 7.27: Long-time polarimetric selection concerning the target T_2. First, the samples belonging to the same stationary process are grouped in $I_{B_{TDV}}$ by studying the stability of the normalized-to-span Pauli's (NPCs) components (a). Then, $I_{B_{TDV}}$ is split into subsets $I^{w}_{B_{TDV}}$ containing samples belonging to the same day of measurements and the stability of amplitude and absolute phase one-day profiles is checked in the different polarimetric channels separately (small triangles in b). The final set of selected samples $I^{Tot}_{B_{TDV}}$ is provided by the intersection among the day-by-day selection in the three polarimetric channels (dark circles in c). The values of the thresholds used for the filtering procedure are: $Th_P = 0.08$, $Th_A = 2dB$, $Th_{\varphi} = 10^{\circ}$, $n_{\min} = 4$.

information in the three polarimetric channels. An example of the selection carried out by the three-step selection procedure when it is applied to the one-year collection of T_2 is shown in Fig. 7.27. The values of the thresholds used for the selection are: $Th_P = 0.08$, $Th_A = 2dB$, $Th_{\varphi} = 10^{\circ}$, $n_{\min} = 4$. The dark circles in Fig. 7.27a mark the samples given by $I_{B_{TDV}}$ in Eq. 7.33. The small triangles in Fig. 7.27b show the subsets of $I_{B_{TDV}}$ obtained by studying the daily stability of the corresponding polarimetric amplitude profiles separately. The further application of the phase-stability criterion to each channel of [*S*] and the final intersection described in Eq. 7.34 provides the subset $I^{Tot}_{\underline{B}_{TDV}}$ whose elements are described by the triangles in Fig. 7.27c. A first demonstration of the effective selection performed by the proposed technique may be achieved through the estimation of the time-entropy H_T. According to the study carried out in Section 7.3.3, H_T is

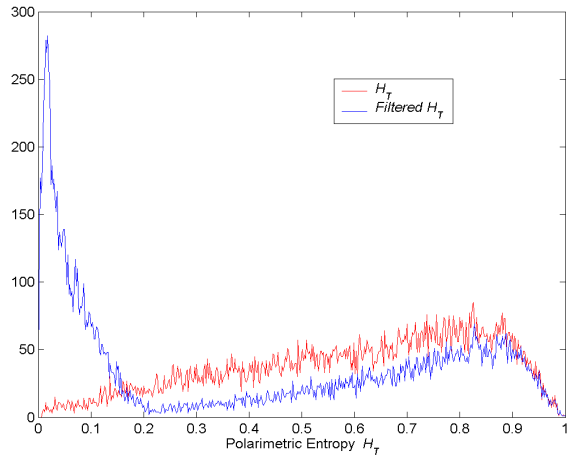

Fig. 7.28: Histograms of H_T estimated over the non-filtered (red) and filtered (blue) one-year collection of gbSAR data within the Station district of Sallent.

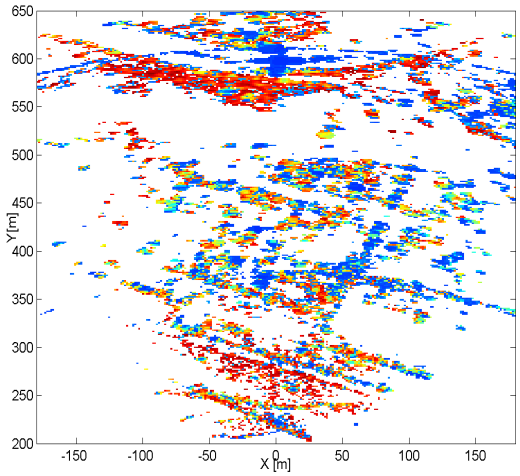

Fig. 7.29: Time entropy H_T estimated over the filtered one-year collection of gbSAR data within the Station district of Sallent..

sensitive to the presence of non-stationary behaviors of the target within the collection of PolSAR acquisitions employed for its estimation. The two histograms in Fig. 7.28 show the distribution of H_T within the district area when the whole one-year collection of gbSAR acquisitions (red) and the subset defined by $I_{B_{TDV}}^{Tot}$ (blue) are employed for the estimation, respectively . A span minimum threshold equal to 5 dB has been also employed to select only pixels belonging to man-made targets. It can be observed that the selection method here proposed is effective on medium-entropy pixels. In fact, they generally pass from an initial value of H_T within the [0.1:0.6] range to a new value lower than 0.1. For instance, the entropy of T_2 in Fig. 7.27 reduces from 0.18 to 0.012.

Concerning the high-entropy pixels, the detection of a subset whose samples fulfil the stability conditions imposed by the selection method is extremely rare. As a matter of fact, the values of histograms for $H_T > 0.85$ are practically identical. This is consistent with the fact the procedure has been tailored to the main properties of urban, i.e. deterministic, targets. From this point of view, the H_T image displayed in Fig. 7.29 confirms that no entropy reduction is obtained over non-deterministic target such as the natural surfaces. Regarding the red points within the Station district, they correspond to pixels for which no useful subset fulfilling the selection requirements was available ($I_{B_{TDV}}^{Tot}$ was empty). In order to avoid any loss of pixels, the entropy has been estimated over the whole long-time collection of gbSAR acquisitions.

7.5 Summary

The one-year measurement campaign driven by the RSLab of UPC in Sallent represents the unique

example of long-time monitoring activity carried out using a polarimetric gbSAR sensor in the remote sensing scientific community. The collections of perfect zero-baseline PolSAR data acquired from June 2006 to July 2007 have given for the first time the opportunity to reveal the high complexity of the backscattering process within an urban environment at X-band. The short time-sampling rate of the gbSAR daily measurements has made it possible to stress the instability of the polarimetric response that man-made structures might present at different time scale. Taking into account the deterministic nature of the observed scene, this instability has been ascribed to non-stationary time behaviors of urban scatterers. Accordingly, the classical technique of Permanent Scatterers (PS) has been shown to be unsuitable for analysis of the district area. In order to cope with the temporal characterization of the urban scatterers within the Sallent test-site, an innovative technique based on the PS model has been put forward. The main idea has been to derive from the PS formulation a regularity criterion to split the non-stationary time-sample sequence of each polarization channel into disjoint time-stationary subsets fulfilling PS hypothesis. In order to analyze possible non-stationarities of the scattering process described by the whole scattering matrix [*S*] at once, a new formulation of the polarimetric entropy in the time domain H_T has been also proposed and assessed. The main conclusion is that the instability of polarimetric temporal profiles does not necessarily turns into a modification of the scattering mechanisms characterizing a pixel. From this point of view, the normalized components of the Pauli's decomposition (NPCs) has offered the opportunity to detect discontinuities in the polarization time evolution which are caused by changes in the nature of the scattering mechanisms and not by common offsets of pixels' amplitude and phase profiles.

In order to achieve a reliable polarimetric characterization of the urban pixels during the one-year collection of gbSAR acquisitions, the two coherent methods, i.e., the modified PS formulation and the NPCs, have been employed to work out a novel long-time filtering procedure at pixel level. Following a multi-scale approach, the regularity of NCPs profiles is used to select the samples in each daily collection showing the same long-time polarimetric scattering behavior ($I_{B_{TDV}}$). This assures that the reciprocal position of the polarization phase centers has not changed among the different days. Afterwards, the polarization channels of each daily subset are analyzed separately by the modified-PS technique and just the common samples are selected ($I^{Tot}_{B_{TDV}}$). Doing this, the polarimetric absolute phase information of each daily subset ($\bigcup_{w=1}^{N} I^{w}_{[S]}$) is preserved. The effectiveness of the filtering procedure has been assessed in terms of reduction of H_T within the

district area. Finally, a general conclusion dealing with the unexpected behavior of pixels within the Station district of Sallent can be drawn from study carried out in this Chapter. Performing a careful study of backscattering time-stationarity within the area of interest is fundamental in order to interpret correctly any quantitative information retrieved through a long-time polarimetric analysis. The filtering procedure here proposed represents a first attempt to cope with the problem of preserving interferometric phase information from non-stationary backscattering contaminations within an urban environment. Nonetheless, it constitutes the essential condition that must be guaranteed in order to define a new research field where polarimetry and differential interferometry may profitably converge. A first demonstration of the advantages of the knowledge of the full scattering matrix with respect to single-polarization measurements for differential interferometric application (PolDInSAR) will be given in Chapter 8.

Chapter 8

Polarimetric Differential gbSAR Interferometry

In this Chapter, the problem of retrieving deformation information from zero-baseline polarimetric gbSAR acquisitions is addressed. To this end, the collection of data sets gathered during the one-year measurement campaign driven by the RSLab of the UPC in the village of Sallent (see Section 4.7.2) is employed. The need to compensate for the phase artefacts arising from troposphere monthly changes and to reduce the number of data sets at disposal is first stressed. Accordingly, a pre-processing chain preparing the gbSAR data to advanced DInSAR analysis is put forward. Then, the Coherent Pixel Technique (CPT) [Mora,03] is employed to investigate the benefits provided by fully polarimetric acquisitions. After applying the classical technique to each channel of [*S*] separately, a new polarimetric criterion for the selection of reliable pixels is introduced. The results achieved with the two approaches are quantitatively compared and the advantages offered by the polarimetric approach are pointed out. Finally, the possibility to employ polarimetric coherence-optimization techniques to enhance the quality of the deformation estimation is looked into.

8.1. Sallent Deformation Process

As it has been explained in Section 7.1, the Station district of Sallent is affected by a subsidence phenomenon. Its causes must be traced back to the salt mining activity of the past century. A multiple set of techniques such as topographic leveling, geological mapping, geophysic prospection, extensometric measurements, drilling, advanced coherence-based differential SAR techniques, have been already employed to evaluate the risk of structure collapse [Blanco,03] [Marturia,05]. The deformation-rate maps retrieved by ERS/EnviSAT acquisitions and high topographic leveling techniques concerning the area of interest are shown in Fig. 8.1a and Fig.

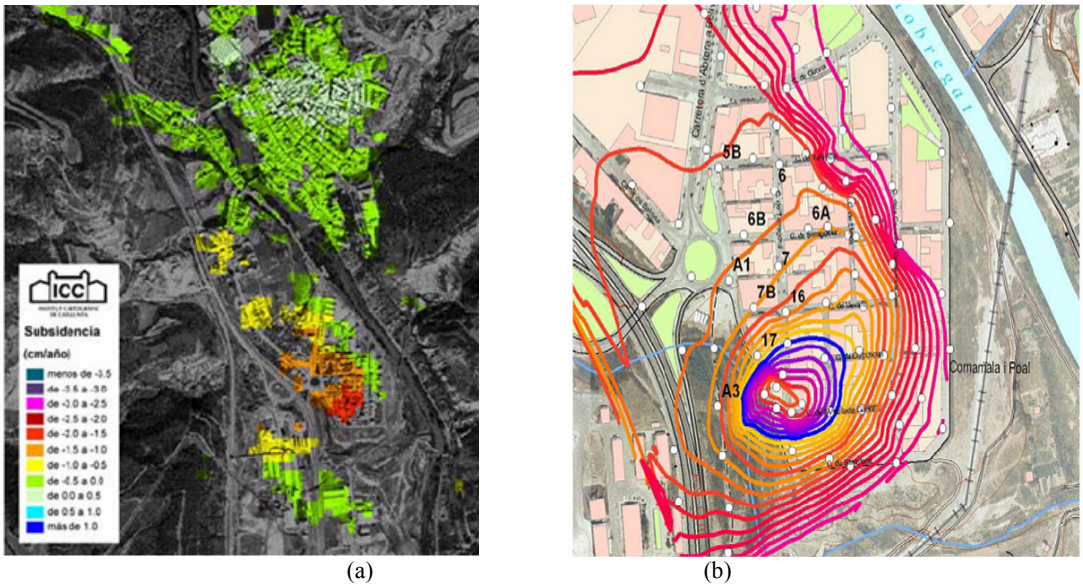

(a) (b)

Fig. 8.1: Deformation-rate map obtained through CPT (a) and topographic leveling techniques (b) from [Marturia,05].

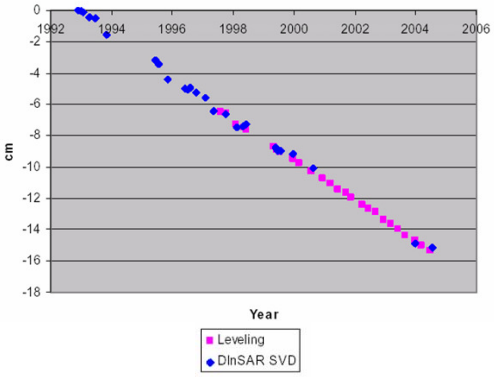

Fig. 8.2: Displacement evolution of the point 6A in Fig. 8.1 retrieved using CPT and high topographic leveling techniques [Marturia,05].

	Date	Time	# of Scans	Time-Delay
DAY 1	29/06/06	11:00 - 16:00	27	10 min
DAY 2	26/07/06	08:00 - 11:30	30	13 min
DAY 3	19/09/06	10:40 - 16:00	39	8 min
DAY 4	20/10/06	09:40 - 15:00	31	7 min
DAY 5	14/11/06	12:30 - 16:30	41	8 min
DAY 6	28-29/11/06	19:00 - 08:40	44	20 min
DAY 7	18-19/12/06	20:45 - 05:00	99	10 min
DAY 8	13-14/02/07	22:00 - 09:55	37	25 min
DAY 9	14-15/03/07	20:00 - 09:50	41	25 min
DAY 10	04-05/07/07	22:00 - 10:50	45	25 min

Table 8.1: Timetable of the measurements campaign in Sallent. Red and blue colors denote the diurnal and nocturnal monitoring activies, respectively.

8.1b, respectively. The linearity of the subsidence phenomenon can be instead observed in Fig. 8.2, where the behavior of the point 6A during a ten-year time span is displayed as example in Fig. 8.1b. The reliability of the displacement information retrieved with the DInSAR technique is demonstrated by the perfect matching with ground-truth measures. Nonetheless, the main limitation of the satellite-based DInSAR study in [Marturia,05] is the loss of resolution introduced by the combined effects of sensor limited resolution and coherence estimation window. In June 2006, the institutions of Catalan Administration (ICC/IGC) signed a collaboration with the RSLab of the UPC for monitoring the district area during a period of approximately one year using its gbSAR sensor. The purpose was twofold. On the one hand, it aimed at improving the spatial accuracy of the retrieved deformation rate map using a terrestrial sensor. On the other hand, it had to evaluate the feasibility of continuously monitoring the hazard subsoil movements by means of

gbSAR systems. Data acquisitions were carried out on ten days from June 2006 to July 2007. Information about number of data sets for each day of measurements and part of the day chosen for the monitoring activity is resumed in Table 8.1. Additional details can be found in *Appendix C*.

8.2. Amplitude vs Coherence-based advanced DInSAR techniques

Differential SAR interferometry (DInSAR) has shown excellent results in the last years of research. Initially, single interferograms were separately employed for the estimation of deformation occurred during the time span separating the two acquisitions [Massonet,93]. The basic relation between differential interferometric phase and deformation information has been introduced in Section 5.2. The next step was the retrieval of the temporal evolution of the deformation through the combination of multi-temporal differential interferograms [Ferretti,00] [Mora,03] [Lanari,04]. A general expression for *i*th interferogram out of the $\binom{N}{2}$ combinations of *N* zero-baseline gbSAR acquisitions is given by

$$\phi_{i,p}(T_i) = 2k(vT_i + \beta_i) + \phi_{atm,i} + \phi_{N_T,i} \tag{8.1}$$

where *p* denotes the polarization channel, *k* is wavenumber, T_i is the temporal baseline (i.e, the temporal gap between acquisitions), *v* and β_i are respectively the linear and non-linear radial deformation components, $\phi_{atm,i}$ accounts for the atmospheric phase and $\phi_{N_T,i}$ for the additive noise. Eq. 8.1 can be directly obtained from [Hanssen,01] under the hypothesis of perfect zero-baseline (*0B*) images, that is, considering the spatial separation of the SAR sensor's trajectories equal to zero. Accordingly, both DEM errors and Doppler centroid differences between each pair of images at disposal turn out to be null by construction (see Section 5.5).

When a few acquisitions are available, the set of differential interferograms to be analyzed is generated by all the possible combination of images. When the number of combination becomes too high, a subset is recommended. This is usually carried out by a 3D triangulation of the available images in the space defined by the spatial baseline, the temporal baseline and the Doppler centroid frequency. In order to reduce the computational and disk storage requirements versus redundant information loss, minimum Spanning Tree (MST) techniques are often employed [Blanco,08]. Two different criteria are mainly employed for the estimation of the pixels' quality: the *coherence* stability and the *amplitude* dispersion. In the first case, the pixels' accuracy for each interferogram in the *p* polarization channel is given by the amplitude γ_p of the complex cross-correlation ρ_p defined in Eq. 5.16 and equal to

$$\rho_p = \gamma_p e^{j\phi_p} = \frac{\sum_{n=1}^{ENL} S_{0,p} S_{1,p}^*}{\sqrt{\sum_{n=1}^{ENL} \left|S_{0,p}\right|^2 \sum_{n=1}^{ENL} \left|S_{1,p}\right|^2}} \tag{8.2}$$

where $S_{0,p}$ and $S_{1,p}$ are the master and slave images acquired in the p polarization, ENL is the number of independent samples within the averaging boxcar, the term ϕ_p is the estimated differential phase information. The value of γ_p varies in the range [0,1] and the two extremes account for the two limit situations of data total uncorrelation and total correlation, respectively. For this reason, a coherence minimum threshold γ_{th} is generally fixed and only pixels whose coherence value is higher than γ_{th} in a certain percentage of the interferograms at disposal, for instance 50%, are selected for the study. In the second case, the quality of the phase information is associated to the dispersion index D_A introduced in Section 7.3.1 and defined as

$$D_A = \frac{\sigma_A}{m_A} \tag{8.3}$$

where m_A and σ_A are the mean and the standard deviation of pixel's amplitude, respectively. D_A is a good approximation of the phase stability for high SNR values. The larger the number of images, the more reliable the statistical analysis. Typically, targets exhibiting a D_A <0.25 are labeled as reliable and referred to as Permanent Scatterers (PSs) [Ferretti,01]. The use of one selection criterion or the other is essentially related to the nature of the targets to work with. Amplitude dispersion is ideal for point-like targets as man-made structure. Besides, it preserves the spatial resolution. In contrast, the coherence stability entails a spatial average of pixels' information. Despite the lower spatial resolution estimation, this second approach is more appropriate for studying distributed targets, as most of natural targets, which do not behave as a PS. Another important issue in deciding which criterion to employ is the number of acquisitions at disposal. If having a low number of them (<30), D_A is not reliable [Ferretti,01], whereas the coherence estimator turns out to be more robust. From a theoretical point of view, there is not a minimum number of images required to apply a coherence-based technique.

Concerning the Sallent measurement campaign, the high number of daily acquisitions cannot be employed as independent sample for the estimation of the deformation process affecting the Station district. The reason lies in the time scale of the subsidence phenomenon which causes undetectable differential phase variations during one day. Accordingly, a reduced number of independent time-samples is really available for the differential study. As a matter of fact, this

number corresponds the ten different dates reported in Table 8.1, as it will be explained in Section 8.3. It follows that even if an amplitude-based approach is likely to be more suitable to the Sallent scenario, a trustful estimation of D_A is unfeasible and only a coherence-based analysis can be successively carried out. Among the different techniques in the literature, the Coherent Pixel Technique (CPT) has been demonstrated in [Mora,03] to guarantee accurate results even when a few interferograms are considered (namely 7). In all these evidences, the CPT algorithm will be employed for the estimation of the deformation within the district area of Sallent. Taking into account the linear evolution of the subsidence phenomena stressed in Fig. 8.2, the study will be mainly focused on the retrieval of linear-component of the deformation, that is, the contribution of β_i in Eq.8.1 will be neglected. A last comment is in order. Possible non-stationary behaviors of urban scatterers described in Chapter 7 must be carefully kept into account. Nonetheless, they are expected to affect more an amplitude-based that a coherence-based analysis. Whereas in the first case the absolute phase quantities at pixel level might be corrupted, the spatial estimation of the second approach should mitigate their effects by extracting the mean phase information within the averaged area. Accordingly, a first analysis will be carried out under hypothesis of time-stationarity of the backscattering process from the district area. Hence, a specific gbSAR data preprocessing chain will be applied to reduce the number of images at disposal and to improve the interferograms' SNR before applying the CPT. Afterwards, the time-stationary hypothesis will be relaxed. The selection method proposed in the Chapter 7 will be employed for averaging the daily collection at pixel level and the whole process will be applied to the new collection of daily-averaged images for a direct comparison.

8.3. Polarimetric gbSAR data preprocessing

The results shown in Fig. 8.2 indicate a linear behavior of the subsidence phenomenon with a vertical displacement mean-rate equal to 2 cm/year. It is reasonable to assume that the time-scale of the deformation process keeps in the order of a few centimeters per year also during the measurement campaign. Therefore, two main assumptions can be drawn: the first one is that the phase information of data acquired during the same day is not sensitive to the deformation process; the second one is that the Signal-to-Noise ratio (SNR) of time-stationary targets can be improved without reducing the image spatial resolution by properly time-filtering the each set of daily collections.

Let N_w be the number of calibrated scattering matrices measured by the gbSAR sensor during the

day *w*. Under the hypothesis of propagation through a homogeneous troposphere (see Section 7.3), the *i*th term of the sequence may be expressed as

$$\left[S'\right]_i^w = \begin{bmatrix} S_{hh}^{i,w} & S_{hv}^{i,w} \\ S_{hv}^{i,w} & S_{vv}^{i,w} \end{bmatrix} e^{-j2k_0\left(n_{1,w}+\Delta n_{i,w}\right)r+j\varphi_{0,w}} + \left[N_T\right]_i^w \quad i=1,..,N_w \tag{8.4}$$

where k_0 is the wavenumber in the vacuum, $n_{1,w}$ is the refractive index of the first acquisition (*master*), $\Delta n_{i,w}$ describes the variation of the propagation properties due to changes of the troposphere between data set *i* and the master scan, and $\varphi_{0,w}$ accounts for the location of the trihedral employed for the polarimetric calibration of day *w* acquisitions of (see Eq. 7.20). In order to increase the signal-to-noise ration (SNR), the atmospheric artefacts introduced by $\Delta n_{i,w}$ must be first compensated for. To do this, the coherence-based technique proposed in Section 6.3 is employed. The differential phase ϕ of high-coherence pixels within the scenario may be projected onto a single range cut and the distribution is fitted to the linear model

$$\hat{\phi}\left(r\right) = -2k_0\,\widehat{\Delta n}_{i,w} r\,. \tag{8.5}$$

Then, selected pixels whose differential phase diverges from the expected artefact are labeled as outlier and filtered out by checking the condition

$$\left|\phi - \hat{\phi}\right| \le \sigma_{\text{mod}} \tag{8.6}$$

where σ_{mod} is the standard deviation of ϕ with respect to the linear model. The description of the atmospheric artefact is obtained by repeating the process of linear fitting using just the phase information of pixels fulfilling Eq.8.6. For each of the N_w-1 slave data sets, the corresponding correction function *f* is obtained as

$$f_{i,w} = e^{-j\hat{\phi}} = e^{j2k_0\widehat{\Delta n}_{i,w}r} \tag{8.7}$$

where $\widehat{\Delta n}_{i,w}$ is the value of $\Delta n_{i,w}$ provided by the second model-fitting estimation without the outlier pixels. Under time-stationary hypothesis of the backscattering process, a higher-quality time-averaged scattering matrix $[\underline{S}]_w$ is finally obtained as

$$\left[\underline{S}'\right]_w = \sum_{i=1}^{N_w}\left[S'\right]_i^w f_{i,w} = \sum_{i=1}^{N_w}\begin{bmatrix} S_{hh}^{i,w}e^{-j2k_0n_{1,w}r} & S_{hh}^{i,w}e^{-j2k_0n_{1,w}r} \\ S_{hh}^{i,w}e^{-j2k_0n_{1,w}r} & S_{hh}^{i,w}e^{-j2k_0n_{1,w}r} \end{bmatrix} e^{j\varphi_{0,w}} = \begin{bmatrix} \underline{S}_{hh}^{w} & \underline{S}_{hv}^{w} \\ \underline{S}_{hv}^{w} & \underline{S}_{vv}^{w} \end{bmatrix} e^{-j2k_0n_{1,w}r+j\varphi_{0,w}}\,. \tag{8.8}$$

This process, hereon denoted with Stationary *Time-Filtering* (*STF*), is repeated for each day reported in Table 8.1. An alternative approach for additive noise reduction sharing the same time-

stationary assumption can be found in [Noferini,08]. The final step deals with the compensation of the different troposphere properties among the master images. From a theoretical point of view, the deterministic nature of the area under study provides sufficient high coherence pixels to apply again the aforedescribed technique. Yet, it must be taken into account that the differential phase is sensitive to atmospheric artefacts as well as to the deformation process to be retrieved. Owing to the linearity of the subsidence phenomena, the deformation contribution is expected to be higher as the time separation between the two data sets increases. In order to avoid any artefact incorrect description, pixels belonging to the district area should be filtered out for time span higher than a fixed time-threshold. The main drawback of this approach solution is the reduced number of remaining high-coherence pixels at disposal for the regression-line estimation.

A way to circumvent this problem is to take advantage of the linearity of the atmospheric phase artefacts under atmosphere homogeneity hypothesis. Let r_l and r_m be the target's range distance on day l and m, respectively. Being $m>l$, the range variation occurred from day l to day m can be expressed as the sum of the displacements occurred between consecutive acquisitions between the two limit days as follows

$$\Delta r_{l,m} = r_m - r_l = \sum_{w=l}^{m-1} \Delta r_{w,w+1} \ . \tag{8.9}$$

Similarly, the total variation of the refractive index between day l and day m may be factorized as

$$\Delta n_{l,m} = n_{1,m} - n_{1,l} = \sum_{w=l}^{m-1} n_{1,w+1} - n_{1,w} = \sum_{w=l}^{m-1} \Delta n_{w+1,w} \ . \tag{8.10}$$

Accordingly, the propagation phase term of day m in Eq. 8.4 can be rewritten as a function of day l as

$$\begin{aligned} \left[\underline{S}'\right]_m &= \left[\underline{S}\right]_m e^{-j2k_0 n_{1,m} r_m + j\varphi_{0,m}} = \left[\underline{S}\right]_m e^{-j2k_0\left(r_l + \sum_{w=l}^{m-1}\Delta r_{w,w+1}\right)\left(n_{1,l} + \sum_{w=l}^{m-1}\Delta n_{w,w+1}\right) + j\varphi_{0,m}} = \\ &= \left[\underline{S}\right]_m e^{-j2k_0 r_l n_{1,l}} e^{-j2k_0\left(r_l \sum_{w=l}^{m-1}\Delta n_{w,w+1}\right)} e^{-j2k_0\left(n_{1,l}\sum_{w=l}^{m-1}\Delta r_{w,w+1}\right)} e^{-j2k_0\left(\sum_{w=l}^{m-1}\Delta n_{w,w+1}\Delta r_{w,w+1}\right)} e^{j\varphi_{0,m}} \end{aligned} \tag{8.11}$$

where the first exponential of the last equality in Eq. 8.11 indicates the propagation condition on day l, the second one accounts for the absolute phase variations due to the change of the refractive index between consecutive time-averaged images, the third one for the phase variation due to the target's displacements from day l to day m with respect to atmospheric conditions of day l, and the last one describes the direct relationship between deformation increments and atmosphere changes. It follows that the problem of removing the phase artifacts arising in the

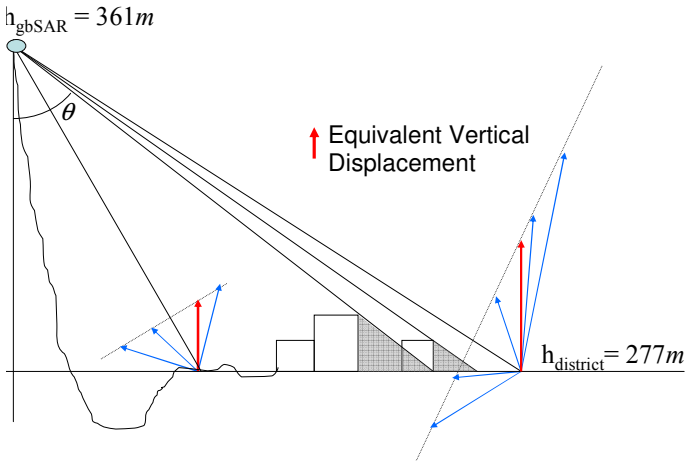

Fig. 8.3: Observation geometry of the UPC sensor in Sallent and equivalent vertical displacement projection.

interferogram of two daily master images reduces to estimating the third exponential term. At this point, it is worth pointing out the effect of $\sum_{w=l}^{m-1}\Delta n_{w,w+1}\Delta r_{w,w+1}$ at X-band can be neglected. The reason is that the phase shifts caused by typical variations of $\Delta n_{w,w+1}$ (a few ppms) are negligible when they are multiplied by displacements in the order of a few centimeters. In order to neglect the other undesired phase contribution and cope with the artefact estimation, one-month-delayed gbSAR acquisitions may be used. In fact, it is important to recall that the mean deformation-rate of 2 cm/year shown in Fig. 8.2 corresponds to a vertical displacement. From the observation geometry sketched in Fig. 8.3, it can be observed that a high incidence angle characterizes the illumination condition in of the Station district in Sallent. As its values range from 72º up to 82º, the contribution of the deformation process to one-month *0B* interferograms turns out to be very small, about a few degrees. This means that when $m = l+1$, Eq. 8.11 simplifies to

$$\left[\underline{S}'\right]_{l+1} = \left[\underline{S}\right]_{l+1} e^{-j2k_0 r_l n_{1,l}} e^{-j2k_0 r_l \Delta n_{l,l+1}} e^{j\varphi_{0,l+1}} . \tag{8.12}$$

and all the coherent pixels within the scenario may be now employed for the estimation of the term $\Delta n_{l,l+1}$. Following this main reasoning, it is possible to create a set of one-month compensation functions defined as

$$F_{w,w+1} = e^{j\hat{\phi}_{w,w+1}} = e^{j2k\Delta\hat{n}_{w,w+1}r} \quad w = 1,..N-1 . \tag{8.13}$$

Hence, the compensating function of the *lm* interferogram is obtained by simply multiplying the *m*-*l*-1 basis functions from day *l* to day *m* as follows

$$F_{l,m} = \prod_{w=l}^{m-1} F_{w,w+1} . \tag{8.14}$$

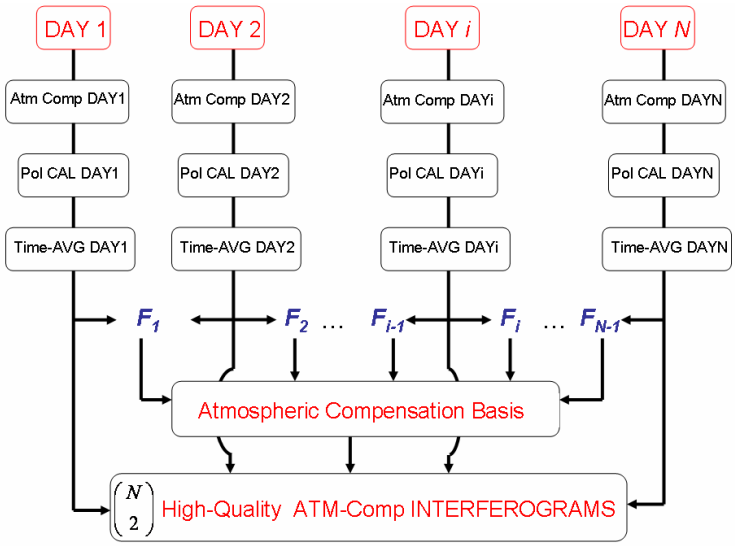

Fig. 8.4: Pre-processing chain for the estimation of the atmospheric phase artefacts in long time span zero-baseline gBSAR acquisitions. The basic functions F_i are obtained from consecutive daily-averaged gbSAR acquisitions where the deformation contribution can be assumed negligible and are linearly combined to cope with the artefact compensation in any time-span gbSAR differential interferogram.

The *0B* compensated interferometric phase $\phi_{l,m}$ obtained from the time-averaged acquisitions of day *l* and day *m* is hence given by

$$\phi_{l,m} = \angle\left(\frac{\sum_{n=1}^{ENL} S_l S_m^* F_{l,m}^*}{\sqrt{\sum_{n=1}^{ENL} |S_l|^2 \sum_{n=1}^{ENL} |S_m|^2}} \right) \tag{8.15}$$

where "$\angle$" denotes the complex number phase operation and *ENL* is the number of independent samples within the averaging boxcar. The blocks-diagram of Fig. 8.4 resumes the whole processing chain. Finally, it is worth pointing out that this approach provides an efficient guideline to cope with the atmospheric artefact removal from gbSAR *0B* acquisitions. It is of key importance to choose the maximum time separation between consecutive independent acquisitions as a trade-off between the time-scale of the temporal decorrelation within the scene and the time-scale of the phenomenon to be monitored.

8.4. Single-polarization Coherent Pixel Technique (SCPT)

After compensating for the atmospheric artefacts, the *i* interferogram out of the $\binom{N}{2}$ combinations of the *N* available time-averaged images may be expressed as

$$\phi_{i,p}\left(T_i, B_{n,i}, \Delta f_{dc,i}\right) = 2k_0 n\left(vT_i + \beta_i\right) + \phi_{N_T,i} + \Delta\varphi_i \tag{8.16}$$

where $\Delta\varphi_i$ accounts for the different calibration phase offset of master and slave images. Note that

in Eq. 8.16 the refractive index *n* does not depend on *i*. The reason is that the interferometric phase fluctuations generated by its variations are negligible since the term $vT_i + \beta_i$ is always in the order of a few centimeters. At this point, the collection of gbSAR interferograms can be processed using the CPT algorithm [Mora,03]. In its classical formulation, hereon is denoted with SCPT, just one polarization channel is analyzed. This means that the term *p* in Eq. 8.16 is a parameter fixed at the beginning of the process. Once the polarization channel of [*S*] is chosen, the values of the differential coherence γ_p are estimated for each pixel of the scene and for all the available interferograms. Afterwards, a time-averaged coherence map is calculated as follows

$$\bar{\gamma} = \frac{2}{N(N-1)} \sum_{i=1}^{N(N-1)/2} \left| \gamma_i \right| \tag{8.17}$$

and only the pixels fulfilling a minimum coherence condition $\bar{\gamma} \geq \gamma_{\min}$ are selected for the phase analysis. It is worth recalling that the phase of individual pixels might be difficult to use because of the phase offsets $\Delta\varphi_i$, which cannot be compensated for due to the lack of any polarimetrically-characterized stable target within the district area. Nonetheless, the CPT circumvents this problem by relating neighboring selected pixel by means of the Delaunay triangulation [Delaunay,34] and working out a relative and not absolute description of the deformation process. Accordingly, the effects of $\Delta\varphi_i$ are nicely solved. This type of triangulation links all the neighboring pixels of irregularly gridded data by generating non-overlapping triangles, as it is sketched in Fig. 8.5. The selected pixels are the *nodes* of the grid and each pair defines an *arc* of the triangulation. The phase increment between two linked pixels may be expressed as

$$\Delta\phi_{i,p}\left(T_i, x_a, y_a, x_b, y_b\right) = \phi_{i,p}\left(T_i, x_a, y_a\right) - \phi_{i,p}\left(T_i, x_b, y_b\right) \tag{8.18}$$

where (x_a,y_a) and (x_b,y_b) are the coordinates of the nodes forming the $arc_{a,b}$ in the slant-range images and T_i is the temporal baseline. Since the linear velocity term is constant for each node of the triangulation scheme in the whole interferograms stack, it is possible to retrieve a good estimation of the deformation-rate increment $\Delta v\left(arc_{a,b}\right)$ between the two connected pixels by adjusting the phase model

$$\Delta\phi_{i,p}^{\mathrm{mod}}\left(T_i, arc_{a,b}\right) = 2k_0 n T_i \Delta v\left(arc_{a,b}\right) \tag{8.19}$$

to the set of the available data $\Delta\phi_{i,p}$. This is performed through the *model adjustment function* $\Gamma(arc_{a,b})$ defined as

$$\Gamma_p\left(arc_{a,b}\right) = \left| \sum_{i=1}^{N(N-1)/2} e^{j\Delta\phi_{i,p}\left(T_i, arc_{a,b}\right)} - e^{j\Delta\phi_{i,p}^{\mathrm{mod}}\left(T_i, arc_{a,b}\right)_i} \right|^2 . \tag{8.20}$$

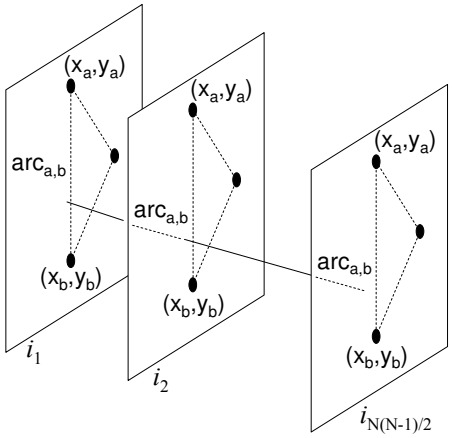

Fig. 8.5: Example of Delauney triangulation: two nodes define an arc along the sequence of interferograms (i_1,i_2,..$i_{N(N-1)/2}$).

The minimization of Γ directly provides the value of Δv describing the linear deformation-rate increment between the two linked nodes. The basic assumption is that the differential phase increment between linked pixels is always lower than π. It is worth stressing that the minimization is carried out in the complex domain. Hence, there is no need to perform any kind of phase unwrapping on the differential interferograms. In general, the larger the number of interferograms, the better the estimation of Δv. From a theoretical point of view, there is not a minimum number of interferograms required for the usage of CPT because the results strictly depend on the specific features of the observed scene. Since the minimization procedure always provides a solution, a *model quality function* γ_{mod} is also required to check the trustworthiness of the results: γ_{mod} is defined for each arc as follows [Mora,03]

$$\gamma_{\text{mod},p}\left(arc_{a,b}\right)=\frac{2}{N(N-1)}\left|\sum_{i=1}^{N(N-1)/2} e^{j\Delta\phi_{i,p}\left(T_i,arc_{a,b}\right)-j\Delta\phi_{i,p}^{\text{mod}}\left(T_i,arc_{a,b}\right)_i}\right| \tag{8.21}$$

and it is equal to 1 if the model perfectly fits the data whereas it tends to zero for completely random phase distribution. Those arcs presenting a quality function below a minimum threshold $\gamma_{\text{mod},th}$ are rejected. If the deformation process under study is known to be linear, as the case of Sallent, a high threshold may be fixed. If no *a priori* information is available, $\gamma_{\text{mod},th}$ is set to a lower value to avoid rejecting all the pixels characterized by a deterministic but non-linear movement that would not get through the linear model test. Finally, the absolute deformation linear component is obtained by spatially integrating the relations among linked nodes. At least one reference point of known deformation, called *seed*, is required to tie the floating solution. In practice, a good distribution of control points helps to reduce the offsets that might appear among zones badly connected. Spatial integration is performed using the Conjugate Gradient Method

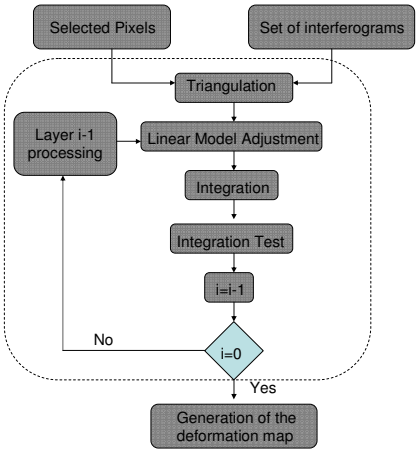

Fig. 8.6: Blocks-diagram of CPT for the retrieval of the linear deformation component.

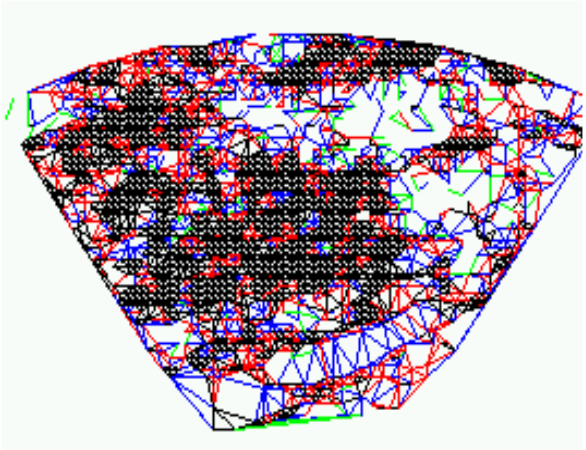

Fig. 8.7: Example of the Delaunay triangulation in the Station district of Sallent. Black, blue, red, and green colors indicate, in the high-to-low order, the quality of the relation between linked pixels.

(CGM), an iterative and efficient method for solving large systems of linear equations [Sarkar,84]. Depending on the chosen coherence threshold, selected pixels as well as the estimation of velocity increments Δv may vary in a wide quality range. As a consequence, incorrect estimations of some arcs are likely to lead to wrong absolute value after the spatial integration step.

In order to maximize pixel density but preserving result quality, a *multi-layer* processing has been also implemented [Blanco,06]. Selected pixels are divided into different quality layers according to the value of their mean coherence value $\overline{\gamma}$ given by Eq. 8.17. Afterwards, the layers are top-down processed following the blocks-diagram sketched in Fig. 8.6: the absolute values of each layer become seeds for the successive one. By doing this, the results obtained at a higher level are preserved and the estimation at lower levels improves. The triangulation scheme obtained with the *hh* collection of gbSAR data in Sallent using four quality layers and a minimum value of γ_{mod} equal to 0.8 is shown in Fig. 8.7. The linear deformation map is obtained after all the layers have been processed. The SCPT makes it possible to calculate also the non-linear component of the displacement. Owing to the extremely linearity of the subsidence phenomenon affecting the area of Sallent under study, the rest of the SCPT chain will not be considered in the frame of this work. A complete description of the technique can be found in [Mora,03] [Blanco,06] [Blanco,08].

8.4.1. Deformation-rate map retrieval

According to the polarimetric study of the urban area carried out in Chapter 7, trihedral-like and dihedral-like reflection mechanisms dominate the scene, whereas the cross-polar backscattering contribution is much lower. For this reason, the SCPT has been applied just to the co-polar

channels of [*S*] separately. As it is well-known, SAR sensors are sensitive just to the radial projection of the movement occurred in the scene. An approximate description of the equivalent vertical displacement may be estimated by keeping into account the gbSAR acquisition geometry in Fig. 8.3 and properly projecting the radial information. An example of the vertical deformation-rate maps obtained from *hh* and *vv* collections is shown in Fig. 8.8a and Fig. 8.8c, respectively. The values of the SCPT setting parameters are detailed in the figures caption. A maximum vertical movement close to 5 cm/year has been estimated. This value, which indicates that the deformation process is speeding up with respect to the results published in [Marturia,05]. Yet, a good agreement can be observed between the shape of the deformation retrieved from the gbSAR data sets and the contour-map in Fig. 8.1b.

Finally, it is worth noting that the high-deformation rate characterizing some isolated pixels is due to the temporal instability of urban targets highlighted in Chapter 7, which affects the polarization channels differently. Although these pixels get through the conditions described by Eq. 8.20 and Eq. 8.21, the variation of their scattering behavior along the time axis leads to a different estimation of *v* depending on the selected polarization. As a matter of fact, the position of red spots in Fig. 8.8a and Fig. 8.8c is not the same.

In the Chapter 7, these temporal changes have been explained in terms of time non-stationarity behavior of man-made structures related to the high observation angles. A first attempt to reduce these anomalous effects may be carried out by applying the filtering criterion of Section 7.4.3 for the detection of time-stationary samples subsets. Briefly, the basic idea is to select at pixel level the collection of time-samples showing similar polarimetric scattering properties in terms of normalized Pauli's components. Then, the amplitude and phase stability is checked within each daily collection to filter out possible polarimetric amplitude and phase common offsets. A minimum number of daily samples is also fixed to guarantee a reliable description of pixels' time behavior. If one pixel gets through these multiple conditions, its phase daily information is estimated by time-averaging only the reliable samples. Otherwise, all the daily samples are employed. This default condition has been preferred in order to avoid the loss of pixels within the district area. In the following, this technique will be referred to as non-*Stationary Time-Filtering* (*nSTF*). The deformation-rate map obtained for the *hh* and *vv* channels by applying the SCPT to the polarimetric-filtered time-averaged collection of gbSAR acquisitions is displayed in Fig. 8.8b and Fig. 8.8d, respectively. By quickly comparing the results, a general improvement in the

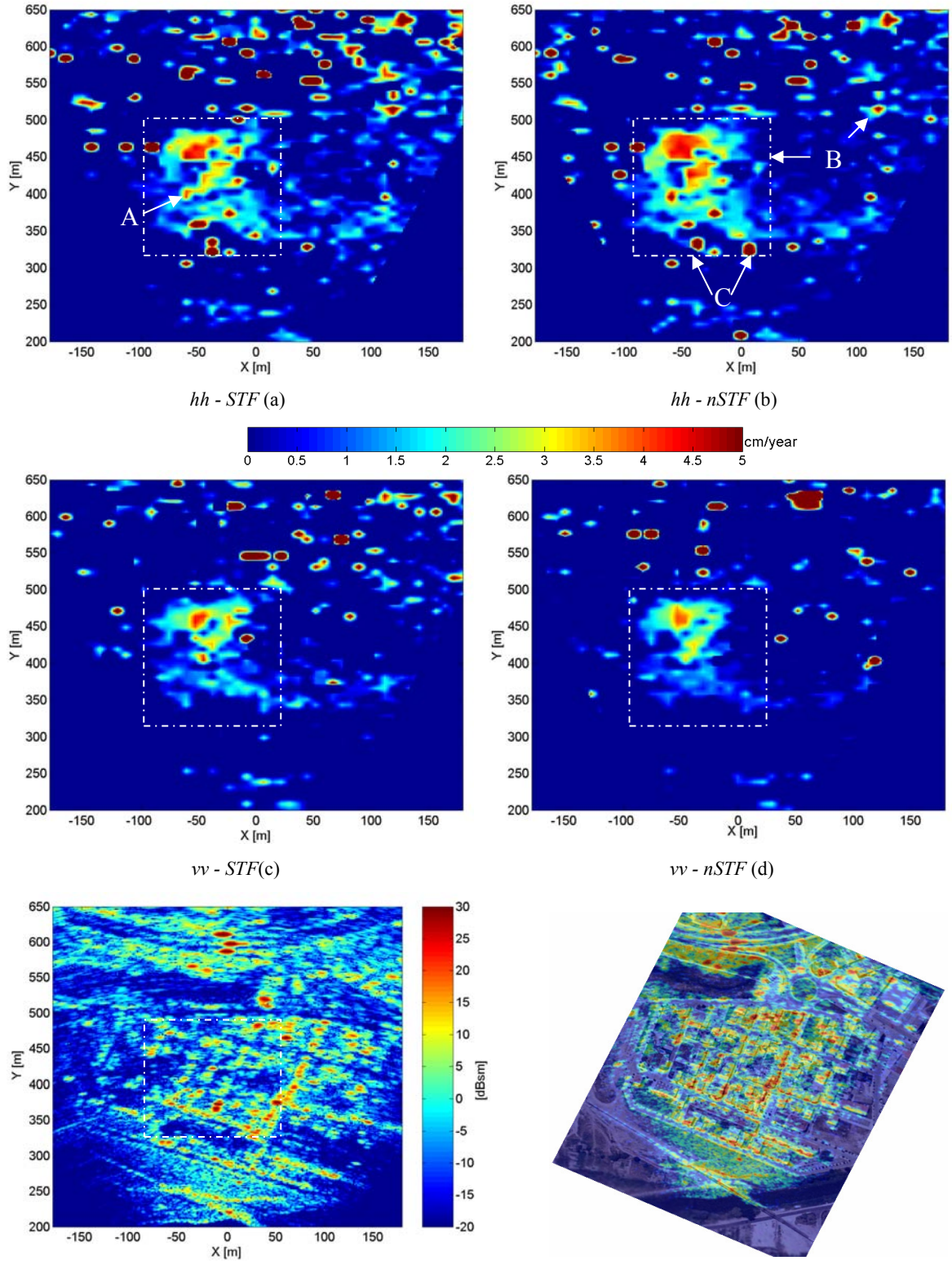

hh - *STF* (a) *hh* - *nSTF* (b)

vv - *STF*(c) *vv* - *nSTF* (d)

(e) (f)

Fig. 8.8: Comparison of the co-polar deformation-rate maps in the radar-plane retrieved by SCPT using the *STF* (a)(c) and the *nSTF* (b)(d) filtering approaches. The pixels' coherence γ has been estimated with a 5x5 pixels boxcar. The SCPT has applied using a 4-layer structure (thresholds: 0.9, 0.8, 0.6, 0.4) and $\gamma_{\mathrm{mod},th}$ equal to 0.8. The *hh* reflectivity information [dBsm] of the corresponding area is displayed in the radar Cartesian coordinates (e) and in UTM coordinates (f) for an easier identification of the different zones within the deformation-rate maps. The points A, B and C, indicate incorrect estimations of the subsidence process.

estimation of the deformation contour is observable for the second approach within the area of the maximum deformation (dotted square). Sudden drops of the displacement velocity appearing as darker stripes around the critical area have been mitigated and in some case eliminated, as it was expected due to the spatial correlation of the subsidence phenomena. The zone A and in Fig. 8.8a is a clear example. In order to make easy the identification of the deformation zones with specific areas of the district, the corresponding reflectivity information is imaged in radar Cartesian and UTM coordinates in Fig. 8.8e and Fig. 8.8f, respectively.

A general reduction of the number of anomalous spots is also detectable, although it is more evident for the *vv* polarization channel. This is in agreement with the results shown in Fig. 7.13, where the scatterers located in this part of the scene have been shown to present a more stable behavior in the *vv* channel. At the same time, it must be taken into account that the absolute deformation-rate estimation is obtained by relating differential phase increments among neighboring pixels. That is, the final estimation is related to the improvement in the quality of each pixel as well as of its natural neighbors. In some cases, the "red spots" disappear, as for the point A in Fig. 8.8a. In other cases, their intensity just decreases, as for points B in Fig. 8.8b. This happens when the path followed by the spatial integration technique to retrieve the absolute deformation-rate value has not changed significantly.

It must be pointed out that where no stable subset of samples was available, *STF* has been applied. This criterion was employed since the number of pixels fulfilling *nSTF*'s constraints was low with respect to the total number of pixels within the area of interest. As a consequence, badly-connected zones aroused after the Delaunay triangulation step and the final result in terms of absolute deformation-rate map was unsatisfactory. Nonetheless, this solution entails two main drawbacks. When no useful subset of samples is detected within an area, the whole collection of daily acquisitions is averaged at pixel level for its long-time description. This is the case of the anomalous red spots that appear exactly at the same position in the two approaches. The second drawback deals with the case when the filtering operation is carried out successfully just for a few pixels within a small area. On the one hand, their differential phase information improves at pixel level. On the other hand, this improvement may be lost when their information is mixed with instable close pixels entering in the boxcar employed for the coherence estimation or during the spatial integration relating neighboring multilooked pixels. This is the main reason for which the shape of some "red spots" slightly changes from the *STF* to the *nSTF* approaches and, in a few

cases, new anomalous spots are generated (points C in Fig. 8.8b). Finally, it is important to remark that this constitutes a preliminary study aiming at working out an effective time-filtering technique based on the detection of time-stationary polarimetric urban patterns. Longer data sets collections are now required to the optimization of the time-samples selection for amplitude-based differential applications.

8.5. Polarimetric differential SAR interferometry (PolDInSAR)

In this section, the basic concept of polarization phase-center position and the way its variation is related to main deformation information are discussed. Let *T* be a generic target illuminated by an electromagnetic plane wave. As it has been stressed in Chapter 2, the properties of the signal backscattered to the sensor strictly depend on the polarization state *p* and the wavenumber vector $\vec{k}$ of the incident wave, as well as on the physical and geometrical properties of *T*. It is well-known that the spatial resolution of any SAR system is much higher than the wavelength of the transmitted signal. Then, each pixel of a SAR image is usually interpreted as the result of the coherent superposition of the backscattering process from all the point-scatterers within the resolution cell. It is worth recalling that whereas the scatterers are 3D distributed, the SAR imaging projects them on the 2D radar domain. A more comfortable description of this process may be obtained by defining an equivalent point scatterer located somewhere within the resolution cell and corresponding to the position where the scattered wave is generated. This point is usually defined as the scattering phase-center (*PC*). As the answer from the same pixel changes with the polarization of the incident wave, it is possible to infer that the location of the *PC* within the resolution cell may vary with the polarization.

Based on the definition of the scattering phase-centers, a simple polarimetric differential scattering model is now put forward. In order to describe the rationale of the model, two main hypotheses are introduced. Then, one of these two assumptions defining the ideal case is relaxed and the model is properly modified to deal with the case of real gbSAR zero-baseline observations. The first assumption is that the deformation characterizing all the scatterers within an observed area is described by the same vector $\Delta\vec{m}$. Being $\vec{k}$ the wavenumber vector defining the propagation direction of the backscattered locally-plane wave, it can be stated that the zero-baseline interferometric phase ϕ_p of a pixel selected within this area is independent of polarization channel *p* employed for the measurement, that is

$$\phi_p(T,x,y) = 2\vec{k}\cdot\Delta\vec{m} = 2k\Delta r \tag{8.22}$$

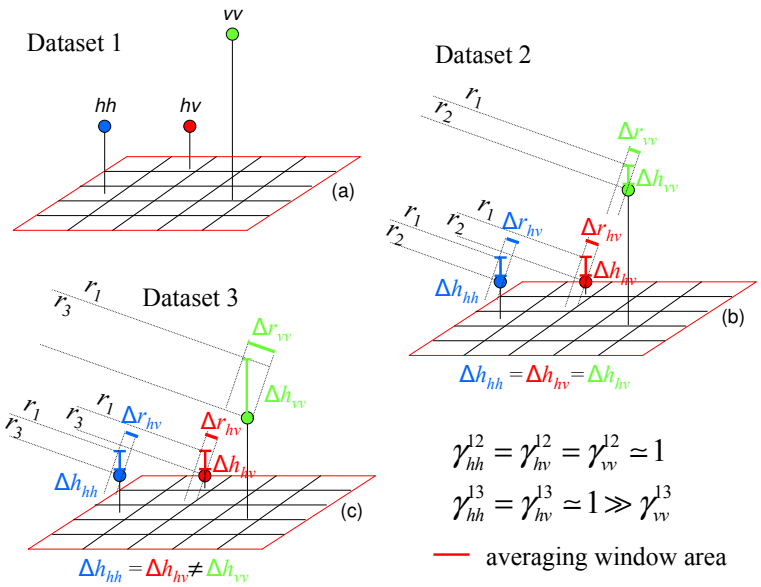

Fig. 8.9: Sketch of the polarimetric differential scattering model. The differential phase ϕ_p contains two main contributions: a polarization-independent deformation component $2k\Delta r$ and a polarization-dependent term ϕ_p^{POL} due to target's temporal decorrelation. The initial position of the phase centers (PCs) within the area of the estimation window (a) changes due to a rigid movement of the whole area (b) or a rigid movement plus a scattering mechanism modification affecting just the *vv* channel (c). In the first case, the differential coherence for the three channels is high and the phase information is the same, i.e., $\phi_{hh} = \phi_{hv} = \phi_{vv} = 2k\Delta r$. In the second case, just *vv* coherence decreases so that $\phi_{hh} = \phi_{hv} = 2k\Delta r \neq \phi_{vv}$ because $\phi_{VV}^{POL} \neq 0$.

where T is the time span between two observations, (x,y) the coordinates of the time-stationary target in the SAR image, "$\cdot$" denotes the scalar vector product and Δr is the radial projection of $\Delta\vec{m}$ onto $\vec{k}$. Essentially, Eq. 8.22 states that in the case of a rigid shift of all the scatterers within the resolution cell, the displacement of all the scattering phase-centers is equal and the absolute phase variation in case of perfect *0B* acquisitions is independent of the transmitting and receiving antennas' polarization. This condition is sketched in Fig. 8.9a-b, where a constant radial variation Δr is observed in the three polarimetric channels of $[S]$ in the $\{\hat{h},\hat{v}\}$ polarization basis after a vertical shift of the illuminated area.

The second hypothesis is that the differential phase variation induced by the area's displacement is lower than π and does not cause any decorrelation effect. That is, the estimation of ϕ_p given by Eq. 8.15 is still independent of the polarization p used for the measurement. In this case, the interpretation of the interferometric phase in terms of phase-centers' displacement is still possible, but they now describe a property of the whole averaged area and not of the single pixel. This reasoning can be now extended to two neighboring pixels P_a and P_b belonging to two time-stationary deterministic targets in a collection of N zero-baseline acquisitions. The differential phase increment between them in the generic interferogram i out of the $\binom{N}{2}$ possible combinations

of master and slave images may be expressed as

$$\Delta\phi_i = \Delta\phi_i(P_a, P_b) = \phi_{p_a,i}(P_a) - \phi_{p_b,i}(P_b) = 2k\left(\Delta r_{a,i} - \Delta r_{b,i}\right) \quad i = 1..N(N-1)/2 \tag{8.23}$$

where p_a and p_b define the polarization state of the electromagnetic wave illuminating the pixels P_a and P_b, respectively. Eq. 8.23 states that the differential phase variation $\Delta\phi_i$ between two pixels associated to two resolution cell that simply translated in space without modifying their scatterers' spatial distribution is independent of the polarimetric channel employed of their description. It can be observed that this conclusion derives from a geometrical description of the problem, which excludes the presence of any decorrelation effect between each pair of SAR images.

When real *0B* gbSAR acquisitions are analyzed, the differential coherence γ_p has been factorized in Eq.5.43 as

$$\gamma_p = \gamma_t^p \gamma_{atm} \tag{8.24}$$

where *p* defines the polarimetric channel while the subscripts *t* and *atm* account for the target's temporal decorrelation and the atmospheric temporal decorrelation, respectively. Under the hypothesis of troposphere homogeneity during the scanning process and absence of rain events, the atmospheric artefacts arising from a variation of the refractive index turn into range phase-ramp (see Section 6.3) the term γ_{atm} can be assume unitary. Then, just the term accounting for the temporal decorrelation of the scatterers is maintained and Eq. 8.24 may be simplified as

$$\gamma_p = \gamma_t^p \,. \tag{8.25}$$

Taking into account the advantages provided by the terrestrial platform, a decrease of γ_t^p can be explained just in terms of changes of the scattering mechanism within the area averaged for the coherence estimation induced by a modification in the spatial distribution of the scatterers. The dependence on *p* stresses that the way these modifications affect the different channels of [*S*] is different. It follows that the movement of the different PCs within the same resolution cell cannot be assumed constant and the first hypothesis of the ideal case described before is not fulfilled anymore. Yet, it is still possible to deal with real gbSAR *0B* observations by modifying Eq. 8.22 as

$$\phi_{p,i}(T, x, y) = 2k\Delta r_i + \phi_{p,i}^{POL} \tag{8.26}$$

where $\phi_{p,i}^{POL}$ accounts for the polarization-dependent displacement due to scatterers' modifications. Indeed, this additional term represents the key factor for polarimetric DInSAR (PolDInSAR)

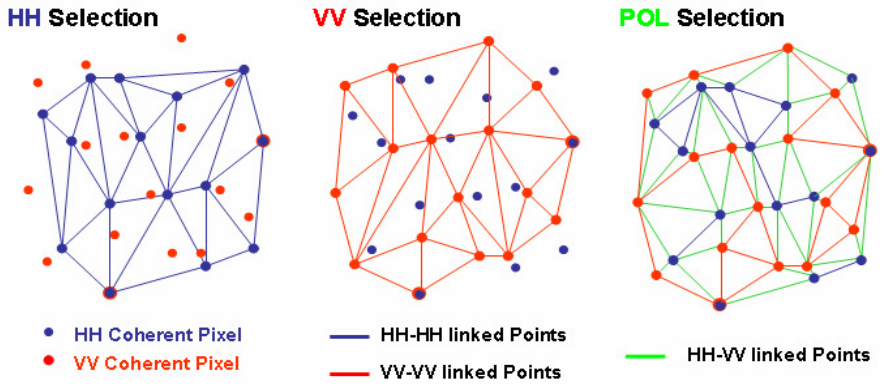

Fig. 8.10: Sketch of selected pixels and triangulation arcs in the case of single-pol and polarimetric selections. For the sake of simplicity, just the relations between the two co-polar channels have been considered in the sketch. Using real data sets, pixels selection is carried out using the full scattering matrix, i.e. *hh, hv* and *vv* information.

formulation: $\phi_{p,i}^{POL}$ arises when the assumption of rigid shift of all the scatterers within the averaging boxcar between the two differential acquisitions fails. Depending on the polarization channel of [*S*] under study, the effects of these changes in the scatterers' distribution might be different. Then, the differential coherence γ_t^p becomes the key parameter for estimating the weight of the scattering decorrelation process in the different polarimetric channels. In the light of this reasoning, the higher value of coherence in a specific channel of [*S*], the lower the contribution of $\phi_{p,i}^{POL}$ and, consequently, the better the estimation of the polarization-independent deformation process within the averaged area. This situation is detailed in the sketch of Fig. 8.9c, where it is shown that the differential phase variation corresponding to the lowest coherence channels (*vv*) contains an additional undesired term. In a first approximation, the set of possible polarization channels may be reduced to *hh*, *hv* and *vv*. In Section 8.7, this hypothesis will be relaxed and the effects of polarization basis transformation will careful analyzed. According to the SCPT formulation, the polarization describing the interferometric phase of all the pixels is the same, that is it is always the case $p_a = p_b$. A first attempt to improve the quality of the differential phase information may be pursued by relaxing this condition and selecting at pixel level the polarimetric channel providing the highest time-averaged coherence. Then, the phase history of each pixel of the image is described by the polarization channel providing the highest time-averaged coherence. Denoting with *M* this polarization, ϕ_i is obtained as

$$\phi_i(T,x,y) = \phi_{M,i}(T,x,y) / \gamma_M(x,y) = \max\left(\overline{\gamma}_{hh}(x,y), \overline{\gamma}_{hv}(x,y), \overline{\gamma}_{vv}(x,y)\right). \tag{8.27}$$

The employment of Eq. 8.27 leads to a significant increase of the number of pixels candidate for the linear-fitting test as well as of spatial relations. This can be observed in Fig. 8.10, where an

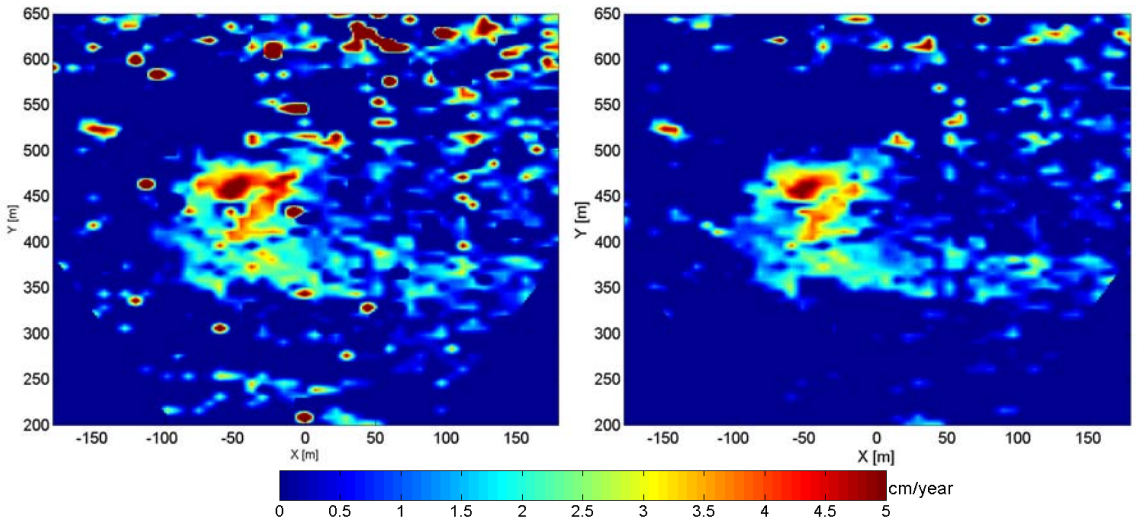

Fig. 8.11: Deformation-rate map in the radar plane using the phase information given, pixel by pixel, by the polarization channel providing the highest mean-coherence $\overline{\gamma}_M$.

Fig. 8.12: deformation-rate map in the radar plane using the phase information given, pixel by pixel and interferogram by interferogram, by the polarization channel providing the highest $\overline{\gamma}'_M$ (*High* method).

example of triangulation obtained in the single-pol case is compared with the result of the new polarimetric approach. For the sake of simplicity, just the relations between the co-polar channels have been considered in the sketch. Contrarily, when real data are analyzed, also the *hv* channel must be taken into account. It is worth pointing out that the temporal evolution of each pixel's phase is still described by the same polarimetric channel. The main difference with respect to the classical approach is that the differential phase information of two linked pixels might come now from two different polarizations (green segments in Fig. 8.10). It is mandatory to carry out an accurate polarimetric calibration of the data sets to avoid the presence of phase offsets among the multi-polarization interferograms.

Once the multi-layer polarimetric selection and the triangulation are performed, linked pixels are fitted to a linear model as described in the classical CPT approach. The process ends up with the integration of spatial increments. An example of deformation-rate map provided by Eq. 8.27 is shown in Fig. 8.11. The multi-layer processing has been performed using the same parameters of the single-polarization study specified in Fig. 8.8. It can be noticed a general improvement in the reconstruction of the deformation bowl. The information contained in the three polarimetric channels has been basically merged in a unique deformation map. Besides, the number of isolated red pixels related to non-stationary behaviors has been reduced with respect to the single-polarization approach. Nonetheless, it has not been possible to completely eliminate them and their presence still constitutes an undesirable effect that should be somehow filtered out. From this point

	STF		*nSTF*			
	Single-Pol CPT		Single-Pol CPT		Polarimetric CPT	
	hh	*vv*	*hh*	*vv*	$\max\left(\bar{\gamma}_{hh},\bar{\gamma}_{hv},\bar{\gamma}_{vv}\right)$	$\max\left(\bar{\gamma}_{hh,i},\bar{\gamma}_{hv,i},\bar{\gamma}_{vv,i}\right)$
L4 [1:0.9)	191	136	190	178	301	364
L3 [0.9:0.8)	239	184	297	278	397	453
L2 [0.8:0.6)	480	456	500	499	561	791
L1 [0.6:0.4)	631	621	646	622	653	1102
Total	1541	1397	1633	1577	1912	2710
%	52%	47%	55%	53%	64%	91%

Table 8.2: Number of reliable pixels selected by the single-polarization CPT and the polarimetric CPT in a 4-layer study using the *Stationary Time Filtering* (*STF*) and *non-Stationary Time Filtering* (*nSTF*) techniques. The total number of pixels within the studied area is 2798.

of view, a significant improvement can be obtained if the constraint of using a fixed polarization channel for the description of pixels' time behavior is relaxed. That is, the set of interferometric phase time-samples concerning the generic pixel (x,y) may be defined as

$$\phi_i(T,x,y)=\phi_{M,i}(T,x,y)\,/\,\gamma_{M,i}=\max\left(\gamma_{hh,i},\gamma_{hv,i},\gamma_{vv,i}\right)\quad i=1,..,N(N-1)/2\,. \tag{8.28}$$

This choice corresponds to select the channel of $[S]$ that is less affected by temporal decorrelation, i.e., with the lower $\phi_{p,i}^{POL}$, for each pair of gbSAR time-averaged acquisitions. This interferogram-by-interferogram and pixel-by-pixel approach will be denoted in the following with *High* method. In this case, the multi-layer analysis can be performed by labeling the quality of each pixel by the definition of the time-averaged hybrid coherence

$$\bar{\gamma}'_M=\frac{2}{N(N-1)}\sum_{i=1}^{N}\gamma_{M,i}\,. \tag{8.29}$$

The deformation rate map obtained with the *High* selection is shown in Fig. 8.12. It can be noticed that the anomalous points detectable in the *hh* and *vv* maps, as well as in the highest mean-coherence approach, have now reduced significantly. The extension of the polarimetric selection to the single interferogram level has made it possible to replace them with a more reliable estimation of the subsidence velocity. The Table 8.2 shows a quantitative comparison between the classical and the modified techniques concerning the district area in terms of number of reliable pixels for each quality layer. This number corresponds to the pixels fulfilling a minimum time-averaged coherence $\bar{\gamma}$ condition and getting through the linear-model fitting test. It can be observed that a higher number of points are obtained when the daily collections of gbSAR acquisitions are filtered at pixel level using the *nSTF* technique. This number further increases when the information

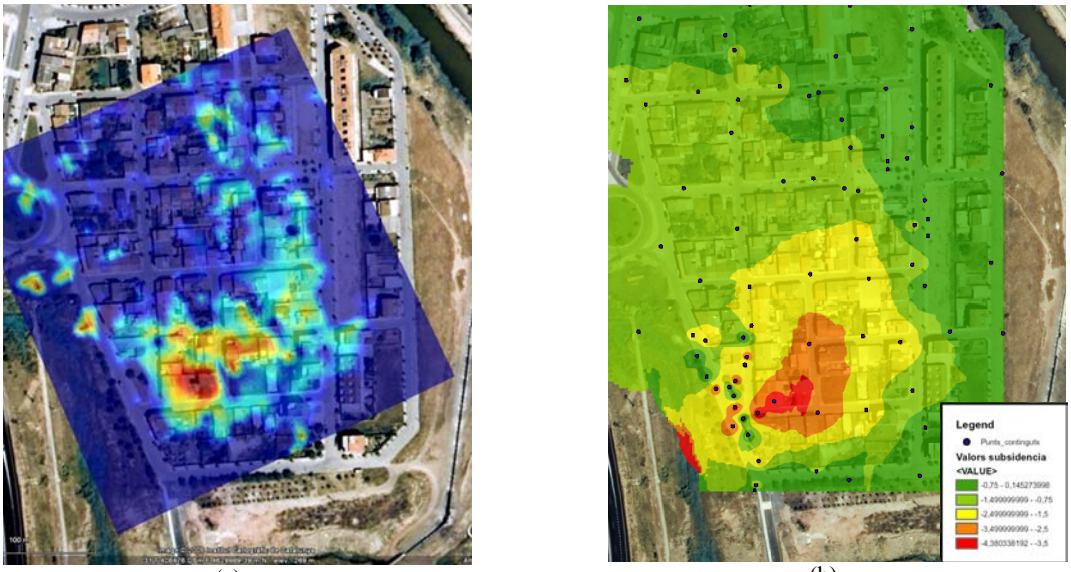

(a) (b)

Fig. 8.13: Geocoded deformation-rate map retrieved by the Polarimetric differential interferometric SAR (PolDInSAR) technique using the *High* method (a) and ground-truth map (b) provided by the Institut Geològic de Catalunya.

carried by the different polarimetric channels is considered at once. The importance of the results provided by the modified versions of CPT is twofold. On the one hand, they show for the first time the benefits of merging the multi-polarization information to improve the quality of differential phase describing the pixels' temporal evolution. On the other hand, they represent a first demonstration of the meaningfulness of overcoming the single-polarization restriction and moving towards a polarimetric-based formulation of advanced DInSAR techniques. Finally, it is important to stress that the polarimetric selection here implemented represents the first step of a new research field to which two up-to-now independent topics, i.e., the SAR Polarimetry and SAR differential interferometry, start converging.

Finally, the geocoded deformation-rate map retrieved by the PolDInSAR approach (*High* method) can be compared with the description of the subsidence phenomena provided by the experts of the Institut Geològic de Catalunya (IGC) in Fig. 8.13. The ground-truth information has been obtained by in-situ lidar measurements gathered during the period monitored by the UPC gbSAR sensor. A very good agreement concerning the spatial description of the deformation process can observed between the two images. The position of the area characterized by the maximum deformation perfectly matches, although the gbSAR measurements lead to a slight overestimation of its displacement rate, 5 cm/year against the 4.4 cm/year given by the in-situ measurements. Finally, it is worth recalling that, due to the time-instability of urban scatterers' polarimetric behavior, the long-time absolute phase information is likely to become unreliable when spatial averaging

operation is performed and several pixels presenting a high coherence value do not get through the linear-fitting test. The small overestimation might be related to the number of points really employed for the spatial integration of the deformation-rate increments. Yet, the results clearly demonstrate the noteworthy advantages that the use of the polarimetric information provides with respect to the single-polarization approach.

8.6. Coherence-Optimized PolDInSAR

In the previous section, it has been shown that the interferometric *0B* coherence between two gbSAR acquisitions is basically affected by temporal decorrelation. The higher the value of the interferometric coherence, the more reliable the interpretation of the corresponding phase information in terms of scatterers' main displacement. A first attempt to improve the reliability of the phase information using the full scattering matrix has been carried out by selecting at pixel level the polarization showing the lower temporal decorrelation. Yet, despite the significant improvement in the description of the deformation process, this approach does not completely exploit the potentials of fully-polarimetric acquisitions. From this point of view, it is meaningful to look into the possibility to further improve the quality of the retrieved deformation information by relaxing the constraint of describing pixels' scattering matrix using the $\{\hat{h},\hat{v}\}$ polarization basis, and finding out the scattering mechanism SM defined in Section 2.5.2 which maximizes the differential coherence. According to Eq. 5.17, a noteworthy improvement in the estimation the corresponding differential phase information is expected.

Concerning the main polarimetric SAR interferometric (PolInSAR) techniques proposed in the literature [Cloude,98] [Colin,06] [Sagues,00], it is important to stress that their mathematical formulation can be directly extended to *0B* gbSAR PolSAR acquisitions by simply substituting the concept of spatial baseline with the time. At the same time, it must be recalled that they have been meant for the retrieval of physical properties from homogeneous distributed scatterers. From this point of view, the urban environment of Sallent does not generally fulfill this hypothesis due to the deterministic nature of the scatterers. This means that their employment for the estimation of the subsidence phenomena within the district area must be considered as an attempt to tackle to problem of optimizing the quality of the retrieved differential information through polarimetric optimization. The results that the different approaches provide concerning the long-time gbSAR collection of Sallent will be carefully discussed before drawing any conclusion about their effectiveness for DInSAR applications.

When fully polarimetric data are collected, the information associated to each pixels of the illuminated scene is represented by the scattering matrix [*S*]. In Section 2.3.2, it has been shown that the matrix can be arranged in a scattering vector form $\vec{k}_\Psi$ by fixing a set of orthogonal 2x2 matrices $[\Psi]$. Among all the possible $[\Psi]$, the Pauli's basis $[\Psi_P]$ is closer to the physical and geometrical properties of the scattering process and is generally used for polarimetric studies.

Let $\vec{k}_P^1$ and $\vec{k}_P^2$ be the scattering vectors of two *0B* PolSAR data sets acquired in the back-scattering configuration in two different time instants. Under the hypotheses of *ergodicity* and spatial homogeneity of the scattering process, it is possible to define the so-called 6×6 PolInSAR Coherency complex matrix $[T_6]$ as follows

$$[T_6] = \left\langle \begin{bmatrix} k_P^1 \\ k_P^2 \end{bmatrix} \begin{bmatrix} k_P^{1\dagger} & k_P^{2\dagger} \end{bmatrix} \right\rangle = \begin{bmatrix} [T_{11}] & [\Omega_{12}] \\ [\Omega_{12}]^\dagger & [T_{22}] \end{bmatrix} \tag{8.30}$$

where $\langle\cdot\rangle$ and † respectively denote the spatial average operation and *Hermitian* transformation, $[T_{11}]$ and $[T_{22}]$ are the 3×3 Coherency matrices of the two acquisitions, and $[\Omega_{12}]$ is a new 3×3 complex matrix containing the differential interferometric information relating the different polarization channels. At this point, it is worth recalling the concept of the scattering mechanism (SM) introduced in Section 2.3.3 and denoted with $\vec{u}$. SM constitutes a useful mathematical tool with a twofold interpretation: it is able to describe at once the polarization state of the transmit (Tx) and receive (Rx) antennas as well as a physical characteristic of the observed scatterer [Neumann,08]. For the monostatic case, $\vec{u} \in \mathbb{C}^3$ but it presents only four degrees of freedom since it is a unitary vector and its first component is real. To obtain the scattering information S_i for a specific combination *i* of Tx/Rx polarizations, the Paulis's vector is projected onto SM as follows

$$S_i = \vec{u}_i \cdot \vec{k}_P \in \mathbb{C}^3 \qquad i \in \{hh, hv, vv\}. \tag{8.31}$$

Accordingly, the estimate of the interferometric coherence and phase for any combination of scattering mechanisms $\vec{u}_i$ and $\vec{u}_j$ is directly given by

$$\gamma_{ij}\left(\vec{u}_i, \vec{u}_j\right) e^{j\phi\left(\vec{u}_i, \vec{u}_j\right)} = \frac{\left\langle \left(\vec{u}_i \cdot \vec{k}_P^1\right)\left(\vec{u}_j \cdot \vec{k}_P^2\right)^\dagger \right\rangle}{\sqrt{\left\langle \left(\vec{u}_i \cdot \vec{k}_P^1\right)\left(\vec{u}_i \cdot \vec{k}_P^1\right)^\dagger \right\rangle \left\langle \left(\vec{u}_j \cdot \vec{k}_P^2\right)\left(\vec{u}_j \cdot \vec{k}_P^2\right)^\dagger \right\rangle}} = \frac{\vec{u}_i^{\,\dagger} [\Omega_{12}] \vec{u}_j}{\sqrt{\vec{u}_i^{\,\dagger} [T_{11}] \vec{u}_i \, \vec{u}_j^{\,\dagger} [T_{22}] \vec{u}_j}} \tag{8.32}$$

In classical DInSAR applications, it is always the case $\vec{u}_i = \vec{u}_j$. It follows that the *hh*, *hv* and *vv* interferometric phase information can be calculated from $[\Omega_{12}]$ as

$$\begin{aligned}
&\vec{u}_i = \vec{u}_j = \vec{u}_{hh} = \frac{1}{\sqrt{2}}[1 \;\; 1 \;\; 0] \Rightarrow \phi_{hh} = \angle \vec{u}_{hh}^{\,\dagger} [\Omega_{12}] \vec{u}_{hh} \\
&\vec{u}_i = \vec{u}_j = \vec{u}_{hv} = [0 \;\; 0 \;\; 1] \Rightarrow \phi_{hv} = \angle \vec{u}_{hv}^{\,\dagger} [\Omega_{12}] \vec{u}_{hv} \\
&\vec{u}_i = \vec{u}_j = \vec{u}_{vv} = \frac{1}{\sqrt{2}}[1 \;\; -1 \;\; 0] \Rightarrow \phi_{vv} = \angle \vec{u}_{vv}^{\,\dagger} [\Omega_{12}] \vec{u}_{vv}
\end{aligned} \quad . \tag{8.33}$$

In order to find the maximum γ_{ij}, three main strategies may be pursued.

8.6.1. Double scattering mechanisms (*DSM*)

The most general solution to the coherence maximization problem was proposed in [Cloude,98] and tackles the problem by optimizing the modulus of the covariance $\vec{u}_i^{\,\dagger} [\Omega_{12}] \vec{u}_j$ for two PolSAR data sets *i* and *j* while keeping the variance of $\vec{u}_i^{\,\dagger} [T_1] \vec{u}_i$ and $\vec{u}_j^{\,\dagger} [T_2] \vec{u}_j$ constant. This is carried out by maximizing the complex Lagrangian *L* defined as

$$L = \vec{u}_i^{\,\dagger} [\Omega_{12}] \vec{u}_j - \lambda_1 \left(\vec{u}_i^{\,\dagger} [T_1] \vec{u}_i - C_1 \right) - \lambda_2 \left(\vec{u}_i^{\,\dagger} [T_2] \vec{u}_i - C_2 \right) \tag{8.34}$$

where λ_1 and λ_2 are Lagrange multipliers and C_1 and C_2 are constant usually set to 1 [Neumann,08]. The solution is represented by three pairs of scattering vectors providing three coherence values, which are referred to as *optimum* coherences and denoted with γ_{opt1}, γ_{opt2} and γ_{opt3} so that $\gamma_{opt1} \geq \gamma_{opt2} \geq \gamma_{opt3}$. According to a widely shared physical interpretation, these optimum coherences may be related to three independent scattering mechanisms coexisting in the averaged area. In the case of non-zero baseline, the corresponding optimum phases may be related to the vertical distribution of the corresponding phase centers and used for the retrieval information about the elevation of vegetation [Papathanassiou,01] or man-made structures [Guillaso,05]. In the case of *0B* acquisitions, the main concern is the retrieval of the optimum phase related to the deformation process. According to the model described in Section 8.5, the higher γ, the lower the effect of the scatterers' temporal decorrelation, and, consequently, the lower the influence of the phase term $\phi_{p,i}^{POL}$. It follows that, among the three optimum coherences provided by the optimization technique, γ_{opt1} is expected to contain the useful information for differential applications. This method is considered the most general one since it allows the selection of different scattering mechanisms at the end of the *spatial* or *temporal* baseline, i.e., it may be $\vec{u}_{opt1}^{\,1} \neq \vec{u}_{opt1}^{\,2}$. Accordingly, it will be referred to as Different Scattering Mechanisms (*DSM*).

8.6.2. Equal scattering mechanisms (*ESM*)

A general optimization routine with the constraint of equal SMs (*ESM*) was instead proposed in [Colin,06]. The main assumption is that the two Coherency matrices $[T_{11}]$ and $[T_{22}]$ are very

similar. Then, it is possible to substitute Eq. 8.32 with the new expression

$$\widetilde{\gamma}_i\left(\vec{u}_i\right)e^{j\tilde{\phi}\left(\vec{u}_i\right)}=\frac{\vec{u}_i^{\,\dagger}\left[\Omega_{12}\right]\vec{u}_i}{\vec{u}_i^{\,\dagger}\left[T_{12}\right]\vec{u}_i} \tag{8.35}$$

where

$$\left[T_{12}\right]=\frac{\left[T_{11}\right]+\left[T_{22}\right]}{2}\,. \tag{8.36}$$

It can be demonstrated that $\widetilde{\gamma}_i$ is always lower than the generalized optimum coherence γ_{ii} and $\widetilde{\gamma}_i$ always lies in the range [0,1]. Moreover, the numerator in Eq. 8.32 and in Eq. 8.35 is the same when $\vec{u}_i=\vec{u}_j$ so that it is always $\tilde{\phi}\left(\vec{u}_i\right)=\phi\left(\vec{u}_i,\vec{u}_i\right)$. Since the optimization of $\widetilde{\gamma}_i$ is not analytically solvable, an iterative method mast be used. An efficient algorithm converging to the solution in a few (two to five) iterations can be found in [Colin,06].

8.6.3. Sub-optimum scattering mechanism (*SOM*)

The last method here recalled was proposed in [Sagues,00]. Although it entails the condition $\vec{u}_i=\vec{u}_j$ as the *ESM* approach, it solves the optimization problem by sweeping all the possible combination of ellipticity/orientation angles (ψ,χ) defining the polarization state of the propagating wave (see Section 2.1). The technique works at [*S*]-level and looks for the polarization state providing the highest among all the co-polar and cross-polar coherence values.

The measured scattering matrix is generally expressed in the linear polarization basis $\left\{\hat{h},\hat{v}\right\}$, that corresponds to $\psi=0$ and $\chi=0$. As it has been described in Section 2.3, the corresponding matrix in a new (ψ,χ) basis is directly given by

$$\left[S\right]_{\psi\chi}=\begin{bmatrix}S_{xx} & S_{xy}\\ S_{xy} & S_{yy}\end{bmatrix}_{\psi\chi}=\left[U_2\right]\left[S\right]_{hv}\left[U_2\right]^T \tag{8.37}$$

where $[U_2]$ can be expressed with respect to (ψ,χ) as

$$\left[U_2\right]=\begin{bmatrix}\cos\psi & -\sin\psi\\ \sin\psi & \cos\psi\end{bmatrix}\begin{bmatrix}\cos\chi & j\sin\chi\\ j\sin\chi & \cos\chi\end{bmatrix}. \tag{8.38}$$

By applying the same (ψ,χ) transformation to the two PolSAR data sets, the co-polar and cross-polar interferometric coherences are obtained as

$$\gamma_{xx}=\left|\frac{\left\langle S_{xx1}S_{xx2}^{*}\right\rangle}{\sqrt{\left\langle\left|S_{xx1}\right|^2\right\rangle\left\langle\left|S_{xx2}\right|^2\right\rangle}}\right| \qquad \gamma_{xy}=\left|\frac{\left\langle S_{xy1}S_{xy2}^{*}\right\rangle}{\sqrt{\left\langle\left|S_{xy1}\right|^2\right\rangle\left\langle\left|S_{xy2}\right|^2\right\rangle}}\right|. \tag{8.39}$$

By graphically representing γ_{xx} and γ_{xy} for every polarization state (ψ,χ) , it is possible to derive the existence of different independent scattering mechanisms inside the averaging area. In the case of a single dominant scattering behavior, both coherence functions generally present only one absolute maximum; in the case of multiple mechanisms, it is possible to identify various local coherence maxima. When non-zero baseline acquisitions are available, they can be used to calculate the height of different layers into which the vegetation target can be decomposed [Sagues,00]. The advantage of this approach is that no hypothesis is assumed on $[T_{11}]$ and $[T_{22}]$. The solution corresponds to the highest coherence value that can be achieved under the constraint $\vec{u}_i = \vec{u}_j$. In the remaining, this last method will be referred to as *SOM*, standing for *Subspace Optimum Method*. With respect to *DSM* and *ESM* solutions, which are calculated almost immediately, approach SOM presents higher computational cost.

8.6.4. **Polarimetric optimization of simulated *0B* interferograms**

In order to assess the improvement of the deformation estimation that the techniques described in Section 8.6.1 are able to provide, simulations are first employed. In [Pipia,05c], it was proposed an efficient algorithm to generate PolSAR and PolInSAR synthetic data concerning homogenous distributed targets. No symmetry hypothesis is assumed and the mathematical restrictions stem from the physical meaningfulness of the second order descriptors used for the generation process. As example, let the set of the theoretical polarimetric matrices $([T_{11}],[T_{22}],[\Omega_{12}])$ be defined as specified in Table 8.3. After generating a synthetic PolInSAR homogeneous data set, that is a *master* and a *slave* PolSAR data sets, it is possible to introduce a deformation-phase component by adding the phase term ϕ_{def} to each slave channel as follows

$$[S_1] = \begin{bmatrix} S_{hh}^1 & S_{hv}^1 \\ S_{hv}^1 & S_{vv\,1}^1 \end{bmatrix} \qquad [S_2] = \begin{bmatrix} S_{hh}^2 & S_{hv}^2 \\ S_{hv}^2 & S_{vv\,1}^2 \end{bmatrix} e^{j\phi_{def}} . \tag{8.40}$$

As the diagonal elements of $[\Omega_{12}]$ are real, the value of the phase provided by the interferometric coherence estimator in Eq. 8.15 is expected to converge to ϕ_{def} , whatever the polarization basis is used for the analysis. Obviously, the higher the number of pixels used for the estimation, the higher the reliability of the retrieved interferometric phase. In Section 5.3, it has been defined the mathematical expression relating the number of independent looks *ENL*, the value of coherence and the interferometric phase dispersion. The plots in the sequence of images displayed in Fig. 8.14a confirm that the simulated distributions are generated correctly. The first three images describe the mean value and the standard deviation of the differential coherence corresponding to

$[T_{11}]$	$[T_{22}]$	$[\Omega_{12}]$
$[D]\begin{bmatrix} 0.92 & 0 & 0.2e^{j\pi/4} \\ 0 & 0.7 & 0 \\ 0.2e^{-j\pi/4} & 0 & 0.85 \end{bmatrix}[D]^{\dagger}$	$[D]\begin{bmatrix} 0.9 & 0.05e^{j\pi/4} & 0.2e^{j\pi/4} \\ 0.05e^{-j\pi/4} & 0.6 & 0 \\ 0.2e^{-j\pi/4} & 0 & 0.75 \end{bmatrix}[D]^{\dagger}$	$[D]\begin{bmatrix} 0.88 & 0.1e^{j\pi/5} & 0 \\ 0.1e^{-j\pi/5} & 0.4 & 0 \\ 0 & 0 & 0.67 \end{bmatrix}[D]^{\dagger}$

Table 8.3: Theoretical second order descriptors $[T_{11}]$,$[T_{22}]$ and $[\Omega_{12}]$, employed for the generation of the synthetic PolDInSAR data sets; the matrix [D] has been defined in Section 2.3.2 and relates the *Covariance* [C] and the *Coherency* [T] matrices.

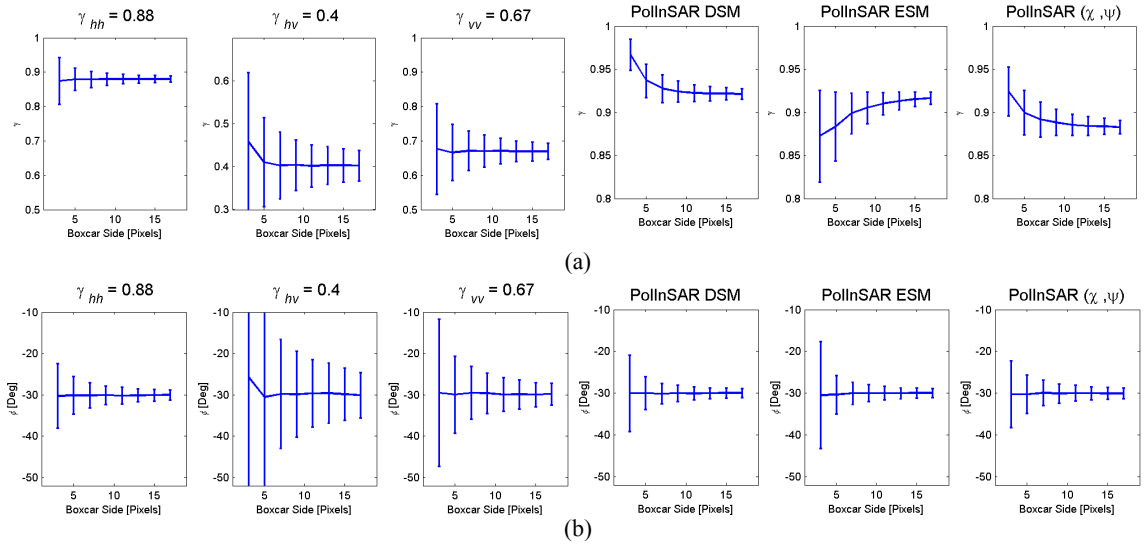

Fig. 8.14: Mean value and standard deviation of differential coherence γ (a) and differential phase ϕ (b) concerning synthetic PolDInSAR data ($\phi_{def} = -30°$) for different combinations of the transmitting and receiving antennas' polarization. The first three columns of each images row correspond to *hh*, *hv*, *vv* polarization channels; the last three ones to the scattering mechanisms (SMs) provided by the *DSM*, *SOM* and *ESM* coherence optimization methods. 2000 simulations have been carried out for the estimation of each parameter. The vertical bars describe the uncertainty of each estimated mean value of γ and ϕ in terms of $\pm$ the standard deviation σ.

hh, *hv* and *vv* channels as a function of the averaging boxcar's side. The other three images show the behavior of the maximum coherence provided by the optimized SMs briefly described in Section 8.6.1. It is worth pointing out that the *DSM* and *ESM* techniques converge to the same optimum coherence: this result was expected, since the two Coherency matrices considered for the simulation and reported in Table 8.3 are almost identical. On the contrary, the fact that *SOM* approach provides a lower optimum coherence must be explained in terms of limited angular sampling step used to describe pixels' polarimetric signature. Nonetheless, shorter $\Delta\chi$ and $\Delta\psi$ lead to coherence values which are always lower or at least equal to γ_{DSM}^{TEO}. The behavior of the corresponding differential phases is plotted in the sequence of images in Fig. 8.14b. It is important to notice that both the original polarimetric channels as well as the optimized SMs lead

to a non-biased estimation of ϕ_{def}. The point is that the standard deviation for the second group is always much lower, i.e. the convergence to the real phase information is faster. A first analysis of the three optimization approaches indicates that *DSM* provides the best performance in terms of coherence optimization. On the contrary, stating if *SOM* or *ESM* must be preferred is not straightforward. On the one hand, the first technique is limited by the sampling step using for the angles (ψ,χ) and seems to converge to the true phase information in a slower way. On the other hand, the second one better optimizes the value of coherence, but this occurs just when $[T_{11}]$ and $[T_{22}]$ are almost identical. When the hypothesis of stationary polarimetric behavior is not fulfilled, its convergence to the optimal solution might not be assured, as it will be discussed in Section 8.6.5. Yet, the simulations clearly show the capability of the three different approaches to reduce the uncertainty of the phase information extracted from homogeneous area.

8.6.5. **Polarimetric optimization of a real gbSAR *0B* interferogram**

The results presented in the previous section prove the meaningfulness of applying the polarimetric coherence-optimization techniques to improve the quality of the estimated differential phase. In this section, two real gbSAR PolSAR data sets with a time span of one month are analyzed. The time separation makes it possible to neglect the contribution of the deformation process, as explained in Section 8.3, and to assume a theoretical zero-mean interferometric phase distribution. For this purpose, the PolSAR time-averaged data sets obtained from the measurements acquired on June 29th and on July 26^{th,} 2006 are employed. The mosaic composition displayed in Fig. 8.15 illustrates the effect of different averaging boxcars on the estimation of the differential coherence provided by the two co-polar channels (*hh*,*vv*), by the channel of [*S*] showing, pixel by pixel, the highest value of coherence (*High*), and by the optimum SMs briefly described in Section 8.6.1-3 respectively. As expected, the use of small boxcar leads to a general overestimation of γ over natural bare surfaces and shadowed areas. Contrary, the position of the urban structures within the scene is characterized by a high coherence in all the images. Concerning the effects of the optimization methods, the qualitative improvement of γ is evident. A quantitative comparison can be instead carried out by observing the histograms in Fig. 8.16. The distribution of γ provided by the different approaches shows that the conclusions drawn using synthetic data are partially confirmed by real data. In fact, *DSM* always provides the highest γ but *SOM* turns out to be more efficient than *ESM*. In order to clear up the reason, it may be employed

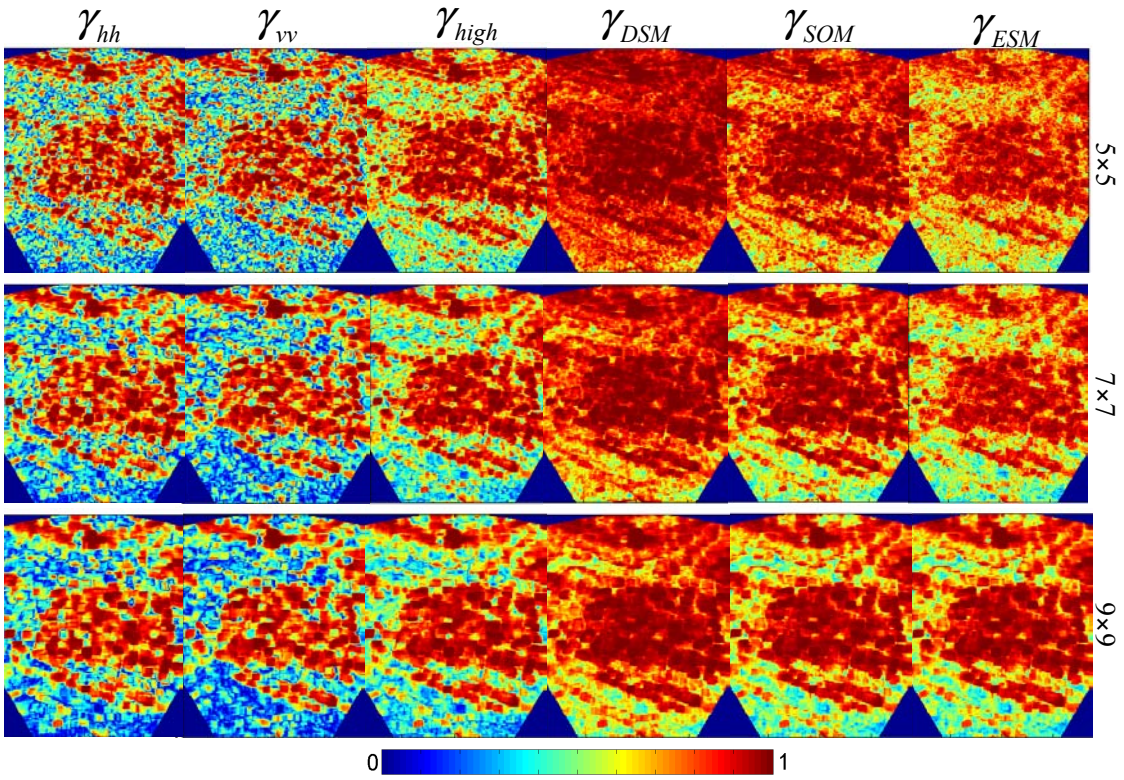

Fig. 8.15: Mosaic of coherence images corresponding to six different combinations of transmitter and receiver polarization (*hh*, *vv*, *High*, *DSM*, *SOM*, *ESM*) for 3 different dimensions (pixels) of the averaging boxcar: 5×5, 7×7, and 9×9. Concerning *SOM*, a sampling step equal to 1° has been employed for the study of pixels' polarimetric signature.

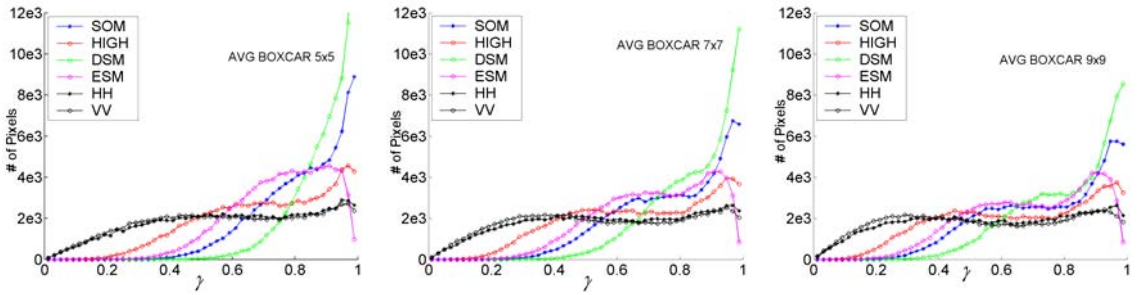

(a) (b) (c)

Fig. 8.16: Histogram of coherence parameter within the Station district in Sallent provided by six combination of transmit and receive antennas polarization (*hh*, *vv*, *High*, *DSM*, *SOM*, *ESM*) for three dimensions (pixels) of the averaging boxcar: 5×5 (a), 7×7 (b), and 9×9(c).

the descriptor of the polarimetric time-stationary hypothesis proposed in [Ferro- Famil,08] and defined as

$$\Lambda = 2\frac{\left\|[T_{11}]\right\|^{\frac{1}{2}}\left\|[T_{22}]\right\|^{\frac{1}{2}}}{\left\|[T_{11}]+[T_{22}]\right\|}, \tag{8.41}$$

where "$\|\ \|$" denotes the matrix norm operator. The distribution of Λ within the district area is shown in Fig. 8.17. It can be noticed that its mean value is around 0.5. According to [Ferro-Famil,08], it is not possible to state that the main hypothesis behind *ESM* formulation is all over

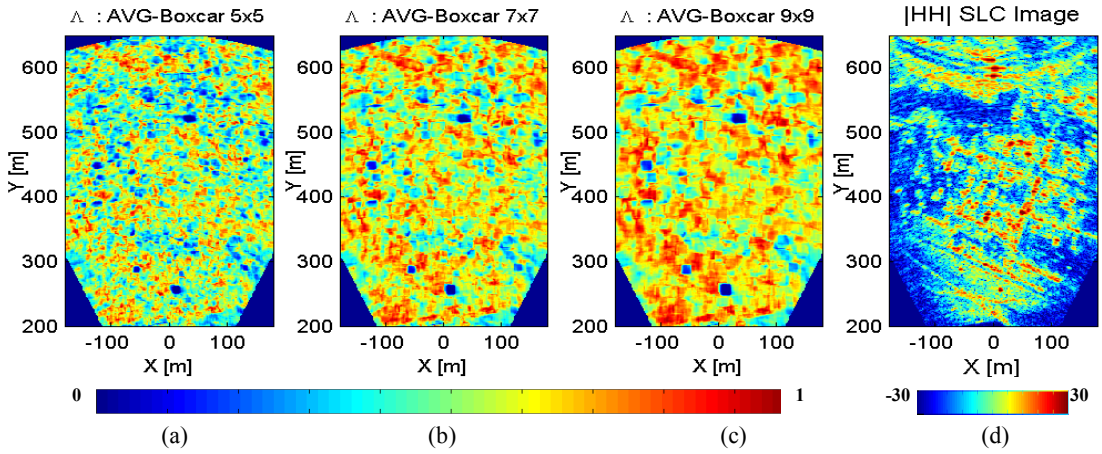

Fig. 8.17: Spatial distribution of the time-stationarity polarimetric descriptor Λ within the Station district of Sallent for different dimensions of the averaging boxcar: 5×5 (a), 7×7 (b), and 9×9 (c). The *hh* reflectivity [dBsm] has been displayed in (d) for an easier interpretation of the first three images.

satisfied and, accordingly, that the method is properly working within the whole are of interest. This constitutes the more likely explanation of the better results provided by *SOM*.

A last comment concerning the *DSM* approach is in order. From a brief comparison of the three optimized images, it can be seen that with respect to the other methods the coherence seems to be saturated. To explain this, it is important to recall that the optimum coherences are given by the eigenvalues of a Hermitian positive, semidefinite 3×3 matrix $[\Pi]$ relating the three matrices $[T_{11}]$, $[T_{22}]$ and $[\Omega_{12}]$ as follows[Cloude,98]

$$[\Pi] = \left(\sqrt{[T_{11}]^{-1}}\,[\Omega_{12}]\sqrt{[T_{22}]^{-1}}\right)^{\dagger}\left(\sqrt{[T_{11}]^{-1}}\,[\Omega_{12}]\sqrt{[T_{22}]^{-1}}\right). \tag{8.42}$$

According to the conclusions drawn in [Lopez,05], the use of the boxcar filtering window for the estimation of the 3×3 Coherency matrix $[T]$ leads to a biased estimation of its three real eigenvalues: the highest eigenvalue is always overestimated while the remaining two are always underestimated. The bias reduces as the number of the size of the boxcar increases. Extending this reasoning to a generic 3×3 matrix obtained by multiplying boxcar-estimated matrices, it is possible to state that the saturation effect in the *DSM* coherence images of Fig. 8.15 is due to the overestimation of γ_{opt1} introduced by the boxcar filtering window.

After analyzing the improvement on γ, the study is focused on the optimized differential phase. The mosaic collection of the *0B* interferometric phase images is displayed in Fig. 8.18. A brief comparison of all the cases reveals that, from the qualitative point of view, no particular benefit seems to be provided by the optimization methods with respect to the *High* technique. In order to

quantitatively demonstrate this, let the *High* method be chosen as reference case. Pixels whose *High* coherence is greater than 0.6 are grouped in 3 main sets defined as follows

$$\begin{aligned} I_1 &= \left\{(x,y) / 0.8 \le \gamma_{High}(x,y) = \max\left(\gamma_{hh}(x,y), \gamma_{hv}(x,y), \gamma_{vv}(x,y)\right)\right\} \\ I_2 &= \left\{(x,y) / 0.6 \le \gamma_{High}(x,y) = \max\left(\gamma_{hh}(x,y), \gamma_{hv}(x,y), \gamma_{vv}(x,y)\right) < 0.8\right\} \\ I_3 &= \left\{(x,y) / 0.4 \le \gamma_{High}(x,y) = \max\left(\gamma_{hh}(x,y), \gamma_{hv}(x,y), \gamma_{vv}(x,y)\right) < 0.6\right\} \end{aligned} \tag{8.43}$$

where (x,y) define the pixel's coordinates. Then, the advantages and drawbacks of each optimization strategy can be easily studied by observing the way the γ and ϕ histograms concerning the three sets modify. As a zero-mean phase distribution is still expected, the standard deviation of the optimized interferometric phase may be employed as an efficiency descriptor of the quality improvement.

The groups of images in Fig. 8.19, Fig. 8.20 and Fig. 8.21, describe the effects of the averaging boxcar dimension on the interferometric parameters estimation. Independently of the boxcar size, the coherence behavior agrees with the global results shown in Fig. 8.16: *DSM* always provides the best coherence optimization, then there is S*OM* and in the end *ESM*. If the interferometric phase histograms and the corresponding standard deviations are observed, it can be noticed that an increment of the mean coherence always determines a reduction of ϕ dispersion. This agrees with the relation stated by Eq.5.23. As expected, the standard deviation decreases as the side of the filtering boxcar increases. Note that this effect is common to all the techniques, since it is related just to the properties of the estimate used to retrieve the interferometric information. Nonetheless, it is worth stressing two important unexpected results.The first one is that, even if a significant improvement of the coherence value is achieved, a low decrease of the standard deviation of ϕ is generally observed. This result is not surprising for the pixels belonging to I_1. In fact, the high coherence level they present in *hh* and *vv* polarizations makes the estimation of the interferometric phase reliable even if no optimization technique is applied. Concerning the medium-coherence pixels, i.e. the set I_2, a more significant benefit was expected instead. A reduction of about 10º is instead obtained for these pixels independently of the size of the averaging window employed for the estimation. Despite the higher computation cost and the limitations introduced by the angular sampling step of 1º, the technique proposed in [Sagues,00] turns out to be the most efficient for this kind of environmental. With the exception of *DSM*, the physical relation between interferometric coherence and phase dispersion is always respected. That is, the higher the coherence betterment, the higher the quality of the phase estimation. The second unexpected result

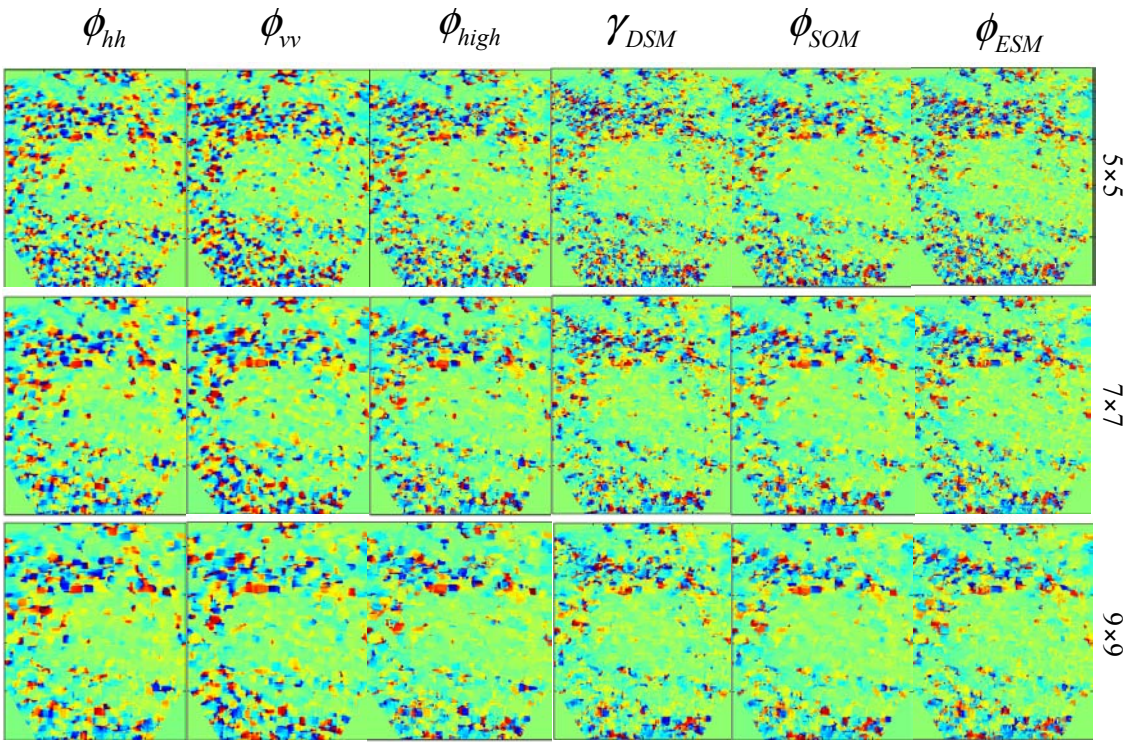

Fig. 8.18: *0B* interferometric phase images corresponding to six different combinations of transmitter and receiver polarization (*hh*, *vv*, *High*, *DSM*, *SOM*, *ESM*) for 3 different dimensions of the averaging boxcar.

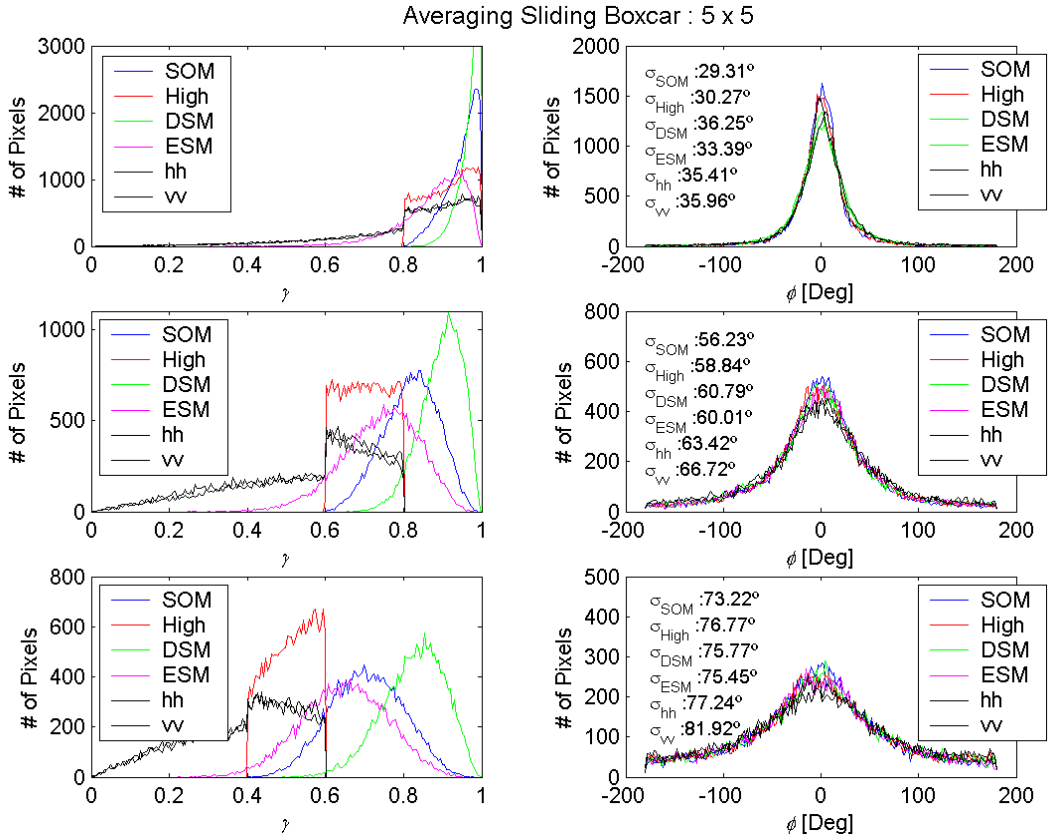

Fig. 8.19: Histograms of *0B* interferometric coherence and differential phase of the subsets I_1,I_2 and I_3 described in Eq. 8.43 for six different combinations of transmitter and receiver polarization (*hh*, *vv*, *High*, *DSM*, *SOM*, *ESM*) estimated by a 5×5 averaging boxcar.

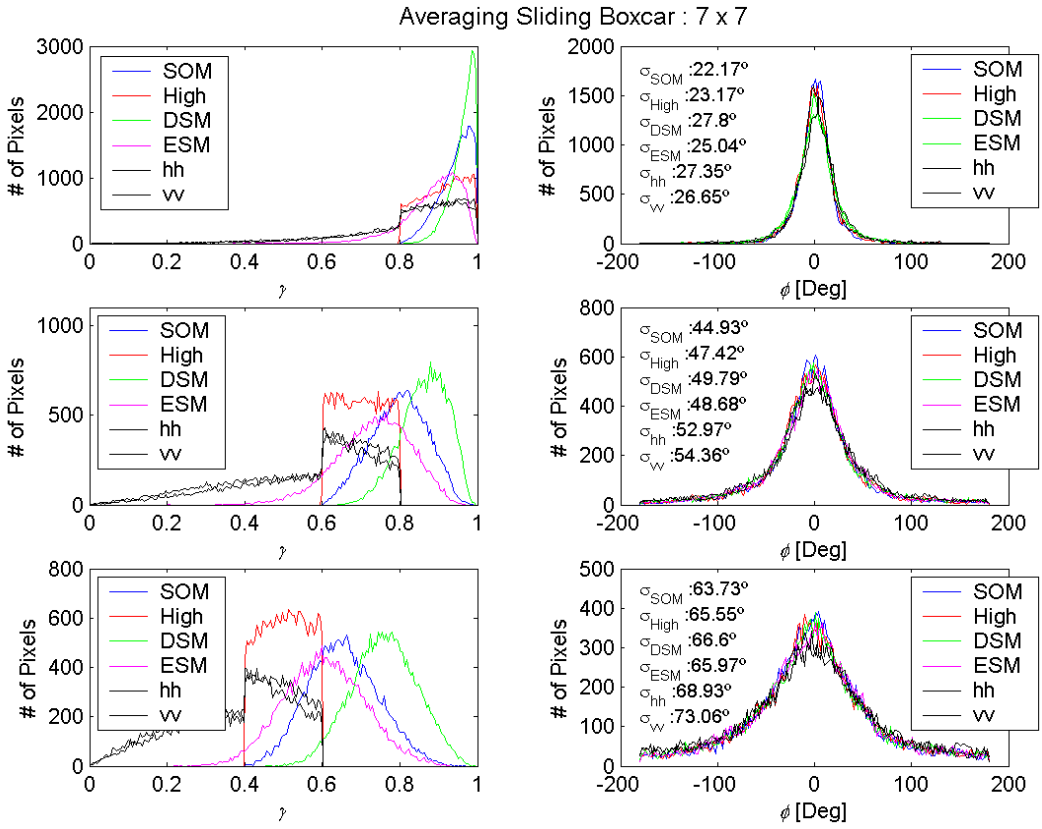

Fig. 8.20: Histograms of *0B* interferometric coherence and differential phase of the subsets I_1,I_2 and I_3 described in Eq. 8.43 for six different combinations of transmitter and receiver polarization (*hh*, *vv*, *High*, *DSM*, *SOM*, *ESM*) estimated by a 7×7 averaging boxcar.

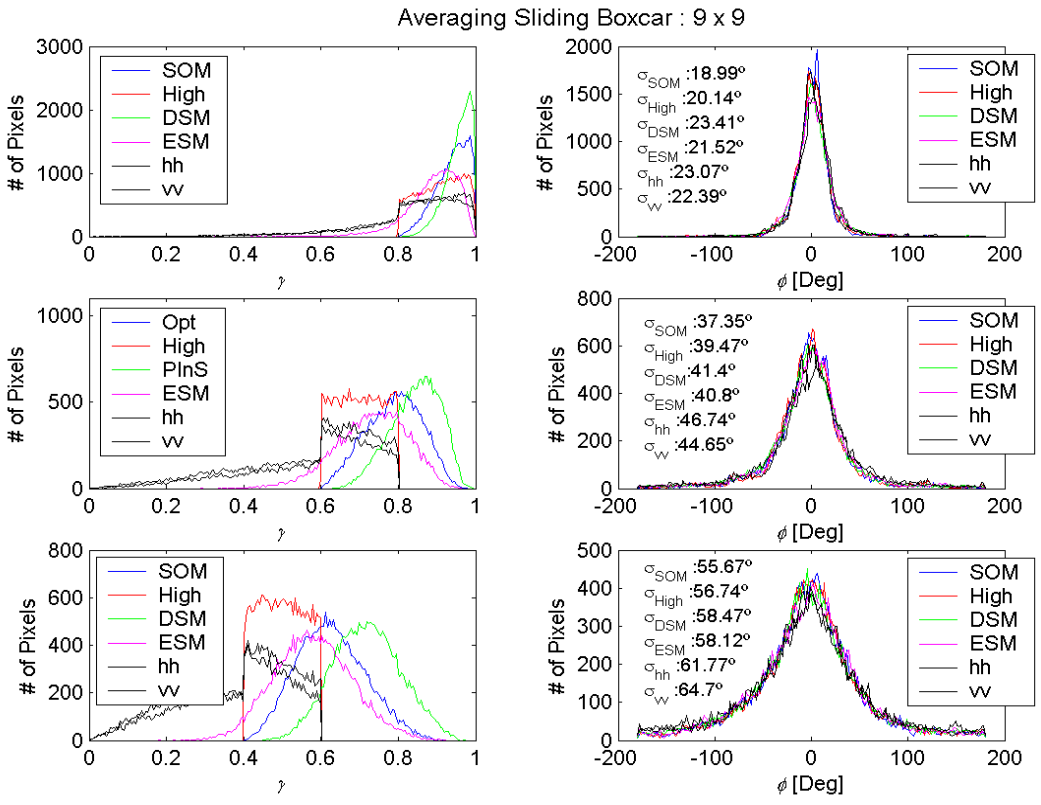

Fig. 8.21: Histograms of *0B* interferometric coherence and differential phase of the subsets I_1,I_2 and I_3 described in Eq. 8.43 for six different combinations of transmitter and receiver polarization (*hh*, *vv*, *High*, *DSM*, *SOM*, *ESM*) estimated by a 9×9 averaging boxcar.

deals with the optimum phase provided by *DSM*. As shown in the mosaic of Fig. 8.15 and in the plots of Fig. 8.19-21, *DSM* is by far the technique providing the best coherence optimization. Nonetheless, the effects on ϕ do not match the expectation. In order to work out a meaningful explanation, some comments are necessary. Contrary to the rest of methods here considered, *DSM* relaxes the constraint that the same polarization basis transformation is applied to the two PolSAR data sets. The synthetic PolInSAR data in Section 8.6.2 have been generated by highly-correlated Coherency matrices ($\Lambda_{SIM} \simeq 0.98$). Being $\vec{u}^{1}_{opt1}$ and $\vec{u}^{2}_{opt1}$ unitary complex vectors, the resemblance of the two vectors may be described by means of the module of their scalar product defined as

$$\rho_{opt} = \left| \vec{u}^{1}_{1opt} \cdot \vec{u}^{2}_{1opt} \right| . \tag{8.44}$$

The mean value and standard deviation of ρ_{opt} concerning the simulation of Section 8.6.1 for the 5×5 boxcar are $\rho_{opt} = 0.9986$ and $\sigma_{\rho_{opt}} = 0.034$, respectively. This means that the optimum vectors $\vec{u}^{1}_{opt1}$ and $\vec{u}^{2}_{opt1}$ are practically the same. If the real case is analyzed, the situation changes significantly. This can be observed in Fig. 8.22a-b, which show the spatial distribution of ρ_{opt} and Λ estimated using the same averaging window. Although a linear relation is not evident, it is possible to state that the areas showing a low ρ_{opt} are characterized by non-parallel optimum vectors. In the case of non-zero baseline acquisitions, this condition arises in areas where volumetric decorrelation occurs [Ferro-Famil,08]. The optimization process performed by *DSM* essentially varies the scattering centers' position to maximize the resemblance between the two optimum mechanisms. The higher the decorrelation, the higher the modifications of scatterers within the averaged area that the optimization method has to compensate for. It is reasonable to extend this interpretation to the *0B* case. When the polarimetric properties of the averaged area can be assumed constant, i.e., high value of Λ, the optimum vectors are almost identical. Then, the optimum phase given by Eq. 8.34 converges to the polarization-independent deformation phase component in Eq. 8.26. Contrarily, when a low Λ characterizes the averaged area, it cannot be guaranteed that the optimization process leads to a better estimation of ϕ_{def}. The results in Fig. 8.19, Fig. 8.20 and Fig. 8.21, show that the convergence of *DSM* optimum phase is not as fast as the rest of optimization methods despite of the higher value of interferometric coherence generally obtained. Yet, it must be pointed out that the urban scenario here observed does not constitute the type of environment coherence optimization techniques has been meant for. The deterministic nature of the pixels is likely to make the averaged area closer to a mixture of different statistical

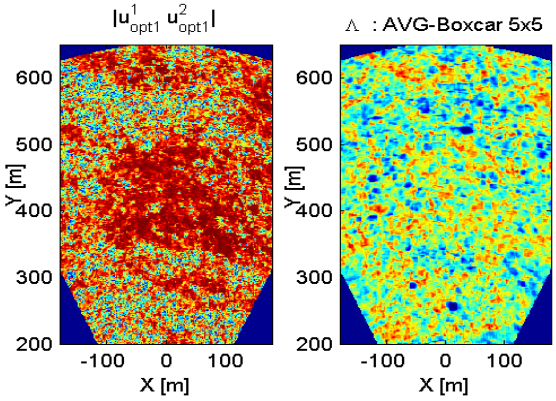

Fig. 8.22: Spatial distribution of ρ_{opt} (a) and of Λ within the Station district in Sallent using a 5×5 averaging boxcar.

process than to a spatial homogeneous distributed target. As far as the two vectors $\vec{u}_i$ and $\vec{u}_j$ in Eq. 8.32 are equal, this is supposed not to affect the retrieval of the mean deformation information. As a matter of fact, the coherence estimation essentially performs a spatial correlation between two complex images. If the relations among the pixels within the averaged area have not changed between the two acquisitions, this correlation keeps high even if they come from different statistical processes. It follows that looking for a unique scattering mechanism optimizing γ means finding out the way to describe the scattering from a specific area so that the local changes, which means at pixel level, are smoother. Contrarily, the selection of two different mechanisms is somehow equal to tuning the way each acquisition is described so that the scattering processes become more resembling. When the polarimetric properties of the area are constant, the two definitions are practically identical. The optimization methods lead to very similar values of coherence and the retrieved phase information is nearly the same. But when the polarimetric properties change, guaranteeing the convergence of the *DSM* to ϕ_{def} is not straightforward. The results shown in Fig. 8.19-21 seem to indicate that, depending on the specific case, the optimization process might bias the estimation of the phase related to the corrupt deformation process.

8.6.6. Coherence-Optimized deformation map retrieval

The CPT is an advanced coherence-based DInSAR technique [Mora,03] [Blanco,06]. The classical formulation of the CPT has been employed in Section 8.4 for the analysis of long-time collections of single-pol SAR data sets. A novel polarimetric formulation has been instead proposed in Section 8.5. The new approach deals with the retrieval of the interferometric phase information through the selection, at pixel level, of the polarization channel providing the highest coherence

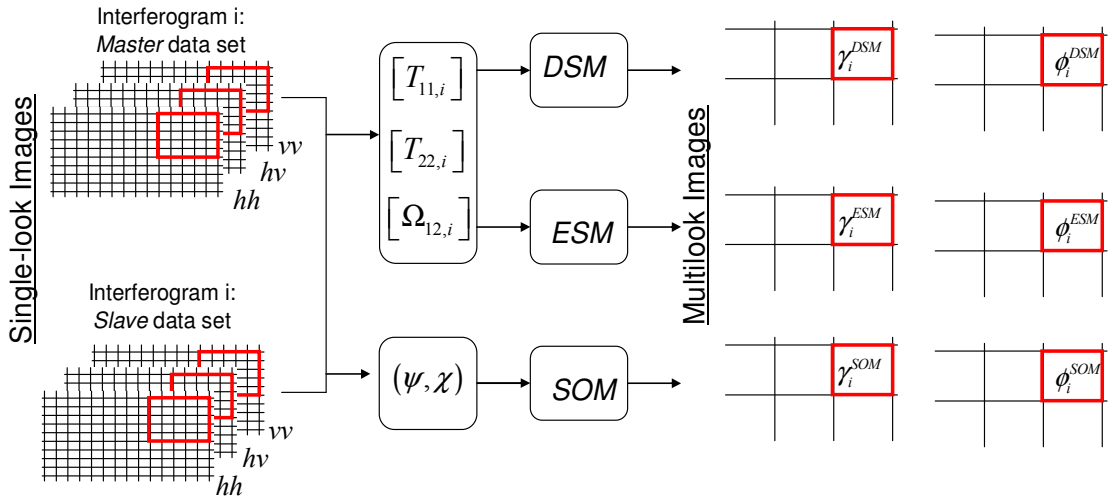

Fig. 8.23: Sketch of the processing-chain applied to the $\binom{N}{2}$ pair of the *N* daily-averaged gbSAR data sets for the generation of the optimized coherence and differential phase multi-looked images.

value. The analysis in terms of deformation-rate map estimation has shown a significant improvement if the selection is performed interferogram by interferogram and not considering a fixed channel for the description of pixels' long-time behavior. In the light of this reasoning, it is now meaningful to look into the possibility to further improve the quality of the retrieved information by employing the optimization techniques described in Section 8.6.1-3. Being *N* the number of the daily-averaged gbSAR data sets, the optimization methods denoted with *DSM*, *SOM* and *ESM* are applied to each of the $\binom{N}{2}$ possible acquisitions pair. The sketch of Fig. 8.23 points out the basic steps leading to the *i*th optimized interferogram. Each pair of master-slave PolSAR acquisitions is incoherently and coherently processed. The first approach estimates, pixel by pixel, the second order polarimetric descriptors using a filtering boxcar and it successively applies the *DSM* and ESM optimizations. The output of each technique is pair of real multi-looked images containing the interferometric coherence and the optimized phase. The second approach is the *SOM*. As it has been previously explained, it fixes an angular step for the ellipticity/orientation angles (ψ,χ) and it looks for the polarization basis transformation of [*S*] providing the highest value among all the possible co-polar and cross polar coherences. Again, the output consists of a pair of multi-looked coherence and phase images. After optimizing all the possible combinations of PolSAR data sets, the SCPT is applied to the stack of optimized interferograms. As example, the deformation-rate maps retrieved using the setting parameters of Section 8.4.1 are shown in Fig. 8.24a-c. In order to make it possible a direct comparison with the result obtained in Section 8.5, the map obtained with the *High* selection method is also displayed in Fig. 8.24d. A visual inspection of the three optimized images reveals the presence of several areas around the district

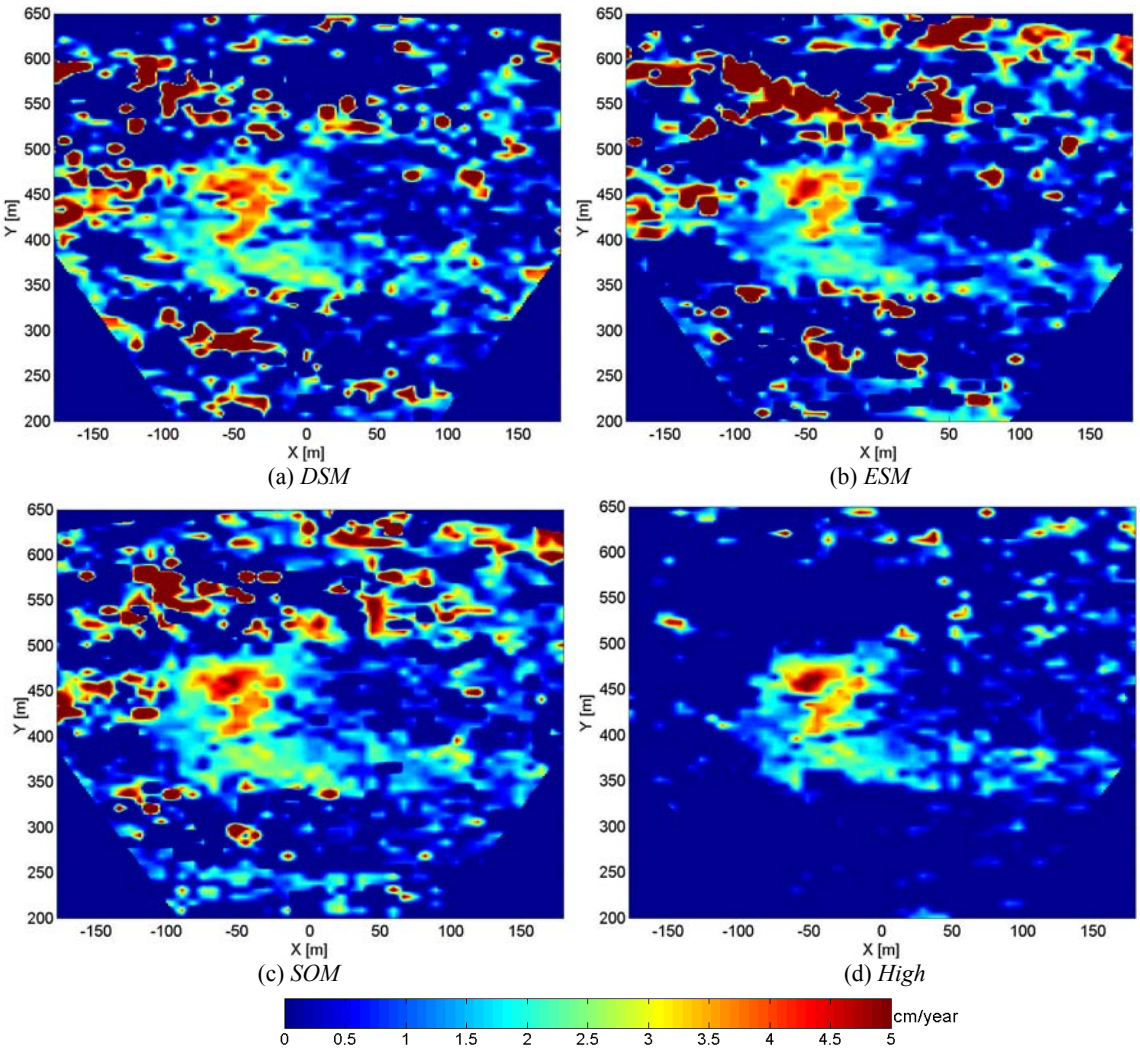

Fig. 8.24: Deformation-rate maps retrieved by SCPT using the *DSM* (a), *ESM*(b), *SOM*(c) techniques and the *High* selection method (d). A 5x5 pixels averaging boxcar has been employed for the estimation of coherence terms. A 4-layers structure (thresholds: 0.9, 0.8, 0.6, 0.4) and $\gamma_{\mathrm{mod},th}$ equal to 0.8 have been used for the CPT setting.

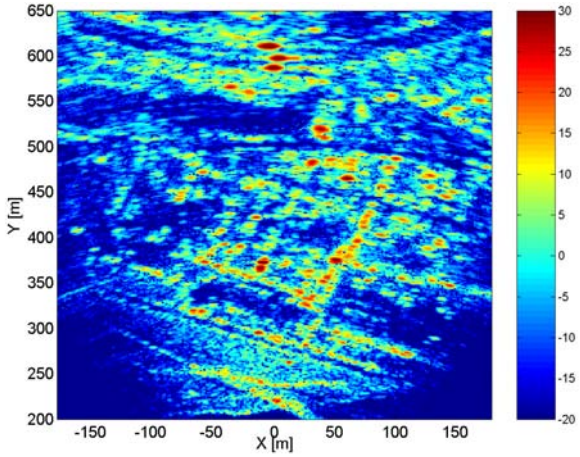

Fig. 8.25: Reflectivity image of the Station district of Sallent in the *hh* polarization.

which are characterized by high deformation-rate values. At the same time, it can be observed that this estimation does not match with the information retrieved by CPT when the *High* method is

	DSM	*ESM*	*SOM*	*High*
L4: [1:0.9)	740	21	729	364
L3: [0.9:0.8)	1070	303	636	453
L2: [0.8:0.6)	996	1463	1212	791
L1: [0.6:0.4)	30	1137	276	1102
Total	2836	2924	2853	2710
%	95%	98%	96%	91%

Table 8.4: Number of reliable pixels fulfilling the mean-coherence and linear model conditions selected by the CPT algorithm in the collections of coherence-optimized interferograms and using the *High* selection method.

employed. The reason lies in the optimization of coherence, which leads to select pixels whose phase information turns out to be unreliable. The *hh* reflectivity information which is displayed in Fig. 8.25 shows that they might correspond to high-reflectivity isolated pixels as well as to low-signal areas. In the first case, pixels are badly connected by the triangulation procedure and the spatial integration of the deformation increments leads to unpredictable values of the absolute velocity. In the second case, the backscattering comes from the side-lobes of strong urban targets located in the closeness. Although they are characterized by low-power levels, their behavior is quite stable in time due to the shadowing effects. In the single-pol selection, they are filtered out by the coherence minimum requirements. After applying the optimization techniques, their coherence level increases and they become trustful points. These pixels partially disappear when bigger boxcars are employed or a higher coherence threshold is fixed. Nonetheless, the scope of this analysis is to carry out a meaningful comparison among all the different approaches under the same conditions. Therefore, an important warning can be already drawn. The use of optimization techniques might lead to the selection of unreliable pixels entering in the lower levels of coherence with respect to single-polarization coherence estimation. Accordingly, more restrictive thresholds should be employed in the second case. In other words, the optimization techniques seem to be useful for the enhancement of the quality of pixels already selected with the single-pol coherence estimation. Otherwise, untrustworthy information is likely to slip in the analysis. The Table 8.4 reports the number of pixels the CPT detected for each coherence layer within the area of the district defined in Fig. 8.8. The label defining the layer to which each pixel belongs is defined by the time-averaged coherence $\bar{\gamma}$ defined in Eq. 8.29. Although this four-layer configuration might not constitute the best solution for each optimized interferograms stack, it allows one to carry out a direct comparison among the different approaches and to draw some general trends. The total number of selected points is approximately the same in the four cases.

The *High* column can be assumed as reference since its elements are obtained without applying any kind of polarization basis transformation or optimization.

Let *ESM* be analyzed first. A general worsening of the pixels' quality is detectable. The number of points in the first two level significantly decreases, meaning that the main condition to be fulfilled in order to obtain an improvement of the coherence value, i.e. $[T_{11}] \approx [T_{22}]$, is likely to be generally unmatched. Concerning the *DSM* technique, it can be noticed that the layer L_4 is almost empty: all the pixels at the end of the process are characterized by an optimum coherence value higher than 0.6. This threshold is generally high for a typical DInSAR study, where coherence values up to 0.3 are often employed. A very high quality map should be obtained. Nonetheless, the map displayed in Fig. 8.24a shows that no betterment is notable with respect to the *High* case. Besides, the shape of the deformation area appears like blurred. This fact seems to confirm what already pointed out in Section 8.6.3: the interferometric phase obtained from the *DSM* optimum scattering mechanisms does not seem to optimize the estimation of the deformation information when polarimetric stationarity hypothesis is not fulfilled. Nonetheless, a more detailed study is now required in order to model the *DSM* optimization process of *0B* PolSAR acquisitions. The *SOM* turns out to be the most promising optimization technique. A remarkable number of points moves towards the upper layers. Besides, the employment of the same SM for the description of each interferometric pair seems to preserve the deformation information. This has been demonstrated in terms of reduction of differential phase's standard deviation *SOM* provides with respect to the *High* reference method. In Fig. 8.24c, it is possible to observe that within the area of the district, where the pixels' density guarantees good connections, the estimation of the deformation-rate is almost identical to the *High* map. Despite a few differences in the area of the maximum movement, the smoother reconstruction of the subsidence shape and an extension of the bowl's contour to areas unselected by the *High* approach must be finally pointed out.

8.7. **Summary**

In this Chapter, the benefits of fully-polarimetric data with respect to single-polarization information for differential applications have been looked into. For this purpose, a coherence-based DInSAR technique, the Coherent Pixel Technique (CPT), has been employed. The classical formulation of the CPT has been used to study two different daily-averaging strategies within the urban environment of Sallent: the coherent sum of all the daily acquisitions (*STF*), and the stationary-pattern-detection-based filtering-technique (*nSTF*). The better results provided by the

second method has pointed out the need to carefully select the daily samples at pixel level to preserve the absolute phase information. Afterwards, a simple PolDInSAR scattering model has been proposed to successfully exploit the information of the fully-polarimetric zero-baseline gbSAR measurements at once. The differential phase retrieved through the estimation of the differential coherence has been factorized into two main contributions: the polarization-independent mean displacement and a polarization-dependent term due to scatterers' temporal changes. Accordingly, the selection of channel of [*S*] showing the highest coherence (*High* method) value has been shown to automatically reduce the second contribution and to improve the quality of the retrieved deformation phase component.

It is important to remark that this approach represents a breakthrough in the differential interferometric formulation. As a matter of fact, it simultaneously employs the full-rank scattering matrix information to enhance the estimation of the polarization-independent differential phase component generated by the subsidence phenomena in Sallent. Significant improvements in the number of reliable pixels detected within the scene as well as in the quality of the retrieved differential phase information have been clearly shown. These results confirm the meaningfulness of the innovative approach proposed in this PhD dissertation, which essentially relaxes the classical restriction of linking pixels only if they behave coherently in the same polarization channel. Indeed, they constitute a first demonstration of polarimetry usefulness for advanced differential applications.

A more insightful analysis of the potentials of polarimetry for DInSAR applications has made it possible to stress the existence of problems up-to-now unknown or barely investigated. Simulations of homogeneous distributed targets have shown the convergence of the most cutting-edge coherence optimization methods (*DSM*, *ESM*, *SOM*) available in the literature to common deformation phase term under the time-starionarity hypothesis of the scattering process. Yet, their application to the real gbSAR data collections of Sallent has stressed that the direct optimization of coherence parameter does not necessarily lead to an improvement of the deformation estimation. Despite the noteworthy increase of the differential coherence within the area of interest that the *ESM* and *DSM* approaches provide, unsatisfactory estimations of the subsidence phenomenon have been finally obtained. In the case of *ESM*, the unexpected result has been related to the time non-stationarity of the Coherency matrix [*T*] describing the urban scatterers' polarimetric behavior. On the contrary, the mismatch between the hypothesis of scatterers' spatial homogeneity and the

deterministic heterogeneity characterizing the Sallent environment represents the most likely reason of the unsatisfactory deformation-rate estimation provided by *DSM*. Finally, encouraging results have been obtained using the *SOM* method: the employment of the same scattering mechanism SM for the description of scatterers' behavior in each pair of *0B* data sets seems to constitute a compulsory condition for retrieving a reliable description of the deformation components. Yet, a more precise scattering physical model is now required to correctly interpret the information retrieved by the different approaches and to work out more efficient filtering and processing procedures.

Chapter 9

Conclusions

The main objective of this PhD dissertation has been to demonstrate the potentials of polarimetry for differential SAR interferometric applications and the possibility to improve the quality of the retrieved deformation information with respect to single-polarization approaches. The analysis has been performed using long-time collections of polarimetric gbSAR data at X-band over an urban environment.

The high-stability of the sensor during the aperture synthesis and the absence of any revisiting time restriction have been indicated as the main advantages of terrestrial platforms, whereas their main drawback is the reduced scenario they are able to illuminate. This limitation has been partially compensated by employing widebeam antennas, but the problem of the meaningfulness of polarimetric measurement had to be tackled. A novel approach for the estimation of polarimetric purity distortions which arise proportionally to the antennas' illumination beamwidth has been worked out and maximum angular thresholds for acquiring meaningful polarimetric SAR data sets have been put forward.

An innovative iterative strategy for retrieving topography information from gbSAR interferometric acquisitions has been also proposed. This approach, which has been obtained by properly adapting a satellite formulation to the Short Synthetic Aperture (SSA) case, allows one to avoid the typical interferometric approximations that might turn out to be incorrect in gbSAR observation geometries. The technique has been assessed using real data and very promising results have been presented.

The time required for the acquisition process has been shown to be of key-importance in order to guarantee the quality of amplitude and phase information in gbSAR acquisitions versus

troposphere changes. Slow scanning processes performed under turbulent atmospheric conditions have been demonstrated to lead to low-quality interferometric data and, in the worst cases, to a dramatically corruption of the reflectivity information. These distortion effects have been explained by linear and non-linear variations of the refractive index *n* during the aperture synthesis and confirmed by both simulations and real measurements. Linear gradients of *n* introduced a rotation of targets proportional to their squint position, generating an image stretching along the cross-range dimension; non-linear evolutions of *n* introduce additional defocusing effects. On the contrary, fast scanning processes make it possible to assume the troposphere medium homogeneous in space and stationary in time during the gbSAR acquisition process. Under these hypotheses, the atmospheric artefacts in zero-baseline gbSAR data have been shown to turn into polarization-independent linear phase-ramps in range induced by different values of *n*. Accordingly, a propagation model has been developed and a novel coherence-based technique has been proposed to compensate for the corresponding differential phase ramp. Essentially, the atmospheric artefact is efficiently estimated by projecting the differential phase of all the high-coherent points within the illuminated scene onto a unique range cut and linear-fitting the resulting phase distribution.

In order to effectively separate differential phase variations due to the troposphere changes from the deformation components in long-time span gbSAR acquisitions, an extended formulation of the technique has been put forward. The underlying principle is the creation of a basic-function set and the description of the long-time phase artefact as a linear combination of short time-span artefacts. By properly choosing the maximum time-separation between successive acquisitions, this approach offers two main advantages. On the one hand, it allows one to neglect any deformation contribution to the differential phase employed for estimating the basic functions. On the other hand, it reduces the temporal decorrelation effects within the illuminated scene, and, consequently, disposes of a higher number of stable pixels for the coherence-based model fitting. Indeed, the extended compensation technique makes it possible to efficiently pre-process long-time collections of gbSAR data sets for advanced differential studies.

The gbSAR polarimetric data sets acquired in the frame of Sallent measurement campaign has stressed, for the first time, the complex dynamics of the EM scattering mechanism within an urban environment. Thanks to the high-sampling rate that only a terrestrial platform is able to provide, the one-day collections have outlined the sensitivity of urban targets' polarimetric response at X-

band to atmospheric changes and, more surprisingly, to human activities. Polarimetric channels have been shown to be differently affected by urban targets' modifications so that the stability of one polarization channel has turned out to be an insufficient condition to assure a constant polarimetric behavior. The classical formulation of Permanent Scatterers (PSs) technique has been demonstrated to be unsuitable to deal with the unexpected time-evolution of the Sallent environment. The main reason is that the time-stationarity hypothesis, which is invoked by PS statistical model, is often unfulfilled. Two novel algorithms have been hence developed for the study of the daily properties of the illuminated area. The first one deals with the extension of the polarimetric entropy concept to the time domain. In the frame of this work, it has been referred to as H_T. This descriptor has been shown to be sensitive to scatterers' non-stationary time behaviors and offers the advantage of analyzing the whole polarimetric information at once. Yet, it is incapable of detecting the existence of independent time-stationary processes alternating in the description of the same pixel directly. This idea has been pursued by implementing a second algorithm. It analyzes one channel of [S] at a time and splits the set of non-stationary time-samples at disposal into time-stationary subsets of acquisitions providing regular amplitude and phase profiles. The comparison of H_T distributions from diurnal and nocturnal gbSAR collections has revealed a higher stability of the district during the night. On the one hand, this has corroborated the interpretation of polarimetric changes as a consequence of human daily habits. On the other hand, it has indicated the night as the optimal condition for carrying out urban environment long-time observations. The same result has been confirmed by the time-stationary subset study. Furthermore, the second technique has made it possible to emphasize the complementary information carried by the different polarization channels due to polarization-dependence of targets' daily stability.

The need to carry out a meaningful description of pixels' long-time behavior has pointed out two main limitations of the procedure employed for the selection of time-stationary daily subsets. The first one is that the filtering technique is sensitive to the amplitude and phase calibration offsets among the different daily collections. These offsets are due to the fact that the reference trihedral was installed before each day of measurement and removed at the end of the acquisition process. The second one is that it is not able to directly describe the scattering mechanism characterizing each pixel of the image since it analyzes just one channel of [S] at a time. In all these evidences, a novel polarimetric filtering technique for the selection of samples in long-time PolSAR data sets

collections has been introduced. The rationale has been to assure first the time-stationarity of the pixels' polarimetric behavior and then the stability of the polarimetric amplitude and absolute phase information. The first issue is coped with by the use of normalized-to-span Pauli's components (NPCs), which present the main advantage of being robust to amplitude and absolute phase offsets. In order to avoid temporal gap in the pixels' long-time description, a condition on the minimum number of samples for each daily collection is checked. Afterwards, the possibility that targets' changes affect the three channels of [*S*] similarly is taken into account. Common amplitude and absolute phase discontinuities are filtered out by imposing the one-day filtering technique to the subset selected at the previous step for each day of measurement. To do this, the *hh*, *hv* and *vv* channels are studied separately and only the common time-samples are maintained. Pixels fulfilling all these requirements are described by a collection of long-time scattering matrices characterized by the same polarimetric properties and are meaningfully comparable for differential interferometric studies.

The subset selected for each day of measurement is coherently averaged to improve the SNR and, consequently, the phase information quality. This selection method has been defined as *non-Stationary Time Filtering* (*nSTF*). On the contrary, the pixels which do not get through the selection method are characterized by an instable long-time behavior. To avoid the loss of these points, all their daily samples are averaged and a sort of daily mean-behavior description is obtained. This "*blind*" approach has been referred to as *Stationary Time Filtering* (*STF*). It is worth pointing out that the *nSTF* technique represents a first attempt to cope with the problem of preserving phase information from non-stationary backscattering contaminations within an urban environment. Yet, its efficiency has been demonstrated in terms of general reduction of the long-time entropy H_T, which confirms the use of this polarimetric descriptor to detect deterministic targets' non-stationary time behaviors. Finally, it is important to stress that the *nSTF* selection procedure has been tailored to the deterministic nature of urban scatterers in Sallent. The fact that it preserves the absolute phase information makes it suitable for enhancing the performance of an amplitude-based differential approach, as the PS, through a polarimetric reformulation of the technique. Nonetheless, this topic cannot be further looked into in the frame of this PhD dissertation due to the insufficient number of time-independent samples at disposal concerning the Station district of Sallent. Longer measurement campaigns are now necessary to continue this very promising line of research.

The benefits of fully-polarimetric data with respect to single-polarization information for differential applications have been demonstrated using the Coherent Pixel Technique (CPT). Its classical single-polarization formulation of CPT has made it possible to study the effect of two different daily-averaging strategies within the urban environment: the *Stationary Time-Filtering* or *STF*, and the *non-Stationary Time-Filtering* or *nSTF*. The better results provided by the second method has pointed out the need to carefully select the daily samples at pixel level if the absolute phase information must be preserved. Yet, the efficiency of the filtering technique is supposed to be underestimated since the boxcar employed for the differential coherence estimation is mixing pixels filtered by both *STF* and *nSTF* methods. Indeed, an amplitude-based differential study is required for the detailed comparison between the two approaches.

In order to successfully exploit the information of the three polarimetric channels of [*S*] at once, a novel zero-baseline polarimetric scattering model has been developed. Its main idea is that the differential phase information given by the coherence estimation over an averaged area contains two main contributions: a term accounting for the polarization-independent mean displacement and a polarization-dependent term due to scatterers' temporal changes. Accordingly, the selection of the channel of [*S*] showing the highest coherence value, which has been referred to as *High* method, has been shown to automatically reduce the second contribution and to improve the quality of the retrieved deformation phase component. Applying this simple idea at pixel level to each interferogram of the differential stack, it has been possible to select a higher number of reliable points and obtain a better estimation of the subsidence phenomena affecting the observed scenario. These results have confirmed the meaningfulness of the innovative approach proposed in this work, which essentially relaxes the classical restriction of linking pixels only if they behave coherently in the same polarization channel. Indeed, they constitute a first demonstration of polarimetry usefulness for advanced differential applications.

In the last part of this PhD dissertation, a more insightful analysis of the potentials of polarimetry for DInSAR applications has stressed the existence of problems up-to-now unknown or barely investigated. The convergence of the cutting-edge coherence optimization methods available in the literature (*DSM* [Cloude,98], *ESM* [Colin,06], *SOM* [Sagues,00]) to the polarization-independent deformation phase contribution has been demonstrated with simulated homogeneous PolSAR data under time-stationarity scattering hypothesis. On the contrary, the analysis of real gbSAR acquisitions has shown that the optimization of the differential coherence does not necessarily lead

to an improvement of the deformation estimation. From a first study, the constraint of applying the same polarization basis transformation to the two zero-baseline data sets seems to be mandatory for differential applications. The reason seems to lie in time non-stationarities of targets' polarimetric response often detected within the urban scenario of Sallent. When this occurs, the *DSM* method provides two significantly different optimum scattering mechanisms and the corresponding differential optimum phase, in a first approximation, does not converge to the polarization-independent deformation term. A possible explanation is that the use of two different SMs generates a phase offset accounting for the radial-projected separation between the phase centers of the two scattering mechanisms.

On the contrary, the other two approaches, i.e., *ESM* and *SOM*, provide a unique sub-optimum scattering vector which seems to be more suitable for differential studies since it does not contain the undesirable offset mentioned for *DSM*. Yet, only *SOM* has turned out to be more efficient than the *High* method described before. In fact, the time-stationary hypothesis invoked by *ESM* is not always fulfilled within the district area and the technique does not always converge to the expected phase information. In contrast, *SOM* is more general because it makes no specific assumption concerning the scatter's statistical properties. Its main drawback is time-consumption, which makes it unfeasible for the analysis of wide scenarios. To speed up the calculation of the sub-optimum scattering mechanism and consequently improve its efficiency, genetic algorithms might be employed. These algorithms are efficient for the detection of maxima in 2-variable smooth functions, and it can be shown that the variations of the differential coherence with respect to the polarization angles (ψ, χ) fulfill this hypothesis.

The first results carried out by adapting CPT processing chain to optimized interferogram stacks are very promising for future applications. The number of pixel selected increases noticeably, but unreliable phase information is also generated over low coherence areas. Developing a model for tracking phase center's displacements as a function of polarization basis transformations is now required in order to understand the effect of the alternative optimization methods and to work out more efficient filtering technique. For this purpose, the generation of simulated PolDInSAR data sets overcoming the constraint of polarimetric time-stationary is considered mandatory. It is important to remark that the conclusions about the optimization technique efficiency have been drawn from the analysis of a specific type of scenario, i.e., an urban environment. This means that they are meant in a relative and not absolute context. Indeed, a higher efficiency of *DSM* and *ESM*

methods for differential applications is expected when the illuminated area better fulfills the statistical hypothesis behind their formulation, for instance natural surfaces or vegetated areas. Nonetheless, new measurement campaigns are now required to answer this question.

Finally, a last comment is in order. The high incidence angles characterizing gbSAR acquisition geometries are supposed to increase the instability effects of urban scatterers highlighted in this PhD dissertation. It follows that the results as well as the conclusions here drawn cannot be considered independent from the illumination conditions entailed by the use of a terrestrial platform. Yet, the algorithms developed for the analysis of these effects are geometrically-independent. This means that they can be meaningfully applied to space-borne long-time PolSAR collections for the characterization of deterministic targets' polarimetric long-time behavior. Similarly, the PolDInSAR formulation here proposed can be easily applied to satellite PolSAR collections. With respect to the gbSAR case, the presence of a polarization-dependent topographic component affecting the differential interferograms must be taken into account. The vertical location of the phase centers corresponding to different polarization channels can be assumed identical just in the case of surface scattering. When vegetated areas or urban environments are analyzed, this hypothesis is likely to be unfulfilled. It follows that their different elevation must be carefully compensated for before linking pixels selected in different polarizations. Yet, the simple but very efficient polarimetric differential model developed in this PhD dissertation is considered very promising for future satellite-based PolDInSAR applications.

Appendix A

Stationary Phase Method Study of *Cosine*-Chirp High-Frequency Components

The cosine-chirp modulated signal of duration T_p transmitted by the UPC gbSAR sensor may be expressed as

$$p(t)=\mathrm{Re}\left\{a(t)e^{j\beta t+j\alpha t^2}\right\}=a(t)\cos\left(\beta t+\alpha t^2\right). \tag{A.1}$$

where $a(t)$ is a *rectangular* function centered at $T_p/2$. Defining the signal backscattered by the *n*th target located within an observed scene as

$$s(t)=\left[\sqrt{\sigma_n}e^{j\phi_n}a(t-t_n)\cos\left(\beta(t-t_n)+\alpha(t-t_n)^2\right)\right], \tag{A.2}$$

the deramping process in the time domain may be decomposed into four contributions as follows

$$\begin{aligned} s_c(t)=p(t)s_c(t)&=1/4\sqrt{\sigma_n}e^{j\phi_n}a(t-t_n)\left[\left(x_{1n}^*+x_{1n}\right)\left(x_{2n}+x_{2n}^*\right)\right]\\ &=1/4\sqrt{\sigma_n}e^{j\phi_n}a(t-t_n)\left[x_{1n}^*x_{2n}+x_{1n}^*x_{2n}^*+x_{1n}x_{2n}^*+x_{1n}x_{2n}\right]\\ &=\left[s_c^I(t)+s_c^{II}(t)+\left(s_c^I(t)\right)^*+\left(s_c^{II}(t)\right)^*\right]\\ &=\left[s_c^I(t)+s_c^{II}(t)+s_c^{III}(t)+s_c^{IV}(t)\right] \end{aligned} \tag{A.3}$$

where $x_{1n}=e^{j\beta(t-t_n)+j\alpha(t-t_n)^2}$ and $x_{2n}=e^{j\beta t+j\alpha t^2}$. Invoking the linearity of Fourier transform, it is possible to factorize the spectrum of $s_c(t)$ as

$$S_c(\omega)=S_c^I(\omega)+S_c^{II}(\omega)+S_c^{III}(\omega)+S_c^{IV}(\omega) \tag{A.4}$$

where

$$S_c^I(\omega)=F\left[\frac{\sqrt{\sigma_n}}{4}e^{j\phi_n}a(t-t_n)e^{j\left(\beta t_n-\alpha t_n^2\right)}e^{j2\alpha t_n t}\right] \tag{A.5}$$

$$S_c^{II}(\omega)=F\left[\frac{\sqrt{\sigma_n}}{4}e^{j\phi_n}a(t-t_n)e^{j\left(\beta t_n-\alpha t_n^2\right)}e^{j(-2\beta-2\alpha t+2\alpha t_n)t}\right]. \tag{A.6}$$

$$S_c^{III}(\omega) = F\left[\frac{\sqrt{\sigma_n}}{4} e^{j\phi_n} a(t-t_n) e^{-j\left(\beta t_n - \alpha t_n^2\right)} e^{-j2\alpha t_n t}\right] \tag{A.7}$$

$$S_c^{IV}(\omega) = F\left[\frac{\sqrt{\sigma_n}}{4} e^{j\phi_n} a(t-t_n) e^{-j\left(\beta t_n - \alpha t_n^2\right)} e^{-j(-2\beta - 2\alpha t + 2\alpha t_n)t}\right]. \tag{A.8}$$

It can be observed that $S_c^{I}(\omega) = \left[S_c^{III}(-\omega)\right]^*$ and $S_c^{II}(\omega) = \left[S_c^{IV}(-\omega)\right]^*$. The analytical solution of Eq. A.5 has been provided in Section 3.2 whereas, due to the symmetry, Eq. A.7 can be solved using the same approach. In order to estimate the spectral components of $S_c^{II}(\omega) = \left[S_c^{IV}(-\omega)\right]^*$, the Stationary Phase method (SPM) can be employed [Raney,92]. This technique deals with the integration of complex functions with wide phase variation. Let the integrand function $f(x)$ be defined as

$$f(x) = g(x) e^{j\varphi(x)} \tag{A.9}$$

where $g(x)$ is the envelope of $f(x)$,. Then, the SPM states that

$$\int g(x) e^{j\varphi(x)} dx = \left[\left(-\frac{\pi}{2\varphi''(x)}\right)^{\frac{1}{2}} e^{-j\frac{\pi}{4}}\right] g(\underline{x}) e^{j\varphi(\underline{x})} \tag{A.10}$$

where the stationary point $\underline{x}$ is given by the solution of the expression

$$\varphi'(x) = 0\,. \tag{A.11}$$

under the assumption that the derivative with respect to x of $\varphi(x)$ is single valued, or it has only one value of physical significance. In order to calculate $S_c^{IV}(\omega)$, Eq. A.8 may be rewritten as

$$S_c^{IV}(\omega) = F\left[\frac{\sqrt{\sigma_n}}{4} e^{j\phi_n} a(t-t_n) e^{-j\beta t_n + j\alpha t_n^2} e^{-(j2\alpha t_n - 2\beta)t} e^{j2\alpha t^2}\right] \tag{A.12}$$

and, substituting $t' = t - t_n$ and after some mathematics, it becomes

$$S_c^{IV}(\omega) = F\left[\frac{\sqrt{\sigma_n}}{4} e^{j\phi_n} a(t') e^{j\beta t_n + j\alpha t_n^2} e^{j(2\alpha t_n + 2\beta)t'} e^{j2\alpha t'^2}\right] \tag{A.13}$$

where $t' \in \left(-t_n, T_p - t_n\right]$. At this point, Eq. A.13 can be further simplified by applying the substitution $\kappa = 2\alpha t_n + 2\beta$ and expressing $S_c^{IV}(\omega)$ as

$$S_c^{IV}(\omega) = S'^{IV}_c(\omega - \kappa) \tag{A.14}$$

where

$$S'^{IV}_c(\omega) = \frac{\sqrt{\sigma_n}}{4} e^{j\phi_n} e^{j\beta t_n + j\alpha t_n^2} F\left[a'(t') e^{j2\alpha t'^2}\right] = \frac{\sqrt{\sigma_n}}{4} e^{j\phi_n} e^{j\beta t_n + j\alpha t_n^2} \int a'(t') e^{j2\alpha t'^2} e^{-j\omega t'} dt' \tag{A.15}$$

The integral expression in Eq. A.15 can be solved by applying Eq. A.10. The stationary phase point $\underline{t}'$ is given by

$$\phi(t') = 2\alpha t'^2 - \omega t' \Rightarrow \left.\frac{d\phi(t')}{dt'}\right|_{t'=\underline{t}'} = 4\alpha t' - \omega\big|_{t'=\underline{t}'} = 0 \Rightarrow \underline{t}' = \frac{\omega}{4\alpha}. \tag{A.16}$$

Accordingly, Eq. A.15 and Eq. A.14 become

$$S'^{IV}_c(\omega) = \frac{\sqrt{\sigma_n}}{4} e^{j\phi_n} e^{j\beta t_n + j\alpha t_n^2} A'\left(\frac{\omega}{4\alpha}\right) e^{-j\frac{\omega^2}{8\alpha}} \tag{A.17}$$

$$S^{IV}_c(\omega) = \frac{\sqrt{\sigma_n}}{4} e^{j\phi_n} e^{j\beta t_n + j\alpha t_n^2} A'\left(\frac{1}{4\alpha}\left[\omega - (2\alpha t_n + 2\beta)\right]\right) e^{-j\frac{(\omega - 2\alpha t_n - 2\beta)^2}{8\alpha}} \tag{A.18}$$

In Eq. A.18, it can be observed that $S^{IV}_c(\omega)$ corresponds to a *sinc* function centered at the angular frequency $\omega^{IV} = 2\alpha t_n + 2\beta$ whose spectral support is given by

$$\Omega_{IV} = \left.\frac{d\angle S^{IV}_c(\omega)}{dt'}\right|_{t'=-t_n}^{t'=T_p - t_n} = 2\alpha t_n + 2\beta + 4\alpha t'\Big|_{t'=-t_n}^{t'=T_p - t_n} = \left[2\beta - 2\alpha t_n, 2\beta + 2\alpha(2Tp - t_n)\right] \tag{A.19}$$

Following the same procedure, and exploiting the symmetry of the problem, Eq. A.6 becomes

$$S^{IV}_c(\omega) = \frac{\sqrt{\sigma_n}}{4} e^{j\phi_n} e^{-j\beta t_n - j\alpha t_n^2} A'\left(\frac{1}{4\alpha}\left[\omega - (-2\alpha t_n - 2\beta)\right]\right) e^{-j\frac{(\omega + 2\alpha t_n + 2\beta)^2}{8\alpha}}, \tag{A.20}$$

which, again, describes a pass-band signal centered at the angular frequency $\omega^{II} = 2\alpha t_n + 2\beta$ and with band support equal to

$$\Omega_{II} = \left[-2\beta - 2\alpha(2Tp - t_n), -2\beta - 2\alpha t_n\right] \tag{A.21}$$

Finally, it is worth pointing out that the two band supports have been obtained under the assumption of *upchirp* modulation, i.e. $\alpha > 0$. In the case of *downchirp*, i.e. $\alpha < 0$, the band support extremes in Eq. A.19 and Eq. A.21 are flipped.

Appendix B

Newton-Raphson's Iterative Algorithm

The Newton-Raphson's algorithm constitutes an efficient method to solve non-linear equations system. Let *S* be a determined non-linear system of *k* continuously differentiable equations in $R_k \to R_k$ defined as

$$S:\begin{cases} F_1(x_1, x_2, ..., x_k) = 0 \\ F_2(x_1, x_2, ..., x_k) = 0 \\ \quad ... \\ F_k(x_1, x_2, ..., x_k) = 0 \end{cases} \Rightarrow F\left(\vec{x}\right) = 0 \tag{B.1}$$

The generic function F_i can be approximated around $\vec{x}_0$ using its first order Taylor expansion as follows

$$F_i\left(\overrightarrow{x_0} + \vec{\delta x}\right) = F_i\left(\overrightarrow{x_0}\right) + \sum_{j=1}^{k} J_{ij}\delta x_j + O\left(\vec{\delta x}\right) \tag{B.2}$$

where J_{ij} is the element at the i^{th} row and j^{th} column of the *Jacobian* matrix calculated at $\overrightarrow{x_0}$ given by the expression

$$J_{ij} = \left.\frac{\partial F_i\left(\vec{x}\right)}{\partial x_i}\right|_{x_i = x_{i0}} \tag{B.3}$$

At this point, Eq. B.2 can be rewritten in a more compact form as

$$F\left(\overrightarrow{x_0} + \vec{\delta x}\right) = F\left(\overrightarrow{x_0}\right) + [J]\big|_{\vec{x}=\overrightarrow{x_0}}\,\vec{\delta x} + O\left(\vec{\delta x}\right) \tag{B.4}$$

where $O\left(\vec{\delta x}\right)$ accounts for the error committed when the series expansion is truncated to the first order. A vector $\overrightarrow{x_0} + \vec{\delta x}$ is solution of Eq. B.4, i.e., of S, if it fulfils the condition $F\left(\overrightarrow{x_0} + \vec{\delta x}\right) = 0$. Neglecting the term $O\left(\vec{\delta x}\right)$, the Eq. B.4 can be expressed as

$$F\left(\overrightarrow{x_0}\right) = -\left[J\right]\Big|_{\vec{x}=\vec{x}_0} \vec{\delta x} \tag{B.5}$$

which constitutes the fundamental equation for an iterative solution. The process starts at $\overrightarrow{x_S}$ and the vectorial increment $\vec{\delta x}$ provided by Eq. B.5 is used to calculate the new value

$$\overrightarrow{x_i} = \vec{x}_{i-1} + \vec{\delta x}_{i-1} . \tag{B.6}$$

The module of $\vec{\delta x}_i$ gives an estimation of the error committed if the real solution is approximated with $\overrightarrow{x_i}$. The iteration process stops when the module of $\vec{\delta x}_i$ becomes lower than the fixed convergence threshold. Concerning the geocoding process of gbSAR images, the *xyz* coordinates of the generic target T in the ellipsoidal reference system are provided by the solution of the following non-linear equations system:

$$\begin{cases} F_1\left(x_T, y_T, z_T\right) = \left(x_M - x_T\right)^2 + \left(y_M - y_T\right)^2 + \left(z_M - z_T\right)^2 - r_M^2 = 0 \\ F_2\left(x_T, y_T, z_T\right) = \left(x_S - x_T\right)^2 + \left(y_S - y_T\right)^2 + \left(z_S - z_T\right)^2 - r_S^2 = 0 \\ F_3\left(x_T, y_T, z_T\right) = \vec{v}_S \cdot \overrightarrow{\mathrm{P_M T''}} = \left|\vec{v}_S\right| \left|\overrightarrow{\mathrm{P_M T''}}\right| \cos\left(\pi/2 + \varphi\right) = 0 \end{cases} \tag{B.7}$$

where the coordinates' subscripts *M* and *S* stand for *master* and *slave* antennas, T for the generic target, the angle φ is the target's squint angle, $\vec{v}_S$ the unitary vector defining the sensor's trajectory, and $\mathrm{T''}$ is the intersection between the *master* radar plane Γ_M and the unique line *l* orthogonal Γ_M passing through P_T. This *xyz* coordinates of $\mathrm{T''}$ are obtained from the following linear equations system

$$l : \begin{cases} x = x_T + \lambda B_x \\ y = y_T + \lambda B_y \\ z = z_T + \lambda B_z \end{cases} \tag{B.8}$$

$$\Gamma_M : B_x x + B_y y + B_z z + \left(B_x x_M + B_y y_M + B_z z_M\right) = 0 \tag{B.9}$$

where B is the baseline vector equal to

$$\mathrm{B} = \left(B_x, B_y, B_z\right) = \left(x_S - x_M, y_S - y_M, z_S - z_M\right) . \tag{B.10}$$

Solving Eq. B.8, it is obtained

$$\lambda\left(x_T, y_T, z_T\right) = \frac{B_x x_T + B_y y_T + B_z z_T - \left(B_x x_S + B_y y_S + B_z z_S\right)}{B_x^2 + B_y^2 + B_z^2} = \frac{B_x x_T + B_y y_T + B_z z_T - K}{\left\|B\right\|^2} . \tag{B.11}$$

Accordingly, the third equation of system in Eq. B.7 can be now rewritten as a function of T as

$$F_3\left(x_T, y_T, z_T\right) = I\left(x_T, y_T, z_T\right) + II\left(x_T, y_T, z_T\right) + III\left(x_T, y_T, z_T\right) + IV\left(x_T, y_T, z_T\right) \tag{B.12}$$

where

$$
\begin{aligned}
&I\left(x_T, y_T, z_T\right) = v_{sx}\left[x_T + B_x\lambda - x_M\right] \\
&II\left(x_T, y_T, z_T\right) = v_{sy}\left[y_T + B_y\lambda - y_M\right] \\
&III\left(x_T, y_T, z_T\right) = v_{sz}\left[z_T + B_z\lambda - z_M\right] \\
&IV\left(x_T, y_T, z_T\right) = -\left\|v_s\right\|\cos\left(\pi/2+\beta\right)\sqrt{\frac{I^{\,2}}{v_{sx}} + \frac{II^{\,2}}{v_{sy}} + \frac{III^{\,2}}{v_{sz}}} = -\left\|v_s\right\|\cos\left(\pi/2+\beta\right)P
\end{aligned}
\quad . \quad \text{(B.13)}
$$

At this point, it is possible to analytically calculate the Jacobian matrix of the non-linear equations system given in Eq. B.7 as follows

$$
\left[J\right] = \begin{bmatrix}
\dfrac{\partial F_1}{\partial x_T} & \dfrac{\partial F_1}{\partial y_T} & \dfrac{\partial F_1}{\partial x_T} \\
\dfrac{\partial F_2}{\partial x_T} & \dfrac{\partial F_2}{\partial y_T} & \dfrac{\partial F_2}{\partial x_T} \\
\dfrac{\partial F_3}{\partial x_T} & \dfrac{\partial F_1}{\partial y_T} & \dfrac{\partial F_3}{\partial z_T}
\end{bmatrix}. \quad \text{(B.14)}
$$

The elements of [J] are one by one described below:

$$
\frac{\partial F_1}{\partial x_T} = -2\left(x_M - x_T\right) \qquad \frac{\partial F_1}{\partial y_T} = -2\left(y_M - y_T\right) \qquad \frac{\partial F_3}{\partial z_T} = -2\left(z_M - z_T\right)
$$

$$
\frac{\partial F_2}{\partial x_T} = -2\left(x_S - x_T\right) \qquad \frac{\partial F_2}{\partial y_T} = -2\left(y_S - y_T\right) \qquad \frac{\partial F_3}{\partial z_T} = -2\left(z_S - z_T\right)
$$

$$
\frac{\partial F_3}{\partial x_T} = \frac{1}{\left\|B\right\|^2}\left[v_{sx}\left(1-B_x^2\right) - v_{sy}B_xB_y - v_{sz}B_xB_z\right] - \left\|v_s\right\|\cos\left(\pi/2+\beta\right)\left[\frac{x_T + B_x\lambda - x_M}{P}\left(1 - \frac{B_x^2}{\left\|B\right\|^2}\right)\right]
$$

$$
\frac{\partial F_3}{\partial y_T} = \frac{1}{\left\|B\right\|^2}\left[-v_{sx}B_xB_y + v_{sy}\left(1-B_y^2\right) - v_{sz}B_yB_z\right] - \left\|v_s\right\|\cos\left(\pi/2+\beta\right)\left[\frac{y_T + B_y\lambda - y_M}{P}\left(1 - \frac{B_y^2}{\left\|B\right\|^2}\right)\right]
$$

$$
\frac{\partial F_3}{\partial x_T} = \frac{1}{\left\|B\right\|^2}\left[-v_{sx}B_zB_x - v_{sy}B_zB_y + v_{sz}\left(1-B_z^2\right)\right] - \left\|v_s\right\|\cos\left(\pi/2+\beta\right)\left[\frac{z_T + B_z\lambda - z_M}{P}\left(1 - \frac{B_z^2}{\left\|B\right\|^2}\right)\right]
\quad \text{(B.15)}
$$

Appendix C

Sallent Measurement Campaign

UPC ground-based SAR sensor configuration parameters

Frequency Carrier :	9.65 *GHz*
Chirp Duration :	50e-6 *sec*
Chirp Time Samples :	4096
Time-average Factor:	128
A/D Sampling Rate :	81.92 Ms/sec
Pulse Repetition Frequency:	20 *KHz*
Chirp Bandwidth :	120 *MHz*
Base-band Signal Bandwidth :	40 *MHz*
Antenna Beamwidth -3dB (-6dB) :	28º (38º)
Synthetic Apertura Length :	2 m
Cross-range Sampling Step :	1 cm
Alias-free angular sector :	± 51
Acquisition Mode :	PolSAR (hh0/hv0/vh0/vv0) – DAY 1/2/3/4/5/6/7 PolInSAR (hh0/hv0/vh0/vv0/hhI/hvI/vhI/vvI) – DAY 8/9/10

Acquisition Scheduling

---------- DAY 0 (7 Data Sets) ----------

Date	Filename	Polarization	Time (hh: mm)	Duration (mm:)
22/06/2006	SallentB01	hh0/hv0/vh0/vv0	16:24	2 : 48
22/06/2006	SallentB02	hh0/hv0/vh0/vv0	16:28	2 : 48
22/06/2006	SallentB03	hh0/hv0/vh0/vv0	16:32	2 : 50
22/06/2006	SallentB04	hh0/hv0/vh0/vv0	16:46	2 : 56
22/06/2006	SallentB05	hh0/hv0/vh0/vv0	16:50	2 : 50
22/06/2006	SallentB06	hh0/hv0/vh0/vv0	16:54	2 : 51
22/06/2006	SallentB07	hh0/hv0/vh0/vv0	16:58	2 : 51

---------- DAY 1 (27 Data Sets)----------

Date	Filename	Polarization	Time (hh: mm)	Duration (mm:)
29/06/2006	20060629Sallent01	hh0/hv0/vh0/vv0	11:00	2 : 41
29/06/2006	20060629Sallent02	hh0/hv0/vh0/vv0	11:10	2 : 41
29/06/2006	20060629Sallent03	hh0/hv0/vh0/vv0	11:20	2 : 41
29/06/2006	20060629Sallent04	hh0/hv0/vh0/vv0	11:30	2 : 40
29/06/2006	20060629Sallent05	hh0/hv0/vh0/vv0	11:40	2 : 41
29/06/2006	20060629Sallent06	hh0/hv0/vh0/vv0	11:50	2 : 41
29/06/2006	20060629Sallent07	hh0/hv0/vh0/vv0	12:00	2 : 45
29/06/2006	20060629Sallent08	hh0/hv0/vh0/vv0	12:10	2 : 43
29/06/2006	20060629Sallent09	hh0/hv0/vh0/vv0	12:20	2 : 43
29/06/2006	20060629Sallent10	hh0/hv0/vh0/vv0	12:30	2 : 43
29/06/2006	20060629Sallent11	hh0/hv0/vh0/vv0	12:40	2 : 43
29/06/2006	20060629Sallent12	hh0/hv0/vh0/vv0	12:50	2 : 41
29/06/2006	20060629Sallent13	hh0/hv0/vh0/vv0	13:00	2 : 41
29/06/2006	20060629Sallent14	hh0/hv0/vh0/vv0	13:40	2 : 41
29/06/2006	20060629Sallent15	hh0/hv0/vh0/vv0	13:50	2 : 41
29/06/2006	20060629Sallent16	hh0/hv0/vh0/vv0	14:00	2 : 44
29/06/2006	20060629Sallent17	hh0/hv0/vh0/vv0	14:10	2 : 44
29/06/2006	20060629Sallent18	hh0/hv0/vh0/vv0	14:20	2 : 44
29/06/2006	20060629Sallent19	hh0/hv0/vh0/vv0	14:30	2 : 41
29/06/2006	20060629Sallent20	hh0/hv0/vh0/vv0	14:40	2 : 41

29/06/2006	20060629Sallent21	hh0/hv0/vh0/vv0	14:50	2 : 41
29/06/2006	20060629Sallent22	hh0/hv0/vh0/vv0	15:00	2 : 42
29/06/2006	20060629Sallent23	hh0/hv0/vh0/vv0	15:10	2 : 43
29/06/2006	20060629Sallent24	hh0/hv0/vh0/vv0	15:20	2 : 43
29/06/2006	20060629Sallent25	hh0/hv0/vh0/vv0	15:30	2 : 41
29/06/2006	20060629Sallent26	hh0/hv0/vh0/vv0	15:40	2 : 43
29/06/2006	20060629Sallent27	hh0/hv0/vh0/vv0	15:50	2 : 41

---------- DAY 2 (30 Data Sets) ----------

Date	Filename	Polarization	Time (hh: mm)	Duration (mm:)
26/07/2006	20060726Sallent01	hh0/hv0/vh0/vv0	07:11	2 : 56
26/07/2006	20060726Sallent02	hh0/hv0/vh0/vv0	07:24	2 : 56
26/07/2006	20060726Sallent03	hh0/hv0/vh0/vv0	07:37	2 : 49
26/07/2006	20060726Sallent04	hh0/hv0/vh0/vv0	07:50	2 : 49
26/07/2006	20060726Sallent05	hh0/hv0/vh0/vv0	08:03	2 : 50
26/07/2006	20060726Sallent06	hh0/hv0/vh0/vv0	08:16	2 : 50
26/07/2006	20060726Sallent07	hh0/hv0/vh0/vv0	08:29	2 : 51
26/07/2006	20060726Sallent08	hh0/hv0/vh0/vv0	08:41	2 : 51
26/07/2006	20060726Sallent09	hh0/hv0/vh0/vv0	08:54	2 : 46
26/07/2006	20060726Sallent10	hh0/hv0/vh0/vv0	09:15	2 : 48
26/07/2006	20060726Sallent11	hh0/hv0/vh0/vv0	09:21	2 : 48
26/07/2006	20060726Sallent12	hh0/hv0/vh0/vv0	09:32	2 : 56
26/07/2006	20060726Sallent13	hh0/hv0/vh0/vv0	09:36	2 : 56
26/07/2006	20060726Sallent14	hh0/hv0/vh0/vv0	09:39	2 : 48
26/07/2006	20060726Sallent15	hh0/hv0/vh0/vv0	09:46	2 : 50
26/07/2006	20060726Sallent16	hh0/hv0/vh0/vv0	09:52	2 : 51
26/07/2006	20060726Sallent17	hh0/hv0/vh0/vv0	09:59	2 : 48
26/07/2006	20060726Sallent18	hh0/hv0/vh0/vv0	10:03	2 : 55
26/07/2006	20060726Sallent19	hh0/hv0/vh0/vv0	10:08	2 : 55
26/07/2006	20060726Sallent20	hh0/hv0/vh0/vv0	10:12	2 : 54
26/07/2006	20060726Sallent21	hh0/hv0/vh0/vv0	10:20	2 : 54
26/07/2006	20060726Sallent22	hh0/hv0/vh0/vv0	10:27	2 : 56
26/07/2006	20060726Sallent23	hh0/hv0/vh0/vv0	10:35	2 : 55
26/07/2006	20060726Sallent24	hh0/hv0/vh0/vv0	10:43	2 : 48
26/07/2006	20060726Sallent25	hh0/hv0/vh0/vv0	10:00	2 : 50
26/07/2006	20060726Sallent26	hh0/hv0/vh0/vv0	10:52	2 : 48
26/07/2006	20060726Sallent27	hh0/hv0/vh0/vv0	11:00	2 : 55
26/07/2006	20060726Sallent28	hh0/hv0/vh0/vv0	11:08	2 : 48
26/07/2006	20060726Sallent29	hh0/hv0/vh0/vv0	11:16	2 : 50
26/07/2006	20060726Sallent30	hh0/hv0/vh0/vv0	11:24	2 : 48

---------- DAY 3 (39 Data Sets) ----------

Date	Filename	Polarization	Time (hh: mm)	Duration (mm:)
19/09/2006	20060919Sallent01	hh0/hv0/vh0/vv0	10:17	2 : 56
19/09/2006	20060919Sallent02	hh0/hv0/vh0/vv0	10:25	2 : 49
19/09/2006	20060919Sallent03	hh0/hv0/vh0/vv0	10:33	2 : 50
19/09/2006	20060919Sallent04	hh0/hv0/vh0/vv0	10:42	2 : 50
19/09/2006	20060919Sallent05	hh0/hv0/vh0/vv0	10:49	2 : 49
19/09/2006	20060919Sallent06	hh0/hv0/vh0/vv0	10:57	2 : 50
19/09/2006	20060919Sallent07	hh0/hv0/vh0/vv0	11:05	2 : 51
19/09/2006	20060919Sallent08	hh0/hv0/vh0/vv0	11:15	2 : 57
19/09/2006	20060919Sallent09	hh0/hv0/vh0/vv0	11:25	2 : 50
19/09/2006	20060919Sallent10	hh0/hv0/vh0/vv0	11:35	2 : 50
19/09/2006	20060919Sallent11	hh0/hv0/vh0/vv0	11:47	2 : 49
19/09/2006	20060919Sallent12	hh0/hv0/vh0/vv0	11:57	2 : 56
19/09/2006	20060919Sallent13	hh0/hv0/vh0/vv0	12:07	2 : 49
19/09/2006	20060919Sallent14	hh0/hv0/vh0/vv0	12:17	2 : 49
19/09/2006	20060919Sallent15	hh0/hv0/vh0/vv0	12:26	2 : 49
19/09/2006	20060919Sallent16	hh0/hv0/vh0/vv0	12:36	2 : 49
19/09/2006	20060919Sallent17	hh0/hv0/vh0/vv0	12:46	2 : 49
19/09/2006	20060919Sallent18	hh0/hv0/vh0/vv0	12:56	2 : 49
19/09/2006	20060919Sallent19	hh0/hv0/vh0/vv0	13:06	2 : 49
19/09/2006	20060919Sallent20	hh0/hv0/vh0/vv0	13:16	2 : 49
19/09/2006	20060919Sallent21	hh0/hv0/vh0/vv0	13:26	2 : 49
19/09/2006	20060919Sallent22	hh0/hv0/vh0/vv0	13:36	2 : 50
19/09/2006	20060919Sallent23	hh0/hv0/vh0/vv0	13:46	2 : 50
19/09/2006	20060919Sallent24	hh0/hv0/vh0/vv0	13:56	2 : 49
19/09/2006	20060919Sallent25	hh0/hv0/vh0/vv0	14:06	2 : 49
19/09/2006	20060919Sallent26	hh0/hv0/vh0/vv0	14:16	2 : 49
19/09/2006	20060919Sallent27	hh0/hv0/vh0/vv0	14:26	2 : 49
19/09/2006	20060919Sallent28	hh0/hv0/vh0/vv0	14:36	2 : 49
19/09/2006	20060919Sallent29	hh0/hv0/vh0/vv0	14:46	2 : 49
19/09/2006	20060919Sallent30	hh0/hv0/vh0/vv0	14:56	2 : 51

19/09/2006	20060919Sallent31	hh0/hv0/vh0/vv0	15:06	2 : 50
19/09/2006	20060919Sallent32	hh0/hv0/vh0/vv0	15:16	2 : 49
19/09/2006	20060919Sallent33	hh0/hv0/vh0/vv0	15:26	2 : 56
19/09/2006	20060919Sallent34	hh0/hv0/vh0/vv0	15:36	2 : 49
19/09/2006	20060919Sallent35	hh0/hv0/vh0/vv0	15:46	2 : 49
19/09/2006	20060919Sallent36	hh0/hv0/vh0/vv0	15:56	2 : 49
19/09/2006	20060919Sallent37	hh0/hv0/vh0/vv0	16:06	2 : 50
19/09/2006	20060919Sallent38	hh0/hv0/vh0/vv0	16:16	2 : 50
19/09/2006	20060919Sallent39	hh0/hv0/vh0/vv0	16:26	2 : 48

---------- DAY 4 (31 Data Sets) ----------

Date	Filename	Polarization	Time (hh: mm)	Duration (mm:)
20/10/2006	20061020Sallent01	hh0/hv0/vh0/vv0	09:11	2 : 55
20/10/2006	20061020Sallent02	hh0/hv0/vh0/vv0	09:18	2 : 48
20/10/2006	20061020Sallent03	hh0/hv0/vh0/vv0	09:25	2 : 48
20/10/2006	20061020Sallent04	hh0/hv0/vh0/vv0	09:32	2 : 49
20/10/2006	20061020Sallent05	hh0/hv0/vh0/vv0	09:39	2 : 51
20/10/2006	20061020Sallent06	hh0/hv0/vh0/vv0	09:46	2 : 51
20/10/2006	20061020Sallent07	hh0/hv0/vh0/vv0	09:53	2 : 49
20/10/2006	20061020Sallent08	hh0/hv0/vh0/vv0	10:00	2 : 49
20/10/2006	20061020Sallent09	hh0/hv0/vh0/vv0	10:07	2 : 56
20/10/2006	20061020Sallent10	hh0/hv0/vh0/vv0	10:14	2 : 49
20/10/2006	20061020Sallent11	hh0/hv0/vh0/vv0	10:21	2 : 49
20/10/2006	20061020Sallent12	hh0/hv0/vh0/vv0	10:28	2 : 49
20/10/2006	20061020Sallent13	hh0/hv0/vh0/vv0	10:35	2 : 49
20/10/2006	20061020Sallent14	hh0/hv0/vh0/vv0	10:42	2 : 49
20/10/2006	20061020Sallent15	hh0/hv0/vh0/vv0	10:49	2 : 49
20/10/2006	20061020Sallent16	hh0/hv0/vh0/vv0	10:56	2 : 49
20/10/2006	20061020Sallent17	hh0/hv0/vh0/vv0	11:03	2 : 49
20/10/2006	20061020Sallent18	hh0/hv0/vh0/vv0	12:47	2 : 58
20/10/2006	20061020Sallent19	hh0/hv0/vh0/vv0	12:53	2 : 50
20/10/2006	20061020Sallent20	hh0/hv0/vh0/vv0	12:59	2 : 49
20/10/2006	20061020Sallent21	hh0/hv0/vh0/vv0	13:05	2 : 50
20/10/2006	20061020Sallent22	hh0/hv0/vh0/vv0	13:11	2 : 50
20/10/2006	20061020Sallent23	hh0/hv0/vh0/vv0	13:17	2 : 50
20/10/2006	20061020Sallent24	hh0/hv0/vh0/vv0	13:23	2 : 49
20/10/2006	20061020Sallent25	hh0/hv0/vh0/vv0	13:29	2 : 50
20/10/2006	20061020Sallent26	hh0/hv0/vh0/vv0	13:35	2 : 49
20/10/2006	20061020Sallent27	hh0/hv0/vh0/vv0	13:41	2 : 50
20/10/2006	20061020Sallent28	hh0/hv0/vh0/vv0	13:46	2 : 50
20/10/2006	20061020Sallent29	hh0/hv0/vh0/vv0	13:52	2 : 39
20/10/2006	20061020Sallent30	hh0/hv0/vh0/vv0	13:58	2 : 40
20/10/2006	20061020Sallent31	hh0/hv0/vh0/vv0	14:04	2 : 50

---------- DAY 5 (41 Data Sets) ----------

Date	Filename	Polarization	Time (hh: mm)	Duration (mm:)
14/11/2006	20061114Sallent01	hh0/hv0/vh0/vv0	11:29	2 : 56
14/11/2006	20061114Sallent02	hh0/hv0/vh0/vv0	11:37	2 : 49
14/11/2006	20061114Sallent03	hh0/hv0/vh0/vv0	11:45	2 : 49
14/11/2006	20061114Sallent04	hh0/hv0/vh0/vv0	11:53	2 : 48
14/11/2006	20061114Sallent05	hh0/hv0/vh0/vv0	12:01	2 : 48
14/11/2006	20061114Sallent06	hh0/hv0/vh0/vv0	12:09	2 : 48
14/11/2006	20061114Sallent07	hh0/hv0/vh0/vv0	12:17	2 : 48
14/11/2006	20061114Sallent08	hh0/hv0/vh0/vv0	12:25	2 : 49
14/11/2006	20061114Sallent09	hh0/hv0/vh0/vv0	12:33	2 : 50
14/11/2006	20061114Sallent10	hh0/hv0/vh0/vv0	12:41	2 : 50
14/11/2006	20061114Sallent11	hh0/hv0/vh0/vv0	12:49	2 : 50
14/11/2006	20061114Sallent12	hh0/hv0/vh0/vv0	12:57	2 : 49
14/11/2006	20061114Sallent13	hh0/hv0/vh0/vv0	12:30	2 : 49
14/11/2006	20061114Sallent14	hh0/hv0/vh0/vv0	12:36	2 : 49
14/11/2006	20061114Sallent15	hh0/hv0/vh0/vv0	12:42	2 : 48
14/11/2006	20061114Sallent16	hh0/hv0/vh0/vv0	12:48	2 : 48
14/11/2006	20061114Sallent17	hh0/hv0/vh0/vv0	12:54	2 : 48
14/11/2006	20061114Sallent18	hh0/hv0/vh0/vv0	13:00	2 : 48
14/11/2006	20061114Sallent19	hh0/hv0/vh0/vv0	13:06	2 : 50
14/11/2006	20061114Sallent20	hh0/hv0/vh0/vv0	13:12	2 : 50
14/11/2006	20061114Sallent21	hh0/hv0/vh0/vv0	13:18	2 : 50
14/11/2006	20061114Sallent22	hh0/hv0/vh0/vv0	13:24	2 : 49
14/11/2006	20061114Sallent23	hh0/hv0/vh0/vv0	13:30	2 : 49
14/11/2006	20061114Sallent24	hh0/hv0/vh0/vv0	13:36	2 : 49
14/11/2006	20061114Sallent25	hh0/hv0/vh0/vv0	13:42	2 : 48
14/11/2006	20061114Sallent26	hh0/hv0/vh0/vv0	13:48	2 : 48
14/11/2006	20061114Sallent27	hh0/hv0/vh0/vv0	13:54	2 : 48

14/11/2006	20061114Sallent28	hh0/hv0/vh0/vv0	14:00	2 : 48
14/11/2006	20061114Sallent29	hh0/hv0/vh0/vv0	14:06	2 : 48
14/11/2006	20061114Sallent30	hh0/hv0/vh0/vv0	14:12	2 : 49
14/11/2006	20061114Sallent31	hh0/hv0/vh0/vv0	14:18	2 : 49
14/11/2006	20061114Sallent32	hh0/hv0/vh0/vv0	14:24	2 : 50
14/11/2006	20061114Sallent33	hh0/hv0/vh0/vv0	14:29	2 : 50
14/11/2006	20061114Sallent34	hh0/hv0/vh0/vv0	14:35	2 : 50
14/11/2006	20061114Sallent35	hh0/hv0/vh0/vv0	14:41	2 : 48
14/11/2006	20061114Sallent36	hh0/hv0/vh0/vv0	14:47	2 : 48
14/11/2006	20061114Sallent37	hh0/hv0/vh0/vv0	14:53	2 : 49
14/11/2006	20061114Sallent38	hh0/hv0/vh0/vv0	14:59	2 : 49
14/11/2006	20061114Sallent39	hh0/hv0/vh0/vv0	15:05	2 : 49
14/11/2006	20061114Sallent40	hh0/hv0/vh0/vv0	15:11	2 : 49
14/11/2006	20061114Sallent41	hh0/hv0/vh0/vv0	15:17	2 : 53

---------- DAY 6 (44 Data Sets) ----------

Date	Filename	Polarization	Time (hh: mm)	Duration (mm:)
28/11/2006	20061128Sallent01	hh0/hv0/vh0/vv0	17:42	2 : 54
28/11/2006	20061128Sallent02	hh0/hv0/vh0/vv0	18:03	2 : 49
28/11/2006	20061128Sallent03	hh0/hv0/vh0/vv0	18:24	2 : 50
28/11/2006	20061128Sallent04	hh0/hv0/vh0/vv0	18:45	2 : 49
28/11/2006	20061128Sallent05	hh0/hv0/vh0/vv0	19:06	2 : 49
28/11/2006	20061128Sallent06	hh0/hv0/vh0/vv0	19:29	2 : 49
28/11/2006	20061128Sallent07	hh0/hv0/vh0/vv0	19:48	2 : 50
28/11/2006	20061128Sallent08	hh0/hv0/vh0/vv0	20:09	2 : 50
28/11/2006	20061128Sallent09	hh0/hv0/vh0/vv0	20:30	2 : 49
28/11/2006	20061128Sallent10	hh0/hv0/vh0/vv0	20:51	2 : 49
28/11/2006	20061128Sallent11	hh0/hv0/vh0/vv0	21:12	2 : 49
28/11/2006	20061128Sallent12	hh0/hv0/vh0/vv0	21:33	2 : 50
28/11/2006	20061128Sallent13	hh0/hv0/vh0/vv0	21:54	2 : 50
28/11/2006	20061128Sallent14	hh0/hv0/vh0/vv0	22:15	2 : 50
28/11/2006	20061128Sallent15	hh0/hv0/vh0/vv0	22:36	2 : 50
28/11/2006	20061128Sallent16	hh0/hv0/vh0/vv0	22:57	2 : 50
28/11/2006	20061128Sallent17	hh0/hv0/vh0/vv0	23:18	2 : 49
28/11/2006	20061128Sallent18	hh0/hv0/vh0/vv0	23:39	2 : 49
28/11/2006	20061128Sallent19	hh0/hv0/vh0/vv0	23:59	2 : 49
28/11/2006	20061128Sallent20	hh0/hv0/vh0/vv0	00:20	2 : 49
28/11/2006	20061128Sallent21	hh0/hv0/vh0/vv0	00:41	2 : 49
28/11/2006	20061128Sallent22	hh0/hv0/vh0/vv0	01:02	2 : 50
28/11/2006	20061128Sallent23	hh0/hv0/vh0/vv0	01:23	2 : 50
28/11/2006	20061128Sallent24	hh0/hv0/vh0/vv0	01:44	2 : 50
28/11/2006	20061128Sallent25	hh0/hv0/vh0/vv0	02:05	2 : 52
28/11/2006	20061128Sallent26	hh0/hv0/vh0/vv0	02:26	2 : 52
28/11/2006	20061128Sallent27	hh0/hv0/vh0/vv0	02:47	2 : 51
28/11/2006	20061128Sallent28	hh0/hv0/vh0/vv0	03:08	2 : 51
28/11/2006	20061128Sallent29	hh0/hv0/vh0/vv0	03:29	2 : 49
28/11/2006	20061128Sallent30	hh0/hv0/vh0/vv0	03:50	2 : 49
28/11/2006	20061128Sallent31	hh0/hv0/vh0/vv0	04:11	2 : 49
28/11/2006	20061128Sallent32	hh0/hv0/vh0/vv0	04:32	2 : 50
28/11/2006	20061128Sallent33	hh0/hv0/vh0/vv0	04:53	2 : 50
28/11/2006	20061128Sallent34	hh0/hv0/vh0/vv0	05:14	2 : 49
28/11/2006	20061128Sallent35	hh0/hv0/vh0/vv0	05:35	2 : 49
28/11/2006	20061128Sallent36	hh0/hv0/vh0/vv0	05:53	2 : 49
28/11/2006	20061128Sallent37	hh0/hv0/vh0/vv0	06:17	2 : 49
28/11/2006	20061128Sallent38	hh0/hv0/vh0/vv0	06:38	2 : 49
28/11/2006	20061128Sallent39	hh0/hv0/vh0/vv0	06:59	2 : 49
28/11/2006	20061128Sallent40	hh0/hv0/vh0/vv0	07:20	2 : 50
28/11/2006	20061128Sallent41	hh0/hv0/vh0/vv0	07:41	2 : 50
28/11/2006	20061128Sallent42	hh0/hv0/vh0/vv0	08:02	2 : 50
28/11/2006	20061128Sallent43	hh0/hv0/vh0/vv0	08:22	2 : 50
28/11/2006	20061128Sallent44	hh0/hv0/vh0/vv0	08:43	2 : 50

---------- DAY 7 (99 Data Sets) ----------

Date	Filename	Polarization	Time (hh: mm)	Duration (mm:)
18/12/2006	20061218Sallent01	hh0/hv0/vh0/vv0	16:45	2 : 52
18/12/2006	20061218Sallent02	hh0/hv0/vh0/vv0	16:55	2 : 49
18/12/2006	20061218Sallent03	hh0/hv0/vh0/vv0	17:05	2 : 49
18/12/2006	20061218Sallent04	hh0/hv0/vh0/vv0	17:15	2 : 49
18/12/2006	20061218Sallent05	hh0/hv0/vh0/vv0	17:25	2 : 49
18/12/2006	20061218Sallent06	hh0/hv0/vh0/vv0	17:35	2 : 48
18/12/2006	20061218Sallent07	hh0/hv0/vh0/vv0	17:44	2 : 48
18/12/2006	20061218Sallent08	hh0/hv0/vh0/vv0	17:54	2 : 48
18/12/2006	20061218Sallent09	hh0/hv0/vh0/vv0	18:04	2 : 48

18/12/2006	20061218Sallent10	hh0/hv0/vh0/vv0	18:14	2 : 48
18/12/2006	20061218Sallent11	hh0/hv0/vh0/vv0	18:24	2 : 48
18/12/2006	20061218Sallent12	hh0/hv0/vh0/vv0	18:34	2 : 48
18/12/2006	20061218Sallent13	hh0/hv0/vh0/vv0	18:44	2 : 48
18/12/2006	20061218Sallent14	hh0/hv0/vh0/vv0	18:54	2 : 48
18/12/2006	20061218Sallent15	hh0/hv0/vh0/vv0	19:04	2 : 48
18/12/2006	20061218Sallent16	hh0/hv0/vh0/vv0	19:14	2 : 48
18/12/2006	20061218Sallent17	hh0/hv0/vh0/vv0	19:24	2 : 48
18/12/2006	20061218Sallent18	hh0/hv0/vh0/vv0	19:34	2 : 48
18/12/2006	20061218Sallent19	hh0/hv0/vh0/vv0	19:44	2 : 49
18/12/2006	20061218Sallent20	hh0/hv0/vh0/vv0	19:54	2 : 49
18/12/2006	20061218Sallent21	hh0/hv0/vh0/vv0	20:04	2 : 49
18/12/2006	20061218Sallent22	hh0/hv0/vh0/vv0	20:14	2 : 48
18/12/2006	20061218Sallent23	hh0/hv0/vh0/vv0	20:24	2 : 48
18/12/2006	20061218Sallent24	hh0/hv0/vh0/vv0	20:34	2 : 48
18/12/2006	20061218Sallent25	hh0/hv0/vh0/vv0	20:44	2 : 48
18/12/2006	20061218Sallent26	hh0/hv0/vh0/vv0	20:54	2 : 48
18/12/2006	20061218Sallent27	hh0/hv0/vh0/vv0	21:04	2 : 48
18/12/2006	20061218Sallent28	hh0/hv0/vh0/vv0	21:14	2 : 48
18/12/2006	20061218Sallent29	hh0/hv0/vh0/vv0	21:24	2 : 48
18/12/2006	20061218Sallent30	hh0/hv0/vh0/vv0	21:34	2 : 48
18/12/2006	20061218Sallent31	hh0/hv0/vh0/vv0	21:44	2 : 48
18/12/2006	20061218Sallent32	hh0/hv0/vh0/vv0	21:54	2 : 49
18/12/2006	20061218Sallent33	hh0/hv0/vh0/vv0	21:04	2 : 49
18/12/2006	20061218Sallent34	hh0/hv0/vh0/vv0	21:14	2 : 49
18/12/2006	20061218Sallent35	hh0/hv0/vh0/vv0	21:24	2 : 48
18/12/2006	20061218Sallent36	hh0/hv0/vh0/vv0	21:34	2 : 48
18/12/2006	20061218Sallent37	hh0/hv0/vh0/vv0	21:44	2 : 48
18/12/2006	20061218Sallent38	hh0/hv0/vh0/vv0	21:54	2 : 48
18/12/2006	20061218Sallent39	hh0/hv0/vh0/vv0	22:04	2 : 48
18/12/2006	20061218Sallent40	hh0/hv0/vh0/vv0	22:13	2 : 48
18/12/2006	20061218Sallent41	hh0/hv0/vh0/vv0	22:23	2 : 48
18/12/2006	20061218Sallent42	hh0/hv0/vh0/vv0	22:33	2 : 48
18/12/2006	20061218Sallent43	hh0/hv0/vh0/vv0	22:43	2 : 48
18/12/2006	20061218Sallent44	hh0/hv0/vh0/vv0	22:53	2 : 48
18/12/2006	20061218Sallent41	hh0/hv0/vh0/vv0	23:03	2 : 48
18/12/2006	20061218Sallent41	hh0/hv0/vh0/vv0	23:13	2 : 48
18/12/2006	20061218Sallent42	hh0/hv0/vh0/vv0	23:23	2 : 48
18/12/2006	20061218Sallent43	hh0/hv0/vh0/vv0	23:33	2 : 48
18/12/2006	20061218Sallent44	hh0/hv0/vh0/vv0	23:43	2 : 48
18/12/2006	20061218Sallent45	hh0/hv0/vh0/vv0	23:53	2 : 48
18/12/2006	20061218Sallent46	hh0/hv0/vh0/vv0	00:03	2 : 48
18/12/2006	20061218Sallent47	hh0/hv0/vh0/vv0	00:13	2 : 48
18/12/2006	20061218Sallent48	hh0/hv0/vh0/vv0	00:23	2 : 48
18/12/2006	20061218Sallent49	hh0/hv0/vh0/vv0	00:32	2 : 48
18/12/2006	20061218Sallent50	hh0/hv0/vh0/vv0	00:42	2 : 48
18/12/2006	20061218Sallent51	hh0/hv0/vh0/vv0	00:52	2 : 49
18/12/2006	20061218Sallent52	hh0/hv0/vh0/vv0	01:02	2 : 49
18/12/2006	20061218Sallent53	hh0/hv0/vh0/vv0	01:12	2 : 49
18/12/2006	20061218Sallent54	hh0/hv0/vh0/vv0	01:22	2 : 49
18/12/2006	20061218Sallent55	hh0/hv0/vh0/vv0	01:32	2 : 49
18/12/2006	20061218Sallent56	hh0/hv0/vh0/vv0	01:42	2 : 49
18/12/2006	20061218Sallent57	hh0/hv0/vh0/vv0	01:52	2 : 49
18/12/2006	20061218Sallent58	hh0/hv0/vh0/vv0	02:02	2 : 49
18/12/2006	20061218Sallent59	hh0/hv0/vh0/vv0	02:12	2 : 48
18/12/2006	20061218Sallent60	hh0/hv0/vh0/vv0	02:22	2 : 48
18/12/2006	20061218Sallent61	hh0/hv0/vh0/vv0	02:32	2 : 48
18/12/2006	20061218Sallent62	hh0/hv0/vh0/vv0	02:42	2 : 48
18/12/2006	20061218Sallent63	hh0/hv0/vh0/vv0	02:52	2 : 48
18/12/2006	20061218Sallent64	hh0/hv0/vh0/vv0	03:02	2 : 48
18/12/2006	20061218Sallent65	hh0/hv0/vh0/vv0	03:12	2 : 48
18/12/2006	20061218Sallent66	hh0/hv0/vh0/vv0	03:21	2 : 48
18/12/2006	20061218Sallent67	hh0/hv0/vh0/vv0	03:31	2 : 48
18/12/2006	20061218Sallent68	hh0/hv0/vh0/vv0	03:41	2 : 48
18/12/2006	20061218Sallent69	hh0/hv0/vh0/vv0	03:51	2 : 48
18/12/2006	20061218Sallent70	hh0/hv0/vh0/vv0	04:01	2 : 48
18/12/2006	20061218Sallent71	hh0/hv0/vh0/vv0	04:11	2 : 48
18/12/2006	20061218Sallent72	hh0/hv0/vh0/vv0	04:21	2 : 48
18/12/2006	20061218Sallent73	hh0/hv0/vh0/vv0	04:31	2 : 48
18/12/2006	20061218Sallent74	hh0/hv0/vh0/vv0	04:41	2 : 48
18/12/2006	20061218Sallent75	hh0/hv0/vh0/vv0	04:51	2 : 48
18/12/2006	20061218Sallent76	hh0/hv0/vh0/vv0	05:01	2 : 49
18/12/2006	20061218Sallent77	hh0/hv0/vh0/vv0	05:11	2 : 49
18/12/2006	20061218Sallent78	hh0/hv0/vh0/vv0	05:21	2 : 49
18/12/2006	20061218Sallent79	hh0/hv0/vh0/vv0	05:31	2 : 49
18/12/2006	20061218Sallent80	hh0/hv0/vh0/vv0	05:41	2 : 49

18/12/2006	20061218Sallent81	hh0/hv0/vh0/vv0	05:51	2 : 49
18/12/2006	20061218Sallent82	hh0/hv0/vh0/vv0	06:01	2 : 49
18/12/2006	20061218Sallent83	hh0/hv0/vh0/vv0	06:11	2 : 48
18/12/2006	20061218Sallent84	hh0/hv0/vh0/vv0	06:20	2 : 48
18/12/2006	20061218Sallent85	hh0/hv0/vh0/vv0	06:30	2 : 48
18/12/2006	20061218Sallent86	hh0/hv0/vh0/vv0	06:40	2 : 48
18/12/2006	20061218Sallent87	hh0/hv0/vh0/vv0	06:50	2 : 48
18/12/2006	20061218Sallent88	hh0/hv0/vh0/vv0	07:00	2 : 48
18/12/2006	20061218Sallent89	hh0/hv0/vh0/vv0	07:10	2 : 48
18/12/2006	20061218Sallent90	hh0/hv0/vh0/vv0	07:20	2 : 48
18/12/2006	20061218Sallent91	hh0/hv0/vh0/vv0	07:30	2 : 48
18/12/2006	20061218Sallent92	hh0/hv0/vh0/vv0	07:40	2 : 48
18/12/2006	20061218Sallent93	hh0/hv0/vh0/vv0	07:50	2 : 48
18/12/2006	20061218Sallent94	hh0/hv0/vh0/vv0	08:00	2 : 48
18/12/2006	20061218Sallent95	hh0/hv0/vh0/vv0	08:10	2 : 48
18/2/2006	20061218Sallent96	hh0/hv0/vh0/vv0	08:20	2 : 48
18/12/2006	20061218Sallent97	hh0/hv0/vh0/vv0	08:30	2 : 48
18/12/2006	20061218Sallent98	hh0/hv0/vh0/vv0	08:40	2 : 48
18/12/2006	20061218Sallent99	hh0/hv0/vh0/vv0	08:50	2 : 48

---------- DAY 8 (41 Data Sets) ----------

Date	Filename	Polarization	Time (hh: mm)	Duration (mm:)
13/02/2007	20070213Sallent01	hh0/hv0/vh0/vv0/hhI/hvI/vhI/vvI	18:14	4 : 38
13/02/2007	20070213Sallent02	hh0/hv0/vh0/vv0/hhI/hvI/vhI/vvI	18:39	4 : 30
13/02/2007	20070213Sallent03	hh0/hv0/vh0/vv0/hhI/hvI/vhI/vvI	19:04	4 : 29
13/02/2007	20070213Sallent04	hh0/hv0/vh0/vv0/hhI/hvI/vhI/vvI	19:29	4 : 30
13/02/2007	20070213Sallent05	hh0/hv0/vh0/vv0/hhI/hvI/vhI/vvI	19:53	4 : 34
13/02/2007	20070213Sallent06	hh0/hv0/vh0/vv0/hhI/hvI/vhI/vvI	20:18	4 : 32
13/02/2007	20070213Sallent07	hh0/hv0/vh0/vv0/hhI/hvI/vhI/vvI	20:43	4 : 30
13/02/2007	20070213Sallent08	hh0/hv0/vh0/vv0/hhI/hvI/vhI/vvI	21:08	4 : 30
13/02/2007	20070213Sallent09	hh0/hv0/vh0/vv0/hhI/hvI/vhI/vvI	21:32	4 : 30
13/02/2007	20070213Sallent10	hh0/hv0/vh0/vv0/hhI/hvI/vhI/vvI	21:57	4 : 29
13/02/2007	20070213Sallent11	hh0/hv0/vh0/vv0/hhI/hvI/vhI/vvI	22:22	4 : 29
13/02/2007	20070213Sallent12	hh0/hv0/vh0/vv0/hhI/hvI/vhI/vvI	22:47	4 : 29
13/02/2007	20070213Sallent13	hh0/hv0/vh0/vv0/hhI/hvI/vhI/vvI	23:11	4 : 29
13/02/2007	20070213Sallent14	hh0/hv0/vh0/vv0/hhI/hvI/vhI/vvI	23:37	4 : 29
13/02/2007	20070213Sallent15	hh0/hv0/vh0/vv0/hhI/hvI/vhI/vvI	00:01	4 : 29
13/02/2007	20070213Sallent16	hh0/hv0/vh0/vv0/hhI/hvI/vhI/vvI	00:26	4 : 29
13/02/2007	20070213Sallent17	hh0/hv0/vh0/vv0/hhI/hvI/vhI/vvI	00:50	4 : 30
13/02/2007	20070213Sallent18	hh0/hv0/vh0/vv0/hhI/hvI/vhI/vvI	01:15	4 : 30
13/02/2007	20070213Sallent19	hh0/hv0/vh0/vv0/hhI/hvI/vhI/vvI	01:40	4 : 30
13/02/2007	20070213Sallent20	hh0/hv0/vh0/vv0/hhI/hvI/vhI/vvI	02:05	4 : 30
13/02/2007	20070213Sallent21	hh0/hv0/vh0/vv0/hhI/hvI/vhI/vvI	02:29	4 : 29
13/02/2007	20070213Sallent22	hh0/hv0/vh0/vv0/hhI/hvI/vhI/vvI	02:54	4 : 26
13/02/2007	20070213Sallent23	hh0/hv0/vh0/vv0/hhI/hvI/vhI/vvI	03:19	4 : 30
13/02/2007	20070213Sallent24	hh0/hv0/vh0/vv0/hhI/hvI/vhI/vvI	03:43	4 : 30
13/02/2007	20070213Sallent25	hh0/hv0/vh0/vv0/hhI/hvI/vhI/vvI	04:08	4 : 30
13/02/2007	20070213Sallent26	hh0/hv0/vh0/vv0/hhI/hvI/vhI/vvI	04:33	4 : 29
13/02/2007	20070213Sallent27	hh0/hv0/vh0/vv0/hhI/hvI/vhI/vvI	04:58	4 : 29
13/02/2007	20070213Sallent28	hh0/hv0/vh0/vv0/hhI/hvI/vhI/vvI	05:22	4 : 29
13/02/2007	20070213Sallent29	hh0/hv0/vh0/vv0/hhI/hvI/vhI/vvI	05:47	4 : 29
13/02/2007	20070213Sallent30	hh0/hv0/vh0/vv0/hhI/hvI/vhI/vvI	06:12	4 : 32
13/02/2007	20070213Sallent31	hh0/hv0/vh0/vv0/hhI/hvI/vhI/vvI	06:37	4 : 32
13/02/2007	20070213Sallent32	hh0/hv0/vh0/vv0/hhI/hvI/vhI/vvI	07:02	4 : 29
13/02/2007	20070213Sallent33	hh0/hv0/vh0/vv0/hhI/hvI/vhI/vvI	07:26	4 : 29
13/02/2007	20070213Sallent34	hh0/hv0/vh0/vv0/hhI/hvI/vhI/vvI	07:51	4 : 29
13/02/2007	20070213Sallent35	hh0/hv0/vh0/vv0/hhI/hvI/vhI/vvI	08:16	4 : 29
13/02/2007	20070213Sallent36	hh0/hv0/vh0/vv0/hhI/hvI/vhI/vvI	08:41	4 : 29
13/02/2007	20070213Sallent37	hh0/hv0/vh0/vv0/hhI/hvI/vhI/vvI	09:05	4 : 29
13/02/2007	20070213Sallent38	hh0/hv0/vh0/vv0/hhI/hvI/vhI/vvI	09:30	4 : 29
13/02/2007	20070213Sallent39	hh0/hv0/vh0/vv0/hhI/hvI/vhI/vvI	09:55	4 : 29
13/02/2007	20070213Sallent40	hh0/hv0/vh0/vv0/hhI/hvI/vhI/vvI	10:20	4 : 32
13/02/2007	20070213Sallent41	hh0/hv0/vh0/vv0/hhI/hvI/vhI/vvI	10:44	4 : 33

---------- DAY 9 (41 Data Sets) ----------

Date	Filename	Polarization	Time (hh: mm)	Duration (mm:)
14/03/2007	20070314Sallent01	hh0/hv0/vh0/vv0/hhI/hvI/vhI/vvI	17:19	4 : 37
14/03/2007	20070314Sallent02	hh0/hv0/vh0/vv0/hhI/hvI/vhI/vvI	17:44	4 : 27
14/03/2007	20070314Sallent03	hh0/hv0/vh0/vv0/hhI/hvI/vhI/vvI	18:09	4 : 29
14/03/2007	20070314Sallent04	hh0/hv0/vh0/vv0/hhI/hvI/vhI/vvI	18:34	4 : 28
14/03/2007	20070314Sallent05	hh0/hv0/vh0/vv0/hhI/hvI/vhI/vvI	18:58	4 : 28
14/03/2007	20070314Sallent06	hh0/hv0/vh0/vv0/hhI/hvI/vhI/vvI	19:23	4 : 28
14/03/2007	20070314Sallent07	hh0/hv0/vh0/vv0/hhI/hvI/vhI/vvI	19:48	4 : 28

14/03/2007	20070314Sallent08	hh0/hv0/vh0/vv0/hhI/hvI/vhI/vvI	20:12	4 : 27
14/03/2007	20070314Sallent09	hh0/hv0/vh0/vv0/hhI/hvI/vhI/vvI	20:37	4 : 28
14/03/2007	20070314Sallent10	hh0/hv0/vh0/vv0/hhI/hvI/vhI/vvI	21:02	4 : 28
14/03/2007	20070314Sallent11	hh0/hv0/vh0/vv0/hhI/hvI/vhI/vvI	21:27	4 : 29
14/03/2007	20070314Sallent12	hh0/hv0/vh0/vv0/hhI/hvI/vhI/vvI	21:51	4 : 28
14/03/2007	20070314Sallent13	hh0/hv0/vh0/vv0/hhI/hvI/vhI/vvI	22:16	4 : 28
14/03/2007	20070314Sallent14	hh0/hv0/vh0/vv0/hhI/hvI/vhI/vvI	22:41	4 : 28
14/03/2007	20070314Sallent15	hh0/hv0/vh0/vv0/hhI/hvI/vhI/vvI	23:05	4 : 28
14/03/2007	20070314Sallent16	hh0/hv0/vh0/vv0/hhI/hvI/vhI/vvI	23:30	4 : 27
14/03/2007	20070314Sallent17	hh0/hv0/vh0/vv0/hhI/hvI/vhI/vvI	00:55	4 : 27
14/03/2007	20070314Sallent18	hh0/hv0/vh0/vv0/hhI/hvI/vhI/vvI	00:20	4 : 28
14/03/2007	20070314Sallent19	hh0/hv0/vh0/vv0/hhI/hvI/vhI/vvI	00:44	4 : 27
14/03/2007	20070314Sallent20	hh0/hv0/vh0/vv0/hhI/hvI/vhI/vvI	01:09	4 : 28
14/03/2007	20070314Sallent21	hh0/hv0/vh0/vv0/hhI/hvI/vhI/vvI	01:34	4 : 27
14/03/2007	20070314Sallent22	hh0/hv0/vh0/vv0/hhI/hvI/vhI/vvI	01:58	4 : 28
14/03/2007	20070314Sallent23	hh0/hv0/vh0/vv0/hhI/hvI/vhI/vvI	02:23	4 : 28
14/03/2007	20070314Sallent24	hh0/hv0/vh0/vv0/hhI/hvI/vhI/vvI	02:48	4 : 28
14/03/2007	20070314Sallent25	hh0/hv0/vh0/vv0/hhI/hvI/vhI/vvI	03:13	4 : 28
14/03/2007	20070314Sallent26	hh0/hv0/vh0/vv0/hhI/hvI/vhI/vvI	03:37	4 : 28
14/03/2007	20070314Sallent27	hh0/hv0/vh0/vv0/hhI/hvI/vhI/vvI	04:02	4 : 28
14/03/2007	20070314Sallent28	hh0/hv0/vh0/vv0/hhI/hvI/vhI/vvI	04:27	4 : 28
14/03/2007	20070314Sallent29	hh0/hv0/vh0/vv0/hhI/hvI/vhI/vvI	04:51	4 : 27
14/03/2007	20070314Sallent30	hh0/hv0/vh0/vv0/hhI/hvI/vhI/vvI	05:16	4 : 27
14/03/2007	20070314Sallent31	hh0/hv0/vh0/vv0/hhI/hvI/vhI/vvI	05:41	4 : 28
14/03/2007	20070314Sallent32	hh0/hv0/vh0/vv0/hhI/hvI/vhI/vvI	06:06	4 : 28
14/03/2007	20070314Sallent33	hh0/hv0/vh0/vv0/hhI/hvI/vhI/vvI	06:30	4 : 27
14/03/2007	20070314Sallent34	hh0/hv0/vh0/vv0/hhI/hvI/vhI/vvI	06:55	4 : 28
14/03/2007	20070314Sallent35	hh0/hv0/vh0/vv0/hhI/hvI/vhI/vvI	07:20	4 : 28
14/03/2007	20070314Sallent36	hh0/hv0/vh0/vv0/hhI/hvI/vhI/vvI	07:45	4 : 28
14/03/2007	20070314Sallent37	hh0/hv0/vh0/vv0/hhI/hvI/vhI/vvI	08:09	4 : 27
14/03/2007	20070314Sallent38	hh0/hv0/vh0/vv0/hhI/hvI/vhI/vvI	08:34	4 : 28
14/03/2007	20070314Sallent39	hh0/hv0/vh0/vv0/hhI/hvI/vhI/vvI	08:59	4 : 27
14/03/2007	20070314Sallent40	hh0/hv0/vh0/vv0/hhI/hvI/vhI/vvI	09:23	4 : 28
14/03/2007	20070314Sallent41	hh0/hv0/vh0/vv0/hhI/hvI/vhI/vvI	09:48	4 : 28

---------- DAY 10 (45 Data Sets) ----------

Date	**Filename**	**Polarization**	**Time (hh: mm)**	**Duration (mm:)**
04/07/2007	20070704Sallent01	hh0/hv0/vh0/vv0/hhI/hvI/vhI/vvI	19:33	5 : 44
04/07/2007	20070704Sallent02	hh0/hv0/vh0/vv0/hhI/hvI/vhI/vvI	19:54	5 : 35
04/07/2007	20070704Sallent03	hh0/hv0/vh0/vv0/hhI/hvI/vhI/vvI	20:15	5 : 36
04/07/2007	20070704Sallent04	hh0/hv0/vh0/vv0/hhI/hvI/vhI/vvI	20:35	5 : 33
04/07/2007	20070704Sallent05	hh0/hv0/vh0/vv0/hhI/hvI/vhI/vvI	20:56	5 : 35
04/07/2007	20070704Sallent06	hh0/hv0/vh0/vv0/hhI/hvI/vhI/vvI	21:17	5 : 34
04/07/2007	20070704Sallent07	hh0/hv0/vh0/vv0/hhI/hvI/vhI/vvI	21:38	5 : 38
04/07/2007	20070704Sallent08	hh0/hv0/vh0/vv0/hhI/hvI/vhI/vvI	21:59	5 : 33
04/07/2007	20070704Sallent09	hh0/hv0/vh0/vv0/hhI/hvI/vhI/vvI	22:20	5 : 33
04/07/2007	20070704Sallent10	hh0/hv0/vh0/vv0/hhI/hvI/vhI/vvI	22:41	5 : 37
04/07/2007	20070704Sallent11	hh0/hv0/vh0/vv0/hhI/hvI/vhI/vvI	23:01	5 : 37
04/07/2007	20070704Sallent12	hh0/hv0/vh0/vv0/hhI/hvI/vhI/vvI	23:22	5 : 34
04/07/2007	20070704Sallent13	hh0/hv0/vh0/vv0/hhI/hvI/vhI/vvI	23:43	5 : 37
04/07/2007	20070704Sallent14	hh0/hv0/vh0/vv0/hhI/hvI/vhI/vvI	00:04	5 : 33
04/07/2007	20070704Sallent15	hh0/hv0/vh0/vv0/hhI/hvI/vhI/vvI	00:25	5 : 33
04/07/2007	20070704Sallent16	hh0/hv0/vh0/vv0/hhI/hvI/vhI/vvI	00:46	5 : 40
04/07/2007	20070704Sallent17	hh0/hv0/vh0/vv0/hhI/hvI/vhI/vvI	01:07	5 : 33
04/07/2007	20070704Sallent18	hh0/hv0/vh0/vv0/hhI/hvI/vhI/vvI	01:27	5 : 39
04/07/2007	20070704Sallent19	hh0/hv0/vh0/vv0/hhI/hvI/vhI/vvI	01:48	5 : 33
04/07/2007	20070704Sallent20	hh0/hv0/vh0/vv0/hhI/hvI/vhI/vvI	02:09	5 : 38
04/07/2007	20070704Sallent21	hh0/hv0/vh0/vv0/hhI/hvI/vhI/vvI	02:30	5 : 33
04/07/2007	20070704Sallent22	hh0/hv0/vh0/vv0/hhI/hvI/vhI/vvI	02:51	5 : 39
04/07/2007	20070704Sallent23	hh0/hv0/vh0/vv0/hhI/hvI/vhI/vvI	03:12	5 : 33
04/07/2007	20070704Sallent24	hh0/hv0/vh0/vv0/hhI/hvI/vhI/vvI	03:33	5 : 39
04/07/2007	20070704Sallent25	hh0/hv0/vh0/vv0/hhI/hvI/vhI/vvI	03:54	5 : 33
04/07/2007	20070704Sallent26	hh0/hv0/vh0/vv0/hhI/hvI/vhI/vvI	04:15	5 : 39
04/07/2007	20070704Sallent27	hh0/hv0/vh0/vv0/hhI/hvI/vhI/vvI	04:35	5 : 38
04/07/2007	20070704Sallent28	hh0/hv0/vh0/vv0/hhI/hvI/vhI/vvI	04:56	5 : 33
04/07/2007	20070704Sallent29	hh0/hv0/vh0/vv0/hhI/hvI/vhI/vvI	05:17	5 : 33
04/07/2007	20070704Sallent30	hh0/hv0/vh0/vv0/hhI/hvI/vhI/vvI	05:38	5 : 33
04/07/2007	20070704Sallent31	hh0/hv0/vh0/vv0/hhI/hvI/vhI/vvI	05:59	5 : 33
04/07/2007	20070704Sallent32	hh0/hv0/vh0/vv0/hhI/hvI/vhI/vvI	06:20	5 : 33
04/07/2007	20070704Sallent33	hh0/hv0/vh0/vv0/hhI/hvI/vhI/vvI	06:41	5 : 38
04/07/2007	20070704Sallent34	hh0/hv0/vh0/vv0/hhI/hvI/vhI/vvI	07:02	5 : 33
04/07/2007	20070704Sallent35	hh0/hv0/vh0/vv0/hhI/hvI/vhI/vvI	07:23	5 : 33
04/07/2007	20070704Sallent36	hh0/hv0/vh0/vv0/hhI/hvI/vhI/vvI	07:44	5 : 34
04/07/2007	20070704Sallent37	hh0/hv0/vh0/vv0/hhI/hvI/vhI/vvI	08:04	5 : 37

04/07/2007	20070704Sallent38	hh0/hv0/vh0/vv0/hhI/hvI/vhI/vvI	08:25	5 : 33
04/07/2007	20070704Sallent39	hh0/hv0/vh0/vv0/hhI/hvI/vhI/vvI	08:46	5 : 38
04/07/2007	20070704Sallent40	hh0/hv0/vh0/vv0/hhI/hvI/vhI/vvI	09:07	5 : 38
04/07/2007	20070704Sallent41	hh0/hv0/vh0/vv0/hhI/hvI/vhI/vvI	09:28	5 : 34
04/07/2007	20070704Sallent42	hh0/hv0/vh0/vv0/hhI/hvI/vhI/vvI	09:49	5 : 39
04/07/2007	20070704Sallent43	hh0/hv0/vh0/vv0/hhI/hvI/vhI/vvI	10:09	5 : 38
04/07/2007	20070704Sallent44	hh0/hv0/vh0/vv0/hhI/hvI/vhI/vvI	10:30	5 : 33
04/07/2007	20070704Sallent45	hh0/hv0/vh0/vv0/hhI/hvI/vhI/vvI	10:51	5 : 38

Appendix D

Journal Articles

- **L. Pipia,** X. Fabregas, A. Aguasca, and C. López-Martínez, "Atmospheric Artefacts Compensation in ground-based DInSAR Applications," *Geoscience and Remote Sensing Letters,* Vol. 5, No. 1, January 2008, pp. 88-92.

- **L. Pipia,** X. Fabregas, A.Aguasca, C. López-Martínez, S. Duque, J.J Mallorqui, and J. Marturià, "Polarimetric Differential SAR Interferometry: First Results With Ground-Based Measurements," *Geoscience and Remote Sensing Letters,* Vol. 6, No. 1, January 2009, pp. 167-171.

Conference

- **L. Pipia**, V. Alberga, M. Migliaccio, and M. Chandra, "Quantitative Assessment of the Efficency of Supervised Classification Using Coherent and Incoherent Polarimetric SAR Observables", EUSAR2002, Koln, July 2002, Germany, pp. 729 - 732.

- V. Alberga, M. Chandra and **L. Pipia**: "Supervised classification of coherent and incoherent polarimetric SAR observables: comparison and accuracy assessments", Proceedings of SPIE-SAR Image Analysis, Modeling, and Techniques V; Agia Pelagia, September 2003, vol. 4883, pp. 181-191, Greece.

- **L. Pipia** and X.Fabregas, "Generation of Pol-SAR and Pol-In-SAR Data for Homogeneous Distributed Targets Simulation," PolinSAR 2005 Workshop, Frascati, January 2005, Italy.

- **L. Pipia**, A. Aguasca, X. Fabregas, J.J. Mallorqui, and C.López-Martínez, "A Polarimetric Ground-Based SAR System: first results at X-Band", URSI Commission F Symposium on Microwave Remote Sensing of the Earth, Oceans, Ice, and Atmosphere URSI 2005, Ispra, April 2005, Italy. (Invited)

- **L. Pipia**, A. Aguasca, X. Fabregas, J.J. Mallorqui, C.L. Martinez, "Temporal Decorrelation in Polarimetric Differential Interferometry using a Ground-Based SAR Sensor", International Geoscience and Remote Sensing Symposium IGARSS'05, Seul, July 2005, Korea, pp- 4108-4111. (Invited)

- G. Margarit, X. Fabregas, J.J. Mallorqui, **L. Pipia**, and A. Broquetas, "Polarimetric SAR Interferometric simulator of complex target", International Geoscience And Remote Sensing Symposium, IGARSS'05, Seul, 25-29 July 2005, Korea, pp. 2015 - 2018.

- **L. Pipia**, X. Fabregas, A. Aguasca, and J.J. Mallorqui, "Atmospheric Artefact Estimation and Compensation in Differential Polarimetric GB-SAR Acquisitions," 6th European Conference on Synthetic Aperture Radar Conference EuSAR2006, Dresden, 16-18 May 2006, Germany.

- **L. Pipia**, X. Fabregas, A. Aguasca, and J.J. Mallorqui, "A comparison of different techniques for atmospheric artefact compensation in GBSAR differential acquisitions," International Geoscience And Remote Sensing Symposium IGARSS'06, Denver, Colorado, 31 July - 4 August 2006, USA, pp. 3739-3742.

- **L. Pipia**, X. Fabregas, C. López-Martínez, A. Aguasca, and J.J. Mallorqui, "Polarimetric Temporal Decorrelation Studies by means of GBSAR sensor data," International Geoscience And Remote Sensing Symposium IGARSS'06, Denver, Colorado, 31 July - 4 August 2006, USA, Vol. 1, pp. 79-82. (Invited)

- **L. Pipia**, X. Fabregas, A. Aguasca, C. López-Martínez, J.J. Mallorqui, and O. Mora, "A Subsidence Monitoring Project using a Polarimetric GB-SAR Sensor," Polinsar 2007 Workshop, Frascati, 22-26 January 2007, Italy.

- **L. Pipia**, X. Fabregas, A. Aguasca, J.J. Mallorqui, C. López-Martínez, , and Jordi Marturià, "Mining Induced Subsidence Monitoring in Urban Areas with a Ground-Based SAR," Urban Remote Sensing Joint Event, Paris, 11-13 April 2007, France, pp. 1-5. (Invited)

- **L. Pipia**, X. Fabregas, A. Aguasca, C. López-Martínez, J.J. Mallorqui, and O.Mora, "Polarimetric Temporal Information for Urban Deformation Map Retrieval," International Geoscience And Remote Sensing Symposium IGARSS'07, Barcelona, 23-27 July 2007, Spain, vol. 1, pp. 192-195. (Invited)

- **L. Pipia**, X. Fabregas, A. Aguasca, C. López-Martínez, and J.J. Mallorqui, "Urban Environment Characterization using a PolSAR GB Sensor: short and long temporal analysis at X-Band," Advanced SAR Workshop 2007, Vancouver, 11-13 September 2007, Canada.

- G. Margarit, J.J. Mallorqui, I. Corney**, L. Pipia**, C. López-Martínez, X. Fabregas, and A. Aguasca, "Analysis of Urban Areas Scattering with Simulated SAR Imagery," Fringe'07 Workshop, Frascati, 26-30 November 2007, Italy.

- **L. Pipia**, X. Fabregas, A. Aguasca, and C. López-Martínez, "Urban Environment Characterization using a PolSAR GB Sensor: short and long temporal analysis at X-Band," 7th European Conference on Synthetic Aperture Radar Conference EuSAR2008, 2-5 July 2008, Friedrichshafen, Germany. (Invited)

- G. Margarit, J.J. Mallorqui, I. Corney**, L. Pipia**, C. López-Martínez, X. Fabregas, and A. Aguasca, "Scattering Analysis of Urban Targets with Simulated SAR Imagery," 7th European Conference on Synthetic Aperture Radar Conference EuSAR2008, 2-5 de Julio 2008, Friedrichshafen, Germany.

- C. Lopez-Martinez, K. Papathanassiou, and **L. Pipia**, "Analysis and Correction of Speckle Noise Effects on PolInSAR Data Based on Coherent Modeling," International Geoscience And Remote Sensing Symposium IGARSS'08, Boston, 6-11 July 2008, USA, vol. 2, pp. 629-632.

- **L. Pipia**, X. Fabregas, A. Aguasca, S. Duque, J.J. Malloqui, C. López-Martínez, "Deformation Maps Retrieval of Urban Areas Using Ground-Based PolSAR Acquisitions," International Geoscience And Remote Sensing Symposium IGARSS'08 Boston, 6-11 July 2008, USA, vol. 4, pp. 327-330. (Invited)

To be presented

- **L. Pipia,** X. Fabregas, A. Aguasca, C. López-Martínez and J.J Mallorqui, "Polarimetric Coherence Optimization for Interferometrc Differenzial Applications," International Geoscience And Remote Sensing Symposium IGARSS'09, Cape Town, 13-17 July 2009, South Africa. (Invited)

- C. López-Martínez, X. Fabregas, **L. Pipia**, "PolSAR and PolInSAR model based information," International Geoscience And Remote Sensing Symposium IGARSS'09, Cape Town, 13-17 July 2009, South Africa.

- P.J. Ferrer, J. Romeu, J.M. González-Arbesú, A. Aguasca**, L. Pipia**, C. López-Martínez, and X. Fabregas," Transpolarizing Trihedral Measurement using UPC X-bans GBAR," International Geoscience And Remote Sensing Symposium IGARSS'09, Cape Town, 13-17 July 2009, South Africa.

Bibliography

[Aguasca, 04] A. Aguasca, A. Broquetas, J. Mallorqui, and X. Fàbregas, "A Solid State L to X-band Flexible Ground-based SAR System for Continuous Monitoring Applications", *Proceedings of IGRS IEEE Symposium Igarss'04*, Anchorage, USA, September 2004.

[Analog] Direct Digital Synthesizer AD9858 Data-sheet, available on line at http://www.analog.com/UploadedFiles/Data_Sheets/AD9858.pdf .

[Ainsworth, 06] T. Ainsworth, L Ferro-Famil, and J.S.Lee, "Orientation Angle Preserving A Posteriori Polarimetric SAR Calibration," *IEEE Transactions on Geoscience and Remote Sensing*, Vol. 44, No. 4, April 2006.

[Antonello,04] G.Antonello, D. Tarchi, N. Casagli, P. Farina, L. Guerri and D. Leva, D., "SAR interferometry from satellite and ground-based system for monitoring deformations on the Stromboli volcano," *Proceedings of IGRS IEEE Symposium Igarss'04*, Anchorage, USA, September 2004.

[Balanis, 89] C.A.Balanis, *Advanced Engineering Electromagnetics*, John Willey & Sons, New York, 1989.

[Balmer, 98] R. Balmer, and P. Hartl, "Synthetic Aperture radar Interferometry," Inverse Problems 4, R1-R54, 1998.

[Barber, 85] B.C.Barber, "Theory of Digital Imaging from Orbital Synthetic Aperture Radar," International Journal of Remote Sensing, Vol. 6, No. 7, 1985.

[Bennet, 96] J.C. Bennett and K. Morrison, "Development of a ground-based polarimetric synthetic aperture radar", *Proceedings of Aerospace Applications Conference*, Aspen, C olorado, 1996.

[Bernardini, 07] G. Bernardini, P. Ricci, and F. Coppi, "A Ground Based Microwave Interferometer with Imaging Capabilities For Remote Measurements of Displacements", *GALAHAD workshop within the 7th Geomatic Week*, Barcelona, Spain, February, 2007.

[Bernardini, 08] G. Bernardini, P. Ricci , D. D'Aria, A. Monti Guarnieri and F. Rocca, " Impact of atmospheric phase screen and target decorrelation of ground based SAR Differential Interferometry," *Proceedings of the 7th European Conference on Synthetic Aperture Radar* (*EUSAR200*8), Friedrichshafen, Germany,2-5 June 2008,

[Bye, 89] G.D. Bye and R.G. Howell, "Average Radio Refractive Index Lapse Rate of the Lower Troposphere for Locations in NW Europe," *Sixth International Conference on Antennas and Propagation ICAP 89*, Coventry, United Kindom, April 1989.

[Blanco, 06] P. Blanco-Sanchez, J.J. Mallorquí, S. Duque and D. Navarrete, "Advances on DInSAR with ERS and ENVISAT data using the Coherent Pixels Technique (CPT)," *Proceedings of IGRS IEEE Symposium Igarss'06*, Denver, USA, July 2006.

[Blanco, 08] P. Blanco-Sanchez, J.J. Mallorquí, S. Duque, and D.Monells, "The Coherent Pixels Technique (CPT): An Advanced DInSAR Technique for Nonlinear Deformation Monitoring," *Pure Appl. Geophys*., No. 165, pp. 1167-1194, 2008.

[Boerner, 98] W.M. Boerner et al., "Polarimetry in Radar Remote Sensing: Basic and Applied Concepts," Chapter 5 in F.M. Henderson and A.J. Lewis, (ed.) "Principles and Applications for Imaging Radar," vol. 2 of *Manual of Remote Sensing*, Third Edition , John Willey and Sons , New York, 1998.

[Born, 59] M. Born and E. Wolf, *Principles of Optics*, Pergamos Press, 4 & 5 Fitzroy Square, London, W.1., UK, 1959.

[Boithias, 84] Lucien Boithias, *Propagation des ondes radioélectriques dans l'environnement terrestre*, Bordas et CNET-ENST, Paris, 1984.

[Bringi, 01] V.N. Bringi and V. Chandrasekar, *Polarimetric Doppler Weather Radar – Principles and Applications*, Cambridge University Press, United Kingdom, 2001.

[Broquetas, 97] A. Broquetas, R. De Porrata, L. Sagués. X. Fàbregas, and L. Jofre, "A Circular Synthetic Aperture Radar (C-SAR) System from Ground-Based Applications," *IEE Electronic Letters*, Vol. 33, No. 11, May 1997.

[Bruder, 92] J.A. Bruder, *Segmented cylindrical corner reflector*, United States Patent 5134413, 1992.

[Brunfeldt, 84] D.R Brunfeldt and F.R. Ulaby, "Active Reflector for Radar Calibration," *IEEE Transactions on Geoscience and Remote Sensing*, Vol. 22, No. 2, March 1984.

[Cafforio, 91] C. Cafforio, C. Prati, and F. Rocca, "SAR data focusing using seismic migration techniques," *IEEE Transaction on Aerospace and Electronics Systems*, Vol. 27, No. 2, March, 1991.

[Calvo, 04] D. Calvo, *Millora I Integració d'un SAR CW-FM en banda X*, Final Year Project, Universitat Politècnica de Catalunya, Barcelona, Octubre 2007.

[Carlson, 86] A.B. Carlos, *Communication Systems – Third Edition*, McGraw-Hill, Singapore, 1986.

[Cameron, 90] W.L. Cameron, "Feature Motivated Polarization Scattering Matrix Decomposition," Proceedings on IEEE 1999 Radar Conference, May,1990.

[Cameron, 96] W.L. Cameron, N.N.Yousse, L.K. Leung, "Simulated Polarimetric Signature of Primitive Geometrical Shapes," *IEEE Transactions on Geoscience and Remote Sensing*, Vol. 34, No. 3, May 1996.

[Carrara, 95] W.G. Carrara, R.S. Goodman and R.M. Majewski, *Spotlight Synthetic Aperture Radar: Signal Processing Algorithms*, Artech House, Norwood, MA, 1995.

[Carrasco, 98] D.E. Carrasco, *SAR Interferometry for Digital Elevation Model Generation and Differential Applications*, PhD PhD Dissertation, Universitat Politècnica de Catalunya, Barcelona, Spain 1998.

[Celma, 07] J. Benaiges, *Tècniques de Geocodificació directa i inversa per a grounf-based SAR* (*GB-SAR*), Final Year Project, Universitat Politècnica de Catalunya, Barcelona, Junio 2007.

[Cloude, 86] S.R. Cloude, "Group theory and polarisation algebra," *Optik*, Vol. 75, No.1, 1986.

[Cloude, 95] S.R. Cloude, "Lie Groups in Electromagnetic Waves Propagation and Scattering," Chapter 2 in C.E. Baum and H.N. Kritikos, *Electromagnetic Symmetry*, Taylor & Francis, 1995.

[Cloude, 96] S.R. Cloude and E. Poitter, "A review of target decomposition theorems in radar Polarimetry," *IEEE Transactions on Geoscience and Remote Sensing*, Vol. 34, No. 2, March, 1996.

[Cloude, 97] S.R. Cloude and E. Pottier, "An Entropy Based Classification Scheme for Land Applications of Polarimetric SAR," *IEEE Transactions on Geoscience and Remote Sensing*, Vol. 35, No. 1, January, 1997.

[Cloude, 98] S.R. Cloude and K.P. Papathanassiou, "Polarimetric SAR Interferometry," *IEEE Transactions on Geoscience and Remote Sensing*, Vol. 36, No. 5, September 1998.

[Cloude, 99] S. R. Cloude, J. Fortuny, J. M. Lopez-Sanchez and A. J. Sieber, "Wide-Band Polarimetric Radar Inversion Studies for Vegetation Layer," *IEEE Transactions on Geoscience and Remote Sensing*, Vol. 37, No. 5, September 1999.

[Colin, 06] E. Colin, C. Titin-Schnaider, and W. Tabbara, "An Interferometric Coherence Optimization Method in Radar Polarimetry for High-Resolution Imagery," *IEEE Transactions on Geoscience and Remote Sensing*, Vol. 44, No. 1, January 2006.

[Coltelli ,96] M. Coltelli, G. Fornaro, G. Franceschetti, R. Lanari, M. Migliaccio, J.R. Moreira, K.P. Papathanassiou, G. Puglisi, D. Riccio, and M. Schuäbisch, "SIR-C/X-SAR multi-frequency multi-pass Interferometry: A new tool for Geological interpretation," *Journal of Geophysical Research*, vol. 101, no. E10, October, 1996.

[Conciauro,03] G. Conciauro and L. Perregrini, *Fondamenti di onde elettromagnetiche*, McGraw-Hill, Milano, 2003.

[Christensen, 02] E.L. Christensen and J. Dall, "EMISAR: a dual-frequency, polarimetric airborne SAR," *Proceedings of IGRS IEEE Symposium Igarss'02*, Toronto, Canada, June 2002.

[Curlander, 91] J.C. Curlander and R.N. McDonough, *Synthetic aperture radar: systems and signal processing*, New Cork, Wiley, 1991.

[CSA] Canadian Space Agency : RadarSAT1/2: http://www.space.gc.ca/asc/eng/satellites/radarsat1/default.asp, / http://www.space.gc.ca/asc/eng/satellites/radarsat2/ default.asp, Convair C/X-SAR: http://www.ccrs.nrcan.gc.ca/radar/airborne/cxsar/ sbc580 e.php

[CXSAR] Canadian CXSAR airborne sensor web-page : http://ccrs.nrcan.gc.ca/radar/airborne/ /cxsar/index_e.php.

[Daba, 94] J.S. Daba and M.R. Bell, "Statistical Distribution of Partially Developed Speckle Based on a Small Number of Constant Scatterers with Random Phase," *Proceedings of IGRS IEEE Symposium Igarss'94*, Pasadena, USA, August 1994.

[Debois, 02] Dubois-Fernandez, P. du Plessis, O.R. le Coz, D. Dupas, J. Vaizan, B. Dupuis, X. Cantalloube, H. Coulombeix, C. Titin-Schnaider, C. Dreuillet, P. Boutry, J.M. Canny, J.P. Kaisersmertz, L. Peyret, J. Martineau, P. Chanteclerc, M. Pastore, L. Bruyant, J.P, "The ONERA RAMSES SAR system," *Proceedings of IGRS IEEE Symposium Igarss'02*, Toronto, Canada, June 2002.

[Delaunay, 34] B. Delaunay: "Sur la sphere vide", *Bulletin of Academy of Sciences of the USSR*, pp. 793-800, 1934.

[Deschamps, 51] G.A.Deschamps, "Geometrical Representation of the Polarization of a Plane Electromagnetic Wave," *Proceedings of the IRE*, Vol.39, May, 1951.

[DLR] Deutsches Zentrum für Luft-und Raumfahrt e.V (DLR) - E-SAR: http://www.dlr.de/hr/en/desktopdefault.aspx/tabid-2326/3776_read-5679/ TerraSAR-X: http://www.dlr.de/tsx/_main/_mission_en.htm.

[ESA] European Space Agency (ESA) - ERS1/2: http://ers.esa.int/ EnviSAT: http://envisat.esa.int/.

[ESAR] German E-SAR airborne sensor: http://www.dlr.de/hr/en/desktopdefault.aspx/tabid-2326/3776_read-5679/

[Fabregas, 95] J.F.Cànovas, *Localización y Clasificación Polarimétric de contros de Dispersión en Blancos Complejos Mediante Imágenes Radar*, PhD Dissertation, Univertsitat Politècnica de Catalunya, Barcelona, Enero, 1995.

[Farnell] http://www.farnell.com/datasheets/7270.pdf

[Ferretti, 00] A. Ferretti, C. Prati, and F. Rocca, "Nonlinear Subsidence Rate Estimation Using Permanent Scatterers in Differential Interferometry," *IEEE Transactions on Geoscience and Remote Sensing*, Vol. 38, No. 5, September 2000.

[Ferretti, 01] A. Ferretti, C. Prati, and F. Rocca, "Permanent Scatterers in SAR Interferometry," *IEEE Transactions on Geoscience and Remote Sensing*, Vol. 39, No. 1, January 2001.

[Ferro-Famil,08] L. Ferro-Famil and M.Neumann, "Recent Advances in the Derivation of POL-inSAR Statistics: Study and Applications," *Proceedings of the 7th European Conference on Synthetic Aperture Radar EUSAR 2008*, Friedrichshafen, Germany, June 2008.

[Franceschetti,99] G. Franceschetti and R. Lanari, *Synthetic Aperture Radar Processing*, CRC Press, Boca Ratón, Florida, 1999.

[Fornaro, 09] G. Fornaro, D. Reale, and F. Serafino, "Four-Dimensional SAR Imaging for Height Estimation and Monitoring of Single and Double Scatterers," *IEEE Transactions on Geoscience and Remote Sensing*, Vol. 40, No. 1, January 2009.

[Freeman, 90] A. Freeman, Y. Shen and C.L. Werner, "Polarimetric SAR Calibration Experiment using Active Radar Calibrators," *IEEE Transactions on Geoscience and Remote Sensing*, Vol. 28, No. 2, May 1990.

[Freeman, 91] A.Freeman, "A New System Model for Radar Polarimeters," *IEEE Transactions on Geoscience and Remote Sensing*, Vol. 29, No. 5, September 1991.

[Freeman, 92] A.Freeman, "SAR Calibration: An Overview," *IEEE Transactions on Geoscience and Remote Sensing*, Vol. 30, No. 6, November 1992.

[Freeman, 98] A. Freeman and S.L. Durden, "A Three-Component Scattering Model for Polarimetric SAR Data," *IEEE Transactions on Geoscience and Remote Sensing*, Vol. 36, No. 3, May 1998.

[Galtelli, 94] F.Gatelli, A. Guarnieri, F. Parizzi, P. Paquali, C. Prati, F. Rocca, 'The wavenumber shift in SAR Interferometry," *IEEE Transactions on Geoscience and Remote Sensing*, Vol. 32, No. 4, July 1994.

[Gierull,02] C. H. Gierull and I. C. Sikaneta:, "Estimating the Effective Number of Looks in Interferometric SAR Data," *IEEE Transactions on Geoscience and Remote Sensing,* vol. 40, No. 8, August 2002.

[Ghiglia, 98] D.C. Ghiglia and M.D. Prit, *Two-Dimensional Phase Unwrapping: Theory, Algorithms and Software*, John Willey & Sons, New York, 1998.

[Goodman, 76] J.W. Goodman, "Some fundamental properties of speckle", *Optical Society* of *America*, Vol. 66, 1145-1150, 1976.

[Gray, 90] Gray A.L., Vachon P.W, Livingstone C.E., and Lukowski T.I., "Synthtic Radar Aperture Calibration Using Reference Reflectors," *IEEE Transactions on Geoscience and Remote Sensing*, Vol. 28, No. 3, May 1990.

[Graves, 56] C.D. Graves, "Radar Polarization Power Scattering Matrix," *Proceedings of the IRE*, Vol.44, February, 1956

[Guissard, 94] A. Guissard, "Mueller and Kennaugh Matrices in Radar Polarimetry," *IEEE Transactions on Geoscience and Remote Sensing*, Vol. 32, No. 3, May 1994.

[Guillaso,05] S. Guillaso, L. Ferro-Famil, A. Reigber, and E. Pottier, "Building Characterization using L-Band Polarimetric Interferometric SAR Data," *IEEE Geoscience and Remote and Remote Sensing Letters*, vol. 2, No. 3, July 2005.

[Hofmann 97] B. Hofmann-Wellenhof, H. Lichtenegger, and J. Collins, *GPS, Theory and Practice,* SpringerWien, NewYork, 97.

[Hall, 66] M.PM Hall, "Variation of the radio refractive index of the troposphere with height," *IEE Electronic Letters*, vol.2, no. 8, August, 1966.

[Hall, 79] M.PM Hall, *Effect of the troposphere on radio communication*, A.Wheaton & Co, Ltd, Exeter, England, 1979.

[Hanssen, 01] R. F. Hanssen, *Radar Interferometry. Data Interpretation and Error Analysis*, The Netherlands: Kluwer Academic Publishers, 2001.

[Holms, 88] W. A. Holm and R.M. Barnes, "On Radar Polarization Mixed State Target Decomposition Techniques," *Proceedings of the IEEE 1988 National Radar Conference*, April 1988.

[Huynen, 70] J.R.Huynen, *Phenomenological Theory on Radar Targets*, PhD Dissertation, Technical University, Delft, The Netherlands, Bronder-offset, Rotterdam, 1970.

[IDS] Ingegneria dei Sistemi Spa : http://www.idscompany.it/

[IEEE,79] IEEE Standard Number 149-1979, "IEEE Standard Test Procedures for Antennas," IEEE, New York, 1979.

[Ishimaru, 78] A. IIshimaru, *Wave Propagation and Scattering in Random Media, Single Scattering and Transport Theory (Vol. 1)*, Academic Press Inc., California, USA, 1978.

[Just, 94] D. Just and R. Balmer, "Phase Statistics of Interferograms with Applications to Synthetic Aperture Radar", *Applied Optics*, Vol. 33, No.20, July 1994.

[JAXA] Japanease Aerospace eXploration Agency (JAXA) Alos: http://www.eorc.jaxa.jp/ ALOS/, JERS1: http://www.jaxa.jp/projects/sat/jers1/ index_e.html.

[Kennaugh,50] E.M. Kennaugh, "Polarization Properties of Radar Reflection Effect of the type of polarization on echo characteristic," *Tech. Rep., Antenna Laboratory*, Ohio State University, 1951.

[Kennaugh, 51] E.M. Kennaugh, "Effect of the type of polarization on echo characteristic," *Tech. Rep., Antenna Laboratory*, Ohio State University, 1951.

[Kennaugh, 54] E.M. Kennaugh, "Research Studies on the Polarization Properties of Radar Targets," Tech. Rep., Electro Science Laboratory, Ohio State University, 1954.

[Krogager, 90] E. Krogager, "New Decomposition of the Radar Target Scattering Matrix," *IEE Electronics Letters*, Vol. 26, August, 1990.

[Krogager, 93] E. Krogager, *Aspect of Polarimetric Radar Imaging*, PhD Dissertation, Technical University of Denmark, Copenhagen, Denmark, 1993.

[Landes, 07] T. Landes, M. Gay, E. Trouvé, J.M. Nicolas, L. Bombrun, G. Vasile, and I. Hajnsek, "Monitoring temperate glaciers by high resolution Pol-InSAR data: First analysis of Argentière E-SAR acquisitions and in-situ measurements," *Proceedings of IGRS IEEE Symposium Igarss'07*, Barcelona, Spain, July 2007.

[Lavalle , 08] M. Lavalle, D. Solimini, and E. Pottier, "PolInSAR for forest biomass retrieval: Model analysis and PALSAR observations" *Proceedings of IGRS IEEE Symposium Igarss'08*, Boston, USA, July 2008.

[Lee, 80] J.S Lee, "Digital Image Enhancement and Noise Filtering by Use of Local Statistics," *IEEE Transactions on Pattern Analysis and Machine Intelligence*, Vol. PAMI-2, No. 2, March 1980.

[Lee, 81] J.S. Lee, "Speckle Analysis and Smoothing of Synthetic Aperture Radar Images," *Computer graphics and image processing*, Vol. 17, 1981.

[Lee, 02] J.S. Lee, S.R. Cloude, K. Papathanassiou, M.R. Grunes, T.L. Ainsworth, and D.L. Schuler, "Speckle Filtering of Polarimetric SAR Interferometry Data," *Proceedings of IGRS IEEE Symposium Igarss'02*, Toronto, Canada, June 2002.

[Lee, 08] H. Lee, J.H. Lee, S.J. Cho, N.H. Sung and, J.H. Kim ,"An Experiment of GB-SAR Interferometric Measurement of Target Displacement and Atmospheric Correction," *Proceedings of IGRS IEEE Symposium Igarss'08*, July, Boston, USA, July 2008..

[Lanari, 96] R. Lanari, G. Fornaro, D. Riccio, M.Migliaccio, K.P. Papathanassiou, J.R. Moreira, M. Schuäbish, L. Dutra, G.Puglisi, G. Franceschetti, and M. Coltelli, "Generation of digital elevation models by using SIR-C/X –SAR multifrequency two-pass Interferometry: the Etna case study, " *Transactions on Geoscience and Remote Sensing*, Vol. 34, No. 5, September 1996.

[Lanari, 04] R. Lanari, O. Mora, M. Manunta, J.J. Mallorqui, P. Bernardino, and E. Sansoni, "A small-baseline approach for investigating deformation on full-resolution differential SAR interferometry," *IEEE Transactions on Geoscience and Remote Sensing*, Vol. 42, No. 7, July 2004.

[Leva, 03] D. Leva, G. Nico, D. Tarchi, J. Fortuny-Guash and A.J. Sieber, "Temporal Analysis of a Landslide by Means of a Ground-Based SAR Interferometer," *IEEE Transactions on Geoscience and Remote Sensing*, Vol. 41, No. 4, April 2003.

[Levanon,04] N. Levanon and E. Mozeson, *Radar Signal*, John Wiley & Sons, Inc., Hoboken, New Jersey, 2004.

[López., 03] C. López-Martínez, *Multidimensional Speckle Noise, Modelling and Filtering Related to SAR Data*, PhD Disseration, Universitat Politècnica de Catalunya, Barcelona, June 2, 2003

[López, 05] C. López-Martínez, E. Pottier, and S.R. Cloude, "Statistical Assessment of Eigenvector-Based Target Decomposition Theorems in Radar Polarimetry," *IEEE Transactions on Geoscience and Remote Sensing*, Vol. 43, No. 9, September 2005.

[López, 07a] C. López-Martínez, A. Cortes and X. Antonio, "Analysis and improvement of polarimetric calibration techniques," *Proceedings of IGRS IEEE Symposium Igarss'07,* Barcelona, Spain, July 2007.

[López, 07b] C. López-Martínez and E. Poitter, "Coherence estimation in synthetic aperture radar data based on speckle noise modeling," *Applied Optics*, Vol. 46, No. 4, February 2007.

[Ludwig, 73] Ludwig A. C., "The Definition of Cross-Polarization," *IEEE Transaction on Antennas and Propagation*, January, 1973.

[Lüneburg, 95] E. Lüneburg, "Principles of Radar Polarimetry: The consimilarity transformation of Radar Polarimetry versus the similarity transformations in optical Polarimetry," *IEICE Transaction on electronics*, vol. E78-C, no. 10, 1995.

[Lüneburg, 02] E. Lüneburg, "Aspect of Radar Polarimetry," Turkish *Journal of Electrical Engineering & Computer Sciences*, vol. 10, No. 2, 2002.

[Luzi, 04] G. Luzi, M. Pieraccini, D. Mecatti, L. Noferini, G. Guidi, F. Moia and C. Atzeni, "Ground-based Radar Interferometry for Landslides Monitoring: Atmospheric and Instrumental Decorrelation Sources on Experimental Data," *IEEE Transactions on Geoscience and Remote Sensing*, Vol. 42, No.11, November 2004.

[Luzi, 07] G. Luzi, M. Pieraccini, D. Mecatti, L. Noferini, G. Macaluso, A. Tamburini, and C. Atzeni, "Monitoring of an Alpine Glacier by Means of Ground-Based SAR Interferometry," IEEE *Geoscience and Remote and Remote Sensing Letters*, Vol. 4, No. 3, July 2007.

[Madsen, 98] S.N.Madsen and H.A.Zebker, "Imaging Radar Interferometry," Chapter 6 in F.M. Henderson and A.J. Lewis, (ed.) "Principles and Applications for Imaging Radar," vol. 2 of *Manual of Remote Sensing*, Third Edition, John Willey and Sons , New York, 1998.

[Margarit, 06] G. Margarit, J.J. Mallorqui, J.M Rius, and J.Sanz-Marcos, "On the Usage of GRECOSAR, an Orbital Polarimetric SAR Simulator of Complex Targets, for Vessel Classification Studies," *IEEE Transactions on Geoscience and Remote Sensing,* Vol. 44, No. 12, December 2006.

[Martinez, 07] A. Martinez and J. Fortuny-Guasch, "Snow avalanche detection and classification algorithm for GB-SAR imagery," *Proceedings of IGRS IEEE Symposium Igarss'07*, Barcelona, Spain, July 2007.

[Martinez, 08] A. Martinez and J. Fortuny-Guasch, "Averaging and Formulation Impact on GB-SAR Topographic Mapping," *IEEE Geoscience and Remote and Remote Sensing Letters*, Vol. 5, No. 4, October 2008.

[Marturia, 05] J. Marturià, O. Mora, D. Xifre, P. Martinez and A. Roca, "DInSAR Techniques versus High Topographic Leveling Surveys: The Subsidence Phenomena in Sallent," *Proceedings of ECONGEO'06*, Barcelona, Spain, June 2006.

[Massonet,93] D. Massonet, M. Rossi, C. Carmona, F. Adragna, G. Peltzer, K. Feigl, and T. Rabaute, "*The displacement field of the Landers earthquake mapped by radar interferometry*," Nature 364, 138-142.

[Mirsky, 90] L. Mirsky, *An Introduction to Linear Algebra*, Courier Dover Publications, 1990.

[Mette, 03] T. Mette, I. Hajnsek, and K. Papathanassiou, "Height-biomass allometry in temperate forests performance accuracy of height-biomass allometry," *Proceedings of IGRS IEEE Symposium Igarss'03*, Toulouse, France, 2003, July 2003.

[Mittermayer,03] J. Mittermayer and H. Runge, "Conceptual studies for exploiting the TerraSAR-X dual receive antenna", *Proceedings of IGRS IEEE Symposium Igarss'03*, Toulouse, France, July 2003.

[Mora, 04] O.Mora, *Advanced Differential Interferometric SAR techniques for detection of terrain and building displacements*, PhD Dissertation, Universitat Politècnica de Catalunya,, Barcelona, 2004.

[Moreira, 96] A. Moreira, J. Mittermayer, and R. Scheiber, "Extended chirp scaling algorithm for air- and spaceborne SAR data processing in stripmap and scanSAR imaging modes," *IEEE Transactions on Geoscience and Remote Sensing*, Vol. 34, No. 5, September,1996.

[Moriyama, 05] T. Moriyama, S. Uratzuka, T. Umehara, H. MAeno, M. Satake, A. Nadai, and K. Nakamura, "Polarimetric SAR Image Analysis Using Model Fit for Urban Structure," *IEICE Transaction on Cmmunications*, Vol. E88-B, No. 3, March 2005.

[NASA] National Aeronautics and Space Administration (NASA) - Sir-C/X-SAR: http://southport.jpl.nasa.gov/sir-c/, AirSAR : http://airsar.jpl.nasa.gov/.

[Nico,04] G. Nico, D. Leva, G. Antonello, and D. Tarchi, "Ground-Based SAR Interferometry for Terrain Mapping: Theory and Sensitivity Analysis", *IEEE Transactions on Geoscience and Remote Sensing*, Vol. 42, No. 6, June 2004.

[Nico, 05] G. Nico, D. Leva, J. Fortuny-Guash, G. Antonello, and D. Tarchi, "Generation of Digital Terrain Models with a Ground-Based SAR System," *IEEE Transactions on Geoscience and Remote Sensing,* Vol. 43, No. 1, January 2005.

[Noferini, 05] L. Noferini, M. Pieraccini, D. Mecatti, G. Luzi, A. Tamburini, and M. Broccolato, "Permanent Scatterers Analysis for Atmospheric Correction in Ground-Based SAR Interferometry*," IEEE Transactions on Geoscience and Remote Sensing*, Vol. 43, No. 7, July 2005.

[Noferini, 07] L. Noferini, M. Pieraccini, D. Mecatti, G. Macaluso, G. Luzi, and C.Atzeni, "DEM by Ground-Based SAR Interferometry," *IEEE Geoscience and Remote and Remote Sensing Letters*, Vol. 4, No. 4, October 2007.

[Oliver, 98] C. Oliver and S. Quegan, *Understanding Synthetic Aperture Radar Images*, Artech House, Boston, USA, 1998.

[Pagani, 90] C.D.Pagani and S.Salsa, *Analisi Matematica I*, Collana di Matematica, Zanichelli, 1990.

[Partington, 98] K.C. Partington, "Antenna beamwidth and antenna pointing-induced errors in topographic monitoring from satellite radar altimeters," *IEEE Geoscience and Remote and Remote Sensing Letters*, Vol. 36, No. 1, January 1998.

[Press, 92] W.H. Press, B.P.Flannery, S.A.Teukolsky, W.T. Vetterling, *Numerical Recipes in C*, Cambridge University Press, 1992.

[Papathanassiou,99] K.P. Papathanassiou, *Polarimetric SAR Interferometry*, PhD Dissertation, Deutsches Zentrum für Luft-undRaumfahrt, Oberpfaffenhofen, 1999.

[Papathanassiou,98] K.P Papathanassiou and M. Zink, "Polarimetric Calibration of the Airborne Experimental SA System of DLR, " *Proceedings of European Conferenceon Synthetic Aperture Rada, EUSAR'98*, Friedrichshafen, Germany, May 1998.

[Papathanassiou,01] K.P Papathanassiou and S.R. Cloude, "Singel-Baseline Polarimetric SAR Interferometry, " *IEEE Transactions on Geoscience and Remote Sensing*, Vol. 39, No. 11, November 2001.

[Papoulis, 84] A. Papoulis, Probability, Random *Variables and Stochastic Process*, McGraw-Hill, 1984.

[Perna, 08] S. Perna, C. Wimmer, J. Moreira, and G. Fornaro. "X-Band Airborne Differential Interferometry: Results of the OrbiSAR Campaign Over the Perugia Area," *IEEE Transactions on Geoscience and Remote Sensing*, Vol. 46, No. 2, February 2008.

[Pieraccini, 01] M.Pieraccini, G. Luzi and, C. Atzeni, "Terrain mapping by Ground-Based Interferometric Radar," *IEEE Transactions on Geoscience and Remote Sensing*, Vol. 39, No. 10, October 2001.

[Pieraccini, 00] M. Pieraccini, G. Luzi and C. Atzeni, "Ground-based interferometric SAR for terrain elevation mapping ," Electronic Letters, vol. 36, No. 16, August 2000.

[Pipia, 05a] L. Pipia, A. Aguasca, X. Fabregas and J.J. Mallorqui, "A Polarimetric Ground-Based SAR System: first results at X-Band," *URSI Commission F Symposium on Microwave Remote Sensing of the Earth, Oceans, Ice, and Atmosphere URSI 2005*, Ispra, Italy, 20-21 April 2005.

[Pipia, 05b] L. Pipia, A. Aguasca, X. Fabregas and J.J. Mallorqui, "Temporal Decorrelation in Polarimetric Differential Interferometry using a Ground-Based SAR Sensor," *Proceedings of IGRS IEEE Symposium Igarss'05*, Seoul, Korea, July 2005.

[Pipia, 06] L. Pipia, X. Fabregas, A. Aguasca and J.J. Mallorqui, "A comparison of different techniques for atmospheric artefact compensation in GBSAR differential acquisitions," *Proceedings of IGRS IEEE Symposium Igarss'06*, Denver, Colorado, USA, 31 July-4 August, 2006.

[Pipia, 08] L. Pipia, X. Fabregas, A. Aguasca and Carlos López-Martínez, "Atmospheric Artefacts Compensation in ground-based DInSAR Applications," *Geoscience and Remote sensing Letters*, Vol.5, Issue 1, Jan.2008.

[Prats, 05] P. Prats Iraola, *Airborne Differential SAR Interferometry*, PhD Dissertation, Universitat Politècnica de Catalunya, Barcelona, November, 1995.

[Prats, 08] Pau Prats, J.J. Mallorqui, Andreas Reigber, Rolf Scheiber, and Alberto Moreira. "Estimation of the Temporal Evolution of the Deformation Using Airborne Differential SAR Interferometry". *IEEE Transactions on Geoscience and Remote Sensing*, Vol. 46, No. 4, April 2008.

[Proakis, 98] J. G. Proakis and D.G. Manolakis, *Tratamento Digital de Señales 3a* ed., Pearson Education S.A., Madrid, 1998.

[Quegan, 94] S. Quegan, "A Unified Algorithm for Phase and Cross-Talk Calibration of Polarimetric Data: Theory and Observations," *IEEE Transactions on Geoscience and Remote Sensing*, Vol. 32, No. 1, July 1994.

[Raney, 92] Raney, R.K., "A New and Fundamental Fourier Pair," *Proceedings of IGRS IEEE Symposium Igarss'92*, Houston, Texas, USA, May 1992.

[Raney, 94] R. K. Raney, H. Runge, R. Bamler, I. Cumming, and F. H. Wong, "Precision SAR processing using chirp scaling," *IEEE Transactions on Geoscience and Remote Sensing*, Vol. 32, No. 4, July 1994.

[Rius, 93] J.M. Rius, M. Ferrando and L. Jofre, "GRECO: graphical electromagnetic computing for RCS prediction in-real time," IEEE *Antennas and Propagation Magazine*, Vol. 35, No. 2, April 1993.

[Rodriguez, 92] E. Rodriguez and J.M. Martín, "Theory and Design of Inteferometric Synthetic Apertur Radars" *IEE Proceedings F*, Vol. 139, No. 2, April 1992.

[Sagues,00] L. Sagués, J.M. Lopez-Sanchez, J. Fortuny, X. Fabregas, A. Broquetas and A.J. Sieber, "Indoor Experiment on Polarimetric SAR Interferometry," *IEEE Transactions on Geoscience and Remote Sensing*,, Vol. 38, No. 2, March 2000.

[Sarkar, 84] T.P. Sarkar and S.M. Rao, "The application of the Conjugate Gradient Method for the solution of the electromagnetic scattering from arbitrarily oriented wire antennas," IEEE Transactions on Antennas and Propagation, Vol. 32, No.4, April 1984.

[Sarabandi, 90] K. Sarabandi, F.T. Ulaby, M.A. Tassouji, "Calibration of Polarimetric Radar System with Good Polarization Isolation," *Transactions on Geoscience and Remote Sensing*, Vol. 28, No. 1, January 1990.

[Seymour, 94] M. Seymour and I. Cumming, "Maximum Likelihood Estimation for SAR Interferometry," *Proceedings of IGRS IEEE Symposium Igarss'94*, Vol. 4, 2–2275.

[Schwäbisch, 95] M. Schwäbisch and D. Geudtner, "Improvement of phase and coherence map using azimuth prefiltering: examples from ERS-1 and X-SAR", *International Geoscience And Remote Sensing Symposium IGARSS*'95, Florence, 1995.

[Sheiber, 00] R. Scheiber and A. Moreira, "Corregistration of Interferometric SAR Images Using Spectral Diversity," *IEEE Transactions on Geoscience and Remote Sensing*, Vol. 38, No. 5, Vol. 38, No. 5, September 2000.

[Silverstein, 97] J.D. Silverstein, "Measurements and Predictions of the RCS of Bruderhedrals at Millimetric Wavelength", *IEEE Transaction on Antennas and Propagation*, Vol. 45, No.7, July 1997.

[Schreier, 93] G. Schreier, *SAR Geocoding: Data and System*, Wichmann, 1993.

[Schmeider, 69] R. Schmeider, "Stokes Algebra Formalism," Journal of the Optical Society of America, vol. 59, 1969.

[Sidjadi, 06] F. Sadjadi, C.C.S. Chun, A. Sullivan, and G.C. Gaunaurd, "Classifying dielectric mine-like objects using the Huynen-Fork polarization parameters," *Proceedings on IEEE 2006 Radar Conference,* April, 2006.

[Sinclair, 50] G. Sinclair, "The Transmission and Reception of Elliptically Polarized Waves," Proc. IRE, vol. 38,1950.

[SIR-C/X-SAR] http://www.jpl.nasa.gov/radar/sircxsar/.

[Skolnik, 90] M. *Skolnik*, *Radar Handbook*, Mc Graw-Hill. 1990.

[Soumek, 99] M. Soumekh, *Synthetic Aperture Radar Signal Processing*, John Wiley & Sons Inc., New York,1999.

[Stolt, 78] R. Stolt, "Migration by Fourier transform techniques," *Geophysics*, Vol. 43, No. 1978.

[Tarchi, 00] D. Tarchi, H. Rudolf, M. Pieraccini, and C. Atzeni, "Remote monitoring of buildings using a Ground-Based SAR: application to cultural heritage survey," *International Journal of Remote Sensing,* Vol.21, No. 18, 2000.

[TOPSAR] USA TOPSAR airborne sensor web-page: http://southport.jpl.nasa.gov/airsar/topsar/.

[Tough, 95] R.J.A. Tough, D. Blacknell, and S. Quegan, "A Statistical Description of Polarimetric and Interferometric Synthetic Aperture Radar Data," *Proceedings of the Royal Society of London. Series A*, Vol. 449, No. 1937, pp. 567-589, 1995.

[Touzi, 99] R. Touzi, A. Lopes, J. Bruniquel, and P.W. Vachon, "Coherence Estimation for SAR Imagery," *IEEE Transactions on Geoscience and Remote Sensing*, Vol. 37. No. 1, January, 1999.

[Touzi,07] R. Touzi, "Target Scattering Decomposition in Terms of Roll-Invariant Target Parameters," *IEEE Transactions on Geoscience and Remote Sensing*, Vol. 45. No. 1, January, 2007.

[Ulaby, 90] F. T. Ulaby and C. Elachi, *Radar Polarimetry for Geoscience Applications*, Norwood MA: Artech House, 1990.

[Ulaby, 82] F.T Ulaby, R.K. Moore and A.K. Fung, *Microwave Remote Sensing – Active and Passive*, Norwood MA: Artech House, 1982.

[Urlander, 03] H. Ulander, H. Hellsten, and G.S. Tenström, "Synthetic-Aperture Radar Processing Using Fast Factorized Back-Projection," *IEEE Transaction on Aerospace and Electronic Systems*, Vol.39, N.3, July 2003.

[Yegulalp, 99] A.F. Yegulalp, "Fast Backprojection Algorithm for Synthetic Aperture Radar", *The record of the 1999 IEEE Radar Conference*, Waltham, 20-22 April 1999

[Zebker, 86] H. Zebker, and R.M. Goldsteing, "Topographic Mapping from Inteferometric Synthetic Aperture Radar Observations," J*ournal of Geophysical Research*, vol. 91, 1986

[Zebker, 87] H. Zebker, J.J. Van Zyl, and D.N. Held, "Imaging Radar Polarimetry from Wave Synthesis," *Journal of Physical Research*, vol.42, 1987.

[Zhou ,04] Z.S. Zhou, W.M. Boerner and M. Sato, "Development of a Ground-Based Polarimetric Broadband SAR System for Non-invasive Ground-Truth Validation in Vegetation Monitoring," *IEEE Transactions on Geoscience and Remote Sensing,* Vol. 42, No. 9, September 2004.

[Zhou, 05] Z.S. Zhou and S.R. Cloude, "The Development of a Ground Based Polarimetric SAR Interferometer (GB-POLInSAR)," *Proceedings of IGRS IEEE Symposium Igarss'05*, Seoul, Korea, July 2005.

[Zyl, 87] J.J. van Zyl, H. Zebker, and C. Elachi, "Imaging Radar Polarization Signatures: Theory and Application," Radio Science, Vol. 22, No. 4, 1987.

[Zyl, 89] J.J. van Zyl, "Unsupervised Classification of Scattering Behavior Using Radar Polarimetry Data" *IEEE Transactions on Geoscience and Remote Sensing,* Vol. 27, No. 1, 1989.

[Zyl, 90] J.J. van Zyl, "Calibration of Polarimetric Radar Images Using Only Images Parameters and Trihedral Corner Reflectors Response," *IEEE Transactions on Geoscience and Remote Sensing,* Vol. 28, No. 3, 1990.